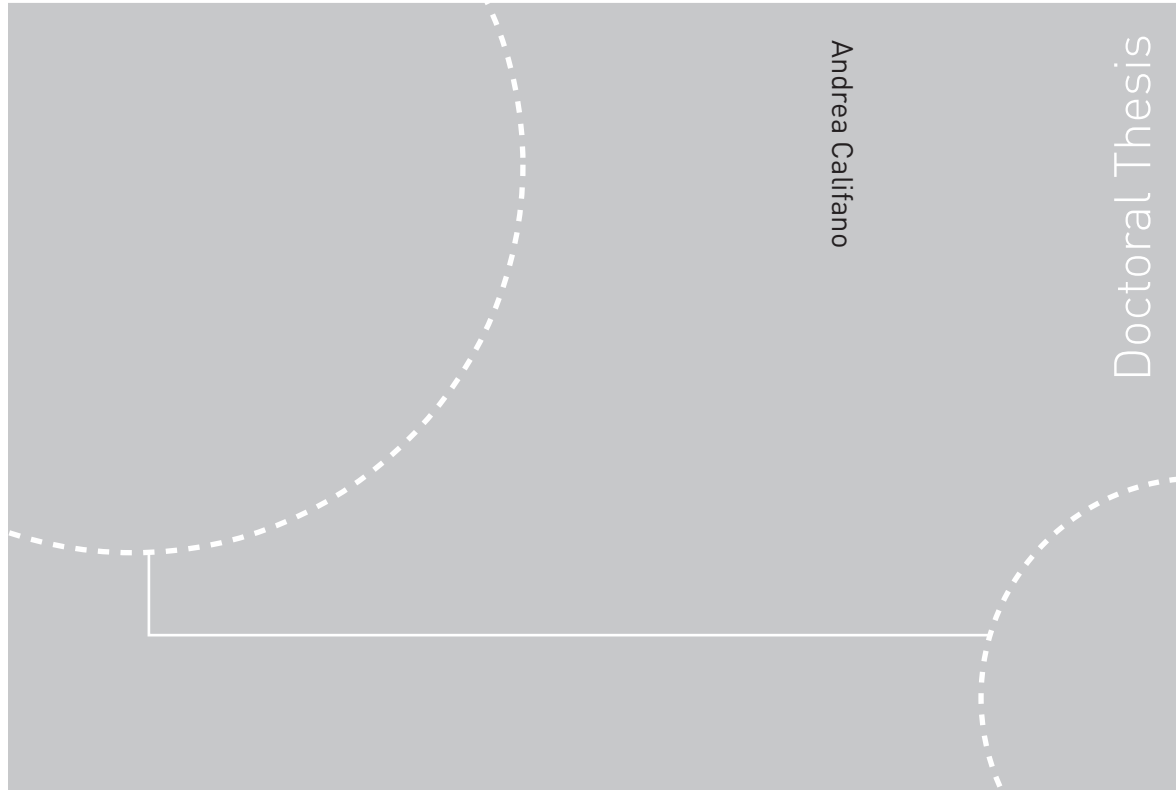


Doctoral theses at NTNU, 2010:252

Andrea Califano  
**Dynamic loads on marine propellers  
due to intermittent ventilation**



ISBN 978-82-471-2504-5 (printed ver.)  
ISBN 978-82-471-2505-2 (electronic ver.)  
ISSN 1503-8181

NTNU  
Norwegian University of  
Science and Technology  
Thesis for the degree of  
philosophiae doctor  
Faculty of Engineering Science and Technology  
Department of Marine Technology

Doctoral theses at NTNU, 2010:252

NTNU

 **NTNU**  
Norwegian University of  
Science and Technology

 **NTNU**  
Norwegian University of  
Science and Technology

Andrea Califano

# Dynamic loads on marine propellers due to intermittent ventilation

Thesis for the degree of philosophiae doctor

Trondheim, December 2010

Norwegian University of  
Science and Technology  
Faculty of Engineering Science and Technology  
Department of Marine Technology



Norwegian University of  
Science and Technology

**NTNU**

Norwegian University of Science and Technology

Thesis for the degree of philosophiae doctor

Faculty of Engineering Science and Technology  
Department of Marine Technology

©Andrea Califano

ISBN 978-82-471-2504-5 (printed ver.)

ISBN 978-82-471-2505-2 (electronic ver.)

ISSN 1503-8181

Doctoral Theses at NTNU, 2010:252

Printed by Tapir Uttrykk

---

## Abstract

Dynamic Positioning (DP) systems are increasingly replacing traditional position-keeping methods—such as jack-up barges and anchoring systems—on board ships operating in ever deeper waters. During these operations, the combined effect of heavy sea states and high propeller loadings have caused a number of damages on azimuth and tunnel thrusters, causing service downtime and requiring costly repairs. Damages in rough seas were reported also during transit operations.

These damages can be caused by dynamic loads on the propeller due to intermittent *ventilation*. Ventilation occurs on thrusters operating at high loadings and low submergence, experiencing continuous cycles in- and out-of water. This leads to sudden thrust losses and violent impact loads.

The present work aims at modeling the dynamic loads during propeller ventilation, in order to predict the corresponding losses. Model tests and numerical simulations were performed in order to better understand the mechanisms of dynamic forces due to ventilation. Furthermore, numerical simulations carry on the challenge of applying a Volume of Fluid (VOF) method to this type of problem.

The performed model tests have shown two main ventilation mechanisms, depending on the propeller submergence, loading and advance ratio: *(i)* at deeper submergence through a free-surface vortex and *(ii)* at moderate submergences through the blade itself piercing the free surface. These two mechanisms can exist separately or at the same time, identifying three distinctive ventilation regimes.

The performed numerical simulations are able to reproduce the main features observed during the experiments: air is drawn from the free-surface and transported along the propeller rotation, for both the ventilation types previously identified. The dynamic loads computed with the numerical model are in satisfactory agreement with the experimental data at the upright position where the blade is piercing the free-surface, whereas thrust is over-estimated at all the other angular positions. Unlike ventilation of surface-piercing propellers with super-cavitating profile, it was found that the tip-vortex has a dominant role in the type of ventilation object of this study.

The tip-vortex was also identified as the most likely factor responsible for the over-estimation found in the numerical simulations of the thrust for the angular positions where the blade is deeply submerged. Other causes for the deviation between numerical simulations and experiments are further discussed.

A qualitative model of the dynamic loads occurring during one propeller revolution was derived, based on the impact of the blade with the air entrained by the tip vortex, leading to two main thrust losses: *(i)* an absolute minimum loss about the angular position of  $\pi/4$  and *(ii)* a local minimum loss about  $3/2 \pi$ .

## Acknowledgments

This work was carried out on a university scholarship, within the Rolls-Royce University Technology Centre in Trondheim. The support from Rolls-Royce Marine, covering experiments and additional funding, is gratefully acknowledged. The support of the Norwegian HPC project NOTUR that granted access to its computer facilities in order to perform long-time calculations is also acknowledged.

I would like to thank my supervisor, Professor Sverre Steen, for giving me the opportunity to perform the present work and for providing useful discussions and suggestions while writing the thesis. A special thanks goes to Professor Mariilena Greco, for the motivation received to accomplish this thesis and for valuable discussions throughout the present work.

The work of the technicians at the MCLab and the support received from the NTNU's IT-department is highly appreciated, providing qualified assistance to perform the experiments and for the computer facilities. Dr. Kourosh Koushan is acknowledged for providing initial experimental data, useful to approach the problem of propeller ventilation from the very beginning. Results from recent experiments were provided by Anna Kozłowska, who is acknowledged also for sharing discussions about ventilation tests. I would also like to thank all my colleagues and friends within the Department of Marine Technology for making the office an enjoyable place to work.

Vorrei ringraziare i miei genitori per il loro supporto, rimasto incondizionato dalla distanza che ci separa. Un ringraziamento speciale va a Marit, per avermi accompagnato con amore anche durante questa esperienza, a Diana e Sunniva, per avermi ricordato durante questi anni di dare alle cose importanti il giusto valore, e a Emre e Aris, per aver portato più luce al nostro futuro.

Trondheim, November 2010  
Andrea Califano

# Contents

<b>1</b>	<b>Introduction</b>	<b>1</b>
1.1	Motivation and background . . . . .	1
1.2	Propeller ventilation . . . . .	4
1.3	Present work . . . . .	6
<b>2</b>	<b>Ventilation theory</b>	<b>11</b>
2.1	Dimensionless parameters . . . . .	12
2.1.1	Scale effects . . . . .	16
2.2	Historical background . . . . .	17
2.2.1	Numerical methods . . . . .	21
2.3	Thrust loss . . . . .	22
2.3.1	Loss of effective disc area . . . . .	23
2.3.2	Hysteresis effect . . . . .	23
2.3.3	Ventilation losses . . . . .	24
2.4	Regimes . . . . .	25
2.5	Momentum theory . . . . .	28
2.6	Inlet Vortex . . . . .	29
2.6.1	Pump sumps . . . . .	30
2.6.2	Ground vortex . . . . .	31
2.6.2.1	Stagnation points . . . . .	32
2.6.2.2	Ambient vorticity and amplification . . . . .	33
2.6.2.3	Ground boundary layer . . . . .	35
2.6.2.4	Unsteadiness . . . . .	35
2.6.2.5	Occurrence and direction of vortex . . . . .	36
2.6.3	Marine propellers . . . . .	37
2.6.3.1	Ventilation inception by vortex formation . . . . .	38
2.7	Dynamic loads . . . . .	39

<b>3</b>	<b>Verification studies</b>	<b>41</b>
3.1	Submerged hydrofoil . . . . .	41
3.1.1	Numerical method . . . . .	43
3.1.2	Results . . . . .	46
3.1.2.1	Fluent . . . . .	46
3.1.2.2	OpenFOAM . . . . .	51
3.1.2.3	$h/c = 0.911$ . . . . .	57
3.1.3	Summary . . . . .	59
3.2	Propeller in open water . . . . .	59
3.2.1	Propeller model . . . . .	59
3.2.2	Numerical method . . . . .	60
3.2.3	Results . . . . .	62
3.2.3.1	Under-estimation of the torque . . . . .	63
3.2.3.2	Sensitivity analysis . . . . .	65
3.2.3.3	OpenFOAM . . . . .	67
3.2.4	Summary . . . . .	72
<b>4</b>	<b>Model tests</b>	<b>73</b>
4.1	Test matrix . . . . .	73
4.2	Experimental set-up . . . . .	74
4.2.1	Test procedure . . . . .	79
4.3	Data analysis . . . . .	79
4.3.1	Filtering . . . . .	80
4.3.2	Angle correction . . . . .	82
4.4	Main results . . . . .	83
4.4.1	Effect of submergence . . . . .	104
4.5	Ventilation inception . . . . .	106
4.5.1	Surface-piercing . . . . .	106
4.5.1.1	Effect of acceleration . . . . .	110
4.5.2	Vortex formation . . . . .	112
4.6	Summary . . . . .	116
<b>5</b>	<b>Numerical simulations</b>	<b>117</b>
5.1	Numerical method . . . . .	117
5.1.1	Solver . . . . .	117
5.1.2	Grid . . . . .	117
5.1.3	Boundary conditions . . . . .	118
5.1.4	Turbulence . . . . .	118
5.1.5	Solution of the Navier-Stokes equations . . . . .	119
5.1.5.1	Pressure-velocity coupling . . . . .	119
5.2	Fully-ventilating propeller . . . . .	121

---

5.2.1	Multiple Reference Frame . . . . .	122
5.2.2	Sliding Mesh . . . . .	124
5.2.3	Turbulence . . . . .	130
5.2.4	Surface tension . . . . .	131
5.2.5	Grid refinement . . . . .	132
5.2.6	Integration time-step . . . . .	133
5.2.7	Under-relaxation factors . . . . .	137
5.3	Surface-piercing propeller . . . . .	143
5.4	Ventilation inception . . . . .	146
5.4.1	Surface-piercing . . . . .	146
5.4.2	Vortex formation . . . . .	149
5.4.3	Comparison . . . . .	154
5.5	Summary . . . . .	155
<b>6</b>	<b>Discussion</b> . . . . .	<b>157</b>
6.1	Dynamic loads . . . . .	157
6.2	Comparison . . . . .	160
6.2.1	Simulation time . . . . .	162
6.2.2	Turbulence . . . . .	162
6.2.3	Cavitation . . . . .	162
6.2.4	Air loss . . . . .	163
6.2.4.1	Through the sliding interface . . . . .	163
6.2.4.2	Within the rotating domain . . . . .	165
6.2.5	Bubbly flow . . . . .	165
6.2.6	Compressibility . . . . .	167
6.2.7	Pressure drop . . . . .	172
6.2.7.1	Tip vortex . . . . .	173
<b>7</b>	<b>Conclusions</b> . . . . .	<b>179</b>
7.1	Summary . . . . .	179
7.2	Recommendations for future work . . . . .	181
<b>A</b>	<b>Experimental results</b> . . . . .	<b>185</b>
A.1	Constant shaft frequency . . . . .	185
A.2	Linear accelerations . . . . .	200
A.3	Effect of submergence [ $J=0.1$ , $n=14$ Hz] . . . . .	203



# Nomenclature

## Acronyms

1D	One dimensional
2D	Two dimensional
3D	Three dimensional
AKPA	AK Propulsor Analysis
BEM	Boundary Element Method
BFW	Body Force Weighted
<i>Cal09</i>	Ventilation tests performed by Califano and Kozłowska in 2009
CFD	Computational Fluid Dynamics
DAQ	Data Acquisition
DNS	Direct Numerical Simulation
DP	Dynamic Positioning
EWT	Enhanced Wall Treatment
HBM	Hottinger Baldwin Messtechnik
HRIC	High Resolution Interface Capturing
KaMeWa	Karlstad Mekaniska Werkstads Aktiebolag, now part of RRM
<i>Kou05</i>	Ventilation tests performed by Koushan in 2005
<i>Koz10</i>	Ventilation tests performed by Kozłowska in 2010
LDA	Laser Doppler Anemometry

- LES Large Eddy Simulations
- MRF Multiple Reference Frame
- MARINTEK Norwegian Marine Technology Research Institute
- MCLab Marine Cybernetics Laboratory
- MULES Multidimensional Universal Limiter for Explicit Solution
- N-S Navier-Stokes
- NTNU Norwegian University of Science and Technology
- PIV Particle Image Velocimetry
- PPE Pressure Poisson Equation
- PC Personal Computer
- PDE Partial Differential Equation
- PISO Pressure Implicit with Splitting of Operators
- RANS Reynolds-Averaged Navier-Stokes equations
- RR Rolls-Royce
- RRM Rolls-Royce Marine
- SM Sliding Mesh
- SIMPLE Semi-Implicit Method for Pressure-Linked Equations
- SST Shear Stress Transport
- SWF Standard Wall Function
- TIFF Tooth Interior Fatigue Fracture
- URF Under-Relaxation Factor
- UTC University Technology Centre
- VOF Volume Of Fluid

**Greek letters**

- $\alpha$  Under-Relaxation Factor

$\beta$	Reduced thrust	$\beta_0\beta_v\beta_H$
$\beta_0$	Reduced thrust due to loss of effective disc area	
$\beta_1$	Reduced thrust due to steady wave motion	
$\beta_H$	Reduced thrust due to hysteresis	
$\beta_Q$	Reduced torque	$K_Q/K_{Q_0}$
$\beta_T$	Reduced Thrust	$K_T/K_{T_0}$
$\beta_v$	Reduced thrust due to ventilation	
$\Delta t$	Time-step size	[s]
$\Delta p$	Pressure jump imposed on the propeller plane	[Pa]
$\eta$	First trough amplitude	[m]
$\eta$	Propeller efficiency	$\frac{J}{2\pi} \frac{K_T}{K_Q}$
$\phi$	Generic variable	
$\phi$	Velocity flux	[Kg/m <sup>2</sup> ·s]
$\Gamma$	Span-wise circulation	[m <sup>2</sup> /s]
$\gamma$	Circulation	[m <sup>2</sup> /s]
$\gamma$	Heat specific ratio	$c_p/c_V$
$\gamma$	Phase fraction	
$\lambda$	Scale factor between lengths in model and full scale	$L_s/L_m$
$\lambda_2$	Second eigenvalue of the tensor $S^2 + \Omega^2$	
$\mu$	Dynamic viscosity	[Pa·s]
$\nu$	Kinematic viscosity	[m <sup>2</sup> /s]
$\Omega$	Antisymmetric component of the velocity gradient tensor	[1/s]
$\pi$		3.1416
$\rho$	Mass density	[Kg/m <sup>3</sup> ]
$\sigma$	Standard deviation	

$\sigma$	Surface tension	[N/m]
$\sigma_{cav}$	Cavitation number	$\frac{p_0 + \rho gh - p_v}{1/2 \rho (2\pi nr)^2}$
$\sigma_{vent}$	Ventilation number	$\frac{2gh}{(2\pi nr)^2}$
$\tau$	Shear stress	[Pa]

### Latin letters

$A$	Coefficient for the discrete velocity in the SIMPLE algorithm	
$a$	Sound speed	[m/s]
$A_0$	Propeller disc area	[m <sup>2</sup> ]
$A_1$	Immersed disc area	[m <sup>2</sup> ]
$b$	Breadth of the dead water region	[m]
$c$	Chord length	[m]
$c$	Specific heat capacity	[J/Kg·K]
$C_F$	Drag coefficient due to skin friction	
$C_f$	Skin friction coefficient	$\frac{\tau_w}{\frac{1}{2} \rho U^2}$
$C_L$	Lift coefficient	
$Co$	Courant number	
$C_p$	Pressure coefficient	$\frac{p - p_\infty}{\frac{1}{2} \rho (nD)^2}$
CR	Capture Ratio	
$C_T$	Propeller loading	$\frac{\Delta p}{1/2 \rho (nD)^2}$
$D$	Propeller diameter	[m]
$E$	Bulk modulus	[Pa]
EAR	Expanded blade Area Ratio	
$f$	Maximum camber	[m]
$F_f$	Volumetric flow rate through the face $f$	[m <sup>3</sup> /s]

$Fr$	Froude number	$\frac{nD}{\sqrt{gD}}$
$Fr_h$	Froude number based on submergence	$\frac{nD}{\sqrt{gh}}$
$g$	Acceleration of gravity	9.81 [m/s <sup>2</sup> ]
$h$	Foil submergence	[m]
$h$	Propeller shaft submergence	[m]
$H_{1/3}$	Significant wave height	[m]
$I$	Submergence ratio	$h/R$
$J$	Advance ratio	$U/nD$
$k$	Constant	
$k$	Current time level	
$K_Q$	Torque coefficient	$\frac{Q}{\rho n^2 D^5}$
$K_T$	Thrust coefficient	$\frac{T}{\rho n^2 D^4}$
$\ell$	Length of a flat plate	[m]
$L$	Characteristic length	[m]
$M$	Mach number	
$m$	Mass	[Kg]
$\dot{n}$	Shaft angular acceleration	[rad/s <sup>2</sup> ]
$N$	Number of blades	
$n$	Shaft frequency	[1/s]
$n^*$	Default shaft frequency	[1/s]
$n_0$	Target shaft frequency	[1/s]
$nD$	Reference velocity (tangential)	[m/s]
$P$	Pitch	[m]
$p$	Pressure	[Pa]

$p_0$	Atmospheric pressure	[Pa]
$p_v$	Vapor pressure	[Pa]
$Q$	Torque	[N·m]
$\mathcal{R}$	Ideal gas constant	8.314 [J/K·mol]
$R$	Propeller radius	[m]
$r$	Blade radial position	[m]
$r$	Radius of curvature	[m]
$Re$	Reynolds number	$\frac{nD^2}{\nu}$
$Ro$	Rosby number	$\frac{U_i}{WD}$
$S$	Symmetric component of the velocity gradient tensor	[1/s]
$s$	Linear skew	[m]
$T$	Absolute temperature	[K]
$T$	Period of a linear wave having the same phase speed as the breaker	[s]
$T$	Thrust	[N]
$t$	Maximum thickness	[m]
$t$	Time	[s]
$U$	Free-stream velocity	[m/s]
$V$	Volume	[m <sup>3</sup> ]
$W$	Free-stream velocity gradient	[1/s]
$We$	Weber number	$nD\sqrt{D\frac{\rho}{\sigma}}$
$x$	Longitudinal coordinate	[m]
$x$	Reduced thrust due to Wagner effect	
$y$	Lateral coordinate	[m]
$y^+$	Non-dimensional wall distance	$\frac{y}{\nu}\sqrt{\frac{\tau_w}{\rho}}$

$z$	Vertical coordinate	[m]
$z_+$	Free-surface vortex rotating along $+z$	
$z_-$	Free-surface vortex rotating along $-z$	

### Operators

$\nabla \cdot$	Divergence
$\sim$	Dimensionless
$d$	Derivative
$\nabla$	Gradient
$-$	Horizontal average (along index $i$ )
$\nabla^2$	Laplace
$\partial$	Partial derivative
$\Re$	Real part
$\Sigma$	Sum
$\cdot$	Time derivative
$\rightarrow$	Vector
$\sim$	Vertical average (along index $j$ )

### Super-Subscript

'	Correction variable
$\infty$	Far upstream
0.7	70% of the radius
1	Blade 1, object of measurement
2	Blade 2, $\pi/2$ rad from $Blade_1$
3	Blade 3, $\pi$ rad from $Blade_1$
4	Blade 4, $3\pi/2$ rad from $Blade_1$
$A$	Axial

<i>a</i>	Stagnation point
<i>air</i>	Air
<i>c</i>	Cell index
<i>dyn</i>	Dynamic
<i>F</i>	Free vortices
$\gamma$	Phase fraction
<i>g</i>	Gaseous phase
<i>h</i>	Hub
<i>i</i>	Index prescribing $x$ direction
<i>i</i>	Inlet
<i>j</i>	Index prescribing $y$ direction
<i>k</i>	Current time level
$\ell$	Index prescribing $x, y$ and $z$ directions, $\ell = 1, 2, 3$
<i>l</i>	Liquid phase
<i>m</i>	Exponent connecting torque to thrust losses
<i>m</i>	Model scale
<i>P</i>	Constant pressure
<i>p</i>	Pressure
<i>rb</i>	Surface normal
*	Initial estimate
<i>s</i>	Full scale
<i>tip</i>	Tip of the blade
<i>u</i>	Velocity along $x$
<i>V</i>	Constant volume
<i>v</i>	Velocity along $y$
<i>w</i>	Wall

# Chapter 1

## Introduction

### 1.1 Motivation and background

In the last 40 years—since the extraction of oil and natural gas from reserves located in the sea had started—Norway has seen an increasing number of offshore platforms along its coast-lines. A rapidly improving technology has allowed for drilling in ever deeper waters, located offshore, characterized by heavy sea states. As an indication, the probability of the significant wave height  $H_{1/3}$  being larger than 2 m in the North Sea is 0.59 (Faltinsen, 1990).

As a consequence, ship operations offshore (Figure 1.1) have also increased, and traditional position-keeping methods such as jack-up barges and anchoring systems became inadequate for those depths, leaving room to Dynamic Positioning (DP) systems.



Figure 1.1: Supply vessel operating in heavy sea, where the emersion of the tunnel thrusters on the bow can be observed. Courtesy of Rolls-Royce Marine (RRM).

Propellers might be required to operate at very high loadings by the DP system in order to maintain a vessel's position and heading in heavy sea states, where thrusters can experience continuous cycles of water-exit and re-entry. In these conditions, a number of accidents with damages to the lower bevel gear and propeller shaft bearings of azimuth and tunnel thrusters (Figure 1.2) have been reported, causing service downtime and requiring costly repairs. Damages caused by transit operations in extremely rough seas have also been reported.



(a) Ulstein Aquamaster azimuth thruster.



(b) Ulstein KaMeWa tunnel thruster.

Figure 1.2: An example of azimuth and tunnel thrusters from RRM.

Based on the analysis of damaged gear wheels, damages are identified as a Tooth Interior Fatigue Fracture (TIFF, Figure 1.3), which is a failure mode believed to be initiated as a fatigue crack in the interior of the tooth of a gear (MackAldener and Olsson, 2000, 2002). The mechanical driving forces for the crack are twofold: (i) a constant residual tensile stress in the interior of the tooth due to case hardening and (ii) alternating stresses due to the idler usage (gears with teeth loaded on both its flanks during each revolution). The crack will continue to propagate towards the flank until it reaches the case-hardening layer where it deflects. When the ultimate failure appears the crack will continue to the surface. Although marine propellers are not subject to idler usage (ii), alternating stresses can arise from excessive torsional vibrations, causing meshing gears to loose contact and re-engage with considerable energy-impact (gear hammering). Large torques and sudden variations of the load conditions can be caused by intermittent *ventilation*, which

occurs on thrusters experiencing continuous cycles of water- exit and re-entry during severe wave-vessel interactions. This leads to sudden thrust losses (Figure 1.4) and violent impact loads. Ventilation has been observed on fully submerged propellers operating at low advance speed and high loadings, thus the propeller does not necessarily require to be surface-piercing for ventilation to occur.

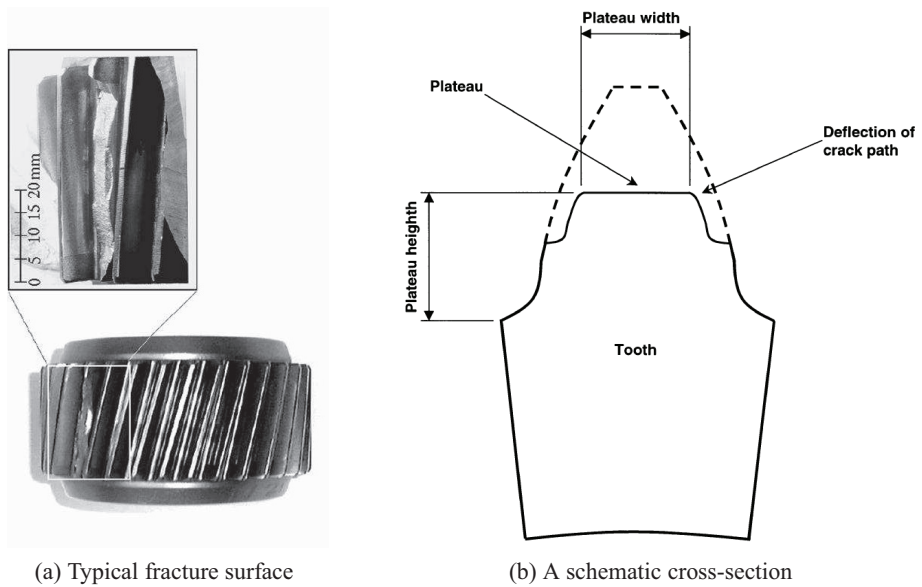


Figure 1.3: TUFF (MackAldener and Olsson, 2000).

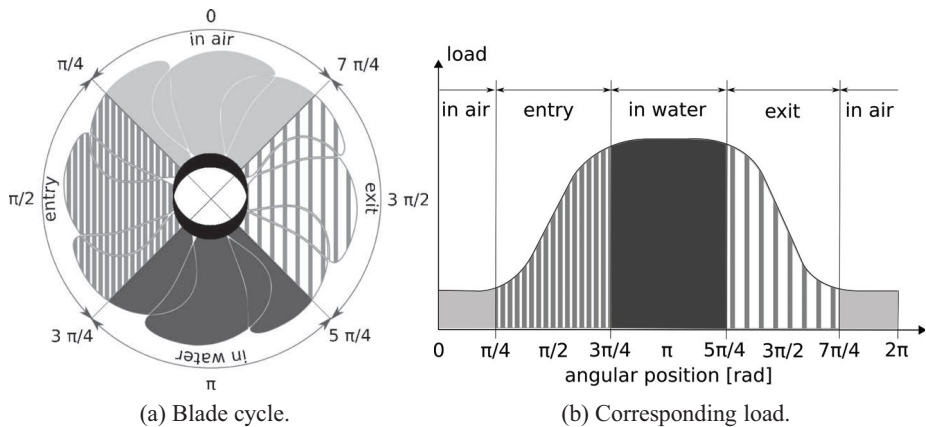


Figure 1.4: Dynamic loads on a surface-piercing propeller (Olofsson, 1996).

Traditionally, ships and propulsion units have been optimized for operations in calm water. Operations in heavy seas have only been accounted for using crude safety factors. While the average thrust loss and loss of efficiency can be estimated using semi-empirical methods, there is little knowledge on how to calculate the dynamic loads. There is also a need for more knowledge of the physics and dynamics of the ventilating propeller in order to identify proper operational strategies and active control systems to reduce the damaging load variations on the propellers. A better knowledge of the mechanisms leading to ventilation inception can help the design of more efficient motor controller able to prevent, or reduce, the occurrence of ventilation.

Another aspect is the state-of-the-art of the development of propeller theory and computation tools. As it is illustrated in Figure 1.5, the advances in propeller computational tools have now become mature enough for a proper modeling of dynamics due to waves and ship motions and related effects.

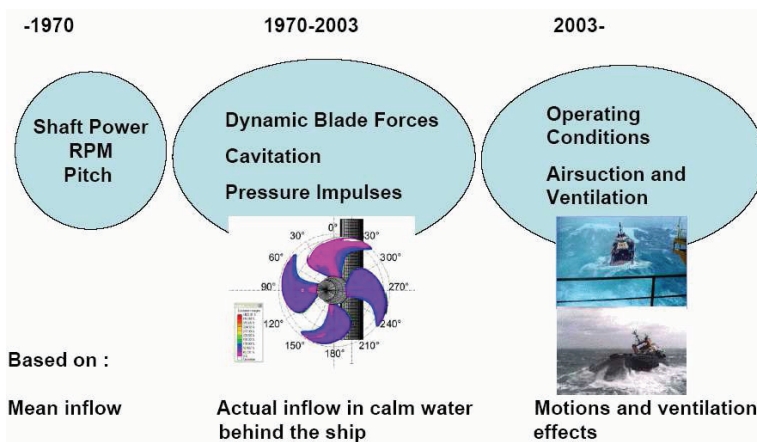


Figure 1.5: Development of propeller theory and computational tools. Courtesy of Kjell Olav Holden.

## 1.2 Propeller ventilation

Propeller ventilation has been historically related to surface-piercing, partially submerged propellers, which were first employed on shallow draught ships, and in a second stage for high-speed craft, with supercavitating-type profile. It is only recently that ventilation of conventional thrusters has gained much attention, due to the increasing demand of offshore vessels and the new challenges encountered.

Shiba (1953) has carried out a comprehensive experimental study of propeller ventilation, including sections with different profiles and analyzing the various

parameters affecting the phenomenon.

Later, during the 1970s, propulsion in a seaway, and the related average loss of thrust and efficiency was studied quite extensively in Germany (Gutsche, 1967; Fleischer, 1973) and in Norway (Faltinsen et al., 1981; Minsaas et al., 1983, 1987). The effort made in understanding and modeling ventilation led to modeling the time-average thrust loss  $\beta = K_T/K_{T_0}$  as a function of the submergence-to-radius ratio  $h/R$  (Figure 1.6), by means of the loss of disc area (Gutsche, 1967) and further including the losses due to the Wagner effect (Minsaas et al., 1983).

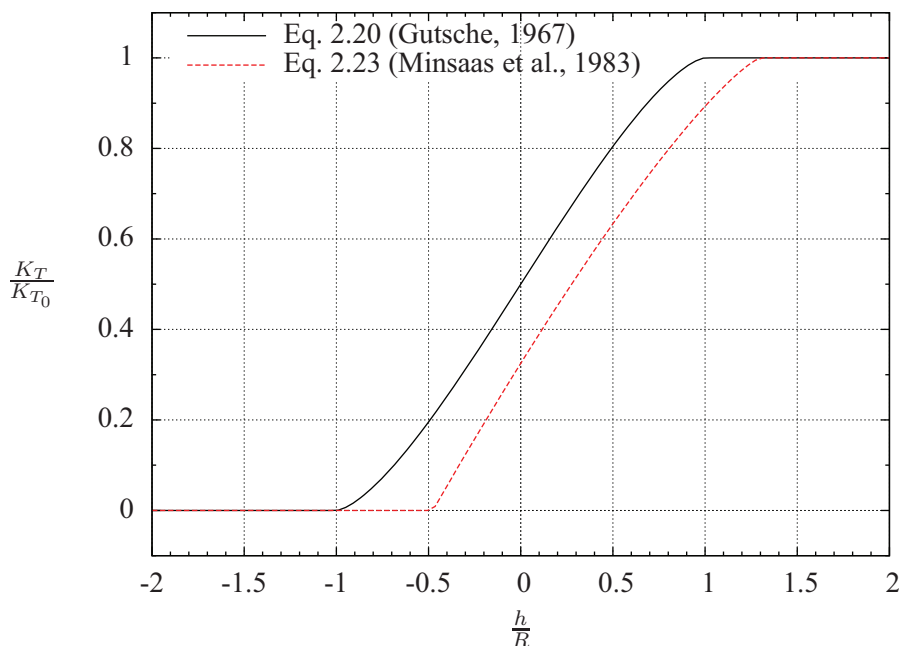


Figure 1.6: Thrust losses according to Eq. 2.20 (Gutsche, 1967) and Eq. 2.23 (Minsaas et al., 1983).

More recently, Koushan performed experiments and measured the dynamic loads of a ventilated propeller in open water (Koushan, 2006b) and with the presence of a duct (Koushan, 2006a), taking into account the influence of factors normally encountered in a seaway, such as waves and thruster azimuthing angle (Koushan, 2006c, 2007b,a), in addition to those commonly used (submergence and advance ratio).

Due to its nature being inherently non-linear and time dependent, the numerical modeling of ventilation is a difficult task. The presence of air cavities, spray and waves makes the mathematical formulation of the phenomenon a real challenge.

Since the beginning of the 1960s, modeling of thrust losses due to ventilation has been attempted modifying *ad hoc* existing methods, such as blade element method, lifting-line and lifting-surface theory.

More recently, a three-dimensional boundary element method was extended by Young and Kinnas (2004) to predict the unsteady performance of surface-piercing propellers during ventilation. This method accounts for the exact cavity detachment location on the suction side by means of an implemented search algorithm.

Although progresses were achieved towards the modeling of propellers piercing the free-surface, all methods present several shortcomings related to the assumptions they are based on, limiting their validity to the global forces or the particular propeller object of the study. It can be seen that a more general purpose model is needed to predict the dynamic loads occurring during ventilation, in all possible flow regimes.

The first known work attempting the modeling of surface-piercing propellers using RANS was performed by Caponnetto (2003). He carried out numerical simulations of a surface-piercing propeller, obtaining a good agreement with the experiments of Olofsson (1996), in terms of blade forces during a rotation cycle.

### 1.3 Present work

Within the framework described above, the present work is an intermediate step towards modeling of the dynamic loads during propeller ventilation, and thus predicting its extent and the corresponding losses. This task requires a deep understanding of the mechanisms underpinning the physical phenomenon, which can be acquired through both model tests and numerical simulations.

The objectives of the study can be summarized as follows:

- Investigate the dynamic and average forces on a propeller subject to ventilation by experiments.
- Establish an understanding of the relation between forces and ventilation using high-speed video recordings synchronized with the measurements.
- Establish a CFD model capable of predicting the extent of ventilation and the dynamics forces due to ventilation.

The accomplishment of the above activities should then lead to the understanding of the mechanisms of dynamic forces due to ventilation, in order to develop a simplified model able to describe them.

An outline of the present work is given below, organized by chapters, where the main contributions are described:

### Chapter 2 *Ventilation theory*

It contains a review of the available literature, which was used to describe the theory behind propeller ventilation and as starting point for the following research. Furthermore, this review study allowed identifying analogies between propeller ventilation started by a free-surface vortex with other phenomena seen in fields different from marine applications, such as the inlet vortex in pump sumps and the ground vortex at the inlet of aircraft engines—for which an extensive literature exists. The mature experience gained through many years of research in these fields not pertaining to marine technology could be transferred to the present work in marine applications, where research studies started more recently.

### Chapter 3 *Verification studies*

This chapter deals with numerical simulations aiming to validate and verify the solver in connection with the most challenging numerical features encountered in propeller ventilation, such as (i) presence of the free-surface and (ii) rotating lifting surfaces. It is divided in two parts, as follows:

- *Submerged hydrofoil*

The present analysis focuses on the validation and verification of the solver adopted in the case of a two-dimensional hydrofoil close to the free surface (Califano, 2008b, 2009). Two cases are studied here, chosen among those tested by Duncan (1983), corresponding to a non-breaking and a breaking wave condition, with submergence ratios  $h/c$  of 1.286 and 0.911, respectively. These studies show that for such a problem, where viscosity is not dominant, the diffusion introduced by the solver affects significantly the accuracy of the results and care must be taken in treating the near wall region for a correct solution. The forces exerted by the foil are the key mechanism driving the deformation of the free-surface.

- *Propeller in open water*

A sensitivity analysis was performed on a propeller in open water conditions, and its results were validated against the available experiments, for a wide range of operating advance ratios (Califano and Steen, 2009). The results of this study show a good agreement for the thrust coefficient, whereas a systematic error affects the torque coefficient, which is under-estimated using `Fluent` code and over-estimated using `OpenFOAM` code. It was found that this deviation in the torque is mainly due to different values for the wall shear stresses, probably resulting from different implementation of the turbulence modeling at the wall: `Fluent` computes too low shear stresses, while `OpenFOAM` presents an over-estimation.

Furthermore, the implementation of a Sliding Mesh (SM) model for the

propeller rotation proved to be more accurate than the Multiple Reference Frame (MRF) model.

#### Chapter 4 *Model tests*

Model tests were performed on a ventilating propeller, having the propeller submergence, loading and advance ratio as main parameters. The analysis of the results shows that the combination of these parameters determines the nature of the ventilation mechanism:

- (i) at deeper submergences  
through a free-surface vortex (Figure 1.7a);
- (ii) at moderate submergences  
through the blade itself piercing the free surface (Figure 1.7b).

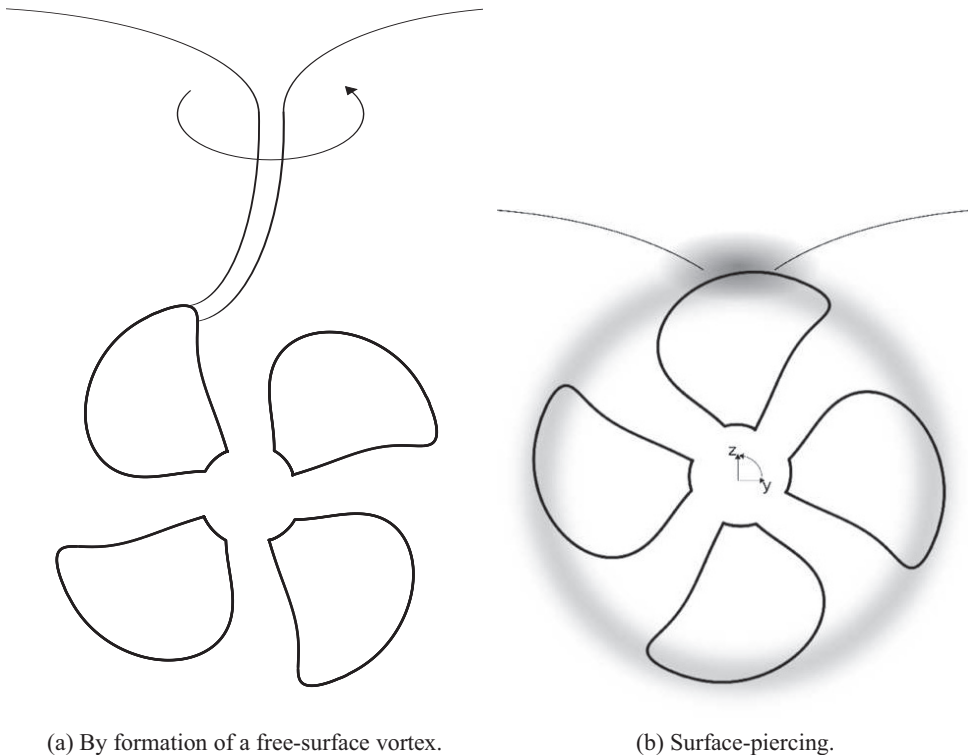
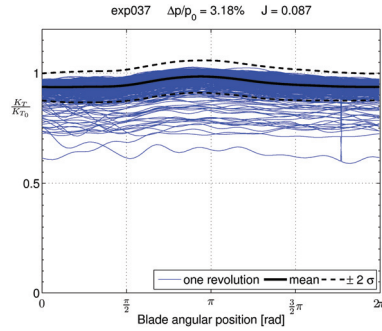


Figure 1.7: Sketch of different types of propeller ventilation.

Using the experimental thrust envelopes (Figure 1.8), three different ventilation regimes could be identified, depending on the influence of the above mentioned mechanisms.

1. *Free-surface vortex*

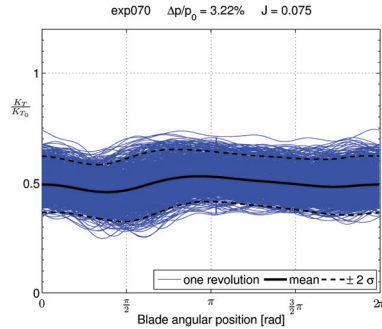
characterized by severe and discontinuous thrust losses occurring when the vortex reaches the blade wall; the amplitude during a ventilation event can deviate significantly from the mean value, which is slightly lower than the nominal one.



(a)  $h/R = 1.88$ .

2. *Surface-piercing*

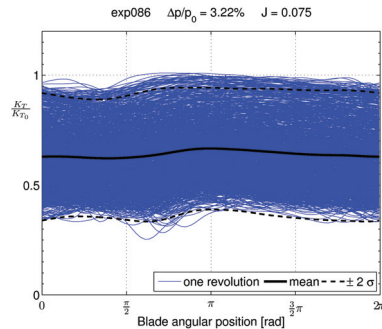
characterized by uniform thrust losses during the complete revolution; the thrust encompasses a narrow amplitude range around the mean value, which is in turn significantly lower than the nominal one.



(b)  $h/R = 1.56$ .

3. *Intermediate*

where both mechanisms (i) and (ii) act alternately during the same test case; the thrust encompasses a broad and uniform amplitude range and the mean value is somewhere in between those found in the previous two regimes.



(c)  $h/R = 1.64$

Figure 1.8: Thrust ratio during each revolution [ $n = 16$  Hz].

The high-speed video recordings synchronized with the measurements allowed establishing a relation between dynamic forces and ventilation. This was achieved both for the ventilation through a free-surface vortex and for the recurring loads occurring during a cycle of full ventilation.

### Chapter 5 *Numerical simulations*

This chapter describes all the results obtained from the numerical simulations of a ventilating propeller, performed with the commercial RANS solver `FLUENT`. Two cases are object of the present investigation, at submergence ratios  $h/R$  of 1.4 and 1.72, corresponding to the two ventilation types previously identified. After starting from rest, ventilation is rapidly occurring and about 15 propeller revolutions were simulated.

The analysis of the first time instants, before a quasi-steady oscillatory solution is achieved, allows a deeper insight into two distinctive types of ventilation inception (Figure 1.9):

(a) *Surface-piercing* at moderate submergence ( $h/R = 1.4$ ): Blades become surface-piercing after the deformation of the free surface.  
 (b) *By free-surface vortex formation* at deeper submergence ( $h/R = 1.72$ ): Vortical structures forming on the free surface reach the propeller tip.

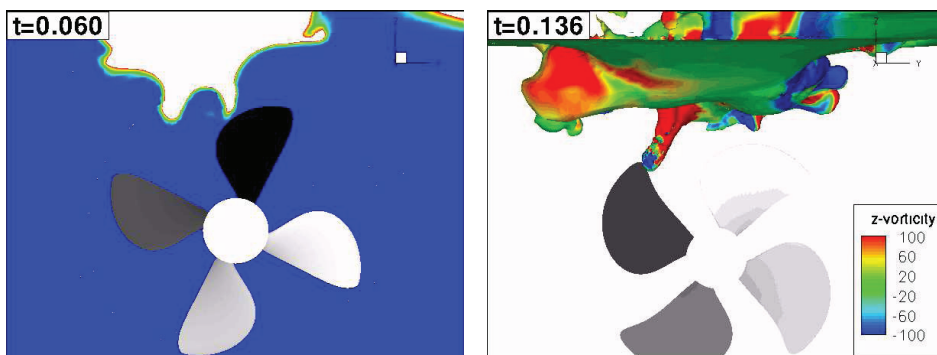


Figure 1.9: Two types of ventilation inception, from numerical simulations.

### Chapter 6 *Discussion*

This chapter presents a summary of the mechanisms underpinning propeller ventilation and an analysis of the deviation of the numerical simulations from the experimental data.

Unlike ventilation of surface-piercing propellers with supercavitating profile, it was found that the tip vortex has a dominant role in the type of ventilation object of this study. A qualitative model was derived based on the analysis of the dynamic loads occurring during ventilation. The complexity of the ventilation phenomenon itself leads to unstable numerical simulations, very sensitive to the used numerical parameters, somehow reflecting the large deviation found in the experiment.

## Chapter 2

# Ventilation theory

Ventilation is the phenomenon of air-drawing seen on structures working below the free-surface, such as hydrofoils, rudders and propellers. Ventilation can be forced, which involves supply of air into the cavity by auxiliary means such as a pump. Otherwise, the most common type of ventilation is natural, when air is supplied to the ventilated cavity by pressure created by the flow itself.

Natural ventilation occurs when the pressure on the body falls below the atmospheric pressure  $p_0$ . In this sense, ventilation is similar to cavitation, which is instead started when the pressure falls below the vapor pressure  $p_v$ . Since  $p_v$  is much smaller than  $p_0$ , one would expect ventilation to occur always before cavitation, but there is another criterion necessary for ventilation: a continuous channel with pressure  $p < p_0$  must exist between the body and the free-surface.

Ventilation on submerged hydrofoils (Nishiyama, 1961) or surface-piercing rudders (Wadlin, 1958) occurs at high angle of attack, starting in the wake region of stagnating flow. The pressure in this region downstream the ventilated object ("dead water region") was investigated by Shiba (1953), who concluded that ventilation occurs when pressure in this region falls below the atmospheric pressure  $p < p_0$ .

For a finite span hydrofoil, ventilation can also occur through the trailing vortex released from the wing tip (Wadlin et al. (1955) and Ramsen (1957)).

An extensive review of ventilation occurring on submerged hydrofoils is given by Acosta (1973), within the framework of hydrofoil craft.

Because of its rotation, propeller ventilation has aspects different from those of bodies which are simply translating. Being the object of this study, a detailed description of the theory and of the historical background will be given in this chapter.

Ventilation may occur when a propeller is operating in the proximity of the free-surface. At low advance ratios  $J$ , if the propeller loading  $C_T$  is sufficiently

high, the pressure on the propeller blades may become low enough to draw air from the free-surface.

A phenomenological description of propeller ventilation has been given by Shiba (1953):

”Air-drawing of a marine propeller signifies the penetration of atmosphere through an air hole or along the blade surface in contact with atmosphere into the dead water region or sub-atmospheric region on the upper surface of propeller blades.”

This definition contains already the main features of the propeller ventilation mechanism, which occurs in presence of the atmosphere, and can reach the propeller through an ”air hole” or ”along the blade surface in contact with atmosphere”. Air-drawing may occur through a funnel created on the free-surface, or by the propeller itself piercing the free-surface. Once ventilation has started, air cavities spread on the propeller blades, reducing profile’s lift and drag, and consequently the thrust and torque of the whole propeller. A fully ventilated propeller may lose as much as 70-80% of its nominal thrust and torque. These high thrust losses occur when the suction side—responsible for about  $\frac{2}{3}$  of the total thrust—is completely covered with air with a pressure close to the atmospheric, thus giving almost zero thrust. For this reason, thrust losses due to ventilation are much higher than those experienced by a cavitating propeller, where the vapor pressure reached on the blade walls still gives a contribution to the thrust.

## 2.1 Dimensionless parameters

In order to extrapolate the results from model tests to full scale, similarity must be ensured on the boundary and working conditions. A dimensional analysis of the governing fluid dynamic equations (Shiba, 1953) leads to the non-dimensional parameters relevant to the ventilated propeller flow.

These parameters will be defined using a velocity proportional to the tangential velocity  $nD$  (being  $n$  the shaft frequency and  $D$  the propeller diameter) of the blade-tip as reference value, instead of the free-stream velocity  $U$  (commonly used in marine applications). This assumption better complies with the characteristic flow around a propeller, where the velocity of advance  $U$  is much smaller than the blade’s tangential velocity, especially at the high propeller loadings considered during this dissertation.

*Advance ratio*

$$J = \frac{U}{nD} \quad (2.1)$$

*Submergence ratio*

$$I = \frac{h}{R} \quad (2.2)$$

where  $h$  is the propeller shaft submergence and  $R$  the propeller radius.

*Froude number, based on diameter  $D$  and submergence  $h$*

$$Fr = \frac{nD}{\sqrt{gD}} \quad (2.3a)$$

$$Fr_h = \frac{nD}{\sqrt{gh}} \quad (2.3b)$$

*Cavitation and ventilation number*

$$\sigma_{cav} = \frac{p_0 + \rho gh - p_v}{1/2\rho(2\pi nr)^2} \quad (2.4a)$$

$$\sigma_{vent} = \frac{p_0 + \rho gh - p_0}{1/2\rho(2\pi nr)^2} = \frac{2gh}{(2\pi nr)^2} = \frac{2/\pi^2}{Fr_h^2} \quad (2.4b)$$

*Reynolds number*

$$Re = \frac{nD^2}{\nu} \quad (2.5)$$

where  $\nu$  is the kinematic viscosity  $\nu = \mu/\rho$ .

A local  $Re$  will sometimes be used:

*Reynolds number at 0.7 radius*

$$Re_{0.7} = \frac{0.7\pi nD \cdot c_{0.7}}{\nu} \quad (2.6)$$

where  $c_{0.7}$  is the chord length at 0.7 radius.

*Weber number*

$$We = nD\sqrt{D\frac{\rho}{\sigma}} \quad (2.7)$$

where  $\sigma$  is the surface tension.

Geometrical similarity between model and full scale with respect to ventilation implies the same submergence ratio  $h/R$ . The same advance number  $J$  will ensure a similar moving path for the blade, thus similar working conditions. The Froude

$Fr$  and Reynolds  $Re$  numbers must be the same in order to satisfy the law of similarity between model and full scale. The Froude number may be defined as the ratio of inertial to gravitational forces and its equality between model and full scale will ensure the same force due to wave making. The Reynolds number may be defined as the ratio of inertial to viscous forces and is used to ensure the same viscous forces between model and full scale.

Shiba (1953) has correlated the occurrence of ventilation with the pressure in the wake flow behind a submerged body, sometimes called "dead water region" by the author, and represented in Figure 2.1 for a surface-piercing cylinder.

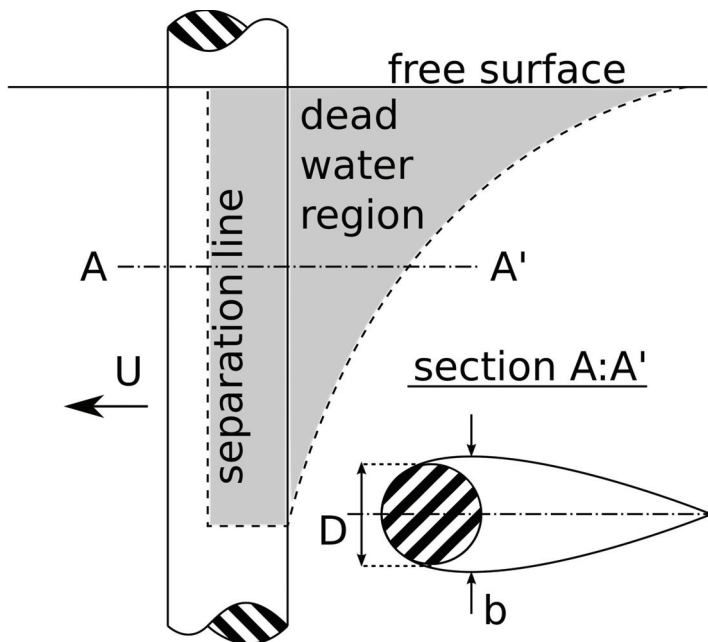


Figure 2.1: Separated flow downstream a surface-piercing cylinder (Shiba, 1953).

He has shown that the characteristics of the wake region of a fully-ventilated propeller depends on  $Fr$  up to values around 3. Most marine propellers present  $Fr$  smaller than 3, a fact that underlines the importance of satisfying the similarity for this parameter when ventilation has already occurred. Similarity of  $Fr_h$  is automatically achieved after satisfying  $Fr$  and submergence ratio  $I$ .

For scaled models towed in water similarity in both  $Re$  and  $Fr$  can not be achieved. Similarity in  $Re$  requires too high velocities to be achieved in practice. In most cases, the differences in  $Re$  will introduce negligible scale effect as long as turbulent flow is attained in model scale. The minimum  $Re$  above which its effect can be neglected was estimated by Kempf (1934) to be  $\mathcal{O}(10^5)$ . Brandt (1973)

uses the local Reynolds number  $Re_{0.7}$  to assess flow-independence from Reynolds number. His conclusion is that for  $Re_{0.7} > 5 \times 10^5$  laminar boundary layer separation ceases to occur, and the effect of  $Re$  on the propeller characteristics vanishes, regardless of flow regime and propeller immersion.

The expression for  $\sigma_{vent}$  shows that it is proportional to  $Fr_h^{-2}$ , thus similarity is automatically satisfied after  $Fr$  and  $I$ .

The propeller model object of this investigation was especially designed for ventilation studies, and is cavitation-free in model scale when fully submerged. Similarity in terms of cavitation is hard to achieve, unless atmospheric pressure in the tunnel can be reduced to match the same  $\sigma_{cav}$  as in full scale<sup>1</sup>. However, the effect of cavitation is believed to be important only for a partially ventilated regime, where a link might exist between ventilation and cavitation.

Similarity of Weber number  $We$  must be fulfilled to take into account the effect of surface tension  $\sigma$ .

Including surface tension, the fluid pressure will be discontinuous at the surface of separation where a curvature with radius  $r$  exists (Lamb, 1932):

$$p_0 - p = \frac{\sigma}{r} \quad (2.8)$$

Surface tension has the effect to prevent air from being sucked down, adding a pressure equal to the ratio between surface-tension and radius-of-curvature. The condition for ventilation to occur can thus be rewritten:

$$p + \frac{\sigma}{r} < p_0 \quad (2.9)$$

Substituting the radius of curvature with half the breadth  $b$  of the dead water region (see Figure 2.1), the condition for ventilation inception can be rearranged as:

$$(p_0 - p) b > 2\sigma \quad (2.10)$$

We can argue from Equation 2.10 that ventilation is more likely to occur where the pressure is low (i.e. on the suction side) and for increasing breadth of the dead water region.

At the instant before ventilation inception, surface tension is dominating relative to the forces due to gravity. The critical advance constant is shown experimentally to depend on  $We$  up to 180 (Shiba, 1953). Although ordinary full-scale marine propellers work in a range much higher than 180, care should be taken in model tests to exceed this value in order to ensure similarity.

---

<sup>1</sup>However, the corresponding full scale propeller might cavitate, due to the higher velocities and thus smaller cavitation number.

Propeller performance characteristics are commonly presented in non-dimensional form, in terms of thrust  $K_T$ , torque  $K_Q$  and efficiency  $\eta$ .

$$K_T = \frac{T}{\rho n^2 D^4} \quad (2.11a)$$

$$K_Q = \frac{Q}{\rho n^2 D^5} \quad (2.11b)$$

$$\eta = \frac{J K_T}{2\pi K_Q} \quad (2.11c)$$

Thrust can sometimes be presented in terms of another coefficient, the propeller loading  $C_T$ , obtained dividing the thrust by the dynamic pressure  $p_{dyn}$  and the propeller disc area  $A_0$ .

$$C_T = \frac{T}{\frac{1}{2}\rho(nD)^2 A_0} = \frac{\Delta p A_0}{\frac{1}{2}\rho(nD)^2 A_0} = \frac{\Delta p}{\frac{1}{2}\rho(nD)^2} \quad (2.12)$$

where  $\Delta p$  is the pressure jump imposed at the propeller plane.

In order to investigate local features of the flow, the pressure coefficient is also introduced:

$$C_p = \frac{p - p_\infty}{\frac{1}{2}\rho(nD)^2} \quad (2.13)$$

### 2.1.1 Scale effects

The fluid pressure in the low-pressure region will in full-scale (subscript  $s$ ) be lower than in the corresponding location in model scale (subscript  $m$ ):  $p_s < p_m$ . The same applies for the pressure difference:

$$p_0 - p_s > p_0 - p_m \quad (2.14)$$

Assuming a laminar boundary layer profile for the dimensionless breadth of the dead water region  $b/x$  (Shiba, 1953) inversely proportional to  $\sqrt{Re}$  through the constant  $k$ :

$$\frac{b}{x} = \frac{k}{\sqrt{Re}} \quad (2.15)$$

the breadth of the dead water region in full scale will be larger than in model scale:

$$\frac{b_s}{b_m} = \frac{L_s}{\sqrt{U_s L_s}} \frac{\sqrt{U_m L_m}}{L_m} = \sqrt{\frac{U_m}{U_s}} \sqrt{\frac{L_m}{L_s}} \frac{L_s}{L_m} = \lambda^{-\frac{1}{4}} \lambda^{-\frac{1}{2}} \lambda = \lambda^{\frac{1}{4}} \quad (2.16)$$

$$\lambda = \frac{L_s}{L_m} > 1$$

where  $\lambda$  is the scale factor of the lengths in full and model scale, therefore larger than unity.

Combining Equation 2.14 and Equation 2.16, the following relationship can be obtained:

$$(p_0 - p_s) b_s > (p_0 - p_m) b_m \quad (2.17)$$

Recalling Equation 2.10, for similar conditions in Froude number  $Fr$  and submergence ratio  $I$  (and thus for the same ventilation number  $\sigma_{vent}$ ), Equation 2.17 shows that ventilation can occur in full scale without occurring in model scale. The same conclusion had been reached by Kempf (1934):

”... experience showed that in certain cases the diminution of thrust of the ship’s propeller was greater than that of the model propeller ...”

This difference was ascribed by Kempf (1934) to the effect of viscosity, and he suggested in his comments that also capillarity (surface tension) might play a significant role. The importance of surface tension in terms of scaling effects was indeed explained with the previous considerations based on Shiba (1953).

## 2.2 Historical background

Propeller ventilation has been historically related to surface piercing, or partially submerged propellers, which were first employed in shallow waters, and in a second stage for high-speed craft.

It is only recently that ventilation of conventional thrusters has gained much attention. With the increasing demand of offshore vessels able to work in heavy sea states at high propeller loadings—as for Dynamic Positioning (DP) operations—a number of cases of damages to the lower bevel gear and propeller shaft bearings on azimuth and tunnel thrusters have been reported. Based on their analysis, damages are believed to be caused by large torque and sudden variation of the load conditions.

Studies related to surface-piercing propellers can be dated back to the mid-19<sup>th</sup> century, when the screw propeller had been the dominant form of marine propulsion, replacing the paddle wheel. The first known patent on surface-piercing propellers was obtained by David Napier in 1841 (Napier, 1912):

Patent No. 8893, 1841. Improvements in Propelling Vessels.

”One part of this invention consisted in placing two wheels or propellers of equal diameter at the stern of the vessel, the axles of both above the level of the water, and one wheel further aft than the other, to permit the blades or float-boards of one wheel working nearly up to the axle of the other. These wheels, on patent drawing, had each eight

oblique blades, radiating from a central disc. A further arrangement in this patent applied to side wheels. The floats, in this case, were connected at their lower edges to a heavy metallic frame, the weight of which kept the floats, all round, in a nearly vertical position.”

In order to achieve shallow-draft propulsion in sheltered waters, where the ”conventional” paddle wheel was performing better with respect to the ”unconventional” screw propeller, much research effort has gone into improving the performance of the propeller working in partially submerged conditions.

The technological achievements in the design of partially submerged propellers—obtained without the benefit of model or ”scientific” investigations—had to face from the very beginning the problem of air-drawing. The first known study on the effect of air-drawing was performed by Reynolds (1874). Based on simple model tests performed at various submergences, he observed three fundamental regimes: start-up, intermittent and fully-developed ventilation.

Since then, the results of a number of investigations have been published. Kempf (1934) was a pioneer of the study of ventilation effects on propellers. He found that thrust and torque diminished in a higher degree than should be expected from the immersed area of the propeller only. He tested three and four-bladed propellers at different revolutions and immersion ratios, and showed the negative effects of ventilation on thrust and torque.

Shiba (1953) has studied the ventilation mechanism in details, performing experiments on simpler geometries, such as surface-piercing cylinders and hydrofoils, and extensively analyzing the parameters affecting propeller ventilation. Ventilation was studied on average thrust and torque, taking into account the effect of different propeller design parameters as well as the rate of revolutions and speed.

As mentioned in the previous section, his conclusion is that ventilation occurs when pressure in the ”dead water region” downstream the ventilated object falls below the atmospheric pressure, with the pressure due to surface tension subtracted

$$p < p_0 - \sigma/r.$$

Most of the blade sections tested were of airfoil type, but he did also include a circular arc section with a flat pressure face and sharp leading edge and noted the difference in the performance curve.

Gutsche (1967) presented results of tests of partially submerged propellers and suggested a procedure for calculating the out-of-water effect on average thrust.

With the growing interest in high-speed craft with high-performance propulsion, partially submerged propeller were seen as a valid propulsion alternative to the fully submerged supercavitating propellers. Their high efficiency is primarily attributed to the reduction of appendage drag, because most of the propeller assembly (e.g., shafts, struts, hub, etc.) is elevated above the water. Other advantages

over conventional submerged propellers include (i) larger propeller size, since it is not limited by minimum blade tip clearance from the hull or the maximum vessel draft, and (ii) avoidance of cavitation damage, because the propeller usually operates at ventilated conditions by drawing air from the surface.

Within this framework, Hadler and Hecker (1968) further investigated the possibility to use propellers with supercavitating-type sections—circular arc section with flat faces and sharp leading edge—in partially submerged conditions.

An extensive test campaign was carried out in order to compare the performance between partially submerged, fully wetted, and supercavitating operation.

As guidance to the understanding of propeller test results, the flow regime around a supercavitating-type section under ventilated flow conditions is shown Figure 2.2.

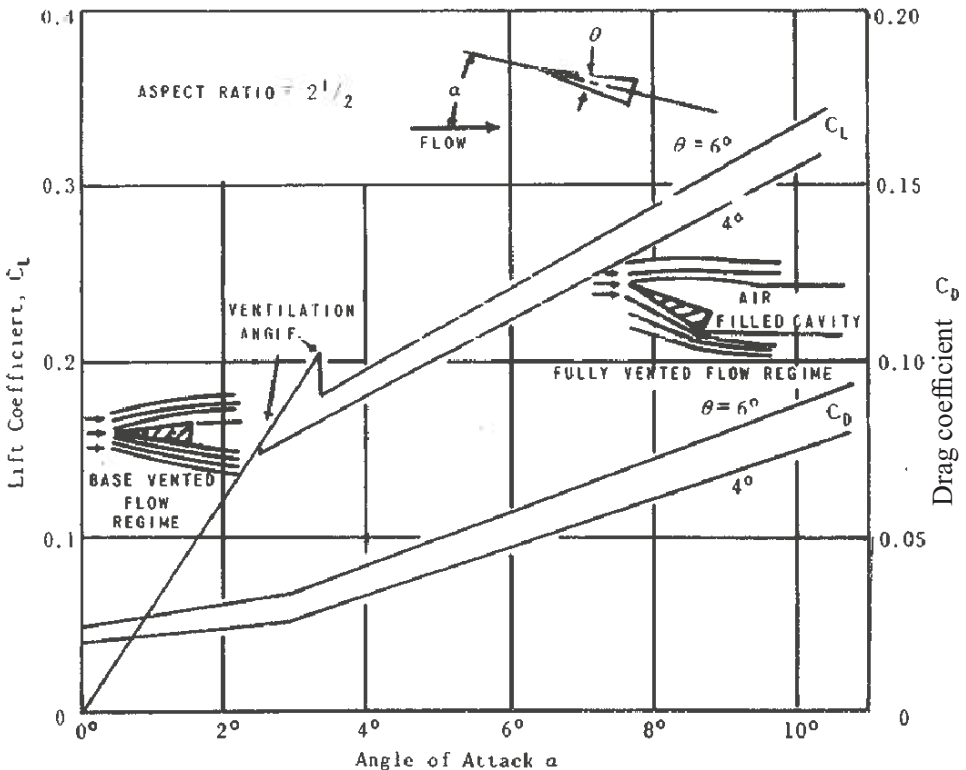


Figure 2.2: Lift and drag coefficients of wedges in various flow regimes (Hadler and Hecker, 1968).

Three main flow regions can be observed:

- *Base-Vented*. The cavity springs from the blunt trailing edge and springs aft. The foil develops its highest lift-to-drag ratio.

- *Partially Cavitating*, between base- and fully-vented. A vapor cavity is confined on the suction side. Forces and moments are unsteady, and oscillations becomes violent (“buffeting”) before transition to the *fully vented region*.
- *Fully Vented*. The cavity of atmospheric pressure cover the suction side, extending from the leading edge for more than one chord-length. The lift experiences a sudden drop.

The propeller experiences the same abrupt drop in thrust and torque when passing from the base-vented to the fully vented operation.

Fleischer (1973) presented average thrust and torque measurements that demonstrated interactions between propeller and hull when the propeller is partly submerged. He also studied the effect of the rate of revolutions on ventilation.

Huse (1973) has studied the dynamic loads on a blade of a ducted propeller due to forced and natural ventilation. His study presents the first discussion about the formation of a free-surface vortex leading to ventilation.

The effect of ventilation on time-average thrust and torque of propellers operating in waves is discussed by Faltinsen et al. (1981); Minsaas et al. (1983, 1987), leading to a general expression for the reduced thrust  $\beta$  as function of the submergence ratio  $h/R$  (Equation 2.23).

Olofsson (1996) conducted a very thorough series of experiments giving a deep insight into the dynamic performance of a surface-piercing propeller. Experiments were conducted at the KaMeWa free surface cavitation tunnel in Sweden. A five-component dynamometer was used to measure the unsteady blade forces. In the experiment, the cavitation number and Froude number scaling were simultaneously satisfied. The influence of Froude and cavitation number at different advance speeds was systematically examined. Tests with different shaft yaw and inclination angles were also performed.

More recently, Koushan performed experiments and measured the dynamic loads of a ventilated propeller in open water (Koushan, 2006b) and with the presence of a duct (Koushan, 2006a), taking into account the influence of factors normally encountered in a seaway, such as waves and thruster azimuthing angle (Koushan, 2006c, 2007b,a), in addition to those commonly used (submergence and advance ratio).

The occurrence of ventilation in the recent years has become a serious problem during Dynamic Positioning (DP) operations. Several authors have studied new control systems able to detect ventilation inception and control the motor in order to reduce the associated thrust losses (Smogeli, 2006; Ruth, 2008).

Paik et al. (2008) have measured the deformation of the free-surface due to the proximity of a propeller under different submergence ratios. Their results showed

that at larger immersion depths, the propeller inflow begins to accelerate from upstream and the rate of acceleration increases gradually with approaching the propeller plane. Moving the propeller close to the free surface caused a decrease in the acceleration of the inflow velocity and greatly influenced the inflow region above the blade tip position. Reducing the propeller submergence, the axial velocity was reduced, both upstream and downstream. This condition would help the formation of a stagnation point, and the subsequent vortex formation. They also found that the vortex structure of the tip vortices and their trajectories depended on both the immersion depth and propeller loading.

### 2.2.1 Numerical methods

Due to its nature being inherently non-linear and time-dependent, the numerical modeling of ventilation is a difficult task. The presence of air cavities, spray and waves make the mathematical formulation of the phenomenon a real challenge.

Olofsson (1996) presents a detailed review of the numerical methods applied to surface-piercing propellers. A shorter review, by no means fully comprehensive, will be given in this section, aiming at underlying the characteristics of the previous methods and the differences with respect to the present study. More details are given in Olofsson (1996), and for a deeper understanding the reader should review the original articles.

Yegorov and Sadovnikov (1961) applied a blade element method based on two-dimensional hydrofoil theory, but ignored the effect of adjacent blades, cavities, and wake vortex sheets.

Oberembt (1968) extended a lifting-line theory including the effect of immersion. This was achieved assuming the propeller to be lightly loaded, such that no natural ventilation occurred, and approximating the free-surface with a horizontal plane with the method of the images.

Later, Wang (1977, 1979) applied a linear theory to study the vertical and oblique water entry and exit of a fully ventilated foil, which is assumed to be fully ventilated during the passage of the water layer.

This method, combined with the supercavitating propeller theory of Cox (1966), was then extended by Furuya (1985) to include the effect of propeller ventilation.

An unsteady lifting surface method was developed by Wang et al. (1992) for the analysis of a fully ventilated surface-piercing propellers, assuming, similar to Furuya (1985), the flow to separate from both the leading edge and trailing edge of the blade, forming on the suction side a cavity that vents to the atmosphere.

More recently, Young and Kinnas (2004) have extended a three-dimensional boundary element method to predict the unsteady performance of surface-piercing propellers in the partially ventilated, transition, and fully ventilated flow regimes.

This method accounts for the exact cavity detachment location on the suction side by means of an implemented search algorithm.

Although progresses were achieved towards the modeling of propellers piercing the free-surface, all methods present several shortcomings related to the assumptions they are based on, limiting their validity to the global forces or the particular propeller object of the study. It can be seen that a more general purpose model is needed to predict the dynamic loads occurring during ventilation, in all possible flow regimes.

The first known work attempting the modeling of surface-piercing propellers using RANS was performed by Caponnetto (2003). He carried out numerical simulations of a surface-piercing propeller, obtaining a good agreement with the experiments of Olofsson (1996), in terms of blade forces during a rotation cycle. Not many details are given about the employed numerical method.

Recently, Califano and Steen (2009) have performed simulations using RANS on a fully submerged ventilating propeller, obtaining a good agreement with the experimental results of the most severe thrust losses. It should be mentioned here that three main differences exist between the present study and those previously described in this section: *(i)* the propeller is fully submerged ( $h/R = 1.4 > 1$ ) and becomes surface-piercing only when ventilation occurs, *(ii)* the blade sections are not of the super-cavitating type (sharp leading edge and thick abrupt trailing edge), but designed with a conventional lifting foil profile (blunt leading edge and sharp trailing edge), and *(iii)* very high propeller loadings were simulated. As a consequence, the present study will present characteristics which will distinguish it from surface-piercing propellers of supercavitating-type: *(i)* ventilation must be triggered by some event (ventilation inception), *(ii)* the blunt leading edge will not work as a sharp interface between the gaseous and liquid phase, and *(iii)* the tip region will be characterized by high non-linearities.

### 2.3 Thrust loss

A propeller on a vessel in a seaway may experience large vertical motions relative to the free-surface. This can result in abrupt thrust losses which can be fairly large, up to the 70-80% of the nominal thrust. The total losses can be thought of to consist of three main contributions: *(i)* loss of effective propeller disc area, *(ii)* ventilation, and *(iii)* a lift hysteresis effect. The term ventilation is commonly referred to the total losses.

The total reduced thrust can then be estimated multiplying the different components which will be described in the following sections.

$$\beta = \beta_0 \beta_v \beta_H \quad (2.18)$$

being  $\beta$  the ratio between the ventilating and non-ventilating thrust (or torque). Thrust and torque losses are closely related, such that the reduced torque factor  $\beta_Q$  should always be larger than  $\beta_T$  in order to have an efficiency not increasing with the thrust losses. Faltinsen et al. (1981) and Minsaas et al. (1983) suggested a simple relationship based on previous experimental results (Kempf, 1934; Gutsche, 1967):

$$\beta_Q = \beta_T^m, \quad 0 < m < 1 \quad (2.19)$$

where typical values for  $m$  are between 0.8 and 0.85 for an open propeller. The empirical relationship between reduced thrust and torque was confirmed by Kozłowska et al. (2009) based on recent experimental results.

### 2.3.1 Loss of effective disc area

During the water-exit phase, the propeller is experiencing a thrust loss due to loss of effective disc area (Gutsche, 1967; Fleischer, 1973). The corresponding reduced thrust  $\beta_0$  can be geometrically found as the ratio between the immersed disc area  $A_1$  and the propeller area  $A_0$ :

$$\beta_0 = \frac{A_1}{A_0} = \Re \left[ 1 - \frac{\arccos(h/R)}{\pi} + \frac{h/R}{\pi} \sqrt{1 - (h/R)^2} \right] \quad (2.20)$$

An alternative representation, where also the propeller hub diameter is accounted for, is given by Koushan (2004), where  $r_h$  the radius of the hub. This loss model is assumed to be valid for any propeller loading.

$$\beta_0 = \left[ 0.5 - \frac{\arcsin(h/R)}{\pi} + \frac{h/R}{\pi} \sqrt{1 - (h/R)^2} \right] \left[ 1 - \frac{|h + r_h| - (h + r_h)}{2(R - r_h)} \right] \quad (2.21)$$

### 2.3.2 Hysteresis effect

During the in- and out-of-water movement of the propeller in waves hysteresis in the production of thrust generally occurs, leading to a reduced thrust  $\beta_H$ . The thrust build-up when the propeller stops ventilating is then slower than the thrust loss when the propeller starts ventilating. According to Koushan (2004), a typical propeller must travel about 4 revolutions at full submergence to re-gain its full thrust.

The hysteresis can be related to the delay in building-up the steady-state lift of an airfoil accelerating instantaneously from rest to a constant velocity  $U$ , a

phenomenon referred to as the Wagner effect (Wagner, 1925). This effect will be analyzed in more detail in § 3.1.2.2, within the study of a submerged 2D foil.

Faltinsen et al. (1981) have proposed an expression taking into account this effect.

$$\beta = \beta_0 \beta_1 x \quad (2.22)$$

where  $\beta_1$  is due to the steady wave motion created by the propeller and  $x$  is due to the Wagner effect. An alternative representation is given in Minsaas et al. (1983):

$$\beta = \begin{cases} 1 - 0.675 (1 - 0.769h/R)^{1.258} & \text{for } h/R < 1.3 \\ 1 & \text{for } h/R \geq 1.3 \end{cases} \quad (2.23)$$

The obtained reduced thrust factors are compared in Figure 2.3 with the reduced thrust  $\beta_0$  only due to loss of effective disc area.

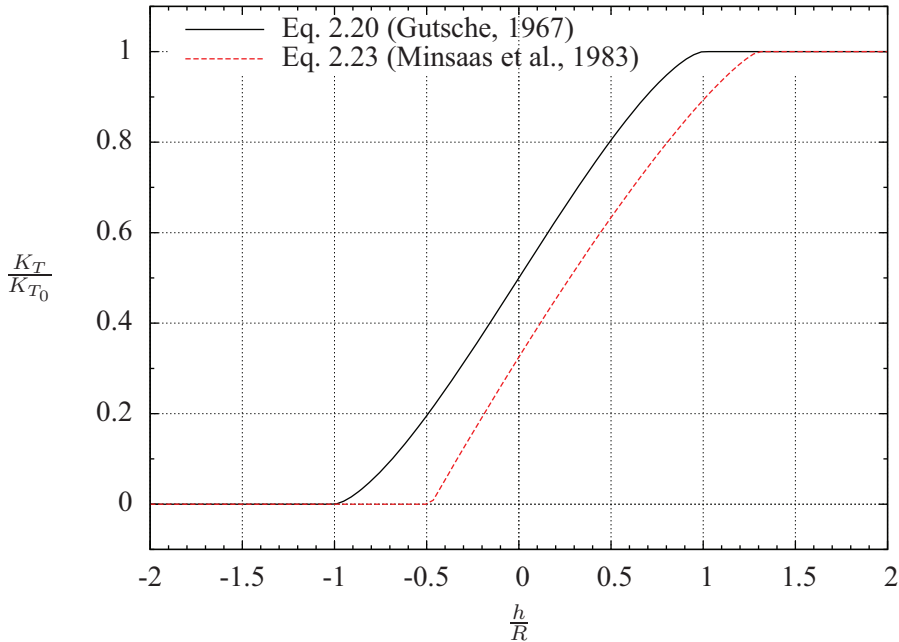


Figure 2.3: Thrust losses according to Gutsche (1967) and Minsaas et al. (1983).

### 2.3.3 Ventilation losses

During ventilation, the propeller experiences a thrust loss not only due to the reduced disk area and Wagner effect previously accounted for. Air is able to "penetrate" the free-surface and invest the blade surface, especially on the suction side, leading to a sudden increase of pressure, and a subsequent thrust loss.

An expression of the reduced thrust solely due to ventilation has been found by Minsaas et al. (1983) assuming that the suction side is fully ventilated—it is subject to atmospheric pressure—and the pressure on the pressure side is static:

$$\beta_v = \frac{1.5EAR}{K_{T_0}} \left[ C_{L(\sigma_v=0)} + \sigma_v \right]_{(r/R=0.7 \div 0.75)} \quad (2.24)$$

Equation 2.24 establishes a direct connection between the reduced thrust and the lift coefficient of an "equivalent section" of the propeller, where  $h/R = 0.7 \div 0.75$ . The lift coefficient is given by the contribution of the pressure side ( $p = p_{static} \Rightarrow \sigma_v = 0$ ) and the suction side ( $p = p_0 \Rightarrow C_L = \sigma_v$ ).

Using a linearized two-dimensional theory, Tulin and Burkart (1955) have established the equivalence between the lift coefficient  $C_L$  of a super-cavitating hydrofoil and the moment coefficient  $\tilde{C}_M$  of the corresponding airfoil. This equivalence has been then expounded in Tulin (1956) and summarized in Tulin (1964):

$$C_{L(\sigma_c=0)} = \tilde{C}_M = \frac{\pi}{2} \alpha \quad (2.25)$$

In analogy with the cavitating case, Kozłowska et al. (2009) have used Equation 2.25 to express the lift coefficient obtained on the pressure side of a ventilating foil, which substituted in Equation 2.24 gives a modified expression for the reduced thrust due to ventilation:

$$\beta_v = \frac{1.5EAR}{K_{T_0}} \left[ \frac{\pi}{2} \alpha + \sigma_{v(r/R=0.7 \div 0.75)} \right] \quad (2.26)$$

## 2.4 Regimes

Experiments performed on submerged propellers with varying geometry and loading characteristics show distinctive features identifying only a small number of ventilation regimes. Within each of these regimes, propellers with different geometry and loading characteristics present the same ventilation patterns, either in terms of applied loads or type of air-drawing.

A first classification of ventilation regimes was given by Nishikawa and Uchida (1989). They observed experimentally that at a given advance ratio  $J$  thrust and torque would decrease following the reduction of the immersion depth. The first thrust losses occurred without any visible ventilation. This thrust loss can be ascribed to the free-surface proximity effect. It has been shown (Hough and Moran, 1969; Faltinsen, 2005) that the lift of a submerged hydrofoil decreases when the Froude number based on the submergence  $Fr_h$  is decreased<sup>2</sup>. All the profiles

<sup>2</sup>This finding does not apply for  $Fr_h \rightarrow 0$ , when the free-surface acts like a rigid wall, causing the lift to increase.

composing the propeller blade would then exert a lower lift—with respect to the infinite fluid case—which would in turn reduce the total thrust produced by the blade.

After the initial thrust loss, ventilation starts abruptly with a further reduction of the submergence. The propeller is subject to a violent decrease in thrust—and torque—with rapid and large fluctuations of the forces. This *partially ventilating* regime is characterized by an unstable air cavity over the propeller blade. This mode persists until the decrease of thrust slows down and ceases to be violently unstable, where a *fully ventilating* mode takes place. This further regime is characterized by a glassy sheet cavity over the whole propeller blade, leading to a considerably low thrust, but rather stable in time.

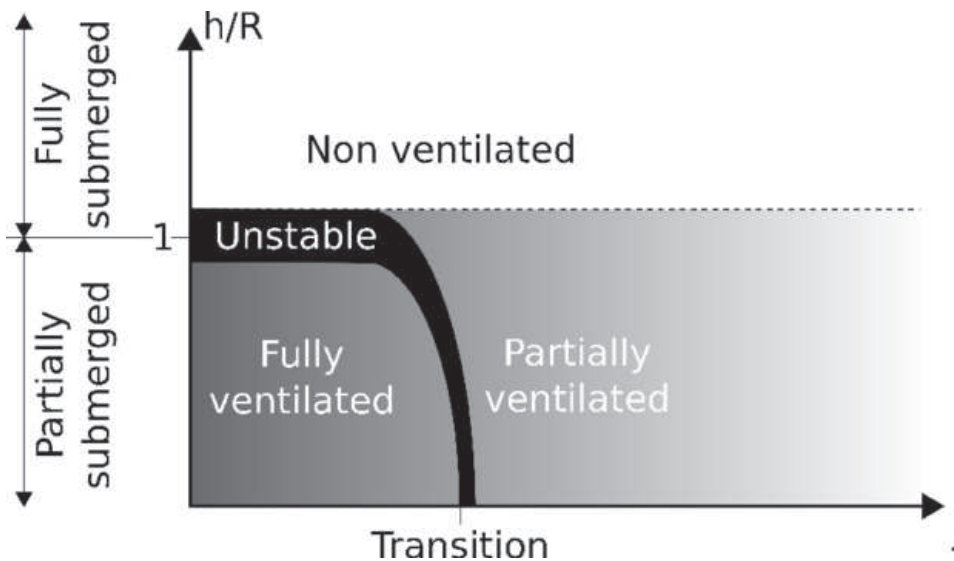


Figure 2.4: Ventilation flow regimes (Olofsson, 1996).

The validity range of the regimes previously described has been plotted in Figure 2.4—adapted from Olofsson (1996)—in terms of the advance number and the submergence ratio.

Another type of classification can be done based on the inception mechanism:

- by vortex-formation  
at deep submergence, where ventilation starts from a free-surface vortex, responsible of further feeding of air to the propeller;
- surface-piercing  
at moderate submergence, where the free-surface is deformed by the rotation

of the propeller until the blades become surface-piercing and air is continuously sucked from the blades crossing the free-surface.

- intermediate stage  
where both phenomena can lead to ventilation, being difficult to assess which one is responsible for its inception. Once the propeller has started ventilating, the surface-piercing-type mechanism is generally dominating.

With the term surface-piercing, one is generally referring to propellers designed to operate always in partially-submerged conditions, already at rest.

The term surface-piercing is here extended to a more general case of a fully submerged propeller, which becomes surface-piercing after ventilation occurs, as sketched in Figure 4.41b.

Ventilation has been until now treated neglecting the presence of cavitation. This was done in order to focus just on ventilation, but one should bear in mind that cavities filled with water vapor might coexist with those filled with air at atmospheric pressure. Although the combined study of ventilation and cavitation is out of the scope of this dissertation, a classification based on the mutual action of the two phenomena will be done, based on the work of Brandt (1973). As shown in Figure 2.5, two main regimes can be identified, of fully cavitating or ventilating flow and partially cavitating or ventilating flow.

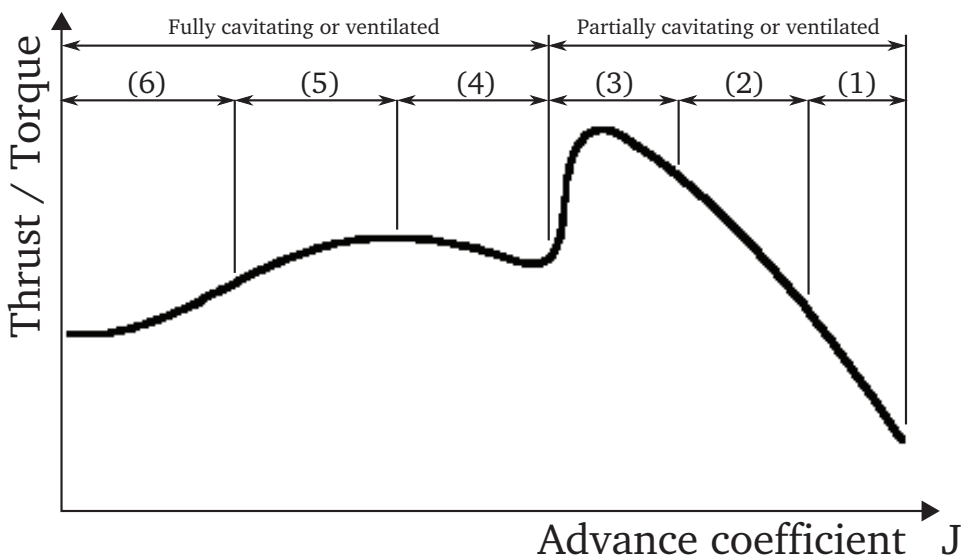


Figure 2.5: Flow regimes of partially submerged propellers (Brandt, 1973).

Within these two main categories, Brandt identified 6 flow sub-regimes:

1. Pressure side cavitation or ventilation;
2. Lightly loaded, partially submerged propeller with partial cavities;
3. Transition regime characterized by unstable flow with partial or full cavities, filled with water vapor or air;
4. Fully ventilating regime, with growing sprays;
5. Spray flow is thrown upstream and the pressure side which is out of water is contributing to the thrust being fully wetted;
6. Propeller fully wetted, also out of the water; both full ventilation and cavitation can coexist.

## 2.5 Momentum theory

The actuator disk theory is a simplification of the flow through the propeller which does not take into account the finite number of blades and the phenomena connected to it. Although simple, this theory alone is able to capture the modifications of the flow-field around the propeller until non-linearities occur, and can explain the deformation of the free-surface leading to surface-piercing ventilation.

The presence of the propeller modifies the undisturbed inflow accelerating the flow through the propeller in the axial direction and superimposing an induced radial velocity which is pulling the surrounding flow towards the propeller, as shown in the diagrams of axial and radial induced velocities computed by Hough and Ordway (1965) with an actuator disk theory (Figure 2.6).

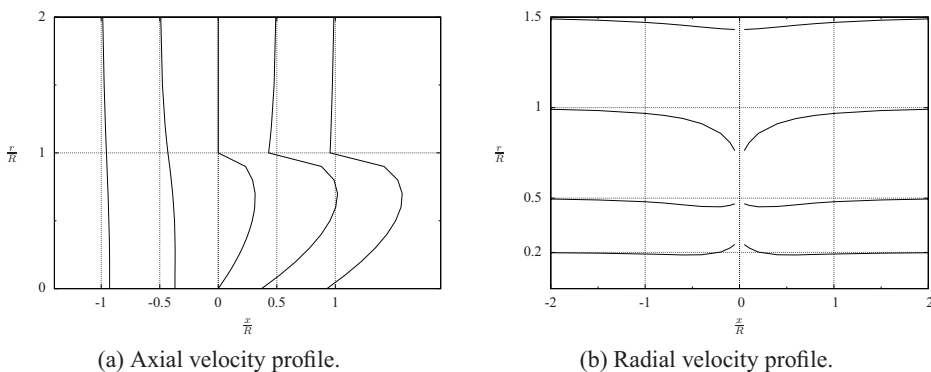
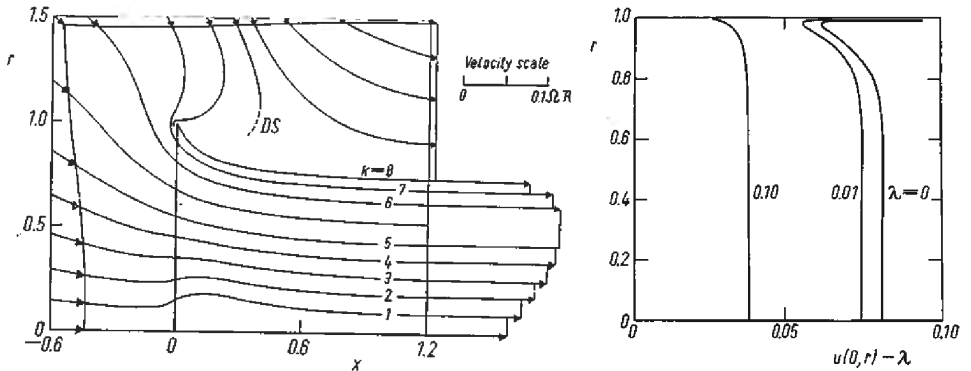


Figure 2.6: Axial and radial velocity profiles (Hough and Ordway, 1965).

In the vicinity of the free surface, these induced velocities are able to deform the interface between the two phases, pulling it towards the propeller, as seen in the experiments performed by Paik et al. (2008).

Based on previous works of Wu (1962) and Hough and Ordway (1965), Greenberg (1972) developed a non-linear actuator disk theory which was used to compute the flow-field around a heavily-loaded actuator disk. Figures 2.7a shows the complexity of the stream-tubes around the tip. Above the tip location a streamline (marked with DS, i.e. Dividing Streamline) is dividing the flow having the same direction of the free-stream from the one in the opposite direction. The nonlinearities around the tip can be better observed in Figures 2.7b, showing the radial distribution of the axial induced velocities through the disc for different propeller loadings.



(a) Stream-tubes for a heavy loaded propeller disc.

(b) Radial distribution of the axial induced velocities through the disc for different propeller loadings.

Figure 2.7: Greenberg (1972).

## 2.6 Inlet Vortex

Ventilation by vortex formation has analogies with other phenomena seen in fields different from marine applications, such as the inlet vortex in pump sumps and the ground vortex at the inlet of aircraft engines. The mature experience gained through many years of research in these latter fields—not pertaining to marine technology—can be applied to the present work in marine applications, where research studies are very recent. Based on these similarities, the description of the mechanisms of ventilation of a marine propeller by vortex formation will be attempted.

### 2.6.1 Pump sumps

The formation of an inlet vortex in pump sumps has been observed and described in literature (Denny, 1956; Markland and Pope, 1956; Swainston, 1974, 1976; Rajendran et al., 1998, 1999; Constantinescu and Patel, 2000). The importance of sump design is given from the fact that air entering the suction inlet through a vortex can seriously reduce both output and efficiency of the pump.

The formation of an air-entraining vortex is sketched in Figure 2.8, according to the description of Denny (1956) for a pump sump:

”...the vortex appeared first as a small dimple in the free surface (a), which gradually deepened to form a cone-shaped hole (b); air bubbles broke away from time to time (c) ... At high velocities the air-core lengthened to reach the suction-inlet and allowed continuous passage of air (d) ...

When the mouth of the pipe was less deeply submerged the vortex formed much closer to the pipe and tended to be less stable ...

With very small submergences the vortex frequently became concentric with the pipe ... Air entrainment of this type was always accompanied by considerable noise.”

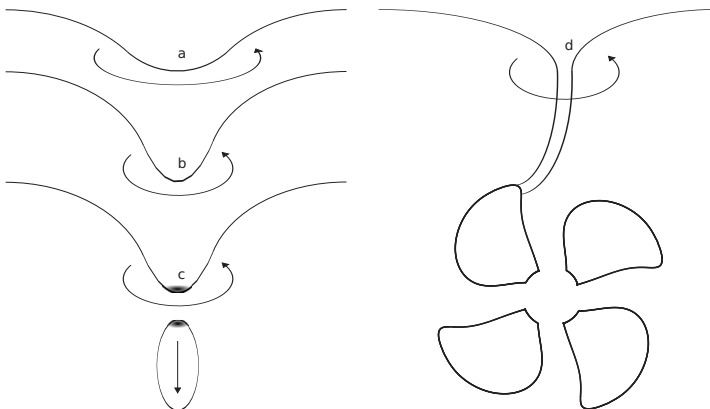


Figure 2.8: Stages in development of an air-entraining vortex. Adapted from Denny (1956) to the present geometry.

The submergence required to prevent air-entrainment was shown to depend largely on the velocity in the suction pipe (Denny, 1956). Using these two parameters (inlet-submergence and pipe-velocity), a borderline between the vortex-free and vortex-forming conditions could be drawn. Several other parameters were tested,

in order to assess their influence to vortex-formation. Among those, only the presence of swirl was relevant for the present work, and it showed to favor the formation of an air-entraining vortex.

### 2.6.2 Ground vortex

Vortex formation has been widely observed on ground, at the inlet of airplane engines. The ground based engine inlet vortex has aroused the interest of the engine designer because of the severe damage caused by solid particles which the vortex sucks up into the engine. In addition, it can also create flow distortions at the engine face that adversely affect the aerodynamic stability of the engine compression system. This phenomenon has been a common object of study in the last 5 decades, thus an extensive literature is available.

The first investigations into this problem (Rodert and Garrett, 1955) identified a vortex developing between the ground and the air inlet as the primary source of the forces which are necessary to lift objects and suck them through the inlet. Air flowing into an engine produces a region on the ground surface under the engine in which there is no flow and which is known as a stagnation region (Figure 2.9).

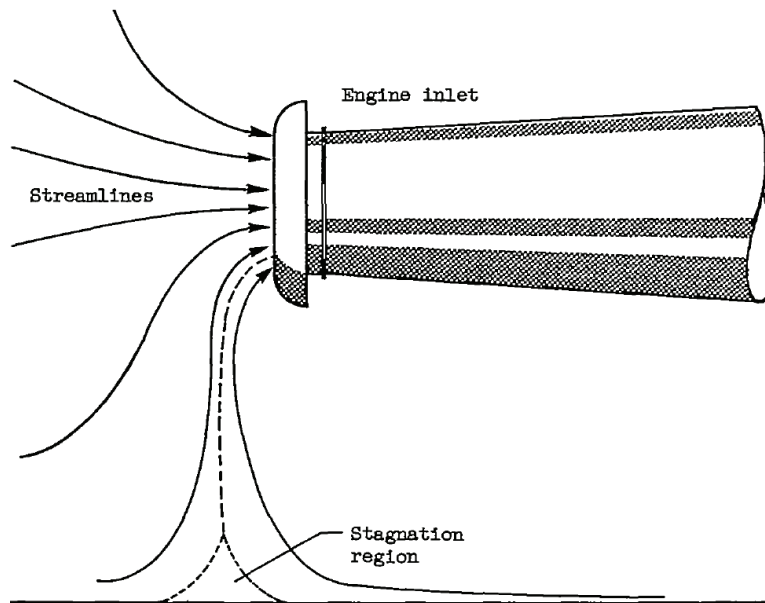


Figure 2.9: Stagnation region under inlet (Rodert and Garrett, 1955).

There will be one streamline extending from the stagnation region on the ground to the inlet, while all other streamlines terminate in the ambient atmo-

sphere. Since the circulation around a vortex line is constant (Helmholtz vortex law), a vortex line can not terminate in a fluid. This implies that a vortex must terminate on a surface, thus the only streamline along which a vortex may form is the one which terminates at the stagnation region.

Later experiments (Bissinger and Braun, 1974) gave a deeper understanding of the underlying physics in the inlet vortex formation. A preliminary survey performed with bubble generators revealed that an inlet vortex never comes alone but rather is an individual of a vortex system consisting of two inlet vortices (the ground based and the trailing one), secondary vortices, and ground vortices. Most of the following discussion about the ground vortex is based on these authors (Bissinger and Braun, 1974).

### 2.6.2.1 Stagnation points

The inlet vortex can only form when there is a stagnation point on the ground. The stagnation points and the flow field are calculated by means of potential flow calculations where the inlet in ground effect is replaced by a sink and an image sink in a uniform flow. These calculations show that one or more stagnation points can be formed on the vertical plane, in number and location(s) depending on the sink strength  $m$ .

Figure 2.10 shows the catching surface separating the fluid caught by the inlet from the fluid not caught by the inlet.

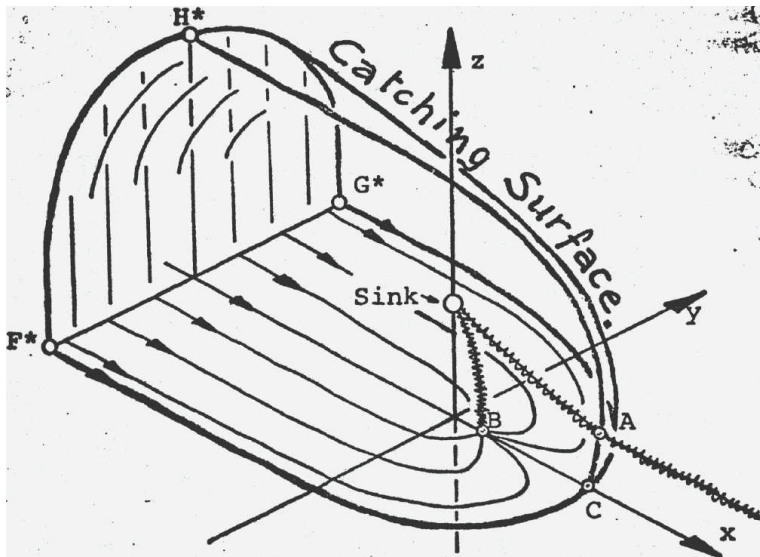


Figure 2.10: Deformation of free stream vorticity (Bissinger and Braun, 1974).

The stagnation point A is the point where the trailing vortex penetrates the catching surface. The flow inside the catching surface approaches A from all sides to be ejected into two directions, upstream towards the sink and downstream into the free stream. It is this flow field around the stagnation points A and B which is responsible for the formation of the inlet vortex system. All particles which pass the line F\*G\* in Figure 2.10 are collected at stagnation point B. If these particles carry vorticity, it is accumulated at B. Because the flow out of B is in z direction, vorticity parallel to the z-axis is stretched. When the accumulation and the stretching are strong enough to overcome the dissipation of vorticity due to viscosity, a ground based inlet vortex will form between the stagnation point B and the sink. Vorticity of particles passing the arc F\*H\*G\* on the catching surface is collected at the stagnation point A. From A the flow continues on streamlines normal to the catching surface. Therefore, the vorticity component parallel to the normal is stretched and a trailing inlet vortex may be formed.

### 2.6.2.2 Ambient vorticity and amplification

An inlet vortex can form only if ambient vorticity exists in the fluid drawn into the inlet, created at a far-upstream location where the existence of the vorticity is independent of the presence of the inlet.

The flow around a stagnation point with radial inflow and axial outflow increases the vorticity component parallel to the outflow direction. This means that this type of stagnation point flow can produce a vortex, if suitable vorticity is transported into the stagnation point. This statement is a modification of analytical and experimental findings by Sadeh et al. (1970a,b). This amplification effect was also found by Rott (1958), who derived an exact solution of the Navier-Stokes equations for the linearized flow. The analytical derivation for the vortex amplification, as it occurs on the ground based inlet vortex, was given in Bissinger's thesis:

$$\omega_z = \frac{C_2}{r^2 Re + 1} \quad (2.27)$$

$C_2$  is an integration constant and  $r$  the distance from the stagnation point.

Equation 2.27 shows that the vorticity component perpendicular to the ground plane is amplified when it approaches the stagnation point ( $r \rightarrow 0$ ). The amplification increases when  $Re$  is increased, i.e. when the vortex strength  $m$  increases, and when the ground distance is reduced.

Vorticity around the stagnation point is then intensified by vortex stretching. Kelvin's theorem states that the circulation around a material loop is constant with time. This implies that axial stretching of vorticity lines increases their vorticity (Figure 2.11).



Figure 2.11: Vorticity amplification after stretching (Green, 1995).

The investigations into a deeper physical understanding on the inlet vortex phenomenon was continued by De Siervi et al. (1982) and Shin et al. (1986a,b). Their works confirm that an inlet vortex can develop when vertical vorticity lines are sucked into the air inlet and are both superimposed on each other and amplified by stretching (Figure 2.12).

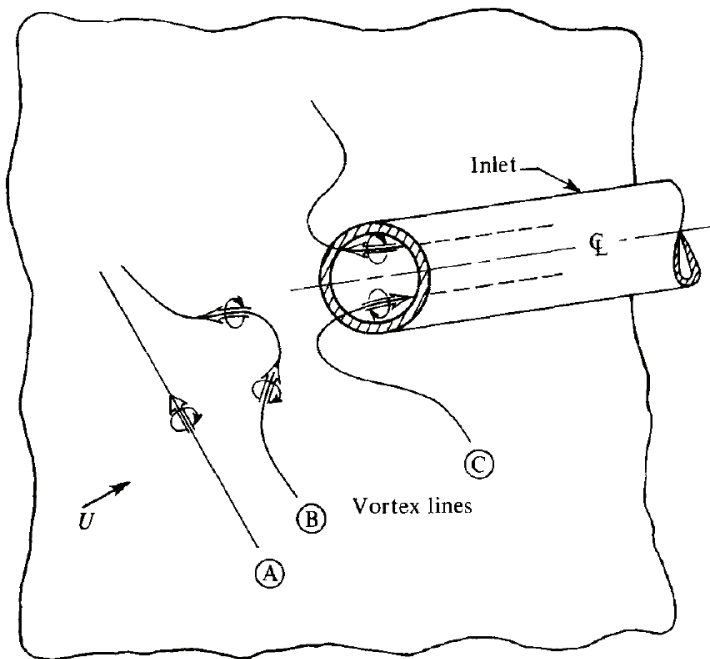


Figure 2.12: Ingestion of a vortex line into an inlet (De Siervi et al., 1982).

It was shown by the same authors that there is another mechanism of inlet-vortex formation, which does not require the presence of ambient vorticity. An inlet vortex can arise in an (upstream) irrotational flow, for an inlet in cross wind. In this situation, the vortex is accompanied by a variation in circulation along the length of the inlet.

The ratio of inlet velocity to upstream velocity  $U_i/U_\infty$  is an important parameter in

determining the appearance of an inlet vortex, controlling the stretching incurred by a vertical vortex line and hence the vorticity amplification.

Shin et al. (1986a) have shown that the inlet vortex and the trailing vortex have essentially equal and opposite circulation. In addition, the production of vorticity, due to vortex stretching, is the mechanism by which both of these are maintained. A parametric study was conducted to define the correlation between the Capture Ratio (CR) and the type and position of the inlet vortex.

### 2.6.2.3 Ground boundary layer

The ground boundary layer is not necessary for the appearance of a ground based inlet vortex. Tests were performed with a flow plane of symmetry, showing the appearance of inlet vortices in spite of the absence of a ground boundary layer.

### 2.6.2.4 Unsteadiness

The inlet vortex is unsteady (and unstable). It is not only moving along an irregular path on the ground plane, it also appears and disappears irregularly. Also the sense of rotation of the ground based inlet vortex and the trailing inlet vortex can be unpredictable, exchanging sometimes their position and role without test parameter change.

More recent experimental and numerical studies (Karlsson and Fuchs, 2000; Moroianu et al., 2004; Secareanu et al., 2005) have shown the complex vortical system arising at an engine intake, contributing to the physical understanding of the unsteady and/or oscillatory phenomena connected to the problem. Karlsson and Fuchs (2000) depict a rather complex vortex system using instantaneous contours of negative  $\lambda_2$ <sup>3</sup>, as a result of Large Eddy Simulations (LES). This vortex system is characterized by two vortices between the ground plane and the air inlet, accompanied by traces of horse-shoe vortices at the foot-points of the inlet vortices, and by several trailing vortices pointing downstream. Secareanu et al. (2005) validated the numerical results of Karlsson and Fuchs (2000) using Particle Image Velocimetry (PIV) and Laser Doppler Anemometry (LDA) measurements and obtained data on the ingestion of particles by a vortex-inlet system.

---

<sup>3</sup> $\lambda_2$  is the second eigenvalue of the tensor  $S^2 + \Omega^2$ . Its negative value identifies vortex cores, as shown by Jeong and Hussain (1995).  $S$  and  $\Omega$  are the symmetric and antisymmetric components of the velocity gradient tensor, respectively.

### 2.6.2.5 Occurrence and direction of vortex

A correlation of the experimental data allows to define a threshold for the formation of the inlet vortex, having as parameters the inlet to free-stream velocity ratio  $U_i/U_\infty$  and the submergence ratio  $h/D_i$  based on the inlet diameter  $D_i$ . The boundary between the vortex forming and non-vortex forming flow regimes seems to follow a straight line, as shown in Figure 2.13 (Jermy and Ho, 2008).

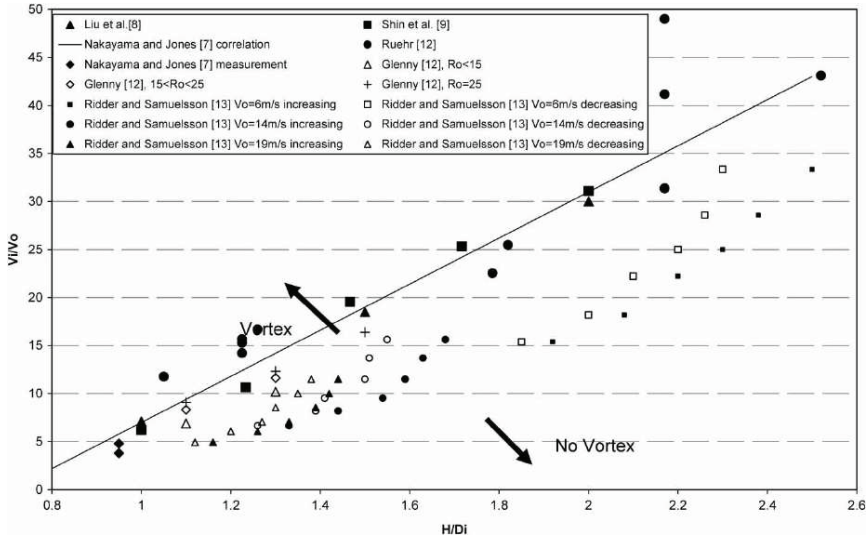


Figure 2.13: Boundary between the vortex forming and non-vortex forming flow regimes (Jermy and Ho, 2008).

In order to take into account the free-stream velocity gradient  $W = \nabla \vec{U}$ , which can be thought of as a "background vorticity", the Rossby number is introduced:

$$Ro = \frac{U_i}{WD} \quad (2.28)$$

Motycka et al. (1973) observed that a decrease in *Rossby* number, i.e. in presence of high velocity gradients, increases the range of conditions at which vortices form.

The results of Nakayama and Jones (1996) indicate that the method based on the potential-flow stagnation point underestimates the occurrence of the vortex, due to the fact that there is a large contraction of the streamlines away from the wall.

The vortex system consists in principle of a vortex pair of two counter-rotating inlet-vortices. The rotation direction changes from high (Figure 2.14a) to low (Figure 2.14b) velocity ratio  $U_i/U_\infty$  (Brix et al., 2000). Between these two sta-

ble regions, there is an unstable transition phase, in which both vortex pairs are existent.

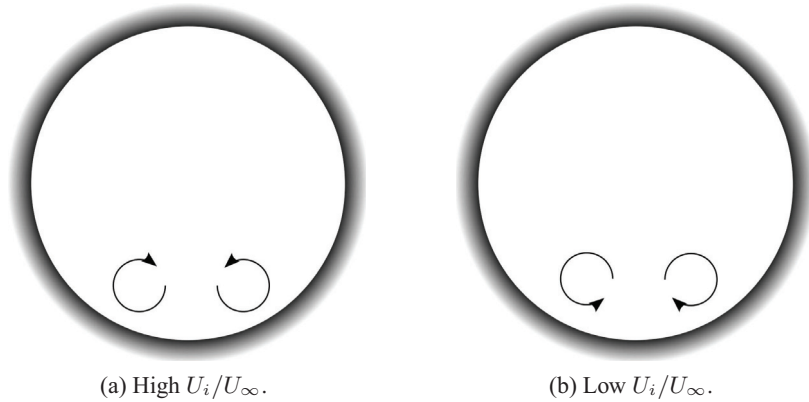


Figure 2.14: Vortex pairs with different rotation direction at high and low velocity ratio  $U_i/U_\infty$  (Brix et al., 2000).

In presence of vertical vortex lines, the vortex with the same rotation direction as the ambient vortex lines will increase in size and strength, prevailing on the opposite vortex—which is weakened until it can no longer be detected.

### 2.6.3 Marine propellers

Shiba (1953) has observed the occurrence of vortices during his ventilation experiments and their continuous feeding of air to the propeller. He describes three kinds of *air holes* produced on the free-surface when the propeller is fully submerged. One which is not rotating while the other two are rotating in opposite directions. Among these last two, the vortex aligned with the blade trailing vortex occurs more frequently and is more stable.

Huse (1973) describes intermittent noise and vibration experienced by fishing vessels in heavy head seas and low speeds, occurring even when the propeller was not piercing the free-surface, but completely submerged.

For ventilation of completely submerged propellers air is drawn from the water surface down to the propeller, where the pressure is locally below atmospheric. This air is transported through an intermediate region where the pressure is generally above atmospheric.

He identifies a second type of ventilation for submerged propellers, characterized by air bubbles. In this case the propeller is ventilated by the air bubbles generated in the boundary layer of part of the hull close the free-surface. This type of ventilation only occurs at relatively high model speeds. Although of great interest

on a real configuration, this type of ventilation will not be further analyzed in the remaining of the present work, which is mainly devoted to ventilation generated by the propeller itself, without the presence of the hull.

Nishiyama (1986) has extended the results of Huse (1973) introducing the influence of cavitation on a vortex stretching between the propeller and the hull. Through a series of experiments carried out in a cavitation tunnel, Nishiyama (1986) showed that cavitation can occur on the tail of the vortex impinging the propeller and then move toward the hull. This is explained assuming the vortex is of Rankine type, where the pressure at its lower and narrow core rapidly decreases until cavitation will occur.

### 2.6.3.1 Ventilation inception by vortex formation

Ventilation inception is defined as the condition at which air is drawn into the low pressure region in a non-cavitating flow, from an external source—as at the free-surface of a liquid.

Following the work of Nakayama and Jones (1996), Brix et al. (2000) and Jermy and Ho (2008), a boundary between the vortex forming and non-vortex forming flow regimes can be drawn. Given a propeller with  $N$  blades, each with a radial circulation  $\Gamma(r)$ , rotating with angular velocity  $n$ , Hough and Ordway (1965) have derived a general expression for the corresponding induced velocity field by means of a Fourier transform in terms of the Legendre functions. Following their analytical derivation, Hough and Ordway (1965) achieved a simplified expression for the steady component of the induced velocity  $U_A$  in the free-stream direction on the propeller plane:

$$U_A = \frac{Nn\Gamma(r)}{4\pi U} \quad (2.29)$$

The ratio between the induced and free-stream velocity can then be simplified to:

$$\frac{U_A}{U} = \frac{N}{4\pi} \frac{\Gamma(r)}{UR} \frac{nR}{V} = \frac{N}{4\pi} \frac{\tilde{\Gamma}(r)}{J} \quad (2.30)$$

where  $\tilde{\Gamma}(r) = \Gamma(r)/UR$  is the dimensionless blade circulation distribution.

The inlet to free-stream velocity ratio is then expressed by  $1 + U_A/U$ .

Having Figure 2.13 in mind, equation 2.30 shows that vortices are formed at high propeller loadings, i.e. at lower advance ratios  $J$ , and for these conditions ventilation by vortex formation is more likely to occur.

The vortex system consists in principle of a vortex pair of two counter-rotating inlet-vortices. The discussion of Brix et al. (2000) about the rotation direction in case of a ground inlet-vortex are applicable also to the case of a marine propeller

below the free-surface. Asymmetry in the vertical vortex lines is introduced in this case by the presence of the propeller, which will modify the ambient vorticity through the vortices trailing from the blade tips. Depending on the rotation direction of the propeller, one direction will prevail on the other, and so will the corresponding free-surface vortices.

## 2.7 Dynamic loads

An attempt to understand the dynamic loads a propeller is subject to during ventilation will be performed describing the single mechanisms underlying this complex phenomenon.

During ventilation, the loads on each propeller blade fluctuate in time as the blade goes through four phases: in-air, blade-entry, in-water, and blade-exit, as shown in Figure 2.15. These fluctuating forces introduce structural loads on the propeller blades.

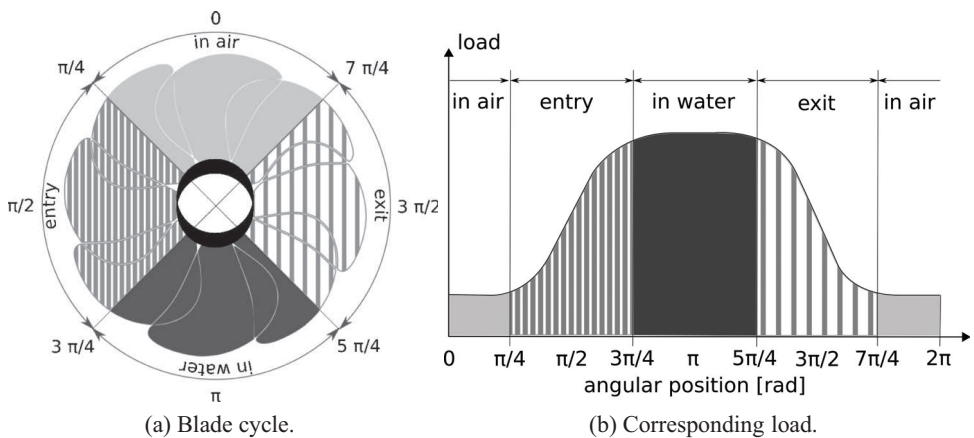


Figure 2.15: Dynamic loads on a surface-piercing propeller (Olofsson, 1996).

The water-entry phase of a rigid body can be further divided into three phases, (i) shock, (ii) flow-forming and (iii) open-cavity. There is less knowledge on the water-exit phase. It is known that the amount of entrained water is a fraction of the body volume, a fact that tends to reduce the vertical force on the propeller. The water-exit flow is also the source of much of the spray generated by the propeller when operating in the base-vented regime.

During the base-vented regime the vertical force is directed upward, implying that water-entry impact forces are significant.

During the fully vented condition the net vertical force is downward, implying that the water-exit spray force is greater than than the water-entry impact force.

Huse (1973) was among the first to observe the force oscillations the blade of a ducted propeller is subject to during an event of ventilation through a free-surface vortex.

In a similar manner, Nishikawa and Uchida (1989) have investigated the vibratory shaft force induced by ventilation. As expected, the shaft force arises when ventilation occurs and increases rapidly with growing up of partial ventilation. At lower submergence the shaft force decreases, until full ventilation occurs, where it reaches a small value. With a further decrease of the submergence, the shaft force increases, due to impact and spray loads during water-entry and exit.

Their conclusions are that the significant vibratory shaft force is induced by partial ventilation, and are characterized by the shaft frequency  $n$ , as the dominant frequency. This last feature makes the phenomenon quite unique with respect to cavitation, where the blade frequency component  $4n$  is dominant. An explanation of this characteristic is given by the authors, based on visual observations: during partial ventilation, some of the blades show a full sheet cavity, typical of the full ventilation pattern occurring in shallow submergence, whereas the remaining blades do not form any cavity as they were fully submerged.

Olofsson (1996) points out that the high frequency dynamic loads during ventilation are important, especially when considering mechanical wear and tear. He observed that large high-frequency dynamic loads occur especially in the transition to-and-from ventilation, i.e. the unstable, partially ventilated regime.

Recent results for the blade loading of a ventilated thruster at low advance velocity can be found in Koushan (2004, 2006). These results confirm that the high-frequency dynamic loading can be significant. The standard deviation of the shaft frequency propeller blade force fluctuations was found to be almost 100% of the average force when the propeller was partially submerged. Large fluctuations were found also for the fully submerged, ventilated condition.

Other types of loads normally occur during operation of surface-piercing propellers, and blade strength, fatigue, and resonant vibration issues must be considered during their design and analysis. Hydro-elastic effects become important at high advance coefficients, due to bending and/or torsional oscillations. Resonant blade vibration may also occur due to the cyclic loading and unloading of the blades associated with the blades entry to and exit from the free surface. During resonance, the vibrations are amplified, and the resulting dynamic load is a combination of hydrodynamic and inertial loads due to fluid-structure interaction. These loads can cause serious problems, since large stress transients may develop, resulting in peak stresses exceeding the yield strength of the blade material and hence causing structural fatigue.

# Chapter 3

## Verification studies

Verification studies were performed in order to test the capabilities of the solver towards the most challenging numerical features one has to cope with while dealing with a ventilating propeller, such as (i) presence of the free-surface and (ii) rotating lifting surfaces.

### 3.1 Submerged hydrofoil

The present analysis focuses on the validation and verification of the solver adopted in the case of a two-dimensional hydrofoil close to the free surface.

This problem has caught much attention after the experiments carried out by Duncan (1983), who observed breaking and non-breaking waves over a hydrofoil model and measured the free-surface profile. Several authors have attempted to reproduce Duncan's experiments using different numerical approaches. Among them, the inviscid BEMs by Landrini et al. (1999) and Faltinsen and Semenov (2008) have reproduced accurately the experimental results until breaking occurs. The following flow evolution can not be handled by potential flow solvers. RANS simulations capture the correct form of the wave and are intrinsically able to handle breaking waves, but tend to under-predict the wave amplitude. Some authors have better captured spilling breakers (Rhee and Stern, 2002; Muscari and Di Mascio, 2003) implementing a breaking-wave model based on empirical data (Cointe and Tulin, 1994).

As depicted in Figure 3.1, a NACA0012 foil at incidence of 5 deg with a chord length  $c = 0.203$  m is fixed in water, subject to an incident current  $U = 0.8$  m/s. Two cases are studied here, chosen among those tested by Duncan (1983), corresponding to a non-breaking and a breaking wave condition, with submergence  $h$  of 0.261 m and 0.185 m, respectively. The bottom of the tank is located 0.175 m below the foil, as in the experiments.

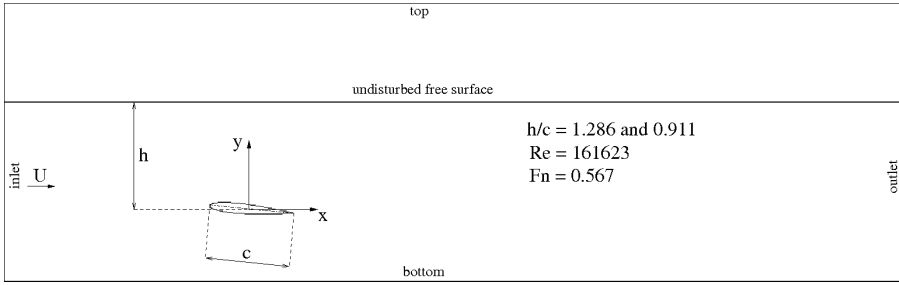


Figure 3.1: Numerical domain and definition of main parameters.

The Froude number based on submergence  $Fr_h$  is equal to 0.50 and 0.27 for  $h/c$  equal to 0.261 and 0.911 respectively, computed according to:

$$Fr_h = \frac{U}{\sqrt{g h}} \quad (3.1)$$

In the approximation of  $Fr_h \rightarrow 0$  the foil is exerting for different values of submergence higher forces with respect to the infinite fluid case, as shown in Figure 3.2 (Hough and Moran, 1969).

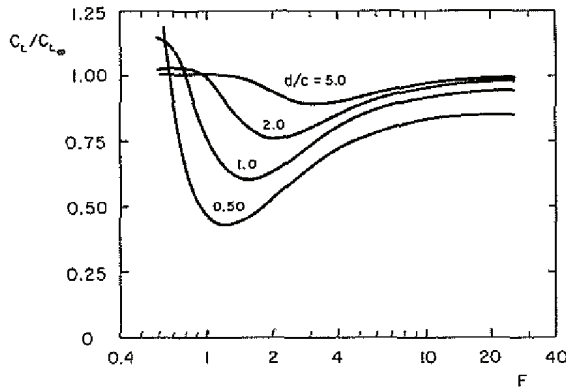


Figure 3.2: Lift ratio as a function of  $Fr_h$  and  $h/c$  (Hough and Moran, 1969).

For these low submergences, the free surface acts like a rigid wall, and the problem becomes similar to a lifting wing close to the ground, experiencing an increase in lift with decreasing distance from the ground. This was shown by Faltinsen (2005, § 6.8.1) using Weissinger's theory (1947) based on the quarter-three-quarter-chord approximation. For this range of  $Fr_h$ , an analytical formula taking into account the free-surface effect is derived (Faltinsen, 2005, eq. 6.143)

for the lift coefficient:

$$C_L \left( \frac{h}{c} \right) = C_L \left( \frac{h}{c} = \infty \right) \left[ 1 + \frac{1}{16} \left( \frac{c}{h} \right)^2 \right] \quad (3.2)$$

when  $Fr_h \rightarrow 0$

### 3.1.1 Numerical method

The described problem is solved assuming a viscous, incompressible, two-phase (air and water) flow. Computations were performed using the commercial RANS code Fluent (2006) and the open source code OpenFOAM (2009).

In order to capture possible unsteadiness of the flow, a time-dependent approach is chosen using a first order implicit scheme.

A short description of the employed numerical methods will be given in the following sections. Further details about the solvers can be found in the Fluent manual (Fluent, 2006) and the OpenFOAM user guide (OpenFOAM, 2009).

**Fluent** The momentum equation and those for the turbulence closure are solved with a second order upwind scheme. The Body Force Weighted discretization algorithm is used to interpolate the node values of the pressure from the cell values, as required by the solver. The pressure-velocity coupling is achieved using a Semi-Implicit Method for Pressure-Linked Equations (SIMPLE) algorithm.

The free surface evolution is handled using an implicit formulation of the Volume Of Fluid (VOF) method with a modified High Resolution Interface Capturing (HRIC) scheme.

**OpenFOAM** The Navier-Stokes equations over a finite volume are solved using the following schemes, all based on the  $2^{nd}$  order Gaussian integration, summarized in Table 3.1.  $\phi$  and  $\phi_{rb}$  are respectively the total and surface-normal velocity flux, while  $\gamma$  is the phase fraction.

	Term	Discretization
<i>Gradient</i>	$\nabla$	linear
<i>Convection</i>	$\nabla \cdot (\rho\phi U)$	limited linearV 1
	$\nabla \cdot (\phi\gamma)$	vanLeer
	$\nabla \cdot (\phi_{rb}\gamma)$	interfaceCompression
<i>Laplacian</i>	$\nabla^2$	linear corrected

Table 3.1: Numerical schemes used in OpenFOAM.

The pressure-velocity coupling is achieved using a Pressure Implicit with Splitting of Operators (PISO) algorithm. The free-surface location is computed using the Multidimensional Universal Limiter for Explicit Solution (MULES) method, based on a VOF method.

**Boundary conditions** At the inlet, the undisturbed free surface elevation and the free stream velocity are assigned, whereas a zero normal derivative for the pressure is specified. A constant dynamic pressure is assigned at the outlet, where the velocity satisfies a zero normal derivative.

A zero flux of all quantities is enforced across the bottom boundary. The same zero flux condition is assigned in `FLUENT` at the top boundary, whereas a constant total pressure and a blended zero-gradient and fixed-value condition is specified in `OpenFOAM`.

Unless otherwise specified, a no-slip condition on the hydrofoil is set.

**Grid** The domain is divided in blocks allowing refinements in the near wall region, around the wake and across the free surface, as depicted in Figure 3.3a. A close up of the near wall mesh region is shown in Figure 3.3b.

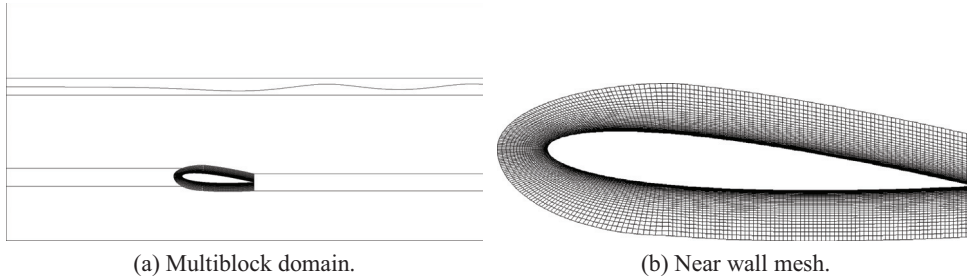


Figure 3.3: Multiblock domain and near wall mesh.

A convergence analysis has been carried out in three manners, refining the grid (*i*) in the whole domain but in the near wall region, (*ii*) locally near the free surface and (*iii*) in the near wall region of the hydrofoil shown in Figure 3.3b.

Two levels of refinement of the whole domain (*i*) with respect to the default grid, leading to about 1.5 million cells, did not produce any significant change in the amplitude of the free surface waves. A very fine mesh size near the free-surface (*ii*), with values of half mm did not produce either significant changes.

Only the results obtained refining the near wall region (*iii*) highlighted an effect on the solution, as discussed in Section 3.1.2. For this last case, four levels of grid refinement were used, as given in Table 3.2.

<i>grid</i>	$y/c \cdot 10^4$	$y^+$
<i>coarse</i>	141.4	50
<i>fine</i>	5.8	4
<i>2fine</i>	2.7	0.75
<i>3fine</i>	1.4	0.35

Table 3.2: Near wall region grid refinement.

The first wall cell of the coarse grid lies within the log layer of the boundary layer, whereas all the three fine meshes are within the sub-viscous layer. The height of the cells located in the free-surface region is 0.0005 m, corresponding to 0.0025 chord lengths.

**Flow features** The near-wall region is modeled with Standard Wall Function (SWF) for the coarse grid, whereas for the three fine grids the viscosity-affected region is resolved with a mesh all the way to the wall, including the viscous sub-layer. Five types of flows were considered, summarized in Table 3.3.

#	Viscosity	Type
1.	inviscid	
2.	viscous	laminar {
3.		
4.		turbulent {
5.		
		SST $k-\omega$
		Realizable $k-\epsilon$

Table 3.3: Flow features.

Two models have been employed for the turbulence closure, the realizable  $k-\epsilon$  (Shih et al., 1995) and the Shear Stress Transport (SST)  $k-\omega$  (Menter, 1994) model. The  $k-\epsilon$  model is robust and widely used in different kinds of fluid flows. The SST  $k-\omega$  model is a variation of the standard  $k-\omega$  model (Wilcox, 1998) incorporating modifications for low-Reynolds-number effects, compressibility, and shear flow spreading. It is widely used in lifting surfaces such as foils and propellers.

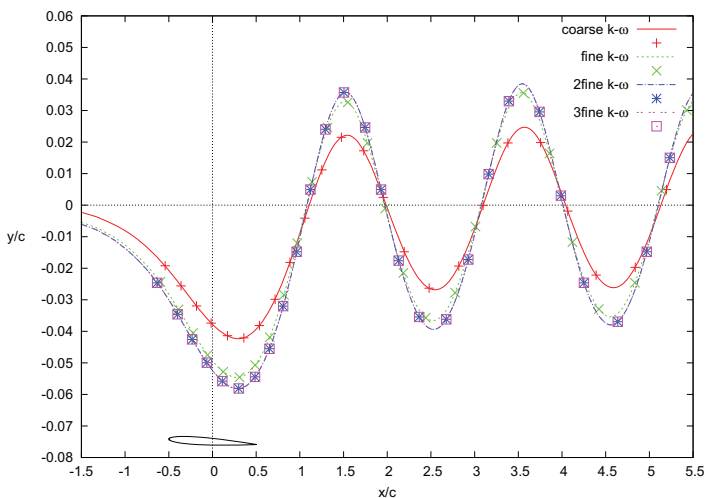
In order to check the influence of the wall boundary condition, additional simulations were performed using free-slip condition on the wall for the viscous cases.

### 3.1.2 Results

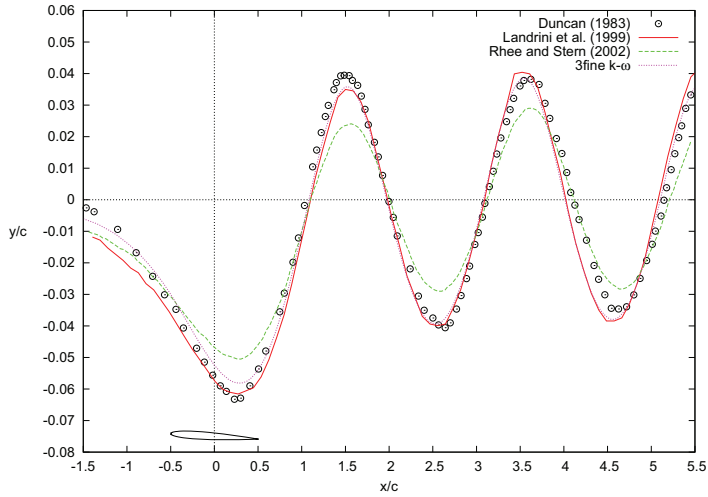
The results of the 2D-foil validation and verification studies are discussed in the following sections, first for the submergence ratio  $h/c = 1.286$  (obtained using both solvers) and for  $h/c = 0.911$  (obtained using FLUENT).

#### 3.1.2.1 Fluent

Figure 3.4a shows the free-surface deformation along the free-stream direction, as predicted by FLUENT with a SST  $k-\omega$  turbulence model. The wave behavior is captured already by the *coarse* mesh, but the wave amplitude is underestimated. The under-predicted wave amplitude was widely found in other RANS simulations (Mori and Shin, 1988; Hino, 1997; Rhee and Stern, 2002; Muscari and Di Mascio, 2003) and could be attributed to the under-prediction of the suction side pressure. Using a finer near wall mesh improves the accuracy up to the *2fine* mesh, for which a mesh independent solution is achieved. Figure 3.4b shows the comparison between the converged results and the experiments by Duncan (1983). The solutions of the BEM by Landrini et al. (1999) and the RANS solver by Rhee and Stern (2002) are also reported, the latter being performed using a SST  $k-\omega$  turbulence model. The improvement of the present solution in terms of wave-height with respect to the RANS simulation by Rhee and Stern (2002) could be ascribed to a greater refinement in the near wall region, but not sufficient details are given in Rhee and Stern to assess it. Among the three numerical solvers, the BEM by Landrini et al. (1999) gives the best results and reproduces correctly the experiments.



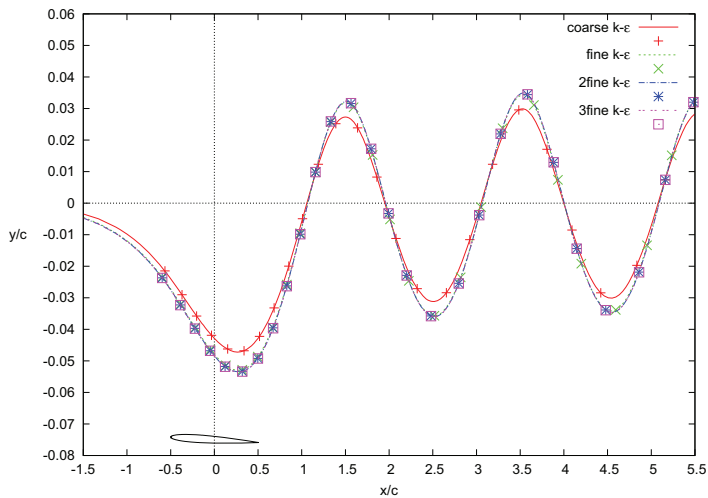
(a) Present results



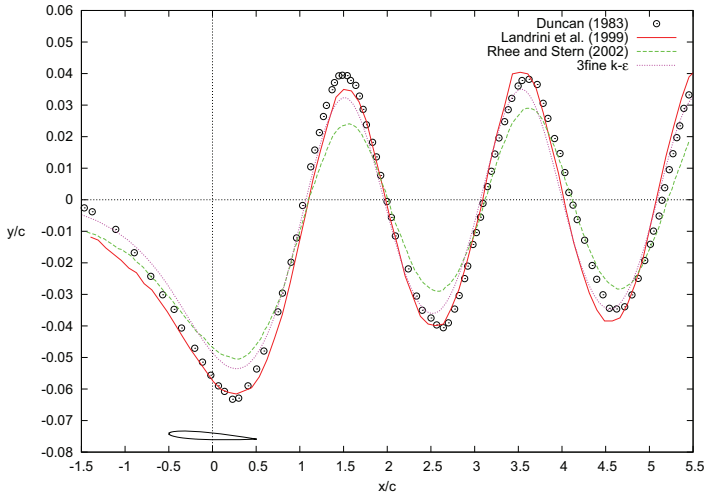
(b) Comparison of  $3fine$  grid with available data

Figure 3.4: Free-surface deformation [ $h/c = 1.286$ , Fluent SST  $k-\omega$ ]

Figure 3.5 gives the same variable, but present results have been obtained with the realizable  $k-\epsilon$  turbulence model. Figure 3.5b shows a larger under-prediction of the wave amplitude, which suggests that the  $k-\epsilon$  model is more diffusive than the  $k-\omega$  model. From Figure 3.5a, using a *fine* near wall mesh improves the accuracy, but further refinements confirm a mesh independent solution.



(a) Present results

(b) Comparison of *3fine* grid with available dataFigure 3.5: Free-surface deformation [ $h/c = 1.286$ , Fluent realizable  $k-\epsilon$ ]

Tzabiras (1997) has simulated an experiment by Duncan (1983) with submergence  $h = 0.193$  m using a standard  $k-\epsilon$  model with wall functions. The corresponding prediction of the free-surface characteristics are in satisfactory agreement with the measured data; the tested ranges of  $y^+$ , from 20 to 40, did not affect the results significantly. The present analysis highlights an effect of the near wall mesh size when resolving the boundary layer directly.

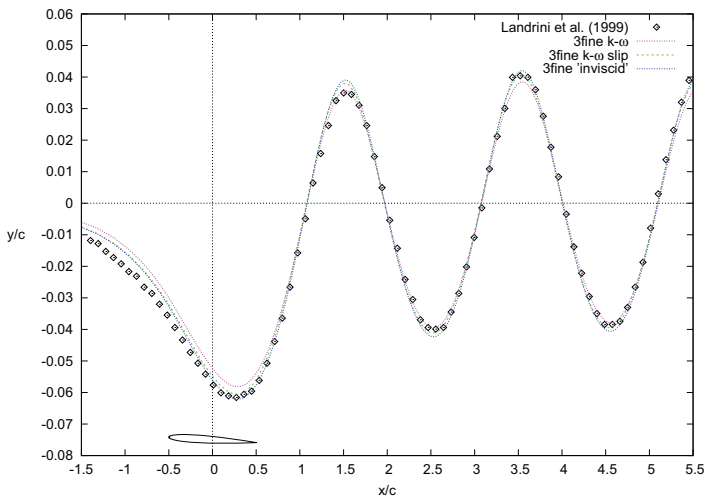
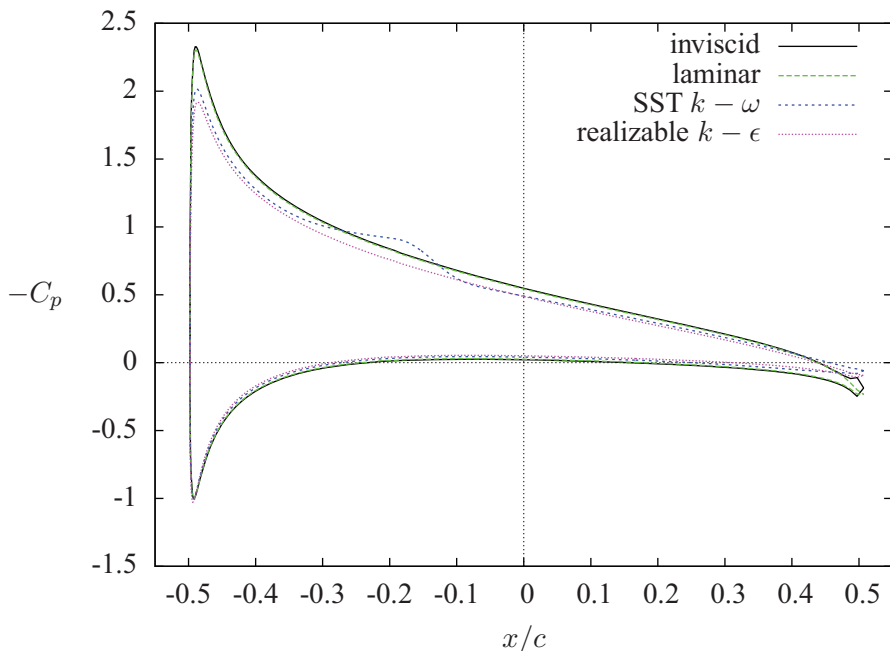
Figure 3.6: Free-surface deformation ( $h/c = 1.286$ , *3fine* mesh)

Figure 3.6 gives the results of the inviscid solution and the SST  $k-\omega$  simulation using a free-slip condition on the wall. Removing the no-slip condition from the turbulent flow improves the accuracy with respect to the corresponding simulation with no-slip condition. The free-slip laminar solution coincides with the free-slip SST  $k-\omega$ , and thus has not been plotted. The inviscid solution is the closest to the BEM results, which in turn match the corresponding experiments.

The pressure coefficient obtained with the *2fine* mesh has been plotted in Figure 3.7a for different viscosity models. Viscosity has no effect in the laminar solution, which is overlapping the inviscid one. The addition of turbulent viscosity reduces the force on the suction side, where a local pressure increase can be noticed around one third of the chord-line for the SST  $k-\omega$  turbulence model. In order to investigate this behavior, a simulation in infinite fluid conditions has been performed, and the results compared to the solution obtained by Tzabiras (1997) (Figure 3.7b). The local pressure increase occurs only for a finer mesh and seems not to be related to the presence of the free-surface, but rather to a special treatment of the body walls. Further details able to explain this behavior of the SST  $k-\omega$  turbulence model could not be found in the FLUENT's user guide.



(a)  $h/c = 1.286$ , *2fine* mesh.

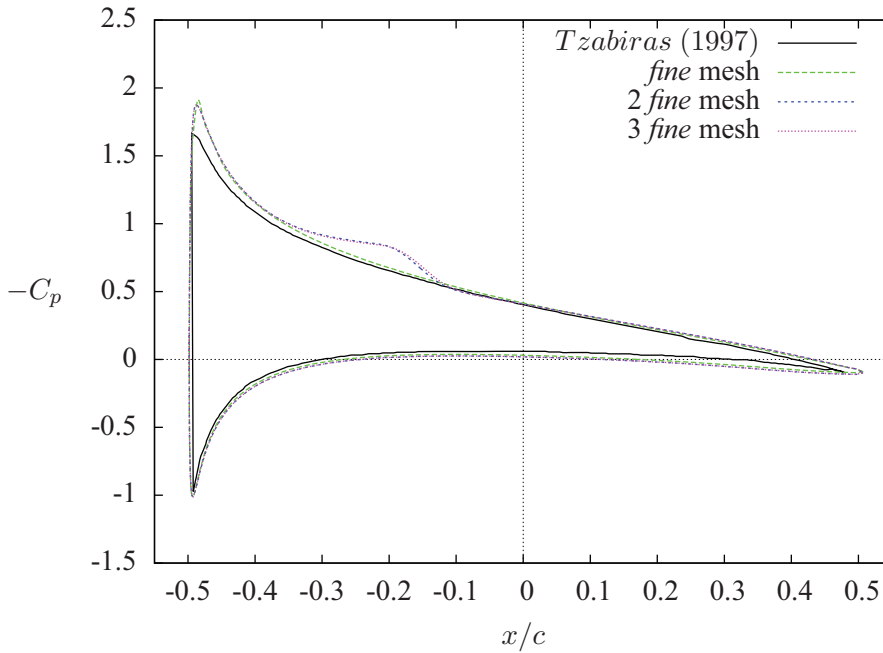
(b)  $h/c = \infty$ , SST  $k - \omega$ .

Figure 3.7: Comparison of the pressure coefficient along the chord line.

Table 3.4 summarizes the present results obtained for the first trough amplitude (Table 3.4a) and the lift coefficient (Table 3.4b), in terms of relative error with respect to the experiments and the BEM solution by Landrini et al. (1999), respectively. An increasing lift coefficient corresponds to a more accurate representation of the free surface. Adopting a turbulent formulation for the present problem, where the influence of the viscosity is negligible, affects significantly the accuracy of the results, by introducing diffusion terms. The advantages of using a SST  $k-\omega$  turbulence model with a fine grid and the effect of different wall conditions are confirmed.

	$k-\epsilon$	$k-\omega$	$k-\omega$ slip	inviscid
<i>coarse</i>	-23.1%	-31.1%		
<i>fine</i>	-13.4%	-11.0%		
<i>2fine</i>	-13.4%	-5.4%		
<i>3fine</i>	-12.6%	-5.4%	-1.4%	1.0%

(a) First trough amplitude

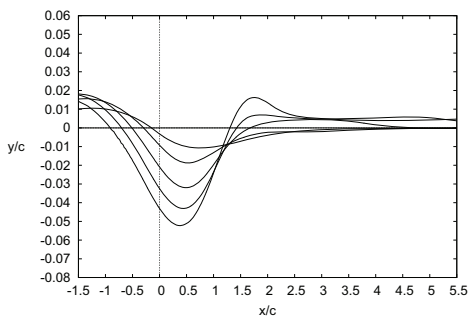
	$k-\epsilon$	$k-\omega$	$k-\omega$ slip	inviscid
<i>coarse</i>	-25.7%	-38.1%		
<i>fine</i>	-12.7%	-11.4%		
<i>2fine</i>	-12.0%	-4.5%		
<i>3fine</i>	-11.7%	-2.3%	2.3%	5.6%

(b) Lift coefficient

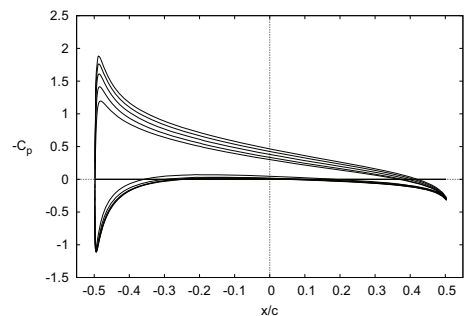
Table 3.4: Relative error of the present solution obtained using `Fluent` with respect to the experiments (a) and the BEM solution (b)

### 3.1.2.2 OpenFOAM

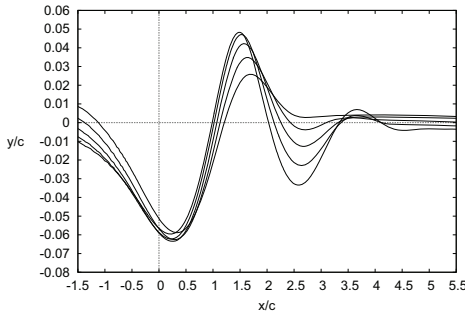
The build-up of the pressure on the hydrofoil and the corresponding free-surface deformation is shown in Figure 3.8. A steady solution for the forces is rapidly achieved, with the pressure coefficients reaching a steady-state behavior already after 8 chord lengths (Figures 3.8b, 3.8d and 3.8f). The corresponding free-surface needs more time to develop and to reach its final steady state. The first trough is developed during the first 4 chord lengths, while the following crest starts forming, as shown in Figure 3.8a. Between 4 and 8 chord lengths (Figure 3.8c) the second trough and crest start emerging from the undisturbed free-surface location, while the formation of the downstream wave pattern occurs afterwards (Figure 3.8e). Both the forces on the foil and the free-surface experience several oscillation cycles before reaching a steady state.



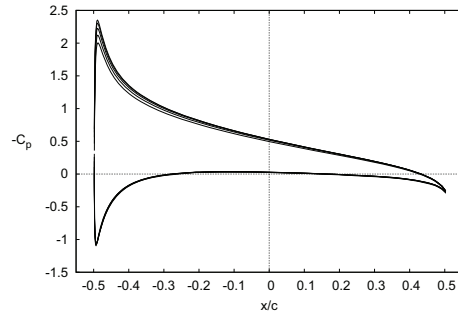
(a) Free surface, from 0 to 4 chord lengths



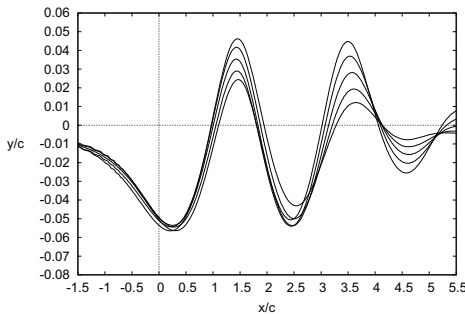
(b) Pressure coefficient, from 0 to 4 chord lengths



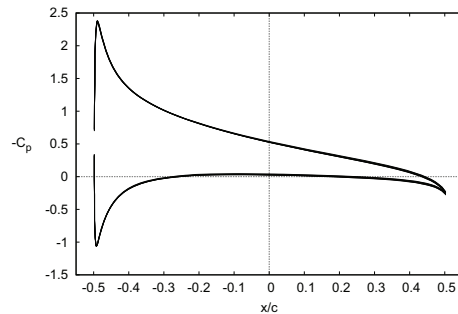
(c) Free surface, from 4 to 8 chord lengths



(d) Pressure coefficient, from 4 to 8 chord lengths



(e) Free surface, from 8 to 12 chord lengths



(f) Pressure coefficient, from 8 to 12 chord lengths

Figure 3.8: Free-surface (left) and pressure coefficient (right) after traveling 12 chord lengths (Curves are plotted with an interval of 0.8 chord lengths). [ $h/c = 1.286$ , *2fine* mesh, OpenFOAM laminar flow with free-slip walls]

The delay in building-up the steady-state lift of an airfoil accelerating instantaneously from rest to a constant velocity  $U$  is referred to as the Wagner effect (Wagner, 1925). This effect can be described by a function, plotted in Figure 3.9 together with the present results. It is observed that for the infinite fluid case only half of the steady-state lift is assumed at once, and 90% is developed after traveling about 8 chord lengths. The same trend is found for the present submerged case, but the curve presents a uniform offset towards higher lift values, such that lift is higher from the very first time instants. The simulation of the flow field following an impulsive start is a difficult task and requires very small simulation time steps. In light of this consideration, the difference between the two curves could be caused by a poor time resolution of the impulsive start, although the presence of the free surface might also have an influence on the proposed solution.

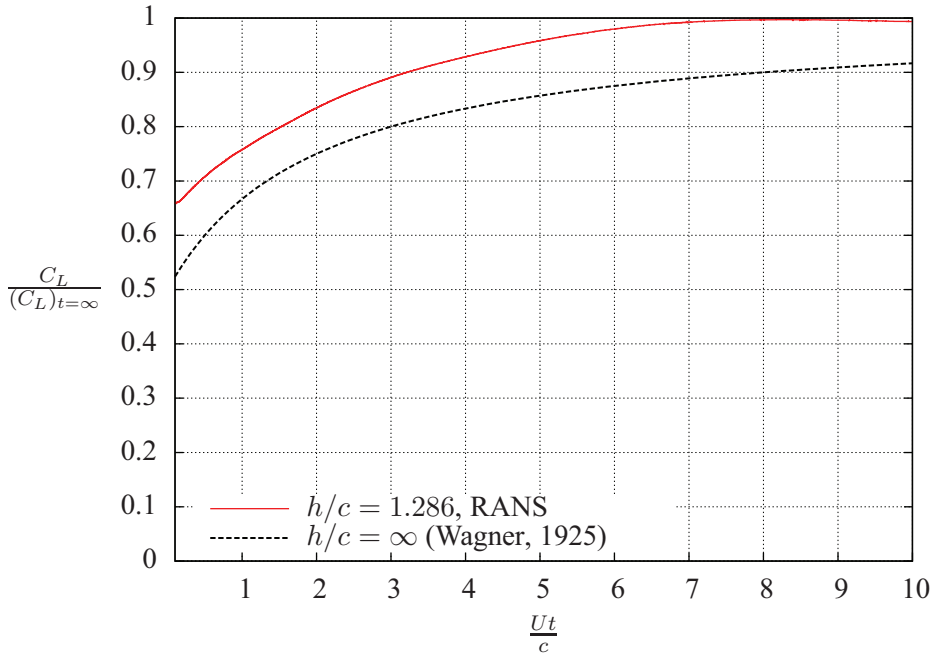
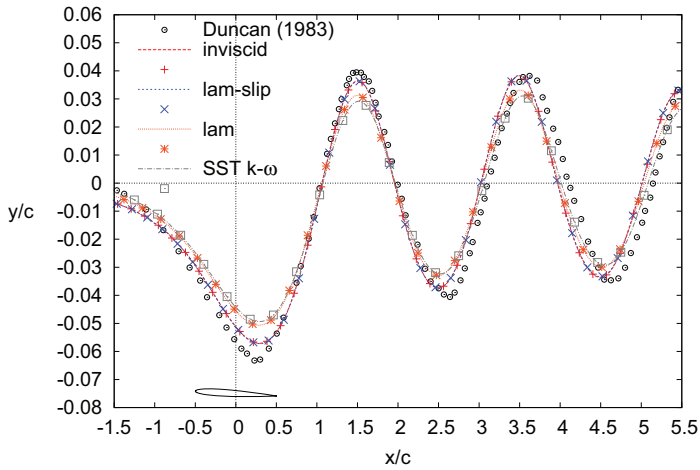


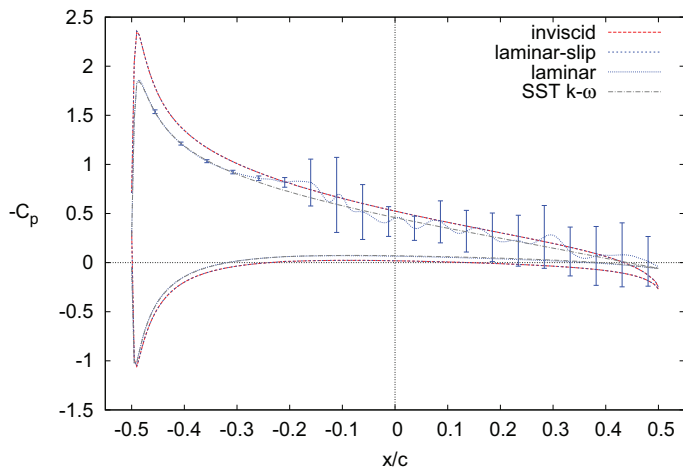
Figure 3.9: Lift ratio for an impulsive flow start.

Refinement of the mesh did not produce significant changes of the free-surface. A comparison of the free-surface deformation obtained with different flows and near-wall treatments is performed in Figure 3.10a. All simulations are in good agreement with the experimental data, but the wave amplitude is underestimated. This under-prediction was already found in the results obtained with `FLUENT` and discussed in that context.

The influence of different wall treatments becomes more evident looking at the pressure coefficients along the walls of the hydrofoil, plotted in Figure 3.10b. Both solutions implementing a free-slip condition on the walls (inviscid and laminar-slip) show pressure distributions higher with respect to the solutions with no-slip conditions. The under-pressure exerted from the suction side is giving the major contribution to the increase of lift with respect to the solutions obtained with no-slip conditions on the walls.



(a) Free-surface deformation.



(b) Pressure coefficient along the chord-line.

Figure 3.10: Comparison [ $h/c = 1.286$ ,  $2_{fine}$  mesh, OpenFOAM].

The solution obtained using a laminar flow presents a wide recirculation area on the aft region of the suction side. Therefore, the mean solution has been plotted together with error bars encompassing the minimum and maximum values. Enforcing a laminar flow weakens the boundary layer which is no longer able to counteract the adverse pressure gradients acting on the suction side, leading to separation.

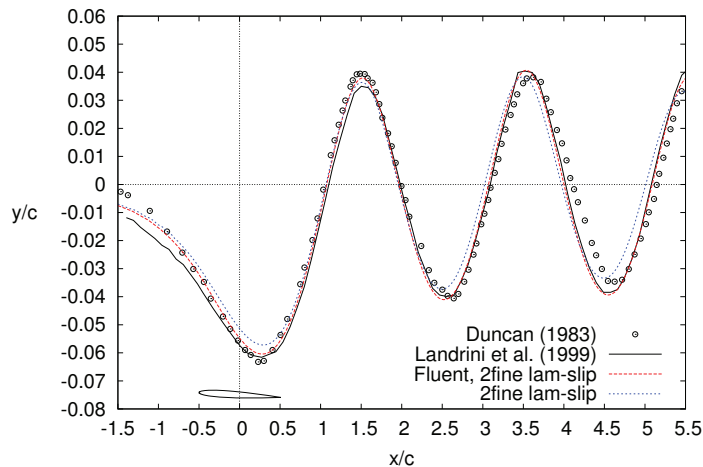
The corresponding turbulent flow obtained using a SST  $k-\omega$  model presents the same average solution but with the boundary layer fully attached. A local pres-

sure increase as found in `Fluent` (Figure 3.7) could not be observed in this case. This difference could be ascribed to a different implementation of the SST  $k-\omega$  turbulence model (Menter, 1994) within the two solvers.

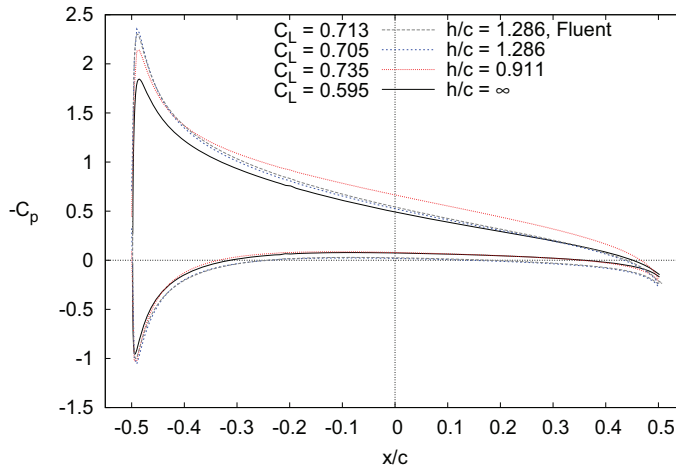
The best viscous solution (laminar flow with free-slip walls) obtained with `Openfoam` is compared in Figure 3.11 with the corresponding `Fluent` solution. The choice of testing laminar and inviscid flows is also dictated by the final goal of the present work, which is the numerical study of propeller ventilation. When ventilation occurs, viscosity plays a minor role with respect to the other quantities involved, and an inviscid solution is already capable to capture the main flow features.

The experimental results and the BEM solution are also plotted as reference values (Figure 3.11a). The solution obtained with the two RANS solvers are in satisfactory agreement with the available benchmark data, almost overlapping, but `Fluent` better approaches the first trough detected during experiments. The same results were obtained for the inviscid solution, thus the results were not plotted.

Figure 3.11b shows a comparison of the pressure coefficient obtained with `Fluent` and the infinite fluid case, also reporting the corresponding lift coefficients. Both RANS solvers predict the same distribution, showing the increase of pressure due to the presence of the free-surface, especially on the suction side, leading to higher forces exerted by the submerged hydrofoil with respect to the infinite fluid case.



(a) Free-surface deformation.



(b) Pressure coefficient along the chord line.

Figure 3.11: Comparison [2-fine mesh, laminar flow with free-slip walls]

The same figure shows the pressure coefficient for a case with shallower submergence,  $h = 0.185$  m, corresponding to a submergence ratio  $h/c = 0.911$ . The converged pressure distribution for this further case is used to confirm that the wave system generated above the hydrofoil requires higher energy in order to attain the same flow speed (Tzabiras, 1997).

The ratio between  $C_L$  and its infinite fluid value is 1.18 and 1.24, respectively for  $h/c$  equal to 1.286 and 0.911. The corresponding values obtained using Equation 3.2 are 1.04 and 1.08. Weissinger's theory shows the correct trend for the lift, which increases at low submergences, but present values are underestimated. This approximation is not valid for the surface-piercing case  $h/c \rightarrow 0$ , where  $C_L \rightarrow \infty$ , and is thus less accurate for intermediate cases.

Table 3.5 summarizes the present results obtained for the dimensionless first trough amplitude  $\eta/c$  and the lift coefficient  $C_L$ , in terms of relative error with respect to the experiments (Duncan, 1983) and the BEM solution by Landrini et al. (1999), respectively. An increasing lift coefficient corresponds to a more accurate representation of the free surface; the effect of different near wall conditions is also confirmed.

			$C_L$	$\eta/c$
SST $k-\omega$		OpenFOAM	-19.3%	-19.4%
<i>inviscid</i>			1.0%	-7.8%
<i>laminar</i>	$\left\{ \begin{array}{l} \textit{no-slip} \\ \textit{slip} \end{array} \right.$	$\left\{ \begin{array}{l} \text{OpenFOAM} \\ \text{Fluent} \end{array} \right.$	-16.4%	-17.8%
			1.0%	-7.8%
			2.1%	-1.4%

Table 3.5: Relative error of the present solution with respect to the experiments (Duncan, 1983) and the BEM solution (Landrini et al., 1999) [ $h/c = 1.286$ ,  $2_{fine}$  mesh]

The same table compares the results for the laminar flow using free-slip conditions for the two RANS solvers. While both lift coefficients approach satisfactorily the BEM solution, OpenFOAM presents a larger deviation in the first trough amplitude, as already pointed out in Figure 3.11a. This large percent deviation corresponds to only 2 grid cells, and the difference among the solvers could be ascribed to the different schemes used to interpolate the interface between air and water.

### 3.1.2.3 $h/c = 0.911$

For this shallower submergence the experiments by Duncan (1983) show a clear spilling breaking-wave condition. Here it is not attempted to capture the fine details of spilling breakers described by Duncan (2001) and investigated by some authors (Muscarì and Di Mascio, 2003; Rhee and Stern, 2002) also including an empirical breaking wave model. No breaking-wave model is adopted, while this more complex case is used to further test the adopted solver as it is.

Only Fluent was used for this submergence. The present converged unsteady simulation for the  $2_{fine}$  mesh shows small oscillations of the forces on the hydrofoil and of the free surface, more pronounced around the breaking region, with a period  $3.8T$ , where  $T$  is the period of a linear wave having the same phase speed as the breaker. A more accurate explicit simulation in time was performed in Fluent obtaining the same oscillating behavior, whose maximum double amplitude could be quantified to 9% for the lift coefficient and 18% for the first trough amplitude, with respect to their corresponding mean values.

No oscillatory behavior is mentioned by Duncan (1983) in the case object of this study. However, Duncan (1981) observed small oscillations in the length of the breaking region while testing the same configuration, but with a free-stream velocity slightly different,  $U = 0.82$  m/s. The experiments showed an oscillation period of  $3.9T$  and Duncan (1981) argued that the oscillations are due to wave

components generated when the foil is started from rest. Qualitative observations showed that the amplitude of the oscillation decreased as the wave progressed. The small amplitude of the oscillation recorded numerically in the present study is deemed as not affecting the speculation on the near wall treatment, but the performed analysis is not sufficient to state whether the oscillation detected by the code is physical or numerical, despite the consistency with observations by Duncan (1981).

Two extremes of these oscillations are shown in Figure 3.12, as representative of the minimum and maximum wave height detected. The present solution is compared with the experiments by Duncan (1983) and the RANS simulations by Muscari and Di Mascio (2003) and by Rhee and Stern (2002), the last two taken without the inclusion of a breaking wave modeling.

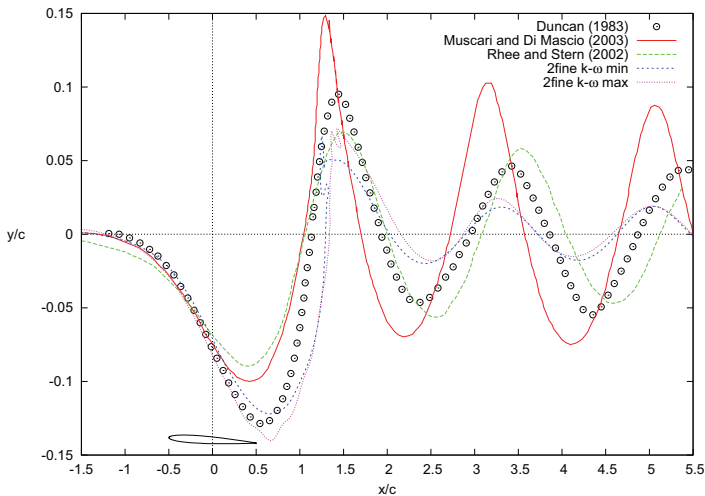


Figure 3.12: Free-surface deformation [ $h/c = 0.911$ , Fluent SST  $k-\omega$ ]

The present results compute a wavy pattern on the first crest, where wave breaking is observed during experiments.

All numerical results show a large deviation from the experimental data with respect to the non-breaking wave case, both in terms of wave amplitude and phase. The present study captures more accurately the first trough amplitude above the hydrofoil, embracing the corresponding experimental value between its two extremes. Despite this apparent improvement, the following wave-train is under-predicted, and a thorough sensitivity analysis would be required to assess the influence of the main numerical parameters.

### 3.1.3 Summary

The results obtained with the two RANS solvers shows a satisfactory agreement with the experimental results (Duncan, 1983) and the potential flow solution (Landrini et al., 1999), both in terms of free surface deformation and lift coefficient, for the non-breaking wave case ( $h/c = 1.286$ ).

A sensitivity analysis shows that for such a problem, where viscosity is not dominant, the diffusion introduced by the solver affects significantly the accuracy of the results and care must be taken in treating the near wall region for a correct solution. The forces exerted by the foil are the key mechanism driving the deformation of the free-surface. The detection of the correct wave amplitudes is improved introducing a free-slip condition on the walls.

The two RANS solvers show an overall good agreement. The same pressure distribution is predicted along the hydrofoil, and the differences found in the free-surface deformation could be ascribed to the different schemes the solvers use in order to interpolate the interface between air and water.

A more complex case corresponding to a breaking-wave condition was used to further test the adopted solver, as it is, without implementing a breaking-wave model. While the first trough amplitude is well captured for this shallower submergence, the breaking wave and the following wave-train are under-predicted. This study confirms the results obtained for the non-breaking case in terms of first trough amplitude, whereas a correct evaluation of the following waves would require an accurate modeling of the breaker.

## 3.2 Propeller in open water

A sensitivity analysis was performed on a propeller in open water conditions, and its results validated against the available experiments, for a wide range of operating advance ratios.

### 3.2.1 Propeller model

The propeller geometry used in open water is later used for ventilation simulations. This model has been extensively used for various kinds of ventilation tests, with and without the presence of a duct. The model has thus a generic design, representing a typical propeller which can be used in different regimes. The propeller tested in open water is mounted on a shaft extending downstream, while a rounded nose is placed upstream. Numerical simulations are performed on the propeller alone, while the hub is extended both upstream and downstream until the domain's boundaries. The thruster is right-handed, with a diameter  $D$  of 0.25 m and a hub diameter  $D_{hub}$  of 0.06 m. Global design pitch ratio  $P/D$  is 1.1 and

blade area ratio  $EAR$  0.595. A propeller drawing is presented in Figure 3.13 and the section characteristics in Table 3.6, where  $c/D$ ,  $t/D$ ,  $s/D$ ,  $P/D$  and  $f/D$  are, respectively, the chord, maximum thickness, skew, pitch and maximum camber for each section, made dimensionless with the propeller diameter. The rake is zero for all the sections.

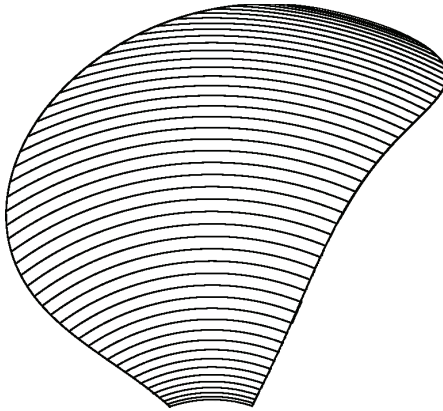


Figure 3.13: Propeller drawing.

$r/R$	$c/D$	$t/D$	$s/D$	$P/D$	$f/D$
0.24	0.13	0.038	0.000	1.08	0.001
0.26	0.15	0.037	0.003	1.08	0.004
0.30	0.18	0.035	0.011	1.08	0.007
0.37	0.23	0.031	0.023	1.09	0.009
0.46	0.29	0.026	0.037	1.09	0.012
0.57	0.34	0.022	0.045	1.10	0.013
0.67	0.38	0.017	0.040	1.10	0.014
0.78	0.40	0.013	0.014	1.09	0.012
0.87	0.38	0.010	-0.030	1.06	0.010
0.94	0.32	0.008	-0.082	1.00	0.006
0.98	0.21	0.006	-0.125	0.95	0.003
1.00	0.03	0.006	-0.141	0.94	0.000

Table 3.6: Section characteristics.

### 3.2.2 Numerical method

The commercial RANS code `FLUENT` has been used to solve the viscous, incompressible flow.

The momentum equation is solved with a second order upwind scheme. The Body Force Weighted discretization algorithm is used to interpolate the node values of the pressure from the cell values, as required by the solver. The pressure-velocity coupling is achieved using a SIMPLE algorithm. The SST  $k - \omega$  model (Menter, 1994) is used for the turbulence closure.

A constant free-stream velocity is assigned at the inlet, and a constant dynamic pressure at the outlet. A zero flux of all quantities is enforced across the remaining boundaries. A no-slip condition is set on the propeller surfaces.

The grid is fully unstructured in the rotating domain, with a superimposed prismatic layer close to the walls, in order to better capture the boundary layer (Rhee and Joshi, 2006). Prisms are extruded upstream and downstream the rotating domain. An ensemble view of the numerical domain is shown in Figure 3.14a. A close up of the mesh topology on the blade is given in Figure 3.14b.

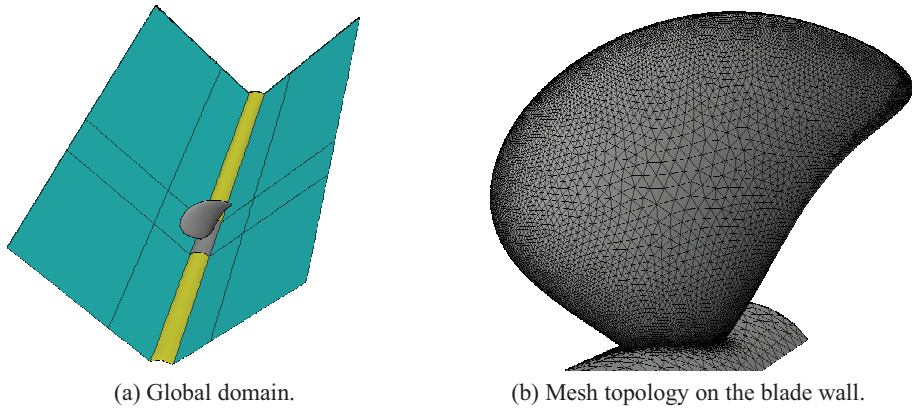


Figure 3.14: Numerical domain.

**Propeller rotation** The propeller geometry is embedded in a cylindrical domain, as shown in Figure 3.15.

The rotation of this domain was achieved both with a Multiple Reference Frame (MRF) model and using Sliding Mesh (SM). In the MRF model the propeller is fixed, while its rotation is taken into account using a local reference frame rotating at the desired propeller rate. The corresponding equations of motion are modified to incorporate the additional acceleration terms arising from the use of a rotating reference frame. This approach is most suitable when the interaction between stationary and moving parts are quasi-steady.

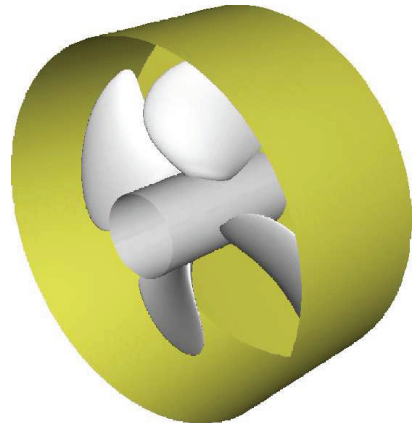


Figure 3.15: Rotating domain

When the unsteadiness of the aforementioned interaction becomes important, a Sliding Mesh model has to be adopted, accounting for the relative motion of stationary and rotating components. The increased accuracy is achieved at the expense of a higher computational time.

The flow around the propeller shows a periodicity of  $2\pi/N$  rad where  $N$  is the number of blades. Using this finding, one can solve the flow only around one blade, or within the passage between two blades. The first approach was chosen, introducing two periodic boundaries (boundary planes in Figure 3.14a) in the do-

main, such that the flow through one periodic boundary is computed using the flow conditions at the fluid cell adjacent to the opposite periodic boundary.

### 3.2.3 Results

Figure 3.16 shows the results in terms of non-dimensional characteristics  $K_T$ ,  $K_Q$  and  $\eta$ , defined in Chapter 2, and rewritten here for sake of clarity.

$$K_T = \frac{T}{\rho n^2 D^4}, \quad K_Q = \frac{T}{\rho n^2 D^5}, \quad \eta = \frac{J K_T}{2\pi K_Q}$$

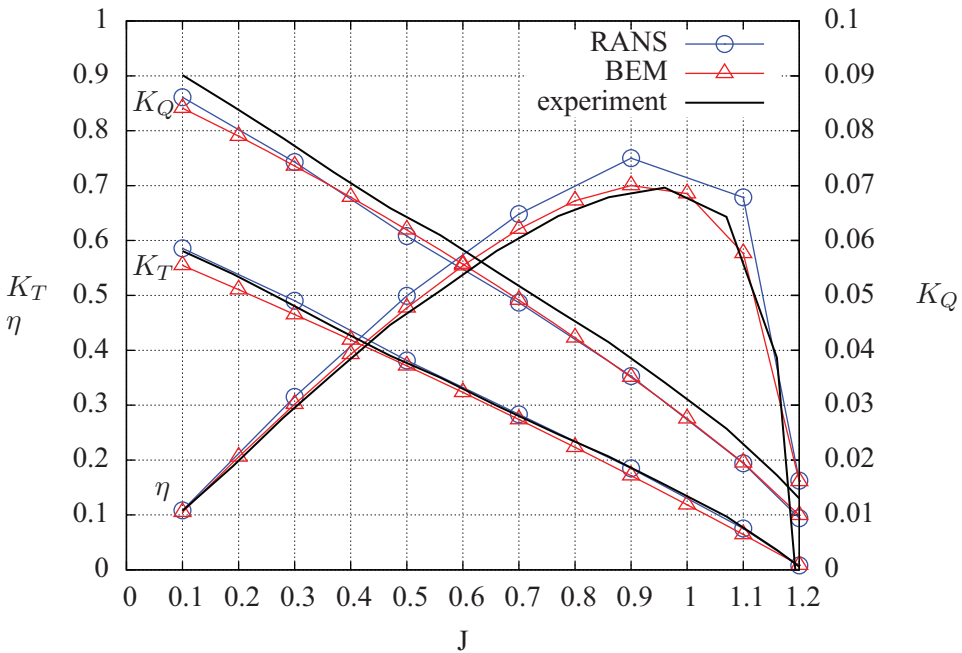


Figure 3.16: Dimensionless thrust, torque and efficiency in open water: comparison between experiments (—), RANS (—●—) and BEM (—△—)

Present results are compared with the available experiments and Boundary Element Method (BEM) computations. Experiments were carried out in the large cavitation tunnel at the Marine Technology Center in Trondheim, Norway. The test section diameter is 1.2 m and the precision error of the test results is found to be smaller than 1% using a 95% confidence interval. The code AK-Propulsor Analysis (AKPA) was used for BEM computations. AKPA is a *velocity based source BEM with modified trailing edge* (Achkinadze and Krasilnikov, 2001) in use at the

Norwegian Marine Technology Research Institute (MARINTEK) for the analysis of marine propulsors.

The corresponding numerical values are reported in Tables 3.7a and 3.7b for the thrust and torque coefficients, respectively, both including the relative error with respect to the experiments.

$J$	exp	RANS	$\Delta\%$	BEM	$\Delta\%$
0.1	0.592	0.586	1.0%	0.555	6.2%
0.3	0.494	0.490	0.7%	0.465	5.8%
0.5	0.394	0.382	3.2%	0.372	5.7%
0.7	0.293	0.283	3.3%	0.274	6.5%
0.9	0.193	0.185	4.2%	0.172	11.0%
1.1	0.081	0.075	7.3%	0.064	20.8%
1.2	0.014	0.008	44.2%	0.008	41.7%

(a) Thrust coefficient.

exp	RANS	$\Delta\%$	BEM	$\Delta\%$
0.089	0.086	2.7%	0.084	4.9%
0.077	0.074	3.2%	0.074	4.2%
0.065	0.061	6.3%	0.062	4.5%
0.052	0.049	6.6%	0.049	5.7%
0.039	0.035	8.9%	0.035	9.4%
0.023	0.019	15.8%	0.020	15.3%
0.014	0.009	31.1%	0.010	27.2%

(b) Torque coefficient.

Table 3.7: Comparison of RANS and BEM results with experiments, including the relative error.

The thrust coefficient computed with RANS is in satisfactory agreement with the available experiments for the whole range of advance ratios. The large relative error obtained for  $J = 1.2$  is due to the fact that nominal values are very small, and division by 0 amplifies the error difference. For high propeller loadings, i.e. for low advance ratios, the deviation is within the precision limit, about 1% for  $J = 0.1$ , the case which has been further investigated including the free surface in Chapter 5.

### 3.2.3.1 Under-estimation of the torque

The torque coefficient shows a systematic under-estimation of the experimental data, which is also seen in the BEM. An error in the torque coefficient has been widely documented in other RANS simulations (Bulten and Oprea, 2005; Rhee and Joshi, 2006; Berchiche and Janson, 2008), where an over-prediction was encountered instead.

The prediction of thrust and torque is related to lift and drag predictions of a 2D profile. Using standard two-equation turbulence models, such as  $k-\epsilon$  and  $k-\omega$ , lift is well predicted, whereas the drag shows a sensible deviation. Bulten and Oprea (2005) attribute this trend to an error in the evaluation of the stagnation point pressure, while for Rhee and Joshi (2006) this can be associated to the lack of a proper laminar-to-turbulent transition model. The correct location of the turbulent transition point along the chord-line can not be predicted by fully turbulent models,

and this uncertainty leads to an error when evaluating the drag for a 2D profile and therefore the torque for a propeller.

Experimental measurements on a flat plate of length  $\ell$  show that the drag coefficient  $C_F$  due to skin friction coefficient  $C_f$  may vary significantly between laminar and turbulent flow (Figure 3.17). The skin friction coefficient is defined as the ratio between the wall shear  $\tau_w$  and the dynamic pressure  $p_{dyn} = 0.5\rho U^2$ , while  $C_F$  is given by the integral of  $C_f$  along the length of the plate.

$$C_f = \frac{\tau_w}{\frac{1}{2}\rho U^2} \quad (3.3a)$$

$$C_F = \frac{1}{\ell} \int_0^\ell C_f dx \quad (3.3b)$$

Its evaluation is especially difficult in the transition region, where the solution lies between the laminar and turbulent curves and the exact location depends on many parameters, such as free-stream turbulence and roughness.

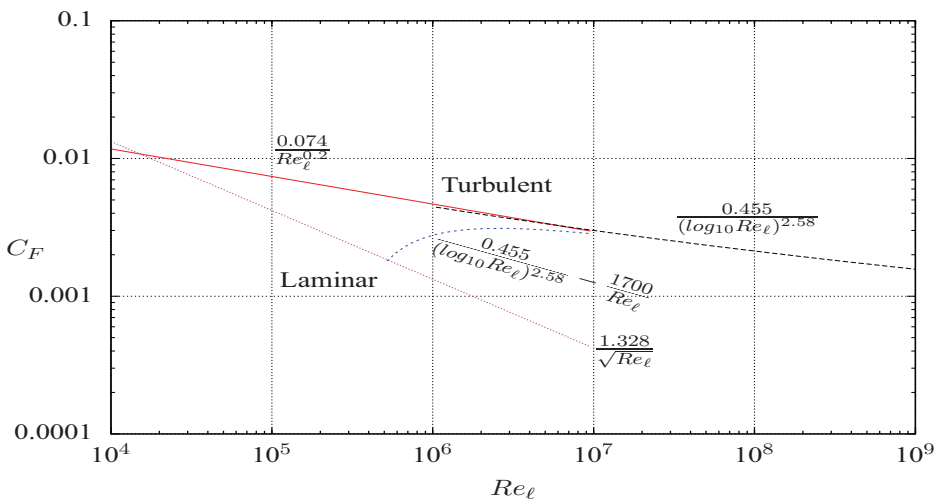


Figure 3.17: Drag coefficient due to skin friction for a flat plate as function of the Reynolds number  $Re_\ell$  based on the plate length  $\ell$ .

The Reynolds number computed at 70% of the radius  $Re_{0.7}$  is  $1.2 \times 10^5$ . According to Figure 3.17 the corresponding skin friction coefficient may vary significantly, depending on whether the flow is (i) laminar, (ii) turbulent or (iii) transition occurs along the chord-line, being the latter case the most common. From his investigation, Brandt (1973) found that laminar boundary layer separation ceases to occur for  $Re_{0.7} > 5 \times 10^5$ . Above this number the effect of  $Re$  on the propeller

characteristics is not so strong, regardless of flow regime and propeller immersion. The fact that the  $Re_{0.7}$  obtained for the present propeller is lower than the critical one found by Brandt (1973) will not ensure independence of the results from the  $Re$  and adds an uncertainty on separation and turbulence transition. The underestimation of the torque coefficient could then be explained by the fact that the solver, even for a turbulent incoming flow, considers the flow on the walls as laminar below a certain  $Re$ , having a lower skin friction coefficient and thus leading to a lower profile-drag and lower propeller-torque. No evidence for this theory is given in the user guide (Fluent, 2006) and the impossibility to access the source code makes its demonstration a hard task.

### 3.2.3.2 Sensitivity analysis

In order to assess the influence of the used numerical parameters on the obtained solution, a sensitivity analysis was performed changing the grid refinement and the turbulence model.

Three levels of grid refinement in the external domain—obtained from the total domain subtracting the prismatic boundary layer—and one level in the boundary layer were applied without producing significant changes in the global forces and moments. The pressure contours for the three levels of refinement obtained for  $J = 0.1$  are plotted in Figures 3.18 and 3.19 for the suction and pressure side, respectively. A sharper capture of the pressure difference can be observed decreasing the mesh size. This sharper contours are particularly visible on the leading edge and on the suction side, where a finer grid better captures the strong gradients existing at the leading edge and in tip-vortex region.

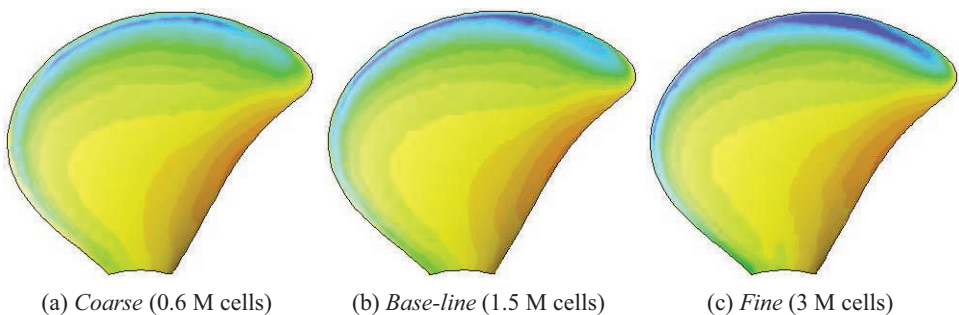


Figure 3.18: Pressure contours on the suction side for three levels of refinement [ $J = 0.1$ ].

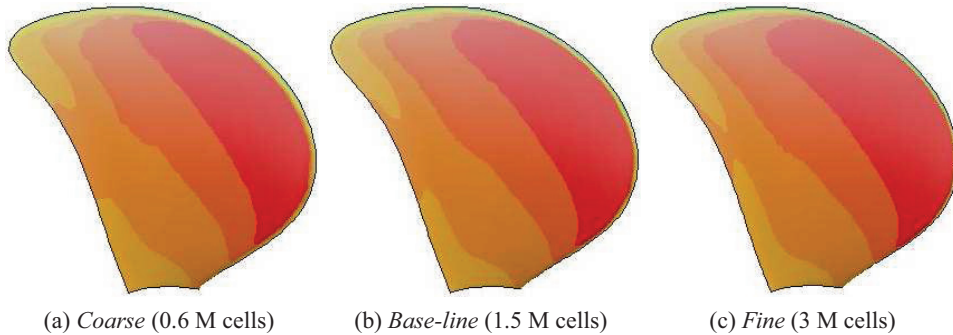


Figure 3.19: Pressure contours on the pressure side for three levels of refinement [ $J = 0.1$ ].

As explained in the previous section, turbulence plays an important role in computing the drag of a lifting surface and might therefore be the key mechanism explaining the differences in the torque coefficient with respect to the experiments. In addition to the SST  $k - \omega$ , the standard  $k - \omega$  and the  $k - \epsilon$  (standard and realizable) turbulence models were also tested without finding significant differences with respect to the presented results.

The turbulence intensity at the inlet is set to 1%, value which is rather low, but reproduces the undisturbed flow conditions of the cavitation tunnel. Simulations were also performed increasing the turbulence intensity up to 10% and removing turbulence (viscosity is only accounted for with its laminar component), obtaining, also in these cases, no significant changes.

Periodic boundaries are generally a good assumption when the flow is rather steady and uniform, and recirculating regions are mainly directed as the propeller rotation. For unsteady, strongly recirculating flow, the existence of a periodic flow can no longer be justified. Unsteadiness and non uniformity occur especially in off-design conditions for a propeller at low advance ratios, close to bollard-pull conditions—where the blade is at high angles of attack with respect to the resulting incoming velocity.

A numerical domain encompassing all the 4 blades was generated and tested with a Multiple Reference Frame (MRF) model at the lowest advance ratio  $J = 0.1$ , condition which will be used for the following simulations with ventilation, described in Chapter 5. For this entire domain, a simulation using Sliding Mesh (SM) was also performed. The results obtained with the MRF model on the entire domain do not differ significantly from the corresponding domain around a single blade. The SM model seems to better capture the inherent unsteadiness of the flow, improving slightly the global characteristics, reported in Table 3.8.

<b>rotation</b>	$K_T$	$\Delta\%$	$K_Q$	$\Delta\%$
<i>MRF</i>	0.586	1.0%	0.086	2.7%
<i>SM</i>	0.595	0.6%	0.088	1.0%

Table 3.8: Comparison between the MRF and SM model, including the relative error with respect to the experiments [ $J = 0.1$ ].

### 3.2.3.3 OpenFOAM

The same grid generated for a single blade with periodic boundary conditions was used for a simulation using OpenFOAM. The Navier-Stokes equations are solved using the following schemes, all based on the  $2^{nd}$  order Gaussian integration, summarized in Table 3.9:

	<b>Term</b>	<b>Discretization</b>
<i>Gradient</i>	$\nabla$	linear
<i>Convection</i>	$\nabla \cdot (\phi U)$	limited linearV 1
	$\nabla \cdot (\phi k)$	limited linear 1
	$\nabla \cdot (\phi \omega)$	limited linear 1
<i>Laplacian</i>	$\nabla^2$	linear corrected

Table 3.9: Numerical schemes used in OpenFOAM.

The results obtained in terms of propeller characteristics are shown in Figure 3.20, and compared with the corresponding experiments and Fluent simulations. A stable solution for the lowest advance ratio could not be achieved in OpenFOAM with the adopted scheme.

The differences between the two solvers in terms of the thrust coefficient are barely visible, whereas the torque coefficient changes significantly, presenting with OpenFOAM an over-estimation of the experimental data, instead of the under-estimation found in Fluent. As explained earlier, an over-estimation of the torque can arise when the laminar-to-turbulent flow transition is not taken into account, and the body wall is considered as completely turbulent. Since the turbulent skin friction coefficient is larger than the corresponding laminar coefficient at the same  $Re$ , the resistance due to skin friction obtained with this assumption will be larger than in reality.

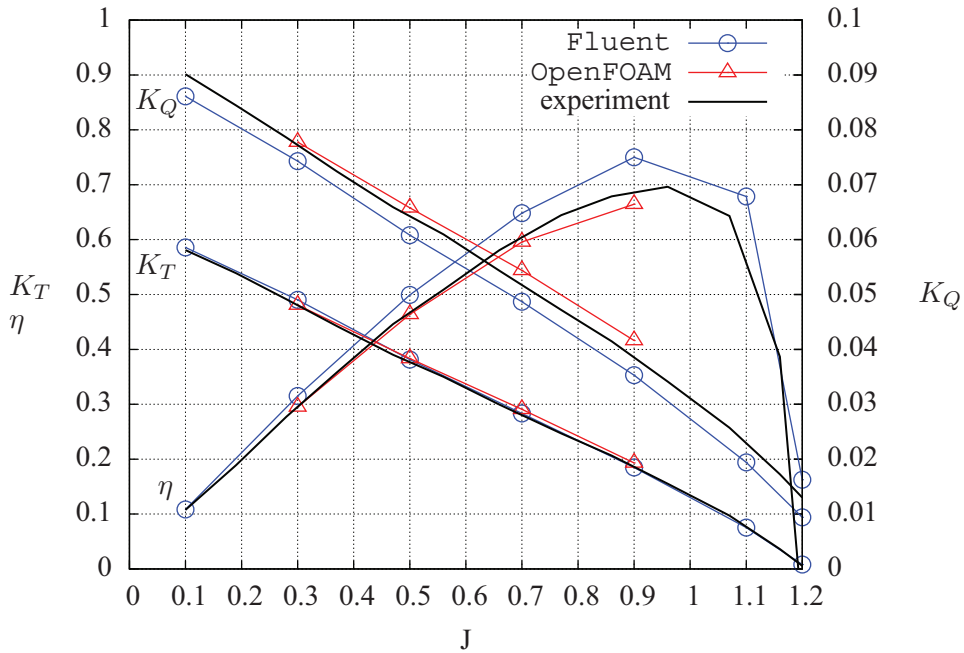


Figure 3.20: Dimensionless thrust, torque and efficiency in open water: comparison between Fluent ( $-o-$ ), OpenFOAM ( $-\triangle-$ ) and experiments ( $-$ ).

Table 3.10 shows the pressure and viscous components of the torque coefficient obtained with Fluent and OpenFOAM. The component due to skin friction is fairly constant for different advance ratios, but is very different between the two solvers. The under- and over- estimation of the torque due to skin friction can explain the total error with respect to the experiments of the tested solvers.

$J$	pressure	viscous	$\frac{\text{viscous}}{\text{total}}\%$	pressure	viscous	$\frac{\text{viscous}}{\text{total}}\%$
0.3	0.0735	0.0008	1.03%	0.0739	0.0039	5.06%
0.5	0.0600	0.0009	1.41%	0.0618	0.0040	6.08%
0.7	0.0478	0.0009	1.93%	0.0503	0.0040	7.39%
0.9	0.0343	0.0009	2.58%	0.0371	0.0045	10.87%

(a) Fluent.

(b) OpenFOAM.

Table 3.10: Pressure and viscous components of the torque coefficient.

The following Figures 3.21 and 3.22 show the pressure coefficient contours

obtained close to design conditions ( $J = 0.9$ ) with the two solvers for the suction and the pressure side, respectively. Although not identical, the contours computed by the two solvers follow the same trend. The contours shown by OpenFOAM are less smoothed, but this difference is deemed to be due to the lower order of cell-to-node interpolation used by the corresponding post-processor.

The pressure coefficient at three different radial stations, 0.5, 0.7 and 0.9 of the propeller radius, is compared in Figure 3.23. The profiles obtained with the two solvers are almost overlapping, with small differences especially close to the leading edge.

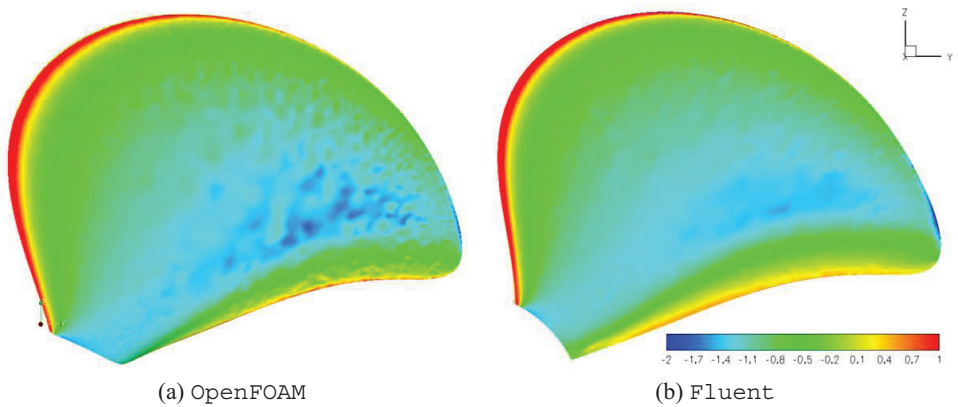


Figure 3.21: Contours of the pressure coefficient on the suction side [ $J = 0.9$ ].

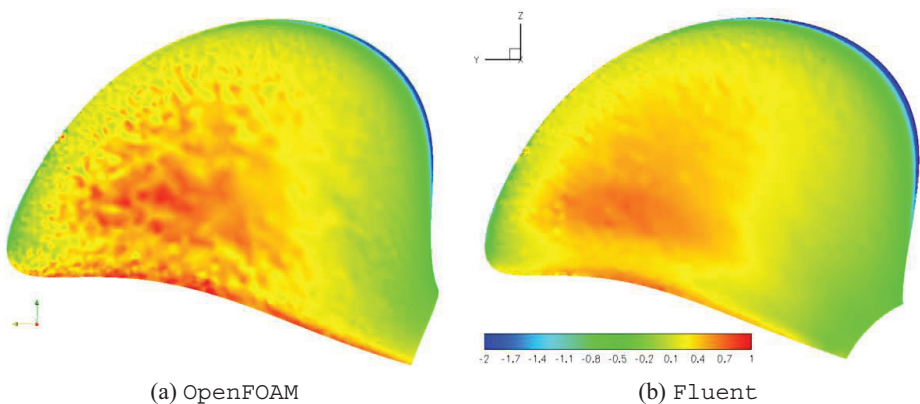


Figure 3.22: Contours of the pressure coefficient on the pressure side [ $J = 0.9$ ].

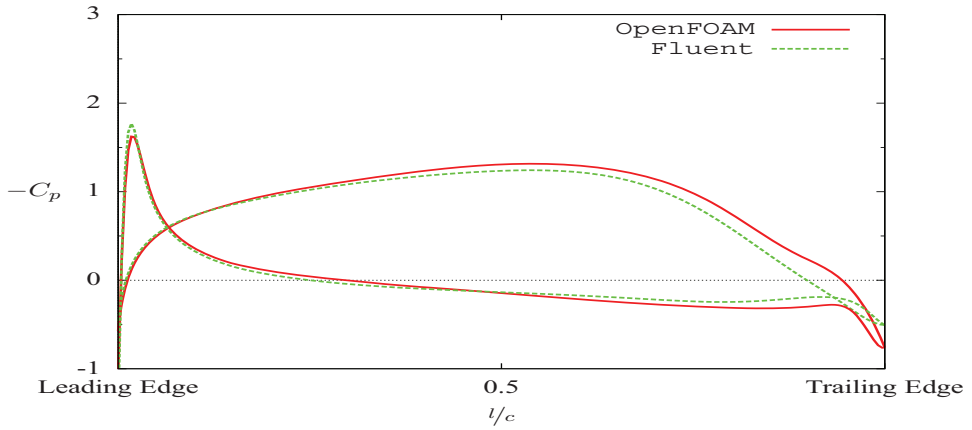
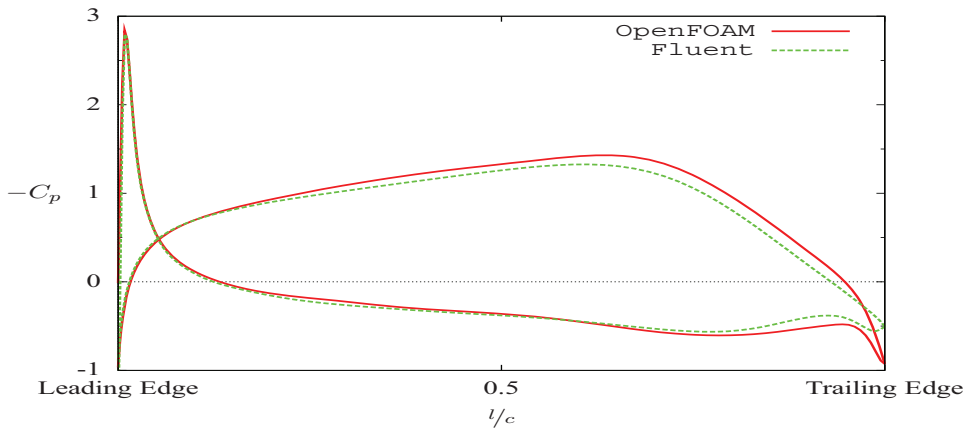
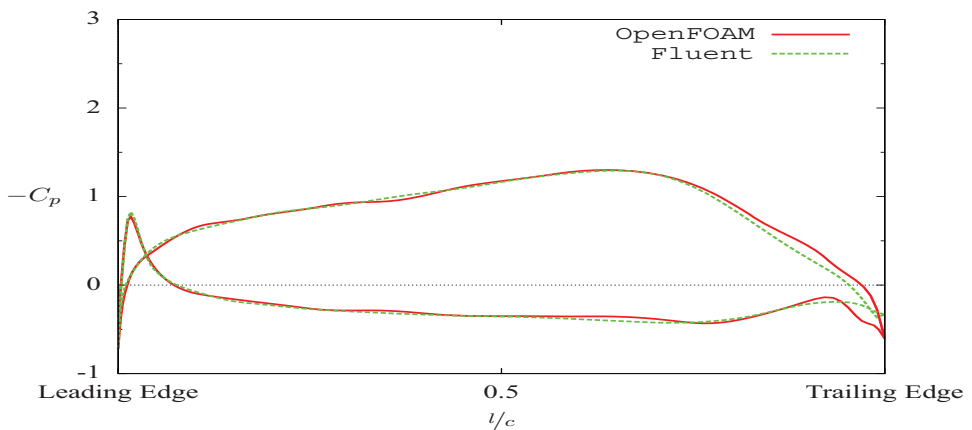
(a)  $r/R = 0.5$ (b)  $r/R = 0.7$ (c)  $r/R = 0.9$ 

Figure 3.23: Comparison of the pressure coefficients obtained with Fluent and OpenFOAM at various radial stations [ $J = 0.9$ ].

The following Figures 3.24 and 3.25 show the skin friction coefficient contours obtained at  $J = 0.9$ , close to design conditions ( $J = 0.86$ ), with the two solvers for the suction side and the pressure side, respectively. The global difference found in Table 3.10 can now be observed locally on the blade. The wall shear stress computed with OpenFOAM is much larger than the one computed with Fluent. This difference could be ascribed to a different treatment of the fluid quantities close to the wall. It should be kept in mind that the present results were obtained using Standard Wall Functions (SWF) in OpenFOAM, while Fluent is using an Enhanced Wall Treatment (EWT) approach close to the boundaries. SWF and other available wall treatments were also tested in Fluent without obtaining significant changes in results.

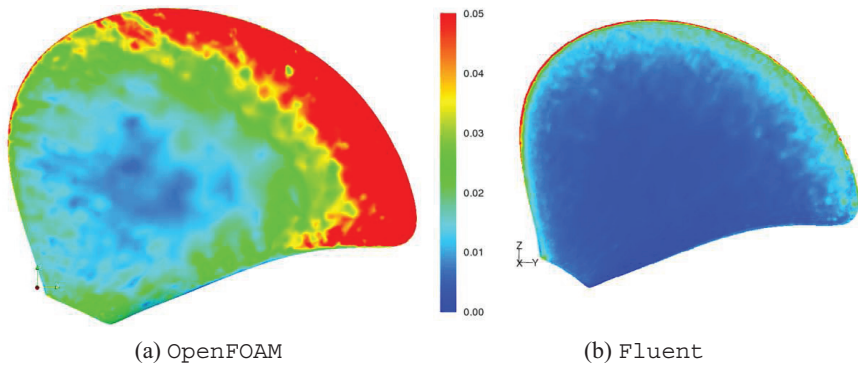


Figure 3.24: Contours of the skin friction coefficient on the suction side [ $J = 0.9$ ].

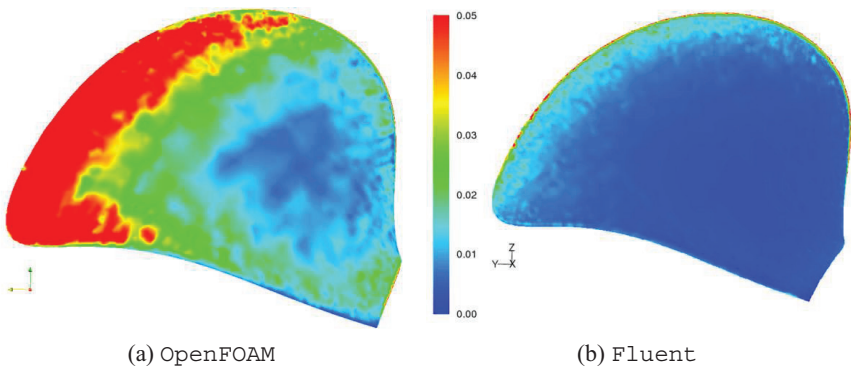


Figure 3.25: Contours of the skin friction coefficient on the pressure side [ $J = 0.9$ ].

### 3.2.4 Summary

A validation and verification analysis of the propeller in open water has been carried out using `Fluent` showing for all range of advance ratio a good agreement for the thrust coefficient, and an under-estimation of the torque coefficient.

A sensitivity analysis was performed in order to assess the influence of the used numerical parameters. A grid independent solution was obtained and the choice of the turbulence model did not show to affect the obtained results. The implementation of a Sliding Mesh (SM) model for the propeller rotation proved to be more accurate than the Multiple Reference Frame (MRF) model.

Part of the range of advance ratio was computed also with `OpenFOAM`. The two RANS solvers show an overall good agreement, but `OpenFOAM` presents instead an over-estimation of the torque coefficient.

The differences found in the torque are mainly due to different values for the wall shear stresses; `Fluent` computes too low shear stresses, while `OpenFOAM` presents an over-estimation.

# Chapter 4

## Model tests

Three different test campaigns are analyzed in the present study, referred to with the corresponding acronym.

Investigator(s)	Year	Acronym
Koushan	2005	<i>Kou05</i>
Califano & Kozłowska	2009	<i>Cal09</i>
Kozłowska	2010	<i>Koz10</i>

Table 4.1: Test campaigns.

Results from *Kou05* were published in Koushan (2006b); Kozłowska et al. (2009) and used for validation by Califano and Steen (2009). The majority of the results presented were obtained during the test campaign *Cal09*, which will generally be addressed to without the acronym. Some cases from the other two test campaigns (*Kou05* and *Koz10*) will be used for comparison or to investigate missing cases relevant to this study, and the test they belong to will always be referenced to by its corresponding acronym.

### 4.1 Test matrix

Tests *Cal09* were conducted at submergence ratios  $h/R$  ranging between 2.97 (identified as infinite fluid case) and 1 (where the blade tip is touching the free-surface).

For all the above water depths, the carriage speed  $U$  and the propeller shaft frequency  $n$  were combined in order to obtain advance ratios  $J$  around 0.1, according to the following test matrix.

		$n$ [1/s]		
		12	14	16
$U$ [m/s]	0.30	0.100	0.086	0.075
	0.35	0.117	0.100	0.088
	0.40	0.133	0.114	0.100

Table 4.2: Advance ratio  $J = U/nD$ , in terms of free-stream velocity  $U$  and propeller shaft frequency  $n$ .

Each test was performed starting the propeller rotation after reaching a constant carriage speed. The desired propeller shaft frequency was reached with a linear acceleration of  $208.7 \text{ rad/s}^2$ .

In order to observe the effect of the acceleration on the inception of ventilation, the default value was reduced by a factor of 2, 4 and 8, only for the submergence ratio of 1.4.

Further details about the test conditions are given in Appendix A, together with all the obtained results.

## 4.2 Experimental set-up

Tests were performed in the Marine Cybernetics Laboratory (MCLab) at the Norwegian University of Science and Technology (NTNU), having dimensions (length  $\times$  breadth  $\times$  depth) of  $40 \text{ m} \times 6.45 \text{ m} \times 1.5 \text{ m}$ . Figure 4.1 shows a sketch of the experimental set-up used to carry out the present experiments. A general purpose Personal Computer (PC) is controlling the acquisition system, which receives all the measured data. The propeller rotation is achieved with an electrical motor, where both the desired rotational speed and the linear ramp used to achieve it can be adjusted. During measurements, images are acquired with a high-speed camera at a sampling frequency ranging between 60 and 480 Hz, depending on the test conditions. This camera is controlled by a dedicated computer providing trigger pulses at each acquired frame. This information is then fed to the acquisition system in order to extract the time where pictures were taken. The entire test set-up is mounted on a carriage, which is translating along the channel and thus giving the velocity of advance. All measurements and images are then saved on an external storage system.

A cartesian reference system is centered in the center of the propeller, having the  $x$ -axis aligned along the propeller axis, the  $z$ -axis pointing upward towards the free-surface, and the  $y$ -axis following a right-handed system, pointing on the port side (Figure 4.2).

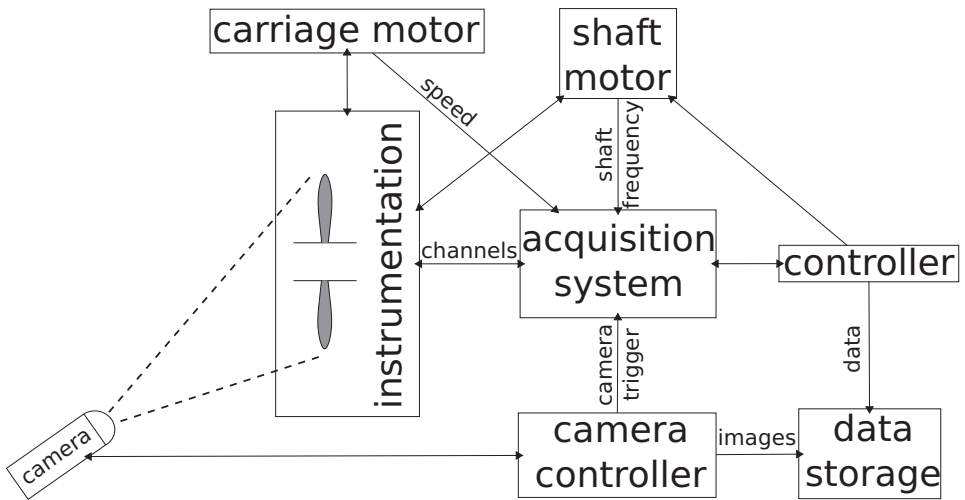


Figure 4.1: Sketch of the experimental set-up.

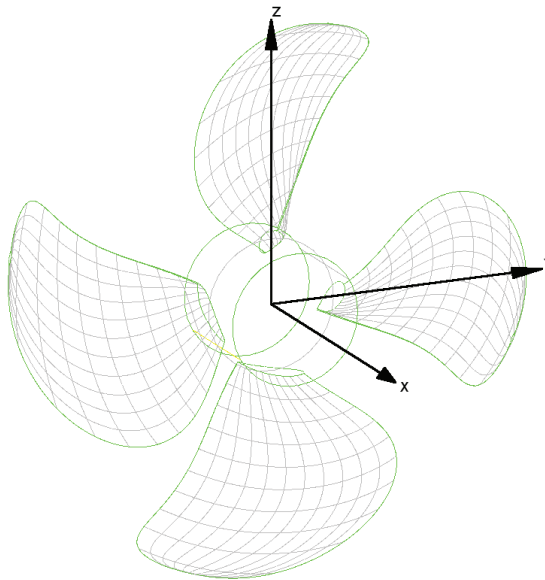


Figure 4.2: Reference system.

Figure 4.3 shows the propeller hosted by a thruster case, with a front and lateral view. The blade dynamo-meter is housed in the root of  $Blade_1$ , where the projection of its axis has been drawn on the suction side for visual inspection of the angular position.

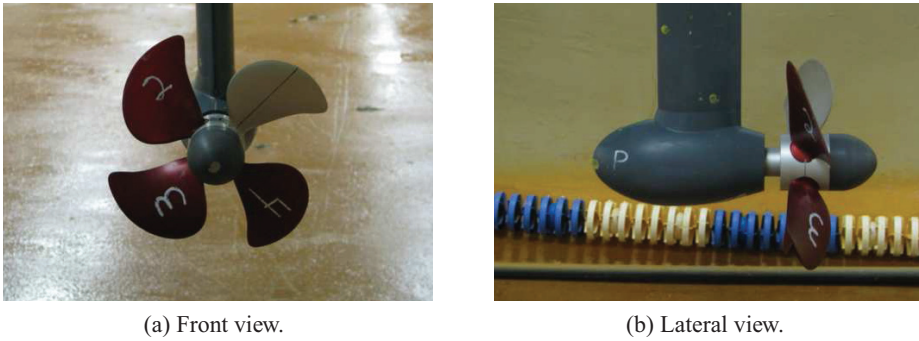


Figure 4.3: Thruster.

The necessary light for the camera acquisition is provided by two underwater lamps. Their configuration and light range is sketched in Figure 4.4. Different views of the used configuration are shown in Figure 4.5.

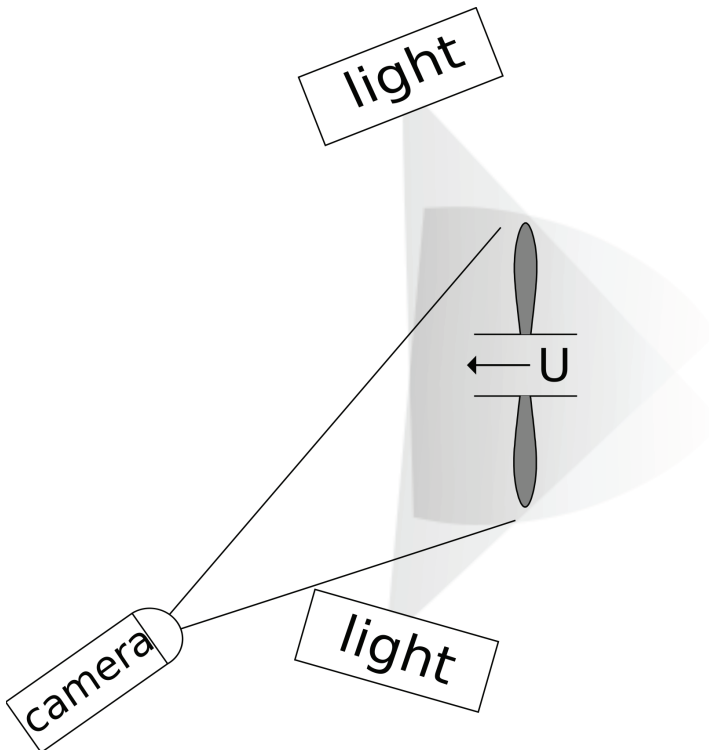


Figure 4.4: Configuration of lights and camera around the propeller.

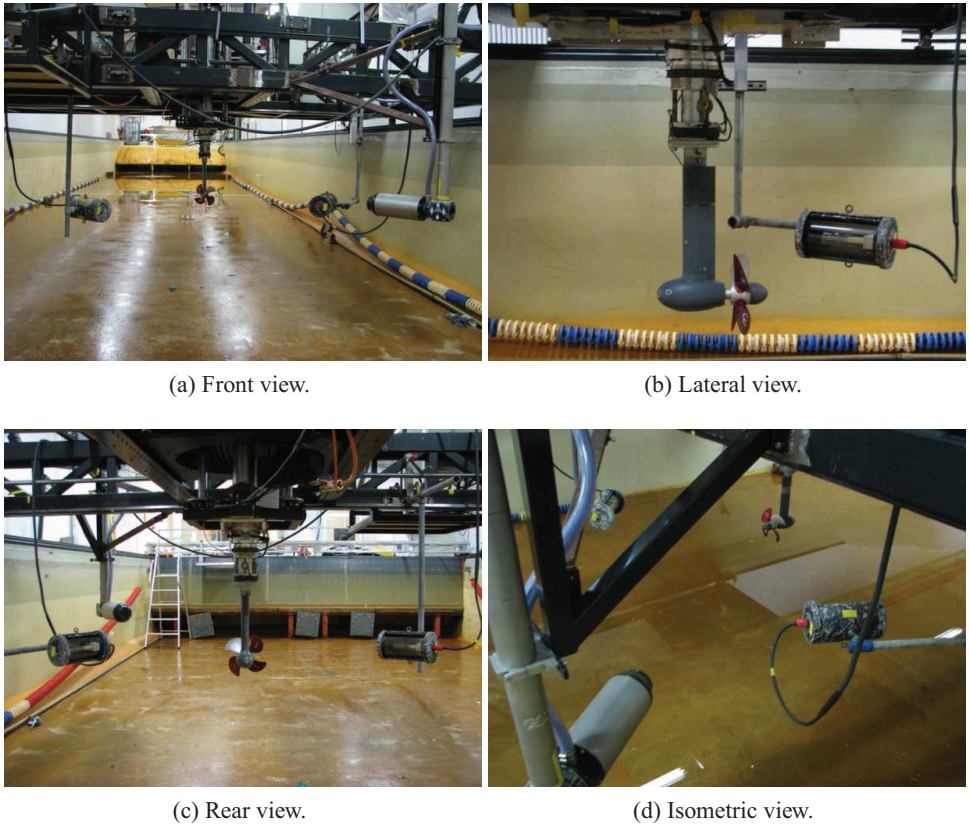


Figure 4.5: Lights and cameras.

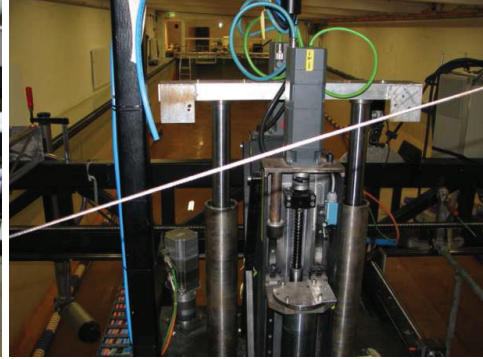
The test set-up is equipped with the following instruments:

- a 5-components blade dynamo-meter ( $x$  and  $y$  forces,  $x$ ,  $y$  and spindle moments);
- a 6-component dynamo-meter for the whole thruster ( $x$ ,  $y$  and  $z$  forces and moments);
- a device measuring the blade angular position;

All this information is given to the acquisition system, together with the carriage and shaft speed. Pictures of the used instrumentation are shown in Figure 4.6.



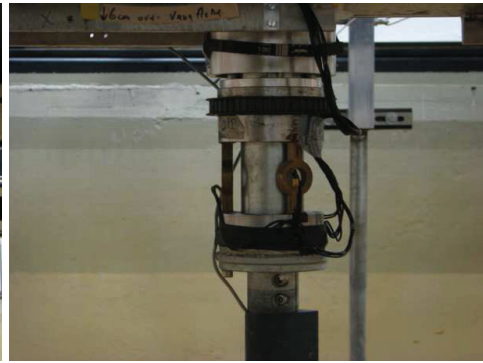
(a) Lateral view.



(b) Top view.



(c) Front view.



(d) View of of the six-component dynamometer for the whole thruster.



(e) Thruster assembly prior to mounting on the carriage.

Figure 4.6: Instrumentation.

The PC controller is provided with the Data Acquisition (DAQ) software catman<sup>®</sup>, using the DAQ system MGCplus, from Hottinger Baldwin Messtechnik (HBM). The signals were acquired at a sampling frequency of 1200 Hz using a 100 Hz 4<sup>th</sup> order Butterworth filter.

### 4.2.1 Test procedure

Tests were performed following a prescribed procedure aiming at reducing the influence of the human factor in the obtained results:

1. start of data acquisition;
2. start of the carriage;
3. start of the propeller motor after steady-state carriage velocity was reached;
4. start of image acquisition after steady-state shaft frequency was reached; acquisition stops after available camera memory is full;
5. end of test:
  - stop data acquisition;
  - stop propeller motor;
  - stop carriage and start moving it back to the initial position;
6. wait until water is calm (at least 5 min);
7. start a new test.

## 4.3 Data analysis

The obtained results are presented in terms of the blade thrust, scaled with respect to the corresponding deepest submergence value ( $h/R = 2.97$ ) that could be obtained in the towing tank with the given set-up. At this submergence, the presence of the free-surface will affect the loads on the blade passing in the up-right position, but its effect is much smaller than the losses due to ventilation, as it will be shown when presenting the obtained results. In the remaining of this chapter, when referring to the present experimental results, the term deep water ( $h/R = \infty$ ) will always be used instead of deepest submergence ( $h/R = 2.97$ ).

The transducers measuring the torque were found to be affected by a calibration error, that was not possible to correct in a post-processing phase. Nevertheless, the torque losses due to ventilation show the same behavior of the thrust (Faltinsen

et al., 1981; Minsaas et al., 1983; Kozłowska et al., 2009), such that the conclusions that will be drawn for the thrust apply also to the torque.

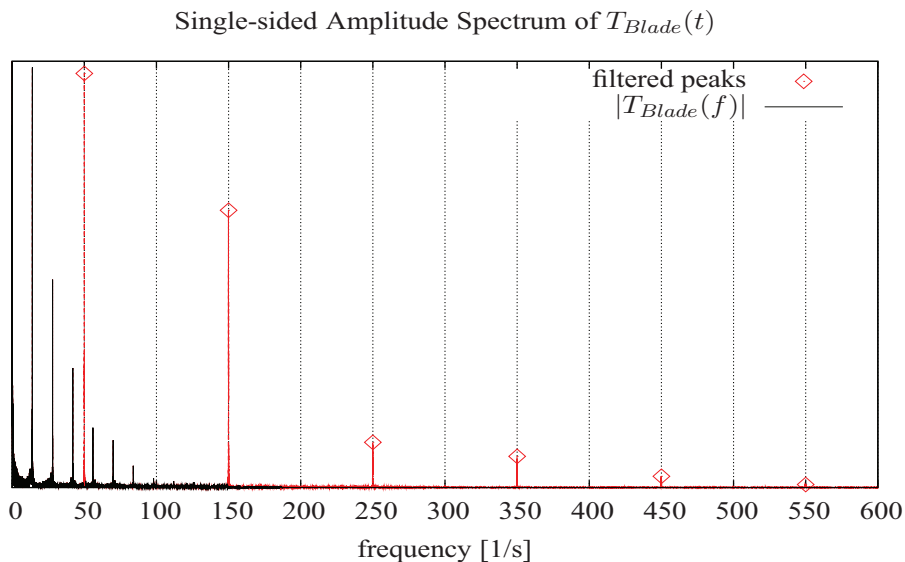
Three steps were taken to post-process the acquired data:

- data filtering;
- correction for the propeller angular position;
- computation of mean and standard deviation for each angular position.

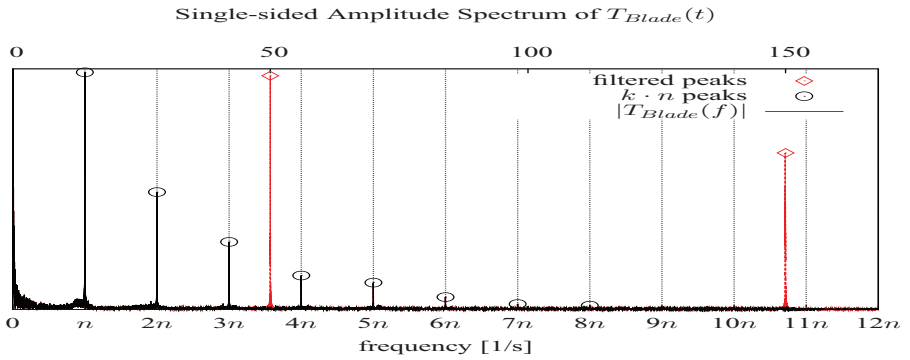
The first two steps require a further description.

### 4.3.1 Filtering

Measured data are affected by an electronic noise at frequencies of 50, 150, 250 Hz and so on, every 100 Hz. These peaks were removed during post-processing applying a low-pass filter with a cutoff frequency of 149 Hz and a notch filter between 49 and 51 Hz. The single-side amplitude spectrum of the blade thrust is plotted in Figure 4.7, where the peaks due to the propeller loads and those due to noise can be noticed. Figure 4.7b shows that the noise peak at 50 Hz lies very close to the third and fourth harmonics of the shaft frequency  $n$ , but is fortunately narrow-banded, and could thus be removed without affecting the measured data. The corresponding raw and filtered data in the time domain can be seen in Figure 4.8.

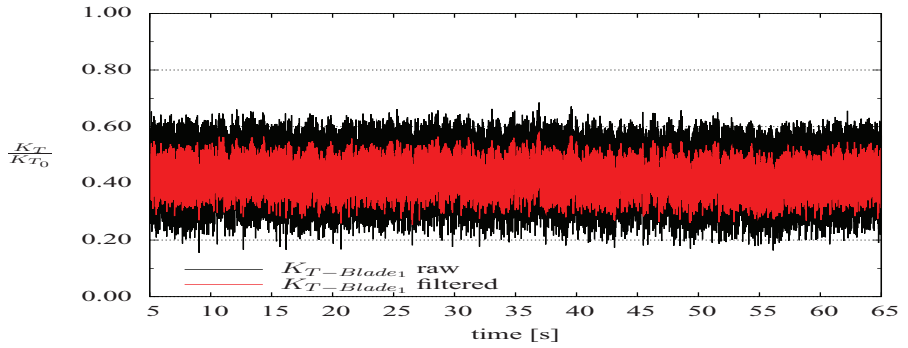


(a) Whole frequency range.

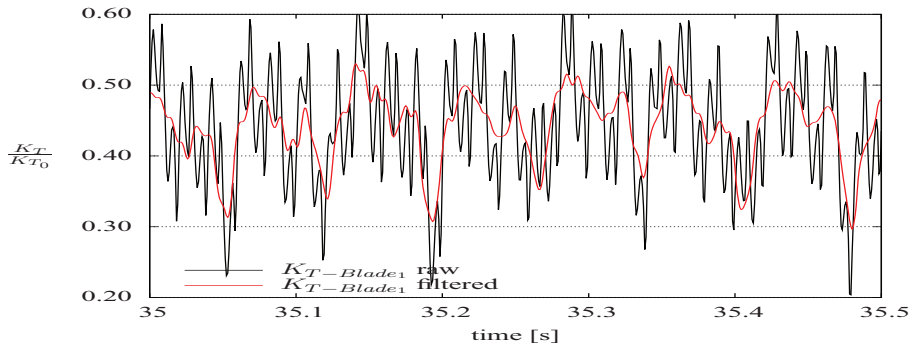


(b) Enlargement around the propeller and blade frequencies.

Figure 4.7: Single-sided amplitude spectrum of the blade thrust for the raw and filtered data, where  $n$  is the shaft frequency [ $h/R = 1.4$ ;  $J = 0.1$ ].



(a) Long time range.



(b) Short time range.

Figure 4.8: Blade thrust coefficient for the raw and filtered data [ $h/R=1.4$ ;  $J=0.1$ ].

### 4.3.2 Angle correction

The instrument measuring the angular position of the blade has shown during post-processing a drift of the null position. An estimation of this deviation was computed comparing the image recordings with the measured values, and is plotted in Figure 4.9 for each experiment performed with the label "computed drift angle". Data have an uncertainty of about  $\pm 5$  deg, obtained by the visual identification of the null position and the interpolation between two measurements. For those cases where measurements were taken when the propeller was at rest another estimation of the drift angle could be determined, which was plotted in Figure 4.9 with the label "real drift angle". Four straight lines have also been plotted in order to guide the eyes through sub-blocks of the measurements data.

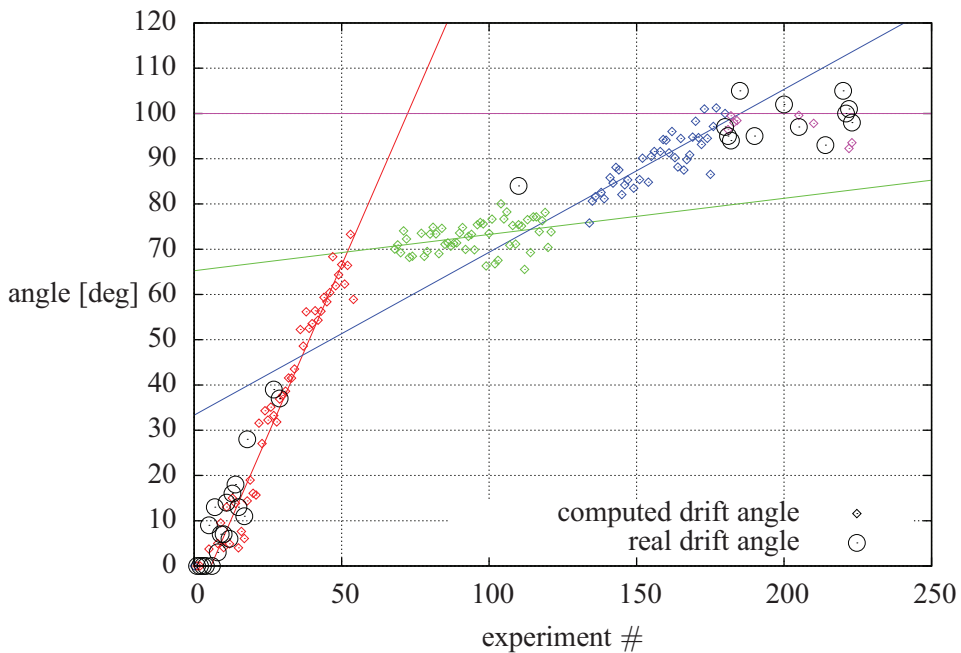


Figure 4.9: Drift angle for each experiment performed.

In the remaining of this chapter data are presented with an angle correction different from the computed drift angle. The used correction angle is the one that moves the thrust peak around  $\pi$  rad. This choice is based on the fact that around  $\pi$  rad the blade is farthest from the free-surface and is thus expected to experience the minimum thrust loss.

Experiments show that the angular position of the minimum and maximum thrust

is changing from revolution to revolution, but averaged values show a distinctive pattern. The choice of correcting the angle is only taken with the purpose of making different experiments more comparable, and better focus on those differences relevant to ventilation.

The values used to correct the angle can be found among the test specifications in Appendix A.

## 4.4 Main results

Figure 4.10 shows the thrust coefficient of the propeller in non-ventilating, deep-water conditions ( $h/R=2.97$ , deepest-water case available). Data were computed multiplying the thrust of a single blade  $K_T$  by the number of blades  $N$  and are compared with the corresponding open water tests performed in the cavitation tunnel at atmospheric pressure, displayed with a  $\pm 1\%$  error bar. The comparison is satisfactory, although present experiments show larger deviations and a different slope with respect to the open water tests. The additional presence of the thruster in the present investigation seems not to affect the results significantly.

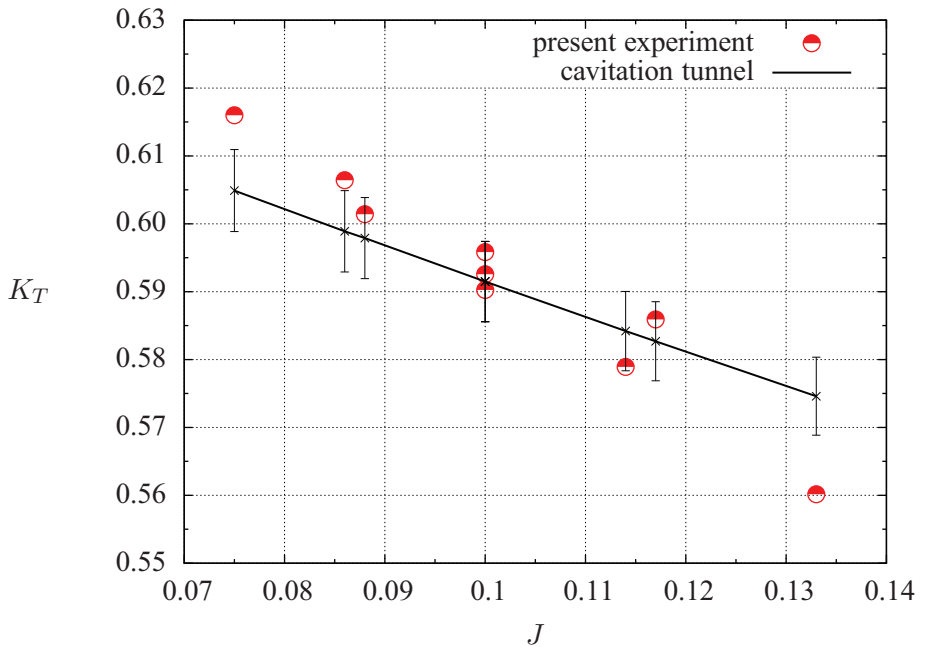


Figure 4.10: Thrust coefficient in non-ventilating conditions for the present experiments ( $\circ$ ) and cavitation tunnel tests ( $\text{---}$ ).

In the remaining of this section data will be presented as a function of the blade angular position, having as parameters the advance ratio  $J$  and a propeller loading presented in terms of percent of pressure jump across the propeller disc divided by the atmospheric pressure, according to the following relationship:

$$\frac{\Delta p}{p_0} \% = \frac{T/A_0}{p_0} \quad (4.1)$$

This propeller loading differs from the one previously defined ( $C_T = \Delta p / 0.5 \rho (nD)^2$ ) by the reference pressure ( $p_0$  in Equation 4.1 and  $p_{dyn}$  in Equation 2.12) used to scale the pressure jump. In this manner, the dependency of the pressure jump from the propeller velocity is removed.

Results are grouped for each submergence, and up to 9 curves will be presented in the same plot, according to the test matrix described in Table 4.2.

In order to help distinguishing among different curves, a common notation has been introduced, summarized in Table 4.3.

<i>Variable</i>		<i>Notation</i>	
<i>Name</i>	<i>Value</i>	<i>Specifications</i>	<i>Type</i>
<b>Advance ratio</b>	0.075	blue	<b>Color</b>
	0.086	red	
	0.088		
	0.100	black	
	0.114	green	
	0.117		
	0.133	purple	
<b>Shaft frequency</b>	12 Hz	... $\triangle$ ...	<b>Symbol</b>
	14 Hz	————	
	16 Hz	- - - o - - -	

Table 4.3: General notation.

### Deep water ( $h/R = 2.97$ )

Figure 4.11 shows the thrust coefficient in non-ventilating conditions ( $h/R = 2.97$ ) as function of the blade angular position. The coefficient was computed multiplying the number of blades  $N$  by the thrust coefficient  $K_T$  of the blade were measurements were taken.

The effect of the free-surface is visible by a thrust loss around 0 deg, in proximity of the free-surface.

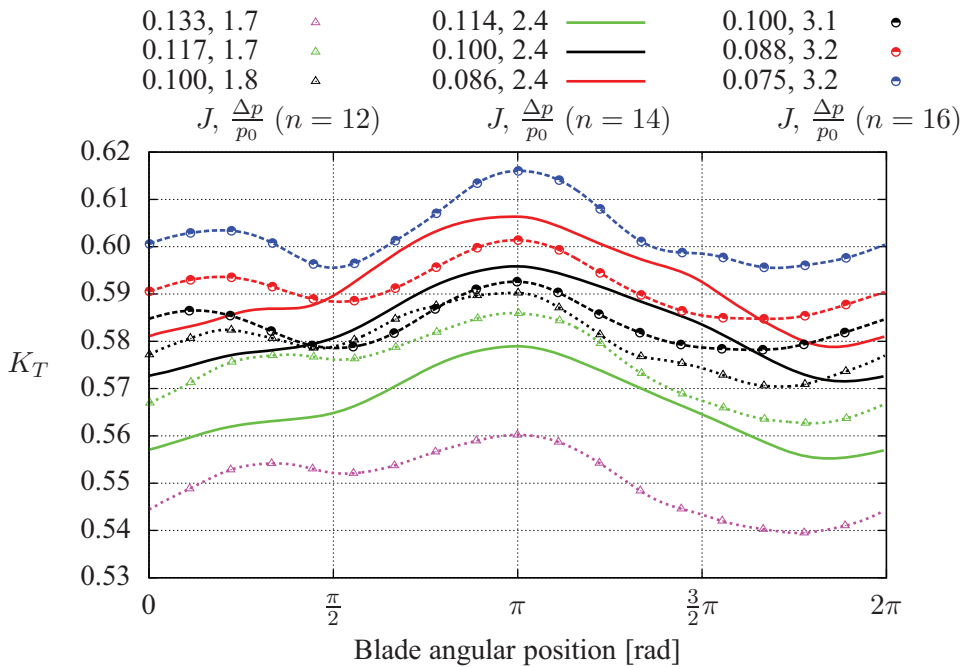


Figure 4.11: Thrust coefficient  $N \cdot K_T$  in non-ventilating conditions, averaged for each blade angular position [ $h/R = 2.97$ ; - -o- -  $n = 16$ , —  $n = 14$ ,  $\cdots \triangle \cdots$   $n = 12$  Hz].

The results presented in Figure 4.11 are averaged for each angular position. The measured thrust coefficient during each revolution have been overlapped in Figure 4.12 as function of the blade angular position, normalized with respect to the non-ventilating value. In the same figure the mean curve (as in Figure 4.11) and the curves obtained adding and subtracting two standard deviations  $2\sigma$  have also been plotted, giving an idea of the upper and lower envelope of the measured data. The thrust coefficient measured during each revolution follows rather well the average trend and is in between the curves at  $+2\sigma$  and  $-2\sigma$ .

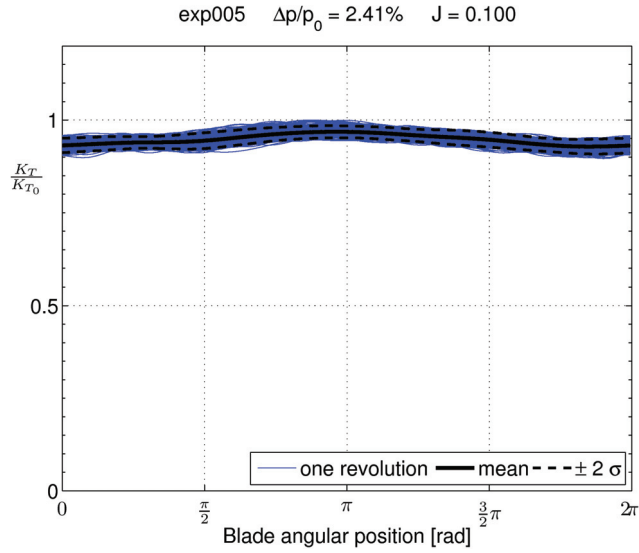


Figure 4.12: Thrust ratio in non-ventilating conditions during each revolution [ $h/R = 2.97$ ,  $n = 14$  Hz].

$$h/R = 2.04$$

The first rare ventilation events are visible at a submergence of 2.04 (Figure 4.13).

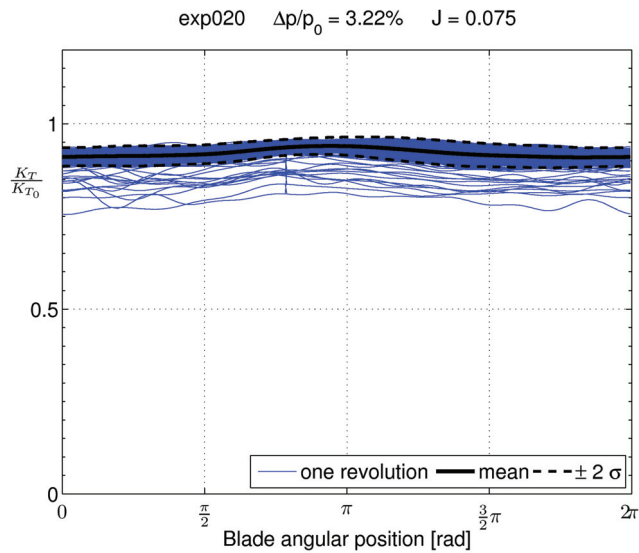


Figure 4.13: Thrust ratio during each revolution [ $h/R = 2.04$ ,  $n = 16$  Hz].

From the envelopes of the thrust ratio during each revolution, curves below the  $-2\sigma$  can be observed, with thrust losses up to 25% of the nominal thrust. These correspond to events where the propeller is drawing air through a free-surface vortex. Details about the mechanism behind this type of ventilation will be given in § 4.5.2, whereas only global characteristics will be covered in this section. The thrust ratio averaged for each blade angular position is plotted in Figure 4.14, where the higher thrust loss occurring at  $J = 0.075$  can be observed.

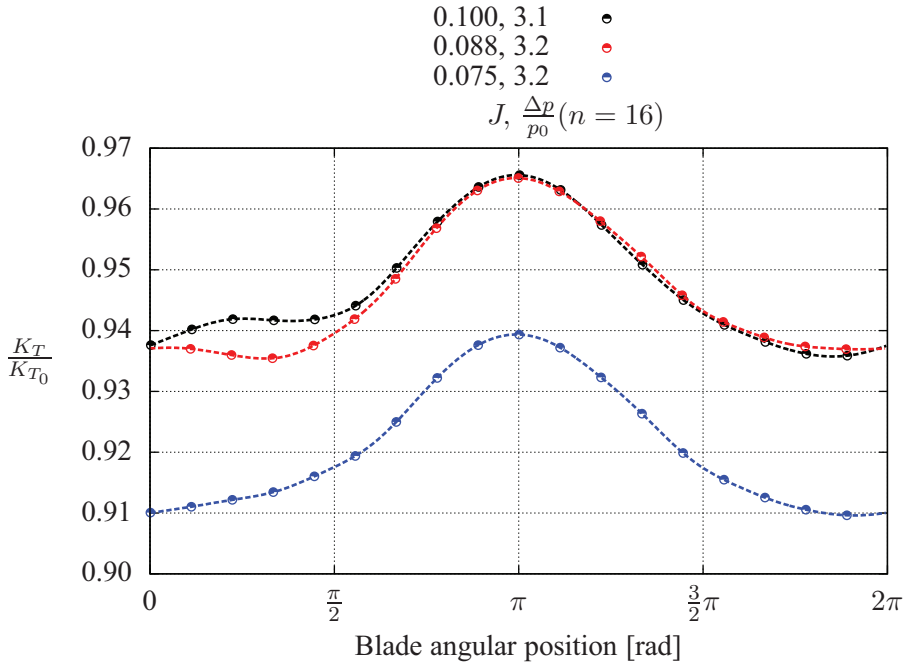


Figure 4.14: Thrust ratio averaged for each blade angular position [ $h/R = 2.04$ ,  $n = 16$  Hz].

$$h/R = 1.96$$

The results for this submergence are similar to  $h/R = 2.04$ , presenting rare ventilation events occurring only at higher propeller loadings. This leads to higher thrust losses only at  $n=16$  Hz, as shown in Figure 4.15, where the thrust ratio averaged for each blade angular position has been plotted.

The corresponding envelope of the thrust ratio is shown in Figure 4.16, where more frequent ventilation events can be observed, with respect to the the case at  $h/R = 2.04$ .

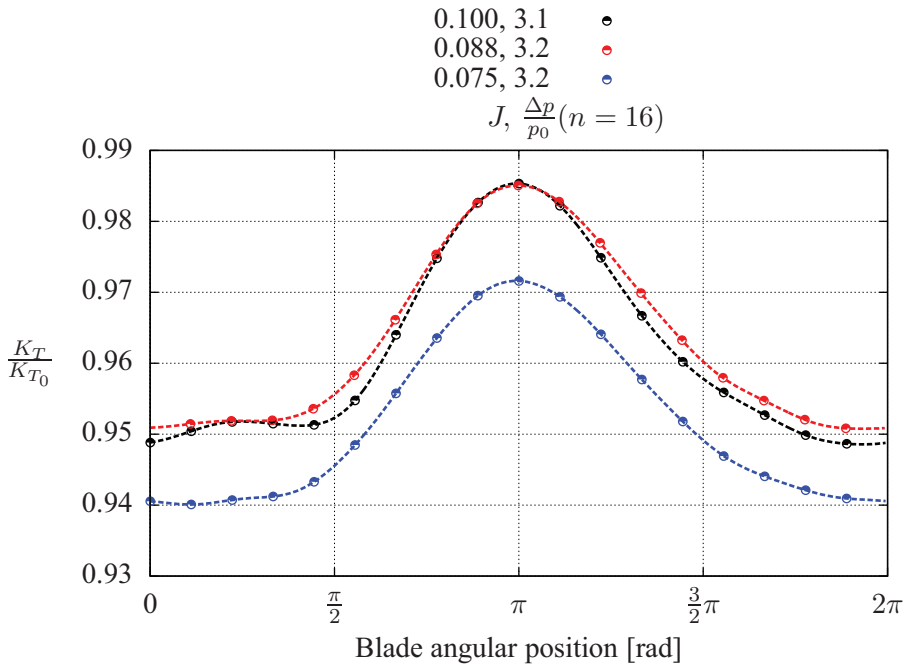


Figure 4.15: Thrust ratio averaged for each blade angular position [ $h/R = 1.96$ ,  $n = 16$  Hz].

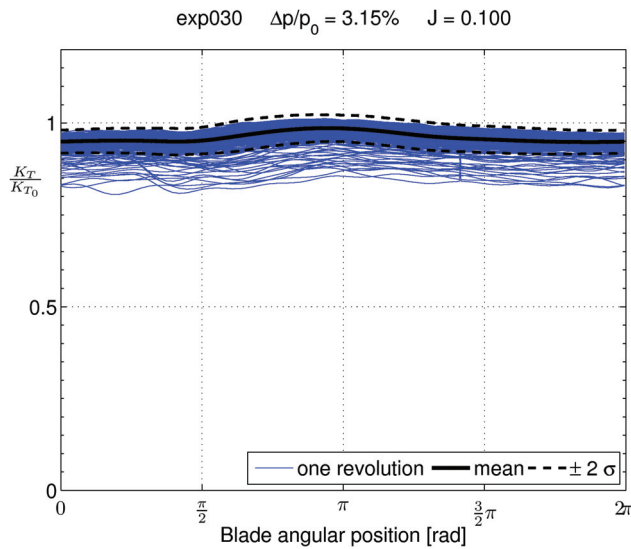


Figure 4.16: Thrust ratio during each revolution [ $h/R = 1.96$ ,  $n = 16$  Hz].

$$h/R = 1.88$$

At this submergence ventilation occurs also at  $n=14$  Hz.

Figure 4.17 shows the thrust ratio averaged for each blade angular position. As expected, lower advance ratios lead to higher thrust loss, but this applies only when the propeller loadings are the same. Figure 4.17 shows similar results between curves with the same propeller loading and different advance ratio. This is the case for  $J=0.1$  and  $J=0.086$  at  $n=14$  Hz, and for  $J=0.1$  and  $J=0.088$  at  $n=16$  Hz.  $n=16$  Hz has smaller deviation between maximum and minimum values with respect to  $n=14$  Hz, indicating that for this latter case at lower propeller loading— $n=14$  Hz—ventilation occurs only around the top most position, whereas for higher propeller loading— $n=16$  Hz—ventilation is more uniform during the entire rotation.

These considerations become more evident looking at the corresponding envelopes of the thrust coefficients plotted in Figure 4.18. The most severe case— $J=0.088$  and  $n=16$  Hz—shows thrust losses up to 40% of the nominal thrust over the entire revolution.

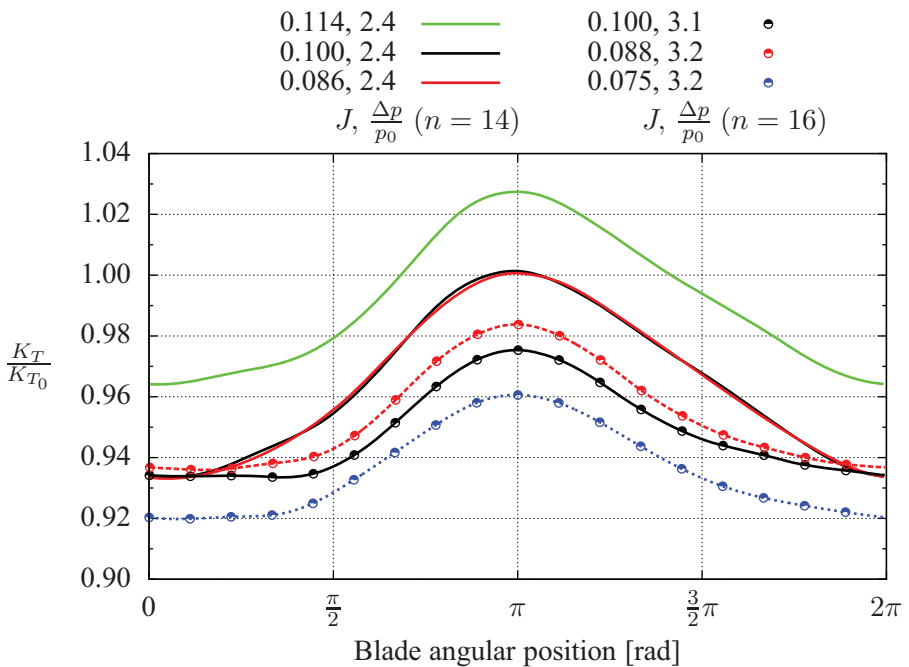


Figure 4.17: Thrust ratio averaged for each blade angular position [ $h/R = 1.88$ ; - - -  $n = 16$ , —  $n = 14$  Hz].

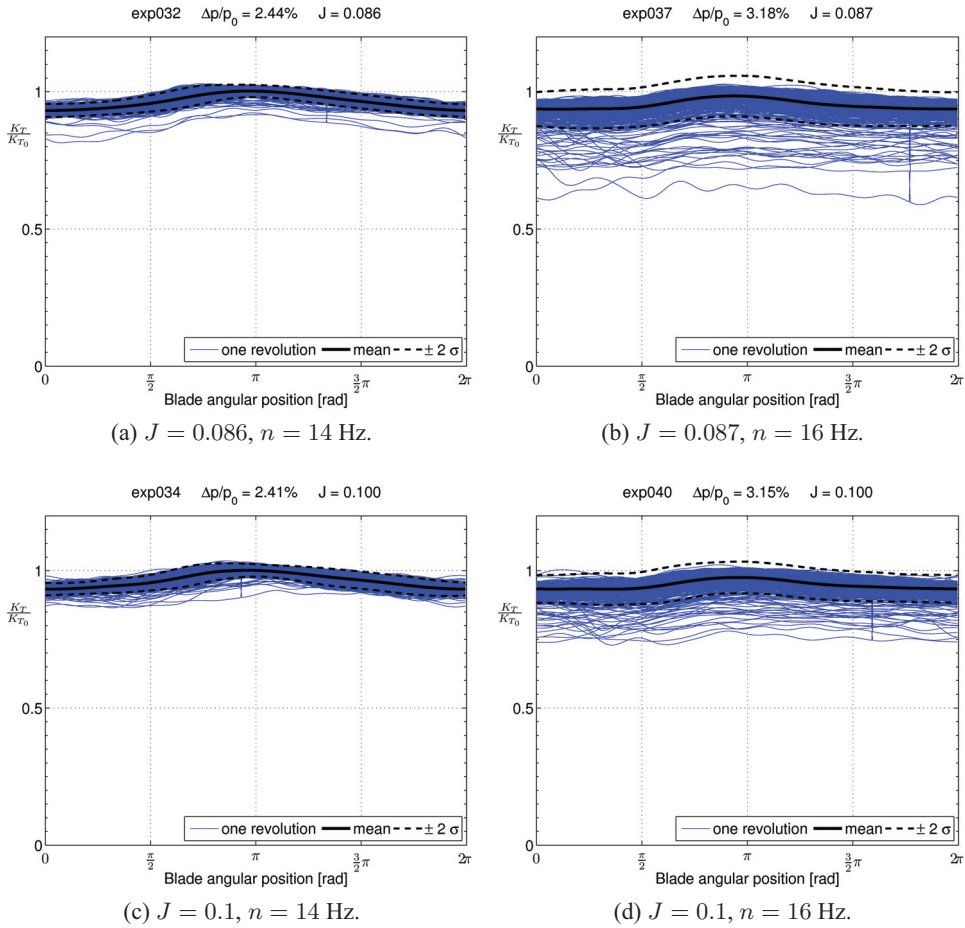


Figure 4.18: Thrust ratio during each revolution [ $h/R = 1.88$ ].

$$h/R = 1.8$$

At this submergence ventilation occurs for all the tested shaft frequencies, in the form of rare events started from a free-surface vortex. Figure 4.19 shows the thrust ratio averaged for each blade angular position.

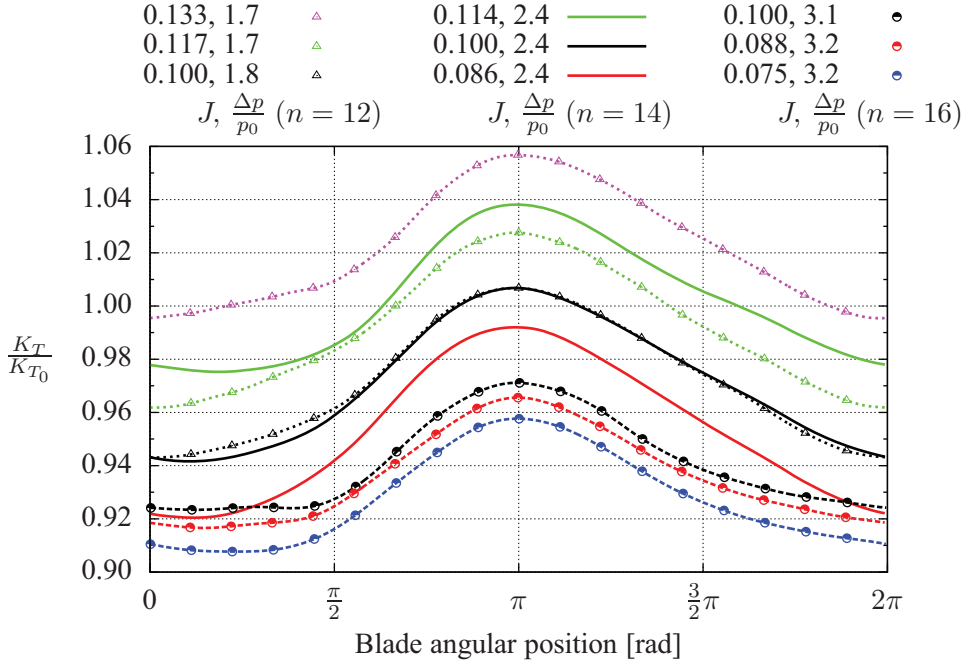


Figure 4.19: Thrust ratio averaged for each blade angular position [ $h/R = 1.80$ ; - - -  $n = 16$ , —  $n = 14$ ,  $\cdots \triangle \cdots$   $n = 12$  Hz].

Lower propeller loadings— $n=12$  and  $n=14$  Hz—show good similarity in the advance ratio; this can be argued comparing the two curves at  $J=0.1$  and the curve-pair  $J=0.114$ -and- $J=0.117$ .  $J=0.1$  at  $n=16$  Hz is not aligned with the other  $J=0.1$ -curves, but presents analogies with the other experiments at the same propeller loading,  $J=0.086$  and  $J=0.075$ .

Thrust losses generally increase with the propeller loading. The only exception is for  $J = 0.114$  and  $\Delta p/p_0 = 2.4\%$ , whose results are aligned with the case with similar advance ratio  $J = 0.117$  but lower loading  $\Delta p/p_0 = 1.7\%$ .

The effect of the propeller loading can be better understood looking at Figure 4.20, showing the envelope of thrust ratio for the three experiments having  $J=0.1$ , but different loadings. The averaged thrust ratio is not able to give a complete picture of the occurrence of ventilation. The results for the two cases at  $n=12$  and 14 Hz with  $J=0.1$  are almost overlapping in Figure 4.19, but the case at  $n=14$  Hz shows in Figure 4.20b a more severe and frequent ventilation compared to  $n=12$  Hz (Figure 4.20c).

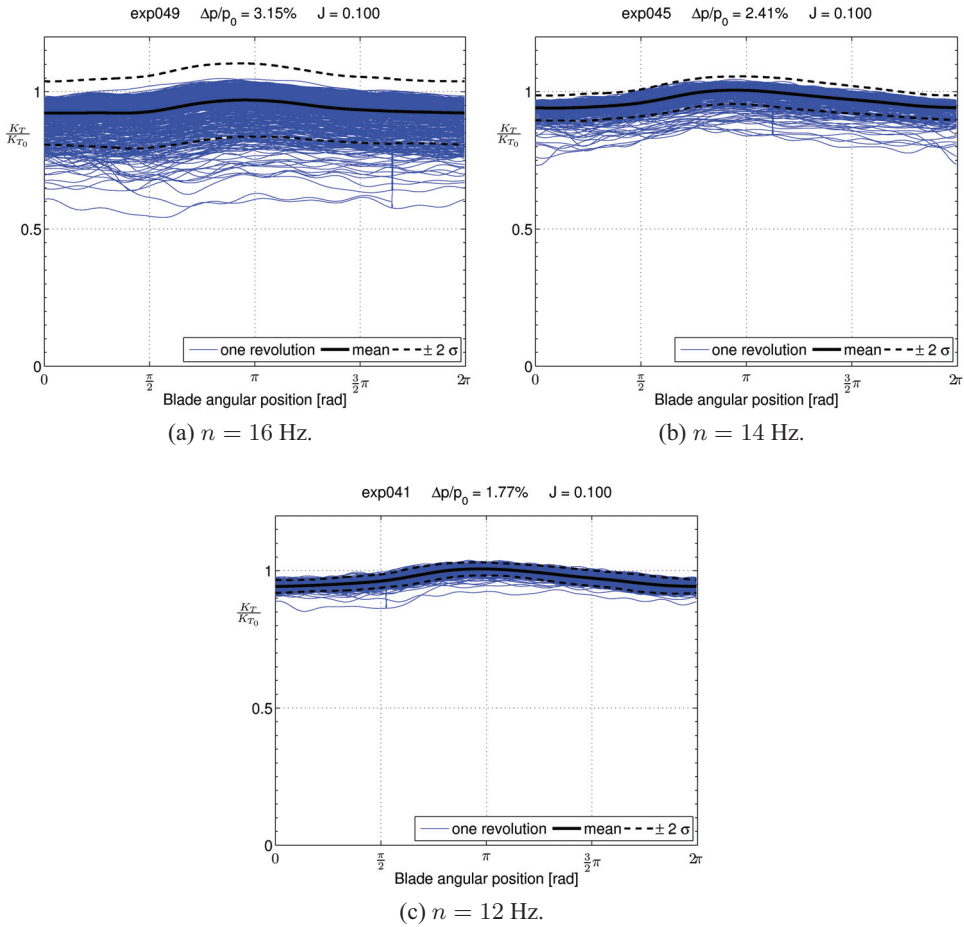


Figure 4.20: Thrust ratio during each revolution [ $h/R = 1.8$ ,  $J=0.1$ ].

Figure 4.21 compares case-pairs with the same advance ratios but different propeller loadings.

At higher advance ratios (Figure 4.21c and Figure 4.21d) different propeller loadings show the same tendency, where higher loading gives more ventilation, but less pronounced than at lower  $J$  (see also average curves in Figure 4.19).

At lower advance ratios (Figure 4.21a and Figure 4.21b), ventilation at  $n=16$  Hz is more severe than at  $n=14$  Hz.

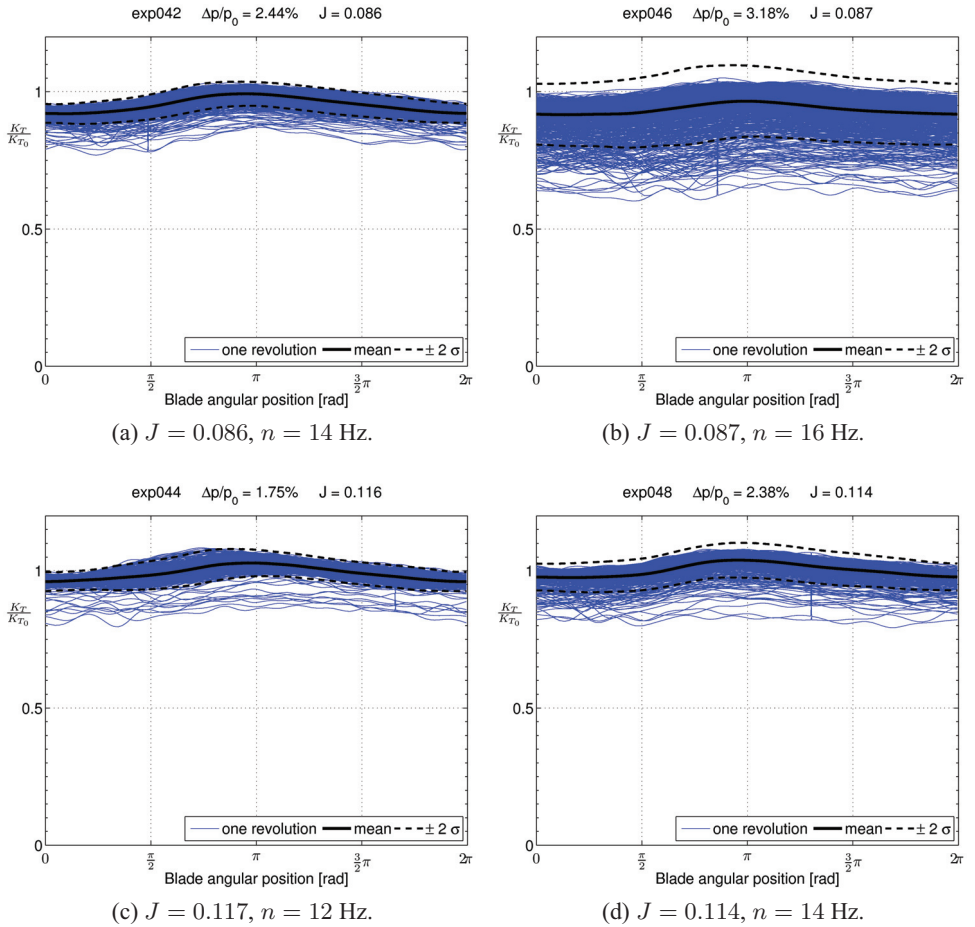


Figure 4.21: Thrust ratio during each revolution [ $h/R = 1.8$ ].

$$h/R = 1.72$$

Figure 4.22 shows the thrust ratio averaged for each blade angular position at a submergence of 1.72. Ventilation started from a free-surface vortex leads to moderate thrust losses, distributed over the whole rotation. Both the effect of the propeller loading and of the advance ratio can be observed, as described in the previous paragraph, for a submergence of 1.8.

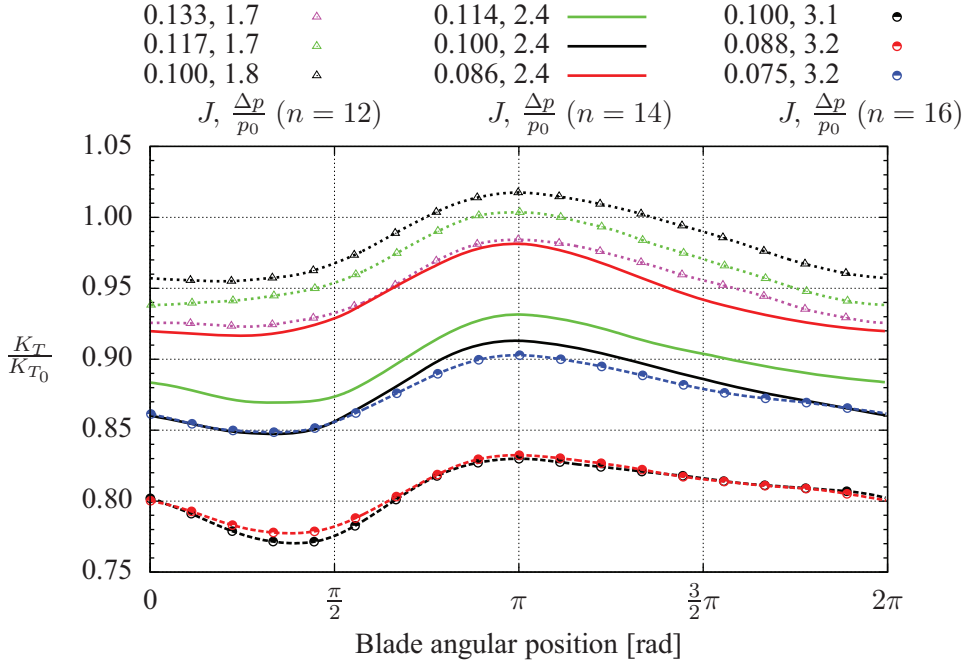


Figure 4.22: Thrust ratio averaged for each blade angular position [ $h/R = 1.72$ ; - - -  $n = 16$ , —  $n = 14$ ,  $\cdots \triangle \cdots$   $n = 12$  Hz].

This case was also tested during two other test campaigns, *Kou05* and *Koz10*, and the obtained average curves are compared in Figure 4.23a. The three curves show a very similar trend, and the main difference is found in the magnitude of the thrust losses. These differences are emphasized in the thrust ratio during each revolution for the three test campaigns (Figure 4.23). Ventilation events in *Kou05* are barely visible, *Koz10* presents a broad and uniform ventilation, whereas *Cal09* shows a broad ventilation with more severe thrust losses up to 60% of the nominal thrust.

The reason for these differences can be found in the inherent nature of the ventilation phenomenon by vortex formation, which was described in Chapter 2 as intrinsically random and very sensible to small flow disturbances.

On the other hand, differences in the set-up between the three test campaigns might also play a role. *Kou05* and *Cal09* are using the same water channel but a slightly different thruster body (a bit bigger in the case of *Kou05*). Tests *Koz10* are performed in a towing tank having dimensions (length  $\times$  breadth  $\times$  depth) of 260 m  $\times$  10.5 m  $\times$  5.6 m, thus bigger for all dimensions than the one used for the other two test campaigns. The thruster body is the same as *Cal09*. It is worth mentioning that during the tests *Koz10* an oil-spill from the hydraulically operated wave maker

had occurred. Although the leakage was promptly cleaned, a very thin layer of oil could have persisted on the free-surface even after its removal, with the effect of changing the surface tension, a parameter which might play an important role in the vortex formation and its further development.

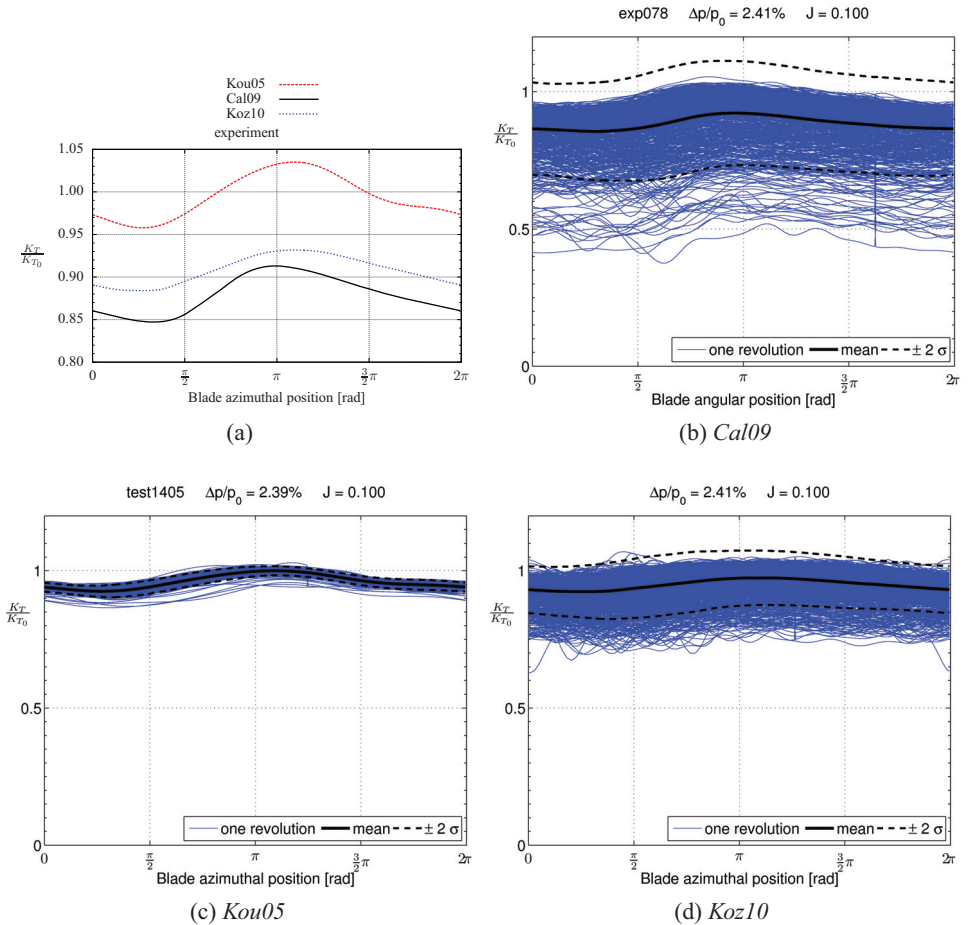


Figure 4.23: Thrust ratio during each revolution for different test campaigns [ $h/R = 1.72$ ;  $J = 0.1$ ,  $\Delta p/p_0 = 2.4\%$ ].

Differences in the test procedure might also play a role. While experiments *Cal09* and *Koz10* were performed according to the procedure described in § 4.2.1, waiting (at least 5 min) for the water to be calm before performing a new test, a shorter time was waited between different tests during the experiments *Kou05*, sometimes performing several test cases during the same run. Residual circulation

in the water might have thus reduced the pressure jump and increased the real advance ratio, avoiding the formation of free-surface vortices.

As a last remark, different blade dynamo-meters were used in all three experiments.

$$h/R = 1.64$$

The average curves computed at a submergence of 1.64 seem to be grouped by the propeller loading, while the advance ratio plays a minor role (Figure 4.24).

This submergence represents an intermediate phase where both ventilation by vortex formation and surface-piercing coexist. The free-surface vortex responsible for the inception of ventilation becomes stronger while the propeller is approaching the free-surface. At higher propeller loadings the propeller becomes partially surface piercing, experiencing severe and uniform thrust losses.

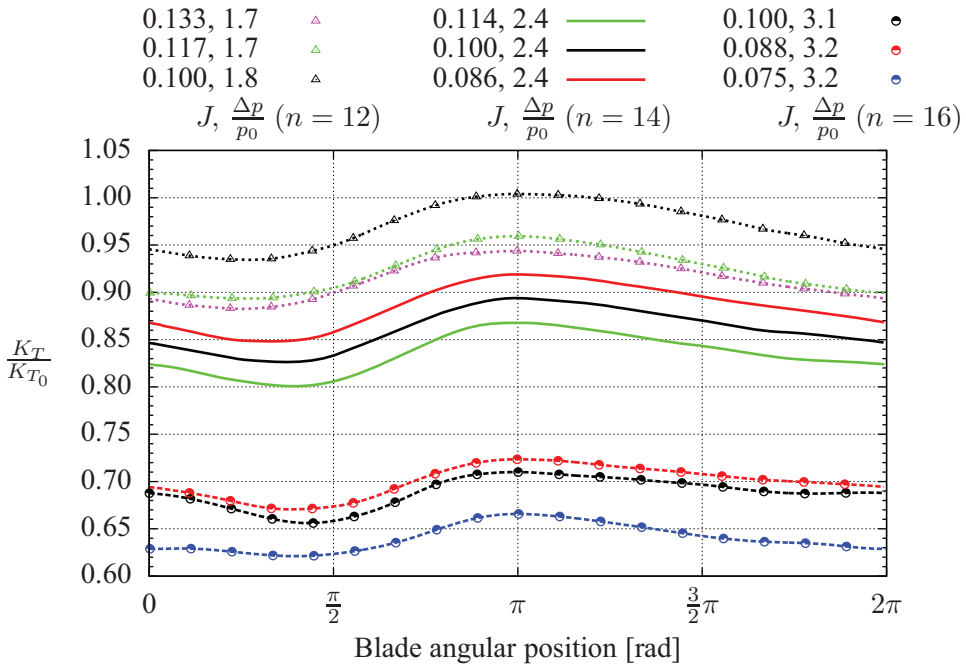


Figure 4.24: Thrust ratio averaged for each blade angular position [ $h/R = 1.64$ ; -○- -  $n = 16$ , —  $n = 14$ ,  $\cdots \triangle \cdots n = 12$  Hz].

The envelopes of the thrust coefficient for the most severe case (Figure 4.25) show the broad range of thrust achieved, which decreases to 30% of its nominal value.

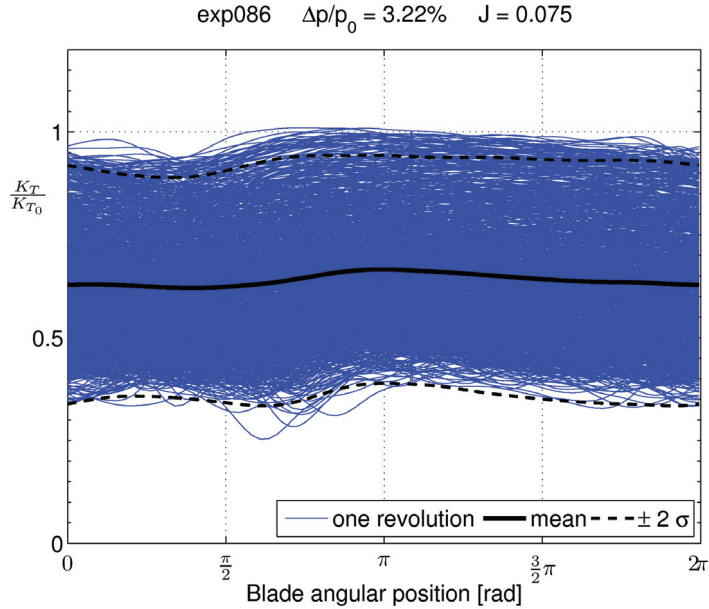


Figure 4.25: Thrust ratio during each revolution [ $h/R=1.64$ ,  $J=0.075$ ].

$$h/R = 1.56$$

At this submergence the first event of ventilation characterized only by surface-piercing propeller occurs. The change of pattern can be observed comparing the present submergence (Figure 4.27), where the thrust range is between 30% and 70%, with the corresponding envelope for  $h/R=1.64$  (Figure 4.25), where the whole range between 30% and 100% is embraced.

The reduced spreading in the present case shows that ventilation is no longer fed by a randomly-appearing free-surface vortex, but by the air sucked by the blade itself piercing the free-surface at each revolution, leading to higher and more uniform thrust losses.

Figure 4.26 shows the thrust ratio averaged for each blade angular position. The average curves at higher propeller loadings have moved farther from the others, indicating the different ventilation mechanisms occurring in this case.

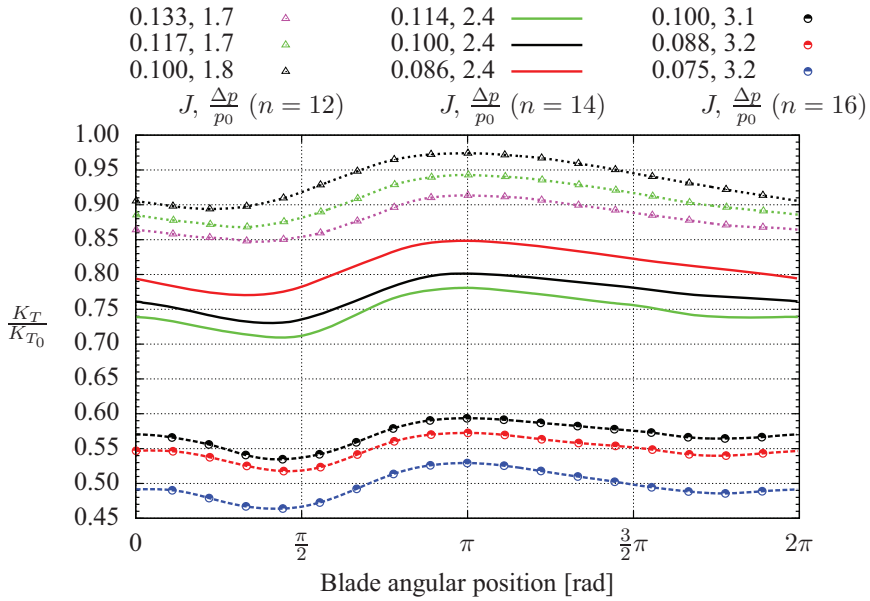


Figure 4.26: Thrust ratio for each blade angular position [ $h/R = 1.56$ ; - - -  $n = 16$ , —  $n = 14$ ,  $\cdots \triangle \cdots$   $n = 12$  Hz].

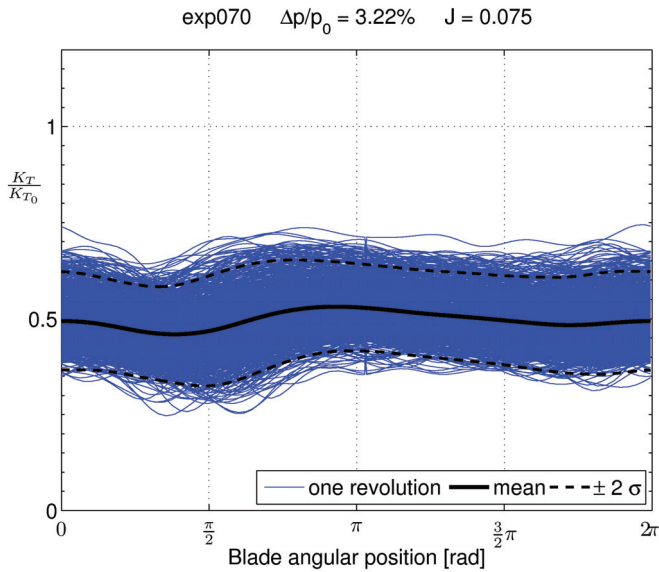


Figure 4.27: Thrust ratio during each revolution [ $h/R=1.56$ ,  $J=0.075$ ].

$$h/R = 1.48$$

Figure 4.28 shows the thrust ratio averaged for each blade angular position. The average curves at  $n=14$  Hz are approaching the higher propeller loadings, indicating that the surface-piercing ventilation is occurring also in this case.

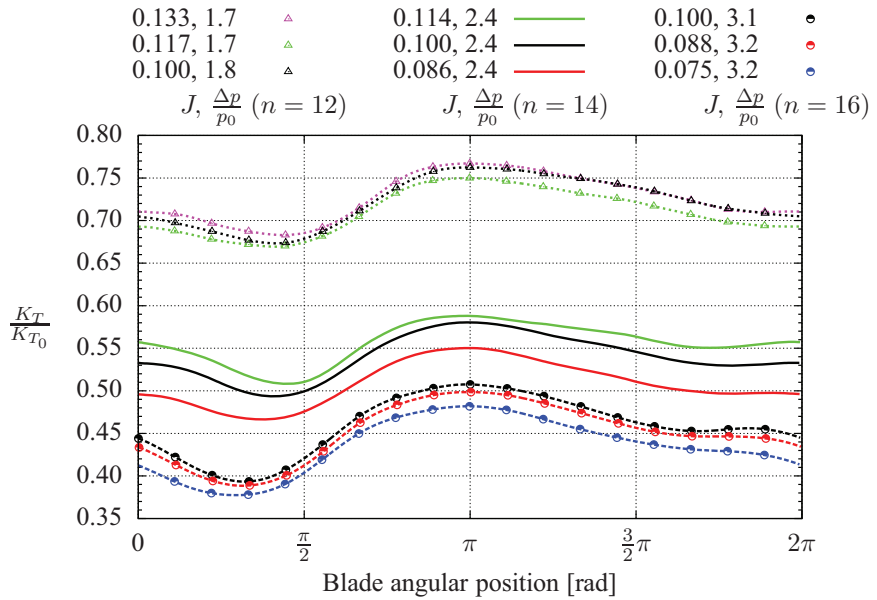


Figure 4.28: Thrust ratio for each blade angular position [ $h/R = 1.48$ ; - - -  $n = 16$ , —  $n = 14$ ,  $\cdots \triangle \cdots$   $n = 12$  Hz].

$$h/R = 1.4$$

Figure 4.29 shows the thrust ratio averaged for each blade angular position. At this submergence average curves are still grouped by the propeller loading, but the distance between the three groups has decreased. Surface-piercing ventilation is the dominating mechanism for all the cases.

As for  $h/R=1.72$ , this submergence was also tested in two other test campaigns, *Kou05* and *Koz10*, and the comparison of the average curves is shown in Figure 4.30a. The three curves show a very similar trend, and the main difference is found in the magnitude of the thrust losses, smaller for *Koz10*. The curves for *Kou05* and *Cal09* are almost overlapping.

The complete envelopes of the thrust coefficient depicted in Figure 4.30 show a good agreement between the three test campaigns, indicating that the same surface-piercing ventilation occurs. As described in Chapter 2, this type of ventilation is

rather stable and depends strongly on the propeller characteristics. Therefore, the differences in set-up between the three test campaigns are not deemed to affect significantly the ongoing ventilation. The difference in magnitude could be ascribed to the different blade dynamometer and calibration used. The residual presence of oil on the free-surface could also be the cause of the increased thrust for *Koz10*, changing the local surface tension.

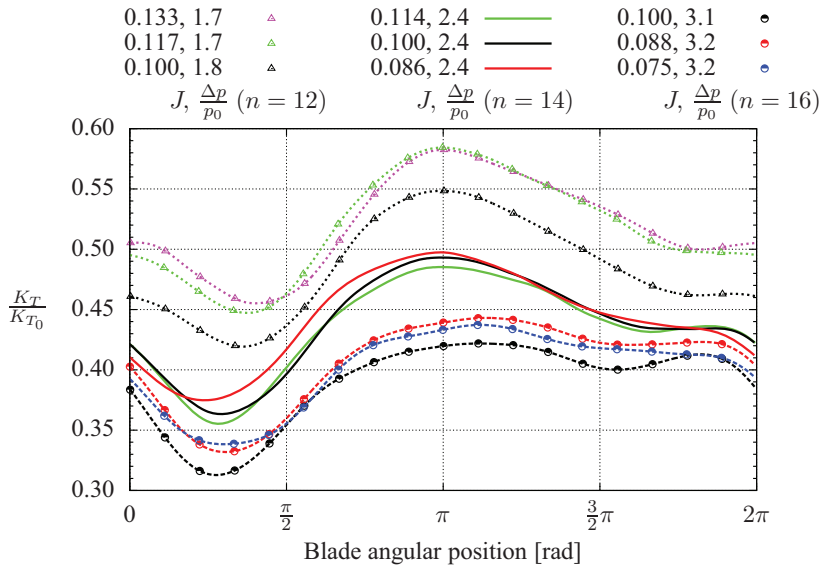
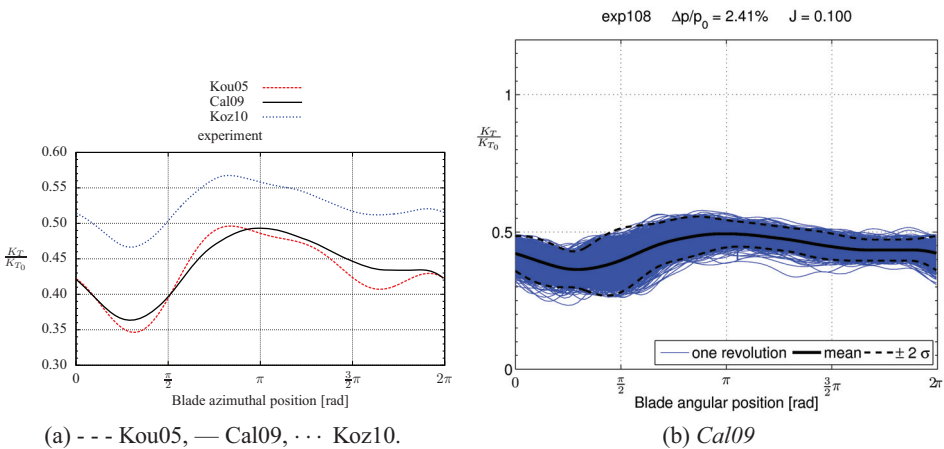


Figure 4.29: Thrust ratio for each blade angular position [ $h/R = 1.4$ ; - - -  $n = 16$ , —  $n = 14$ ,  $\cdots \triangle \cdots n = 12$  Hz].



(a) - - - Kou05, — Cal09,  $\cdots$  Koz10.

(b) Cal09

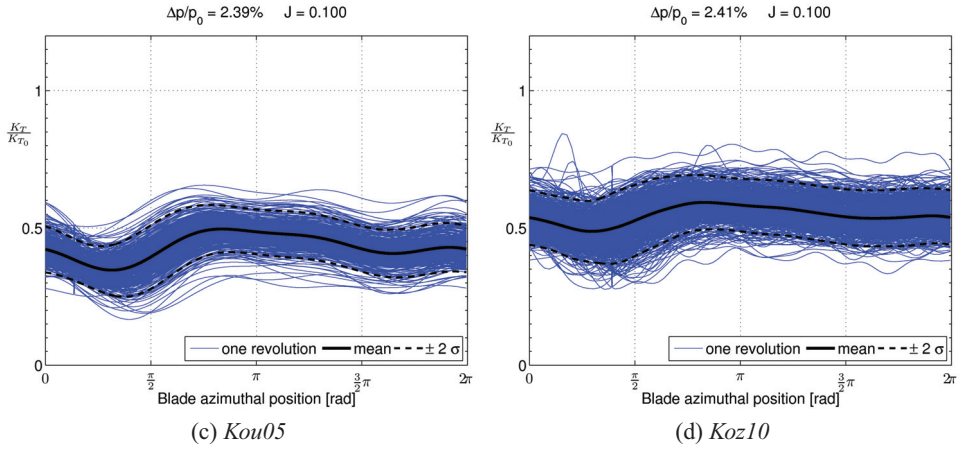


Figure 4.30: Thrust ratio for different test campaigns [ $h/R = 1.4$ ;  $J = 0.1$ ,  $\Delta p/p_0 = 2.4\%$ ].

$h/R = 1.32$

Figure 4.31 shows the thrust ratio averaged for each blade angular position. A further reduction of the propeller submergence leads to increased thrust losses for all the tested configurations.

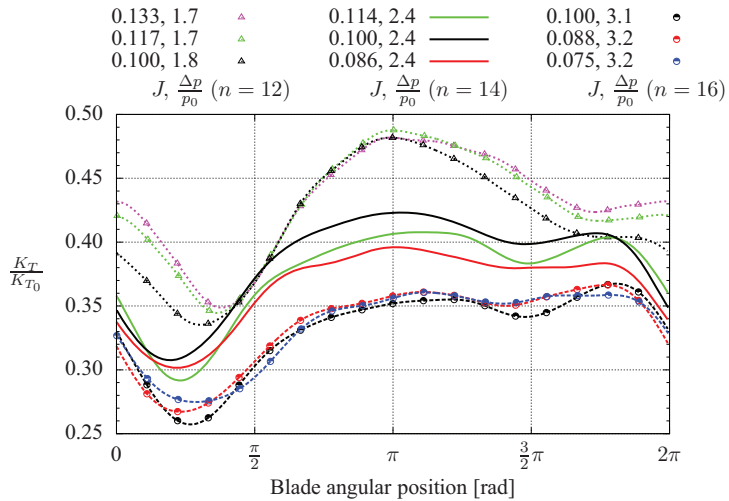
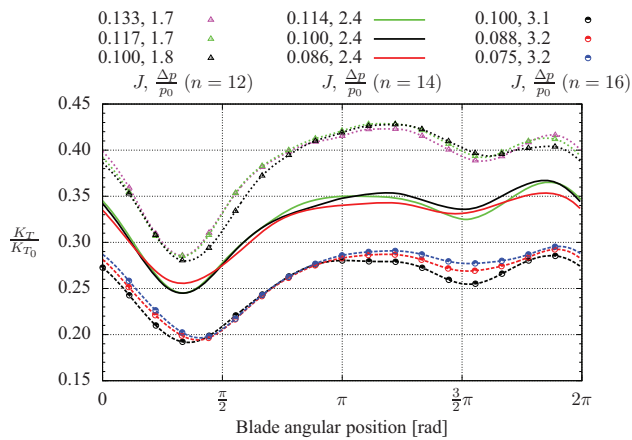


Figure 4.31: Thrust ratio for each blade angular position [ $h/R = 1.32$ ; - - -  $n = 16$ , —  $n = 14$ ,  $\dots \triangle \dots$   $n = 12$  Hz].

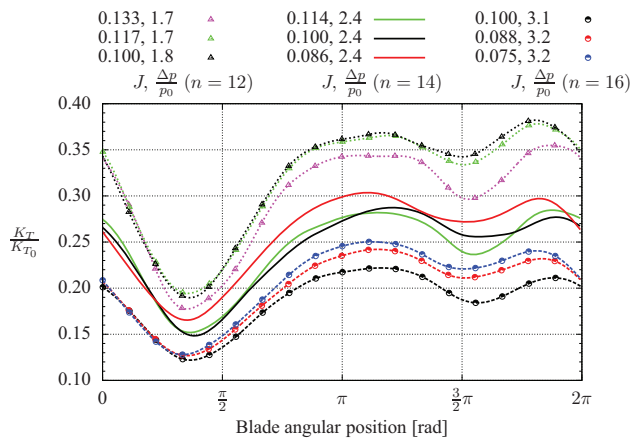
$h/R = 1.24$  **and**  $h/R = 1$

Figure 4.32a shows the thrust ratio averaged for each blade angular position, where the thrust has further decreased ( $h/R = 1.24$ ). Curves with the same propeller loading are perfectly overlapping. This is the result of a reduced deviation during different revolutions, since the surface-piercing ventilation mechanism is now the only source of thrust-loss.

A further decrease of thrust occurs when the propeller tip is first touching the free-surface at rest ( $h/R = 1$ ), as shown for the thrust ratio averaged for each blade angular position in Figure 4.32b.



(a)  $h/R = 1.24$

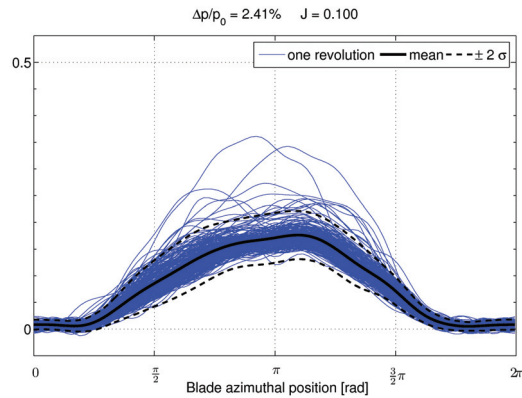


(b)  $h/R = 1$

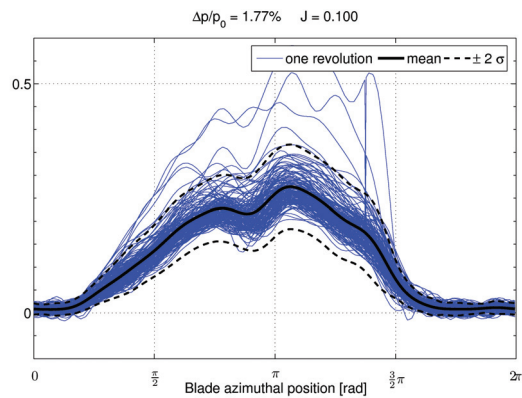
Figure 4.32: Thrust ratio for each blade angular position [ - -○- -  $n = 16$ , —  $n = 14$ ,  $\cdots \triangle \cdots$   $n = 12$  Hz].

$$h/R = 0.24 \text{ Koz10}$$

At this submergence the propeller is surface-piercing already at rest, only the hub remains fully submerged. Figure 4.33 shows the envelop of the thrust ratio during each revolution, obtained during the test campaign *Koz10*. While piercing the free-surface, around 0 deg, the blade is completely out of water and is thus giving zero thrust, while at 180 deg the maximum thrust does not reach 50% of its nominal value. The lower propeller loading at  $n=12$  Hz shows an interesting difference around 180 deg with respect to the higher propeller loading  $n=14$  Hz. After an initial slight decrease before the mid-low position, the thrust is increasing again, before decreasing to zero towards the mid-top position. This difference could be ascribed to the fact that the air-bucket created around the mid-top position is spanning at lower velocity ( $n=12$  Hz) a smaller sector with respect to  $n=14$  Hz.



(a)  $n = 14$  Hz;  $\Delta p/p_0 = 2.4\%$



(b)  $n = 12$  Hz;  $\Delta p/p_0 = 1.8\%$

Figure 4.33: Thrust ratio during each revolution [ $h/R = 0.24$ ;  $J = 0.1$ ; *Koz10*].

$h/R = 0$  *Kou05*

The case where the propeller axis is on the free-surface presents characteristics similar to the previous one. The thrust envelopes obtained during the test campaign *Kou05* show a rather broad range of the thrust amplitude (Figure 4.34). The plotted curves show a pattern more regular than the results previously presented. This regular pattern is the result of low-pass filtering of the raw data with a cutoff frequency below the blade frequency. This treatment was necessary to correct for a measurement error during the test campaign *Kou05* (Califano, 2008a).

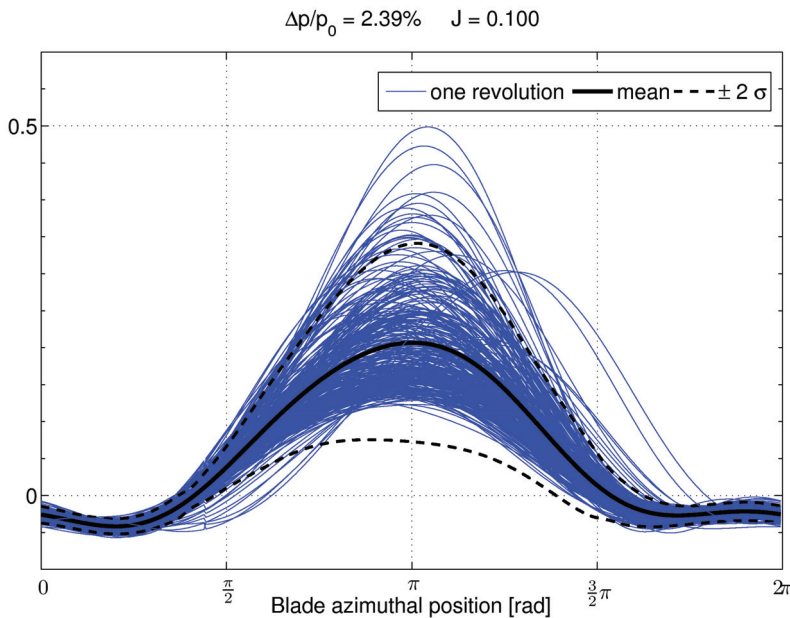


Figure 4.34: Thrust ratio during each revolution [ $h/R = 0$ ;  $J = 0.1$ ;  $\Delta p/p_0 = 2.4\%$ ;  $n = 14$  Hz; *Kou05*].

#### 4.4.1 Effect of submergence

The presented results have been summarized in Figure 4.35, where the mean thrust ratio has been plotted as a function of the submergence ratio, having the advance ratio and propeller loading as parameters.

$h/R > 2$ : at deep submergence all curves are overlapped and thrust losses occur only due to the proximity of the free surface.

$h/R < 1.5$ : at low submergence curves are grouped solely by the propeller loading. The chosen range for the advance ratio is very small (around 0.1, between

0.075 and 0.133), and its influence on the thrust losses can not be observed<sup>1</sup>. In this region, tip vortex is the dominating ventilation mechanism, leading to very high thrust losses. Further reducing the submergence ( $h/R < 1$ ), thrust would continue to fall following the reduction of the submerged disc area.

$1.5 < h/R < 2$ : At intermediate submergence curves are still grouped by the propeller loading, but the spreading is larger, due to the inherently unstable and random nature of the free-surface vortex affecting ventilation in this range of submergences.

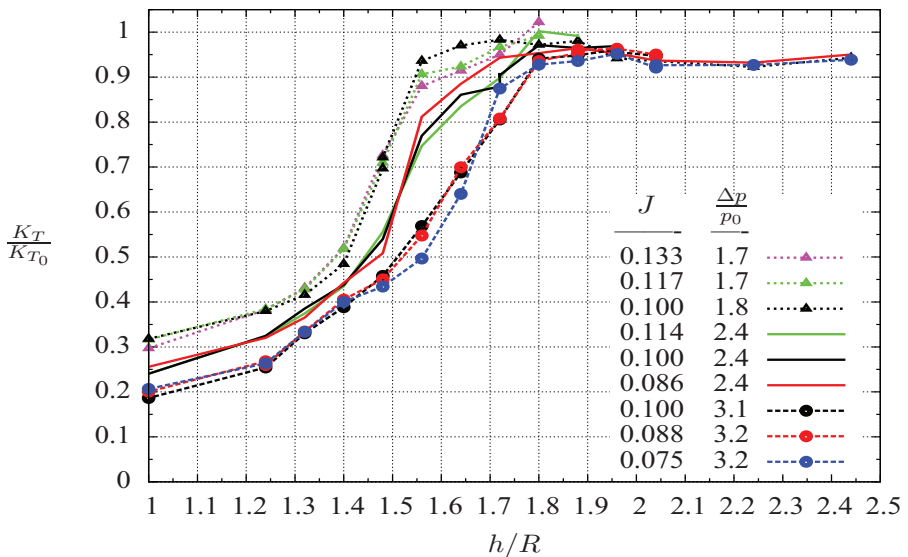


Figure 4.35: Mean thrust ratio as a function of the submergence ratio, having the advance ratio and propeller loading as parameters.

The average thrust ratio as a function of the blade angular position for the case at  $J = 0.1$  and  $n = 14$  Hz is shown in Figure 4.36, having the submergence ratio as parameter. The complete envelopes of the averaged curves can be found in Appendix A.3. The intermediate regime at  $h/R = 1.56$  has been identified in this case as the overlapping region where both types of ventilation coexist, one dominated by free-surface vortex, and the other by the tip vortex. In this latter case blades become surface-piercing after deformation of the free surface. From this intermediate stage, further reducing the submergence leads to an abrupt thrust loss, where ventilation is fed only through the tip vortex.

<sup>1</sup>Differences would have been noticed for higher advance ratios (up to design conditions), where ventilation has less tendency to occur.

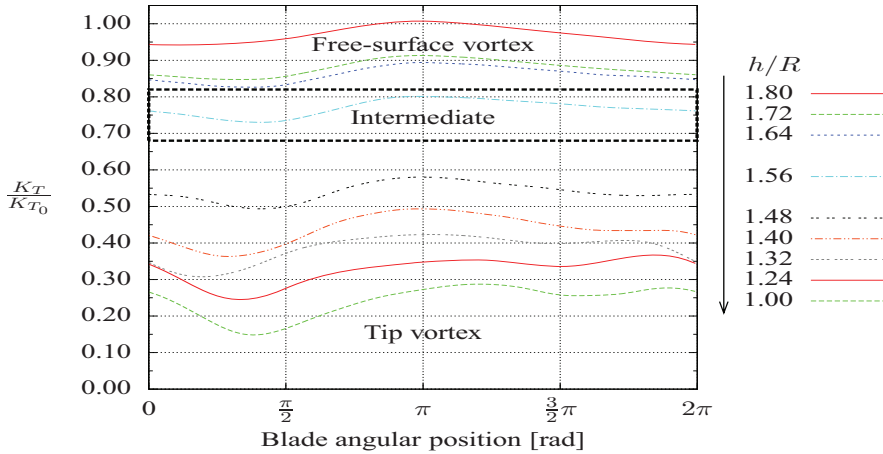


Figure 4.36: Thrust ratio as a function of the blade angular position, having the submergence ratio as parameter [ $J = 0.1$ ,  $n = 14$  Hz].

## 4.5 Ventilation inception

### 4.5.1 Surface-piercing

Figure 4.37 shows the ventilation inception in terms of the thrust ratio of *Blade*<sub>1</sub> and of the whole thruster for the case with  $h/R = 1.4$ ,  $J = 0.133$ ,  $\dot{n} = 208.7$  rad/s<sup>2</sup>. The angular position of *Blade*<sub>1</sub> and the angular velocity are plotted in the same figure.  $t = 0$  corresponds to the time where the shaft frequency  $n$  has reached its desired value  $n_0$ .

The blade thrust ratio averaged among the four blades  $K_{T-\overline{Blade}}$  is the thrust force measured for the whole thruster—thus including hub, pod and strut—normalized using the corresponding non-ventilating value. This approximation is valid assuming that the contribution of the hub, the strut and the pod is negligible with respect to the forces exerted by the propeller during ventilation.

The average thrust increases in a quasi-linear manner with time following the linear increase of the propeller angular velocity  $n$ . This increasing trend is interrupted around -0.14 s where the propeller hits the free-surface for the first time, as shown in Figure 4.38a, where a breaking wave is visible downstream *Blade*<sub>3</sub>.

For this configuration, ventilation is started after the deformation of the free surface due to the induced velocity field imposed by the propeller, and the subsequent sucking of air through the low-pressure region of the trailing vortex. The drop of the free surface at the propeller tip with respect to the undisturbed level (visible on the strut) can also be observed (Figure 4.38a).

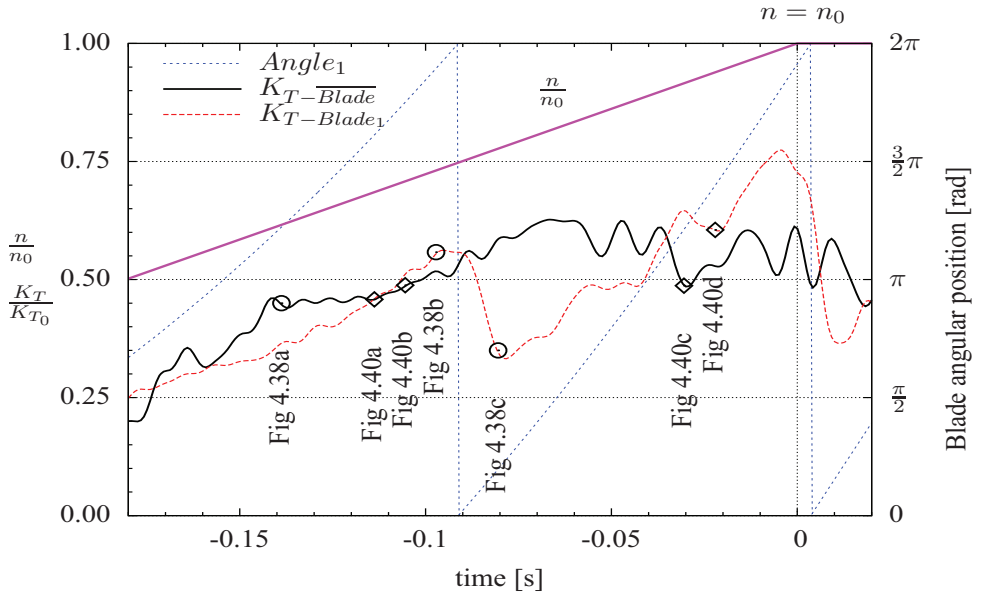


Figure 4.37: Time evolution of the thrust ratio of  $Blade_1$  (---) and the whole propeller  $\overline{Blade}$  (—) [ $h/R = 1.4$ ,  $J = 0.133$ ,  $\Delta p/p_0 = 1.7\%$ ,  $\dot{n} = 208.7 \text{ rad/s}^2$ ].

The increase of thrust of  $Blade_1$  is interrupted around  $-0.1 \text{ s}$ , when the blade hits for the first time the free surface, as shown in Figure 4.38b, where the vortex system around the tip of the  $Blade_1$  and  $Blade_2$  is also visualized by air suction. During its rotation,  $Blade_1$  continues losing its thrust reaching a minimum value around  $-0.08 \text{ s}$ , few degrees after the top vertical position, represented in Figure 4.38c. Starting from this time instant, the thrust of the propeller oscillates around a value which is about half of the non-ventilated one.



(a) First impact of the propeller on the free-surface,  $t = -0.1388 \text{ s}$ . (b) First impact of  $Blade_1$  on the free-surface,  $t = -0.0972 \text{ s}$ . (c) Minimum blade thrust,  $t = -0.0805 \text{ s}$ .

Figure 4.38: Impact of the propeller on the free-surface [ $h/R = 1.4$ ,  $J = 0.133$ ,  $\Delta p/p_0 = 1.7\%$ ,  $\dot{n} = 208.7 \text{ rad/s}^2$ ].

Figure 4.39 compares the propeller thrust for  $h/R = 1.4$  with the infinite fluid case ( $h/R = 2.97$ ). After ventilation occurs around  $t = -0.1$  s, thrust for  $h/R = 1.4$  stops abruptly around 50% of its nominal value, while for  $h/R = 2.97$  it keeps increasing towards its non-ventilating value, which is reached when the shaft frequency reaches its nominal value  $n_0$ .

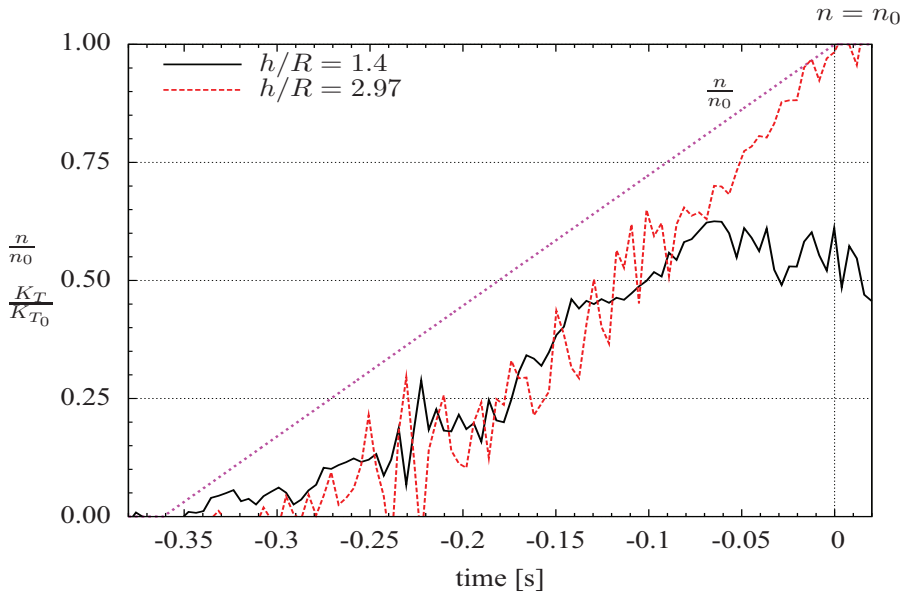


Figure 4.39: Comparison of the thrust ratio of the whole propeller between  $h/R = 1.4$  and  $h/R = 2.97$  [ $J = 0.133$ ,  $\Delta p/p_0 = 1.7\%$ ,  $\dot{n} = 208.7 \text{ rad/s}^2$ ].

The interaction of the tip vortex with the free surface during the first time instants is visualized in Figure 4.40. The tip vortex generated from  $Blade_2$  becomes visible on the port side when it crosses the free surface for the first time, around  $-0.115$  s, as shown in Figure 4.40a. This vortex system becomes visible also starboard after  $Blade_2$  has entrapped more air above the free-surface and transported it in the direction of rotation. This is shown in Figure 4.40b, where the propagation of the tip vortex both port and starboard can be observed.

Figure 4.40c shows the extension of the vortex system all around the propeller, as a continuous vortex tube interrupted only by the free surface. This point represents also a local minimum for the thrust of the thruster. Each blade crossing the free surface entraps more air which is transported around the propeller. In Figure 4.40d  $Blade_1$  has reached on the port side the air sucked through the tip vortex trailing from  $Blade_2$ , leading to a local minimum for its thrust (Figure 4.37).

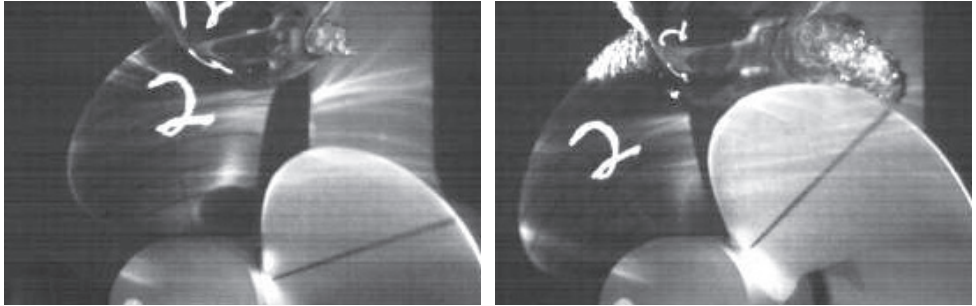
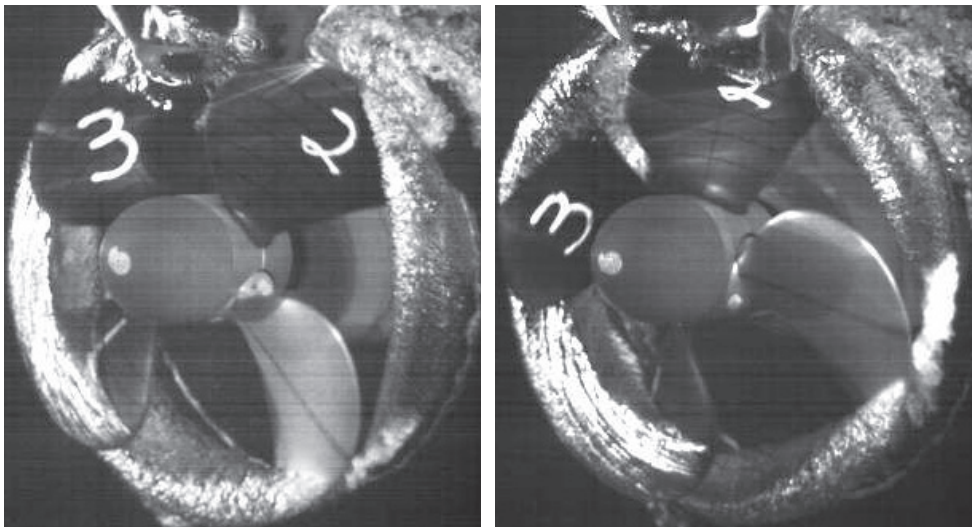
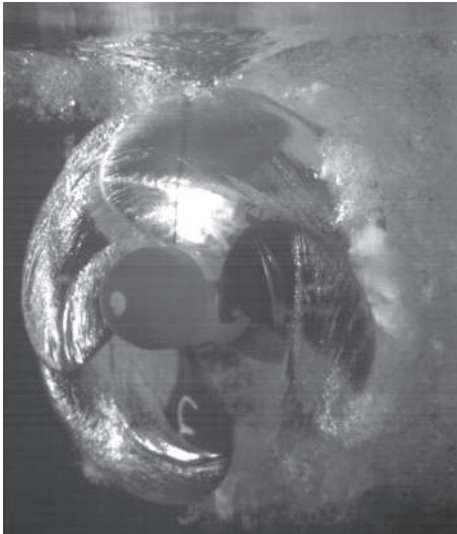
(a) Tip vortex of *Blade*<sub>2</sub>,  $t = -0.1138$  s.(b) Tip vortex: port and starboard,  $t = -0.1055$  s.(c) Tip vortex system all around the propeller,  $t = -0.0305$  s.(d) Local minimum thrust for *Blade*<sub>1</sub> that reaches the tip-vortex trailing from *Blade*<sub>2</sub>,  $t = -0.0221$  s.

Figure 4.40: Visualization of the tip vortices [ $h/R = 1.4$ ,  $J = 0.133$ ,  $\Delta p/p_0 = 1.7\%$ ,  $\dot{n} = 208.7$  rad/s<sup>2</sup>].

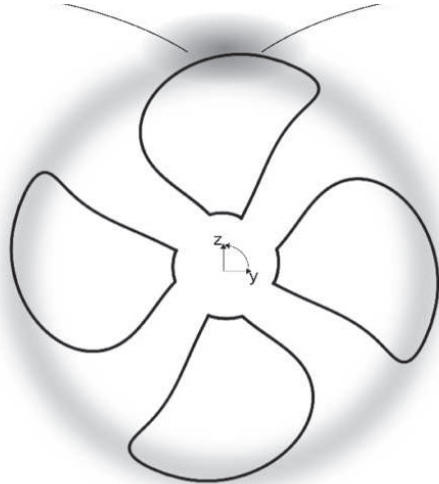
Part of the air vortex generated starboard is leaving the propeller before completing half revolution, transported downstream by the induced axial velocity and the free stream and upward by its buoyancy. The air vortex generated on the port side is propagating in direction opposite to the rotation; a small part of it joins the other tip vortex around  $3\pi/2$  rad, but most part of the air is transported downstream.

When fully ventilating, air is rapidly mixed with water and the resulting mixture is covering the entire propeller, blurring the visualizations of the air-water interface

(Figure 4.41a). However, a vortex ring around the propeller tip can still be observed. This vortex is able to stay attached to the propeller tip—rather than being completely convected downstream—because of the resulting velocity field on the tip of a propeller working at high loadings, characterized by strong recirculation, resulting in an almost zero induced axial velocity (Greenberg, 1972). A sketch of this type of ventilation is drawn in Figure 4.41b.



(a)  $h/R = 1.4$ ,  $J = 0.133$ ,  $\Delta v/p_0 = 1.7\%$ .



(b) Sketch of surface-piercing ventilation.

Figure 4.41: Fully ventilating propeller in surface-piercing regime.

#### 4.5.1.1 Effect of acceleration

Besides the tests performed at the nominal shaft frequencies, additional tests were performed changing the slope of the linear ramp used to reach the desired value. This was done in order to verify the effect of the acceleration on the loads due to ventilation obtained at the inception, and were thus performed only on a case of surface-piercing ventilation, with  $h/R = 1.4$ . Being the default acceleration  $\dot{n}^* = 208.7 \text{ rad/s}^2$ , tests were performed using  $\dot{n}/\dot{n}^* = 1/2, 1/4, 1/8$ . The complete test specifications are given in Appendix A.2.

Figure 4.42 compares the thrust ratio at  $J = 0.1$  for different accelerations and final velocities, while the results obtained at the lower (Figure 4.43a) and higher (Figure 4.43b) advance ratios are also shown.

Results are presented as function of time divided by the time  $t_{ramp}$  needed to reach the desired rotation rate  $n_0$ . In this manner loads on the same  $x$ -axis have the same shaft frequency, but different absolute time.

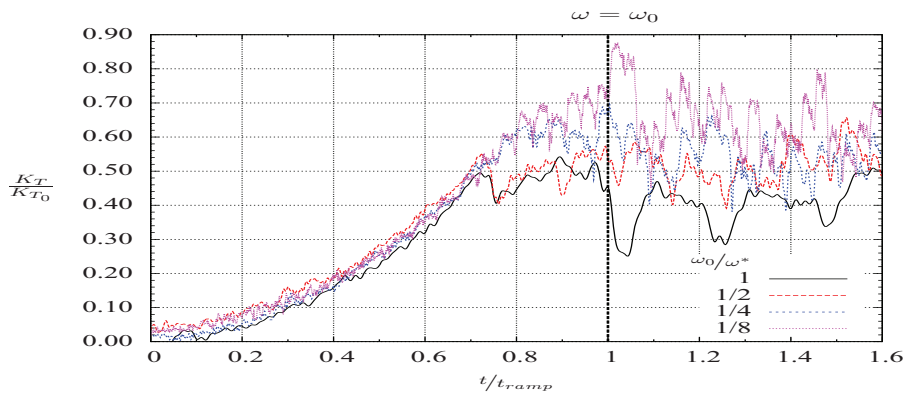
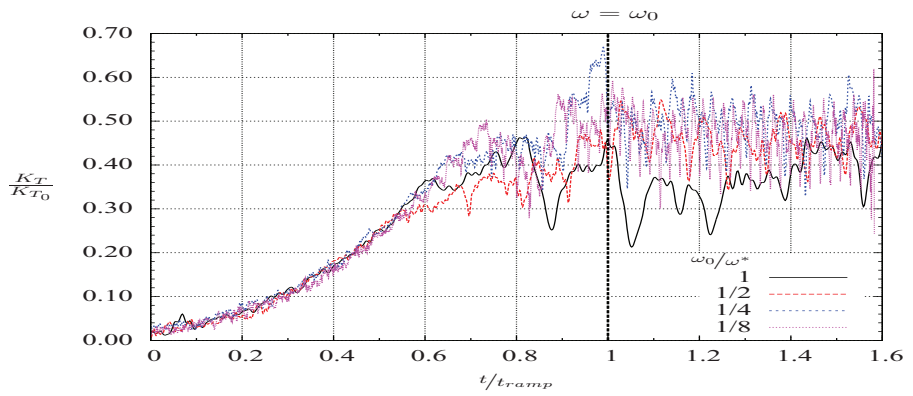
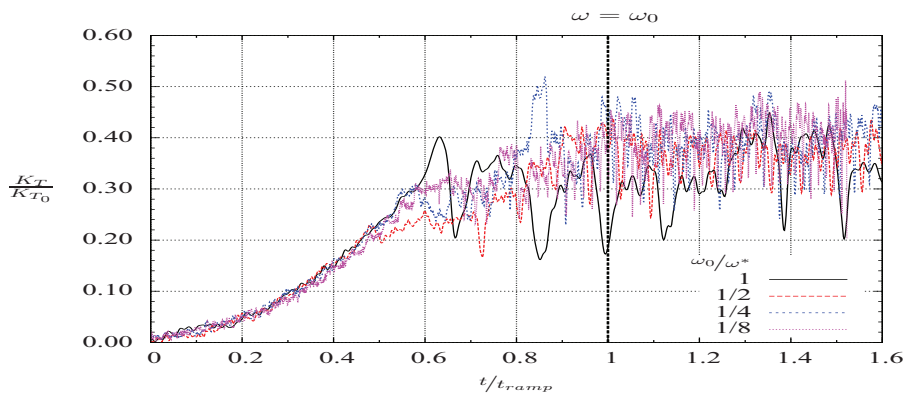
(a)  $n = 12$  Hz.(b)  $n = 14$  Hz.(c)  $n = 16$  Hz.

Figure 4.42: Thrust ratio as function of time divided by the time  $t_{ramp}$  needed to reach constant rotation rate  $n_0$  [ $h/R = 1.4$ ;  $J = 0.1$ ].

The results obtained at  $\dot{n} = \dot{n}^*$  show thrust losses higher than all the other accelerations right after the desired shaft frequency has been reached. After this initial phase, the thrust rapidly increases following the other curves. This difference could be ascribed to the higher loads achieved at higher accelerations. Higher thrust losses are achieved only at the most severe case performed, indicating that a value of the acceleration exists below which its effect is negligible.

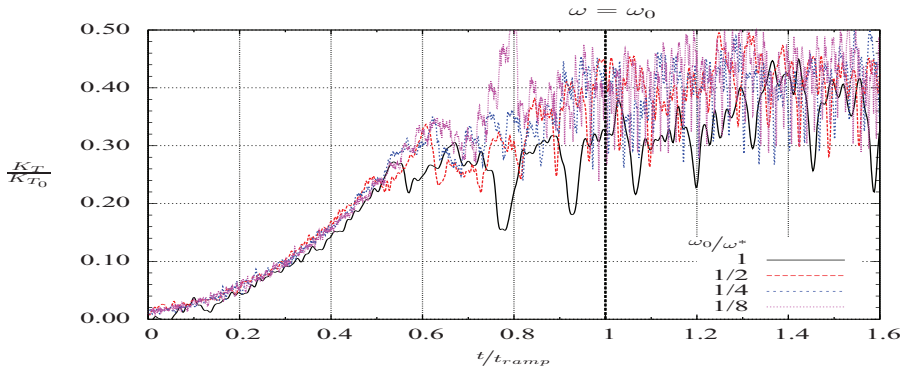
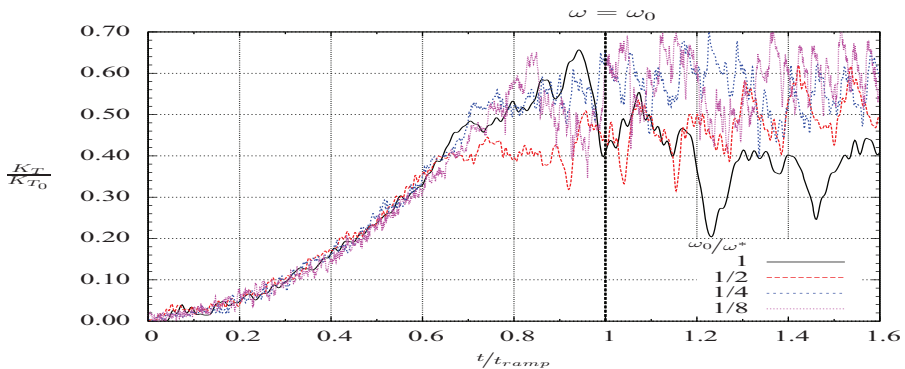
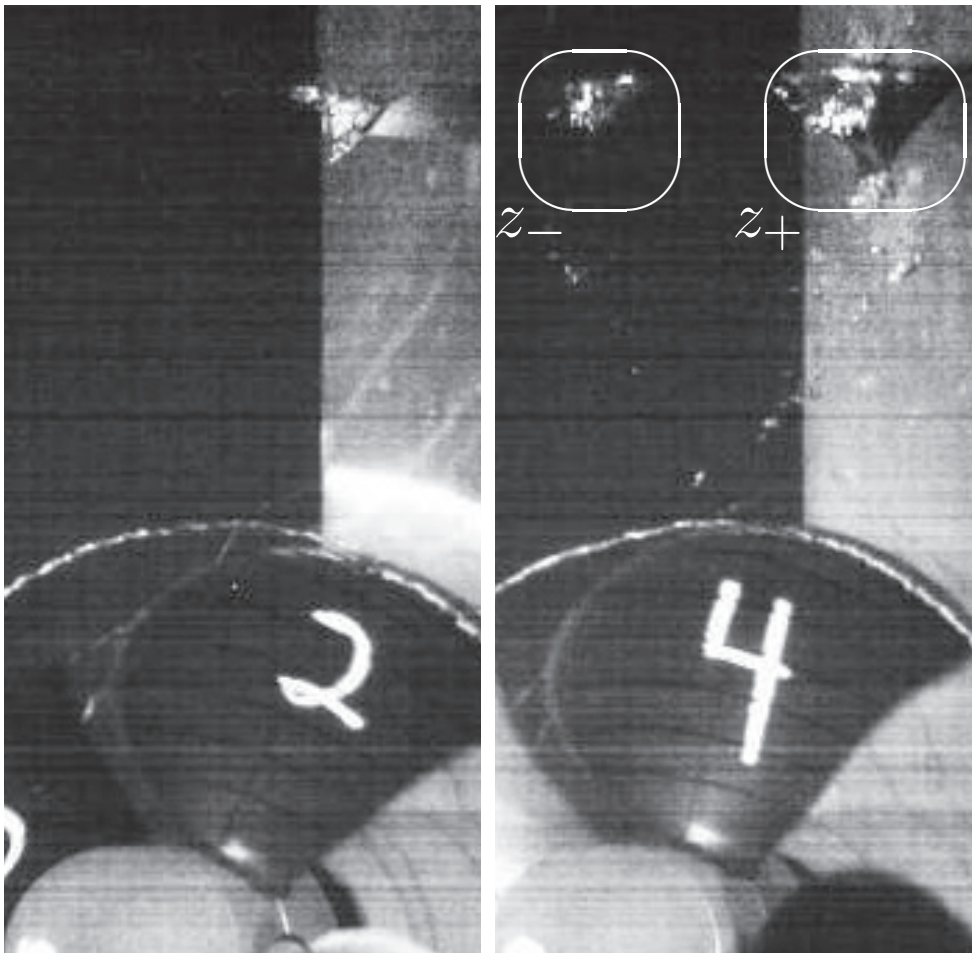
(a)  $J = 0.075$ .(b)  $J = 0.133$ .

Figure 4.43: Thrust ratio as function of time divided by the time  $t_{ramp}$  needed to reach constant rotation rate  $n_0$  [ $h/R = 1.4$ ].

#### 4.5.2 Vortex formation

As described in Chapter 2, ventilation by vortex formation is a phenomenon intrinsically random, and is very sensible to variations of the external flow. Nevertheless, from the images recorded during the experiments, some general characteristics and tendencies of the vortex system could be observed. For brevity, we will define  $z_+$  the vortex rotating along  $+z$  and  $z_-$  the vortex rotating along  $-z$ .

- For very deep water depths, the  $z_+$  vortex tends to be located on the port side, while the  $z_-$  vortex starboard.
- At intermediate submergences the formation of the  $z_-$  vortex is no longer observed, while the  $z_+$  vortex moves towards the mid  $y$ -plane and becomes stronger.
- As a general trend, the  $z_+$  vortex occurs more often, with stronger intensity, longer duration and higher air content.

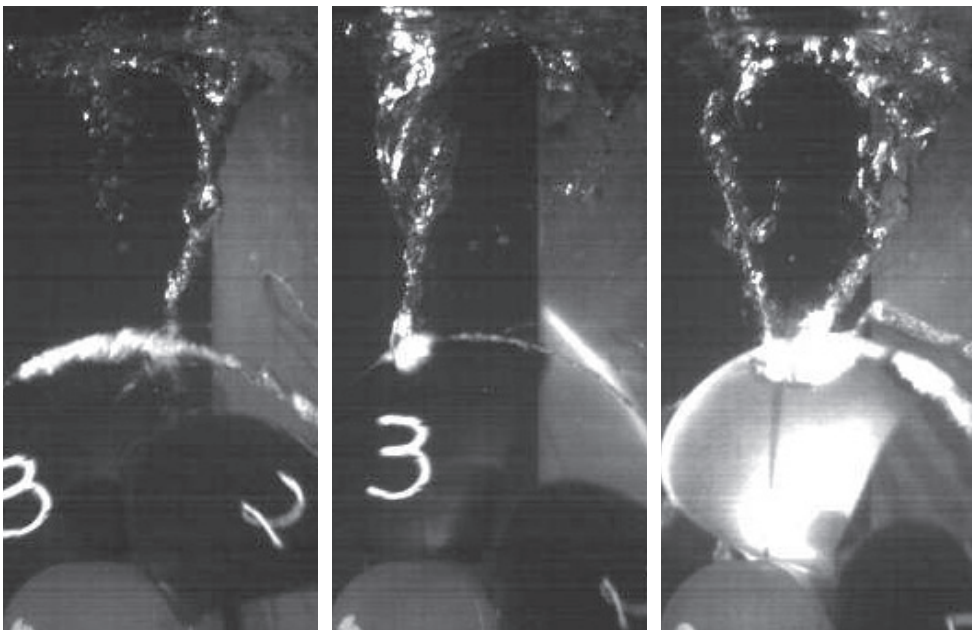


(a) Formation of the  $z_+$  vortex on the port side,  $t = 4.8137$  s. (b) Formation of the  $z_-$  vortex on the starboard side,  $t = 5.0971$  s.

Figure 4.44: Free-surface vortex formation [ $h/R = 2.04$ ,  $J = 0.075$ ,  $\Delta p/p_0 = 3.2\%$ ].

The formation of the  $z_+$  vortex on the port side can be observed in Figure 4.44a, while its further growth and the formation of a counter-rotating  $z_-$  vortex starboard is depicted in Figure 4.44b. They form together a vortex-pair, with an axial velocity between them in the direction of the propeller motion (opposite to the free-stream velocity). This is in agreement with the results obtained by Brix et al. (2000) for the formation of a ground vortex-pair at low velocity ratio  $U_i/U_\infty$  (axial velocity at the propeller plane divided by free-stream velocity).

Instantaneous pictures of the impact of the free-surface vortex on the propeller blades are depicted in Figure 4.45, for the  $z_+$  vortex (Figure 4.45a), the  $z_-$  vortex (Figure 4.45b) and the contemporary action of both (Figure 4.45c). The vortex system shown in the last picture resembles a horse-shoe type vortex, similar to the instantaneous flow field obtained by Secareanu et al. (2005) simulating the ground vortex of an air-intake using LES.



(a) Impact of the  $z_+$  vortex on the blade,  $t = 5.497$  s. (b) Impact of the  $z_-$  vortex on the blade,  $t = 10.307$  s. (c) Impact of both vortices on the blade,  $t = 10.649$  s.

Figure 4.45: Impact of the free-surface vortex [ $h/R = 2.04$ ,  $J = 0.075$ ,  $\Delta p/p_0 = 3.2\%$ ].

The time evolution of the thrust ratio is shown in Figure 4.46, for the blade and the entire thruster. At a submergence greater than the propeller diameter—thus with a propeller-tip clearance greater than the propeller radius—, during a 10

s period the propeller is experiencing several ventilation events where the thrust drops down to 70% of its nominal value (Figure 4.46a).

The thrust loss occurring around 10.65 s is enlarged in Figure 4.46b, where the time instant corresponding to Figure 4.45c (impact of a horse-shoe vortex) is also displayed. The blade thrust oscillates with the shaft frequency, being subject to thrust losses at each passage around 0 deg. It is interesting to notice that the thrust of the propeller oscillates for a limited time period with the same shaft frequency. Following oscillations are as expected at the blade frequency, where the effect of the free-surface vortex is felt by the propeller at the passage of each blade.

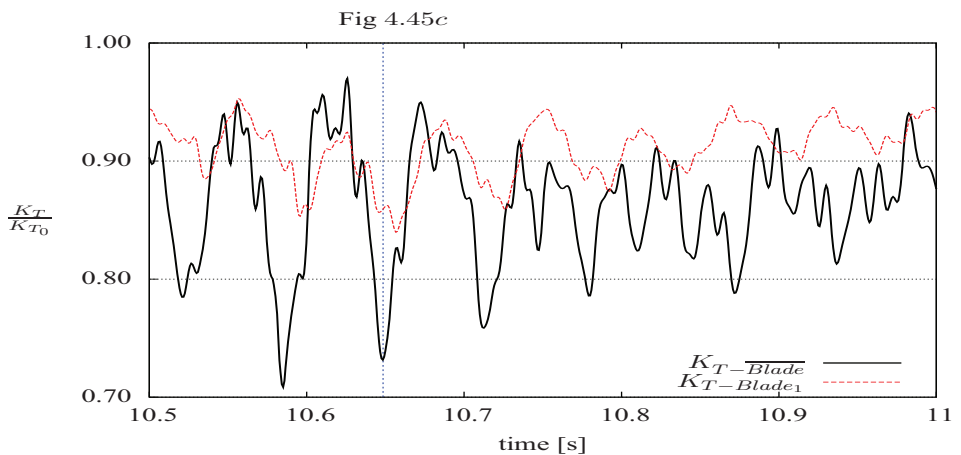
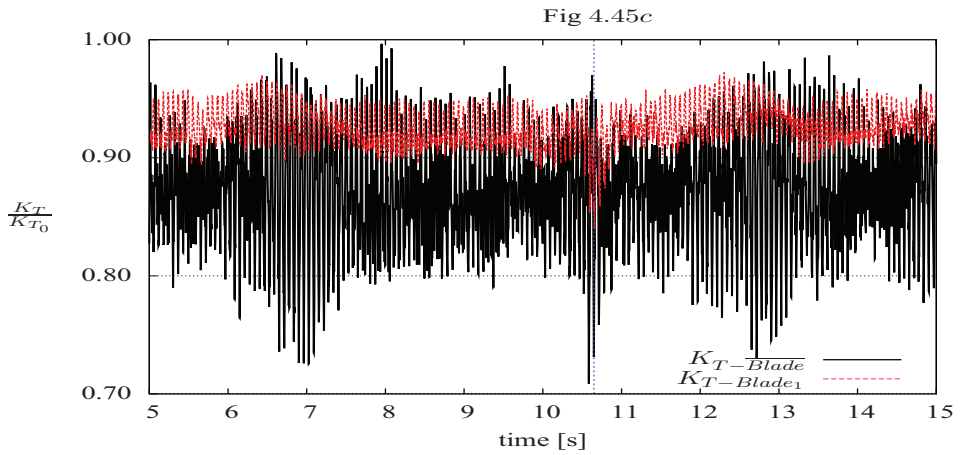


Figure 4.46: Time evolution of the thrust ratio of *Blade*<sub>1</sub> and the whole propeller [ $h/R = 2.04$ ,  $J = 0.075$ ,  $\Delta p/p_0 = 3.2\%$ ].

It was explained in Chapter 2 that ground (and analogous free-surface) vortices are created from the amplification of the local ambient vorticity due to vortex stretching. The preponderance of the  $z_+$  vortex could be ascribed to the higher  $+z$ -vorticity content on the free surface. This could be generated by the presence of the tip vortices, whose intensity is maximum at the blade and is then dissipated while traveling downstream. The blade passing starboard would then create on the free surface stronger  $+z$ -vorticity with respect to the  $-z$ -vorticity generated by the blade passing the port side.

## 4.6 Summary

The presented results have shown that ventilation depends on the propeller submergence, loading and advance ratio. The combination of these parameters determines the nature of the ventilation mechanism, (*i*) at deeper submergences through a free-surface vortex and (*ii*) at moderate submergences through the blade itself piercing the free-surface.

Using the thrust envelopes, three different ventilation regimes could be identified, depending on the influence of the above mentioned mechanisms.

- *Free-surface vortex*  
characterized by severe and discontinuous thrust losses occurring when the vortex reaches the blade wall; the amplitude during a ventilation event can deviate significantly from the mean value, which is slightly lower than the nominal one.
- *Surface-piercing*  
characterized by uniform thrust losses during the complete revolution; the thrust encompasses a narrow amplitude range around the mean value, which is in turn significantly lower than the nominal one.
- *Intermediate*  
where both mechanisms (*i*) and (*ii*) act alternately during the same test case; the thrust encompasses a broad and uniform amplitude range and the mean value is somewhere in between those found in the previous two regimes.

# Chapter 5

## Numerical simulations

### 5.1 Numerical method

#### 5.1.1 Solver

The commercial RANS code `Fluent` has been used to solve the viscous, incompressible, two-phase (air and water) flow. This solver is one of the most used in CFD for a wide variety of applications, for which validation cases are documented (Fluent, 2006).

The choice of this solver is also given by the fact that it is used within the Rolls-Royce (RR) University Technology Centre (UTC), to which the present research is connected. Within this framework, the present work aims at testing the capabilities of the solver to resolve the complex flow features around a ventilating propeller.

#### 5.1.2 Grid

The grid is fully unstructured in the rotating domain, with a superimposed prismatic layer close to the walls, in order to better capture the boundary layer (Rhee and Joshi, 2006). Prisms are extruded upstream and downstream the rotating domain, whereas the remaining cells are fully structured. A total of about 2.35 million cells was used, most of them located around the propeller and across the interface between the two phases. A typical size for the cell at the free surface is 5 mm, 2% of the propeller diameter (Figure 5.1b). An ensemble view of the grid used on the domain's boundaries is shown in Figure 5.1a.

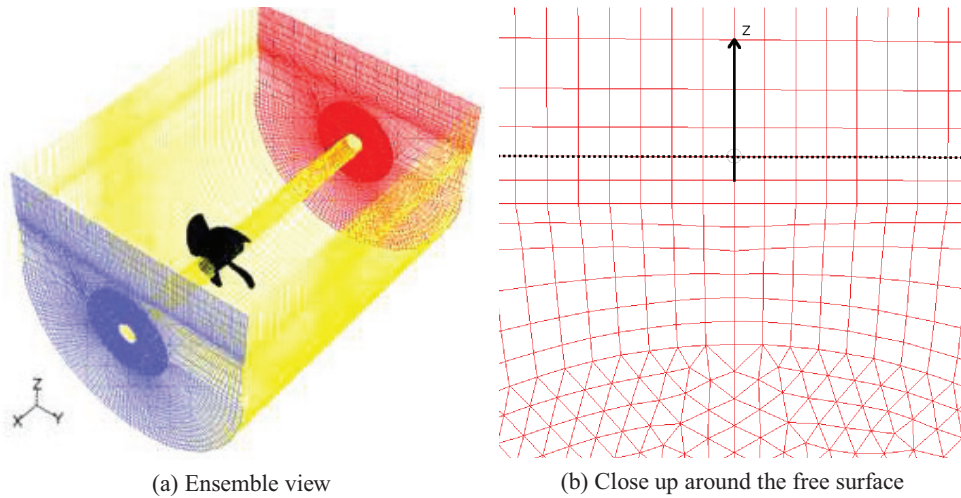


Figure 5.1: Numerical domain.

A closer view of the mesh topology on the blade can be seen in the previously shown Figure 3.14b.

### 5.1.3 Boundary conditions

The undisturbed free-surface elevation is assigned both at the inlet and outlet boundaries. At the inlet the free-stream velocity is also specified. A zero flux of all quantities is enforced across the top and bottom boundaries. A no-slip condition is set on the walls.

### 5.1.4 Turbulence

While a SST  $k - \omega$  model (Menter, 1994) was used in open water conditions, turbulence was removed when simulating the free-surface flow. Performing a laminar computation helped reducing the computational time, and such an approximation is deemed as of minor importance for the present study, where pressure drop is the dominating mechanism leading to ventilation. However, the effect of turbulence can be important after ventilation inception, in the formation/destruction of air bubbles, and in the adhesion of the entrained air to the walls. A simulation including turbulence was thus performed in order to analyze its effect, that will later be presented among the other results.

### 5.1.5 Solution of the Navier-Stokes equations

If the density of a fluid element does not change in time as it moves through space the flow is said to be incompressible. As a consequence, there is no equation of state for pressure, which must be consistent with a velocity field satisfying the zero-divergence condition (continuity equation).

$$\nabla \cdot \vec{U} = 0 \quad (5.1)$$

The momentum equation in the Navier-Stokes (N-S) equations can be expressed in the form:

$$\frac{\partial \vec{U}}{\partial t} + (\vec{U} \cdot \nabla) \vec{U} = -\frac{1}{\rho} \nabla p + \nu \nabla^2 \vec{U} \quad (5.2)$$

The momentum equation is solved with a second order upwind scheme. The Body Force Weighted (BFW) discretization algorithm is used to interpolate the node values of the pressure from the cell values, as required by the solver. The pressure-velocity coupling is achieved using a Semi-Implicit Method for Pressure-Linked Equations (SIMPLE) algorithm. A first order implicit scheme is used to follow the time evolution.

The free surface evolution is handled using an implicit formulation of the Volume Of Fluid (VOF) method with a modified High Resolution Interface Capturing (HRIC) scheme. Surface tension is neglected, but its effect will be verified later in this section.

Further details about the solver can be found in the Fluent manual (Fluent, 2006).

#### 5.1.5.1 Pressure-velocity coupling

The pressure-velocity coupling in the discretized form of the N-S equations is solved with a SIMPLE scheme. A complete derivation of the method can be found in McDonough (2007), whereas only the aspects relevant to the present dissertation will be described here.

The basic assumption employed in constructing the SIMPLE algorithm is that at any given time step the generic flow variable  $\phi$  can be expressed as  $\phi = \phi^* + \phi'$ , where  $\phi^*$  denotes an initial estimate, and  $\phi'$  represents a correction. Formally, all parts of these decompositions are functions of both space and time. Substituting the decomposed variables into the N-S equations and after some manipulation, a solution for the momentum equations can be found using pressure at the current time level  $k$ . However, this solution will not lead to mass conservation at time level  $k + 1$ , and a Pressure Poisson Equation (PPE) for the correction pressure is developed in order to obtain a divergence-free velocity field.

$$\Delta p' = \frac{\nabla \cdot \vec{U}^*}{\Delta t} \quad (5.3)$$

Once  $p'$  has been calculated the pressure and velocity components can be updated.

$$p^{k+1} = p^k + p' \quad (5.4a)$$

$$u_\ell^{k+1} = u_\ell^* - \frac{\partial p'}{\partial x_\ell} \Delta t \equiv u_\ell^* + u'_\ell \quad (\ell = 1, 2, 3) \quad (5.4b)$$

The analysis carried out with the continuous equations does not translate into the discrete numerical algorithm SIMPLE in a completely direct way. Carrying out the derivation in terms of discrete equations can produce results that are rather different from those obtained by merely discretizing the continuous Partial Differential Equations (PDEs). The discrete momentum equations are consistent with the continuous N-S equations up to possible errors in the pressure correction term, which is not necessarily the true physical pressure. A divergence-free velocity field is usually achieved only when steady-state is reached. Assuming the solution to be steady-state within the same time-step, a large number of iterations would in practice lead to the physical solution. Among other difficulties, the pressure corrections at each iteration do not satisfy the boundary conditions for physical pressure.

These characteristics make the SIMPLE scheme different from typical projection methods (Bell et al., 1989; Gresho, 1990), where at each time-step the divergence-free condition is satisfied by the only iteration performed to solve the PPE.

The updates needed to proceed from one iteration to the next during a (pseudo) time step can be rewritten in 2D in the discrete form:

$$p_{i,j}^{k+1} = p_{i,j}^k + \alpha_p p'_{i,j} \quad (5.5a)$$

$$u_{i,j}^{k+1} = u_{i,j}^* + \alpha_u \frac{\Delta t}{A_{i,j}^u \Delta x} (p'_{i,j} - p'_{i+1,j}) \quad (5.5b)$$

$$v_{i,j}^{k+1} = v_{i,j}^* + \alpha_v \frac{\Delta t}{A_{i,j}^v \Delta x} (p'_{i,j} - p'_{i,j+1}) \quad (5.5c)$$

where  $A_{i,j}^{u_\ell}$  are nontrivial additional factors due to the discretization process, contributing to the numerical performance of SIMPLE being rather different from that of typical projection methods. In 2D, for the  $u$  and  $v$  velocities,  $A_{i,j}^u$  and  $A_{i,j}^v$  can be expressed as:

$$A_{i,j}^u = 1 + 4 \frac{\nu \Delta t}{\Delta x} + \frac{\Delta t}{2 \Delta x} \left( \tilde{u}_{i,j}^k - \tilde{u}_{i-1,j}^k + \tilde{v}_{i,j+1}^k - \tilde{v}_{i,j}^k \right) \quad (5.6a)$$

$$A_{i,j}^v = 1 + 4 \frac{\nu \Delta t}{\Delta x} + \frac{\Delta t}{2 \Delta x} \left( \bar{u}_{i,j}^k - \bar{u}_{i-1,j}^k + \bar{v}_{i,j+1}^k - \bar{v}_{i,j}^k \right) \quad (5.6b)$$

where “ $\tilde{\cdot}$ ” and “ $\bar{\cdot}$ ” correspond to horizontal (along index  $i$ ) and vertical (along index  $j$ ) averages.

The coefficients  $\alpha_s$  are Under-Relaxation Factors (URF) with values in the range  $0 < \alpha \leq 1$ . There is no theoretical underpinning to suggest specific values to be assigned, but values between 0.5 and 0.8 usually work and are thus widely used. Smaller values are sometimes needed in order to achieve a stable solution.

An optimum relation between the URFs for velocity and pressures was derived by Raithby (1979) and Ferziger and Perić (2002), based on the assumption that a steady solution is found iterating for an infinite time step.

$$\alpha_p = 1 - \alpha_{u_\ell} \quad (\ell = 1, 2, 3) \quad (5.7)$$

The presence of the URFs shows that a single iteration can not produce a divergence-free velocity field, because they do not appear in the discrete Laplacian being solved for  $p'$ , unless  $\alpha_{u_\ell}$  are equal to unity. But this does not usually lead to convergence of the overall SIMPLE algorithm, so it is necessary to reduce the values of the URFs.

Barron and Neyshabouri (2003) have investigated the effects of changing under-relaxation factors for different variables, convective schemes and grid sizes on turbulent flow simulations. Their work concludes with the definition of a safe range of URFs—such to obtain a non-divergent solution—and a recommended range for fast convergence.

There is another aspect associated with the form of convergence test employed, which reflects the pseudo-time nature of the algorithm. During each pseudo-time step it is not effective to perform iterations until divergence is reduced to a small absolute value. Rather, a relative convergence criterion is used within individual pseudo-time steps, along with a smaller overall tolerance. But even this smaller tolerance is in practice often fairly large—say,  $\mathcal{O}(10^{-3})$  or larger.

The Pressure-Implicit with Splitting of Operators (PISO) pressure-velocity coupling scheme is based on the SIMPLE algorithm, but performs two additional corrections to improve the efficiency of this calculation: neighbor correction and skewness correction. As a common practice, SIMPLE is used for steady-state calculations, while PISO for transient problems.

Barton (1998) has compared SIMPLE- and PISO-type algorithms for transient flows. Overall the PISO scheme was found to predict accurate results and was robust. However, for small time step values, alternative schemes based on SIMPLE can predict accurate results for approximately half the computational cost.

## 5.2 Fully-ventilating propeller

The experimental results presented in Chapter 4 have shown a large deviation among different revolutions within the same test case, even for a fully-ventilating

propeller. Although the ventilation phenomenon is strongly unstable and time-dependent, some recurring characteristics could be observed.

Numerical simulations were thus attempted with the aim to investigate these characteristics, aiming at explaining qualitatively the dynamic loads occurring during ventilation.

### 5.2.1 Multiple Reference Frame

The free-surface deformation obtained using the Multiple Reference Frame (MRF) model is shown in Figure 5.2, where the blade walls are colored with air-volume fraction. The MRF model converges to a steady solution. Although the phenomenon is inherently unsteady, the main features observed during the experiments are captured by this model; air is sucked down from the free-surface and transported through the propeller rotation for more than a half revolution.

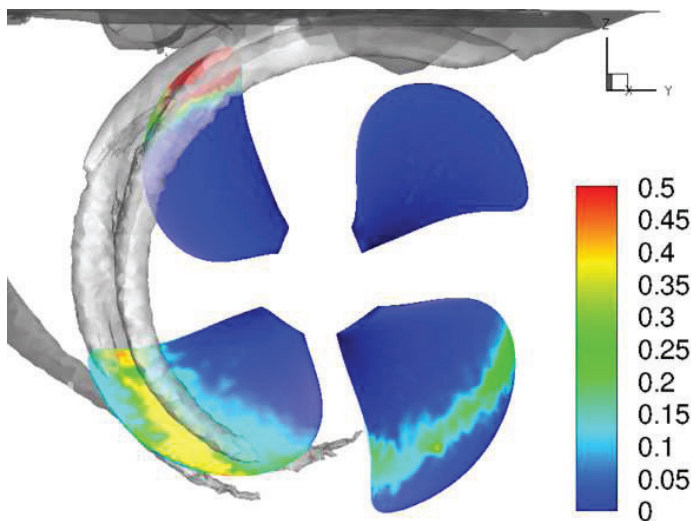


Figure 5.2: Free-surface deformation, blades colored with air-volume-fraction [ $h/R = 1.4$ ; MRF model].

The air-volume-fraction contours on the propeller surfaces are shown in Figures 5.3 (a) and (b), for the suction and pressure side, respectively. Air is sucked from the free surface, covering with air the suction side of the blade tip at  $\pi/4$ . Due to the low axial velocities existing on the tip at this high propeller loading, air is unable to escape downstream and is transported from the propeller along its rotation. Residuals of air are visible on the following blades, at  $3/4 \pi$  and  $5/4 \pi$ , both on the suction and pressure side. The last blade at  $7/4 \pi$  seems not to be invested

by the entrained air, differently from what it was observed during the experiments, where air was present all around the propeller disc.

The corresponding contours of the pressure coefficient, computed as  $\frac{p-p_\infty}{0.5\rho(nD)^2}$ , are shown in Figure 5.4. The pressure on the suction side is higher—with respect to open water conditions—during the first half revolution, due to the presence of air. Differences in pressure between blades at different angular positions are barely visible on the pressure side.

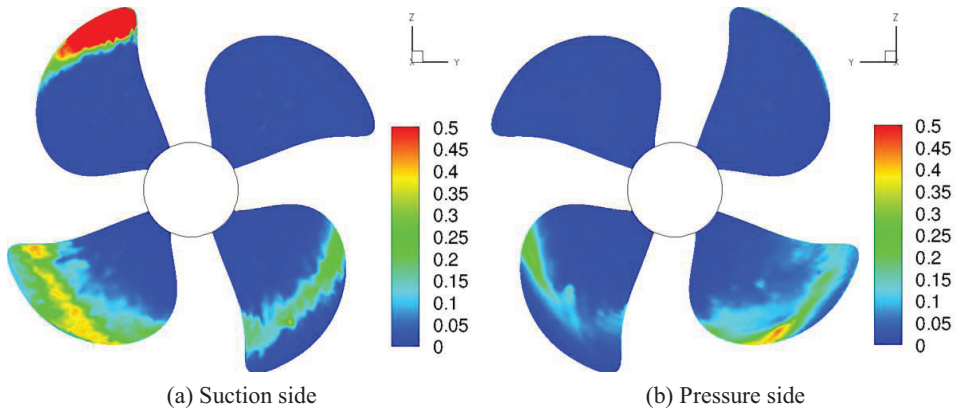


Figure 5.3: Air-volume-fraction contours during ventilation [ $h/R = 1.4$ ; MRF].

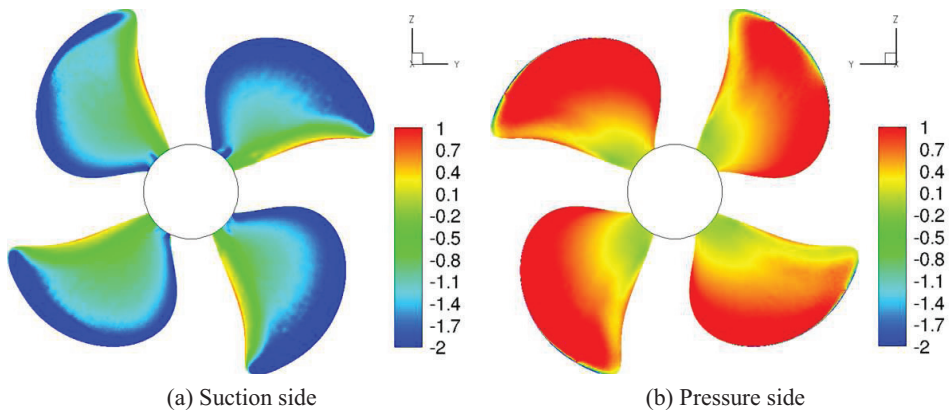


Figure 5.4: Pressure coefficients contours during ventilation [ $h/R = 1.4$ ; MRF].

The resulting thrust coefficient  $N \cdot K_T$  is written in Table 5.1, where the losses due to ventilation can be read. These are generally smaller than those found in the

experiments, where thrust losses up to 60% of the infinite fluid case are obtained.

Ang. position [rad]	Pressure Side	$\Delta\%$	Suction Side	$\Delta\%$	Propeller	$\Delta\%$
$1/4 \pi$	0.15	-26.7%	0.26	-32.0%	0.41	-30.2%
$3/4 \pi$	0.13	-35.2%	0.31	-21.3%	0.43	-26.0%
$5/4 \pi$	0.17	-13.9%	0.37	-5.8%	0.54	-8.5%
$7/4 \pi$	0.19	-5.7%	0.38	-1.9%	0.57	-3.2%

Table 5.1: Thrust coefficient  $N \cdot K_T$  and relative deviation with respect to the open water results  $K_{T_0}$  [ $h/R = 1.4$ , MRF model].

### 5.2.2 Sliding Mesh

The MRF model has shown a good representation of the ventilation phenomenon, although losses are underestimated. In order to handle the unsteady nature of the phenomenon, a Sliding Mesh (SM) model was adopted. The results presented in the remainder of this section were obtained using only the SM model. After the deformation of the free surface, the simulation becomes soon unstable, showing an increase of the residual error for the solved equations. This behavior would in most cases lead to divergence of the numerical solution, which could be stabilized only by reducing the URFs for the solved equations.

A stable solution was reached using  $\alpha_p = 0.1$ ,  $\alpha_{u_\ell} = 0.2$ ,  $\alpha_\gamma = 0.2$  and the thrust ratio obtained during several revolutions is shown in Figure 5.5, for the single blade (a) and the whole propeller (b).

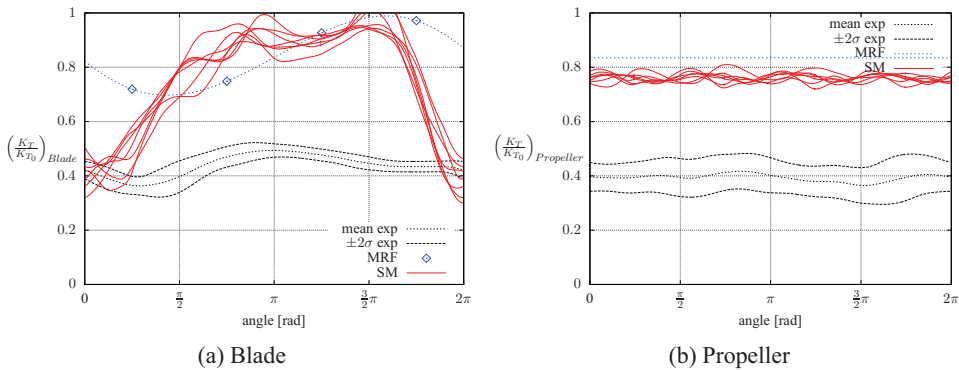


Figure 5.5: Thrust ratio averaged for each angular position [ $h/R = 1.4$ ;  $\alpha_p = 0.1$ ,  $\alpha_{u_\ell} = 0.2$ ,  $\alpha_\gamma = 0.2$ ].

Results from the corresponding experiments are shown by means of the average curves and those at  $\pm 2\sigma$ . As for  $\alpha_p$  and  $\alpha_{u\ell}$ ,  $\alpha_\gamma$  is the URF for the update of the volume-fraction  $\gamma$ .

The propeller thrust losses due to ventilation are under-estimated by about 50% with respect to the experimental data, but the unsteady approach applied with the SM model slightly improved the results obtained with the MRF model, shown in the same figure.

The blade thrust is over-estimated at all angles, except around its upright position, where the agreement with the experimental results is satisfactory. The improvement obtained with respect to the MRF model can also be observed around 0 rad.

The pressure coefficients on the suction side of the blade are shown in Figure 5.6, in steps of  $\pi/4$  rad, and compared with the open water results (Figure 5.6e).

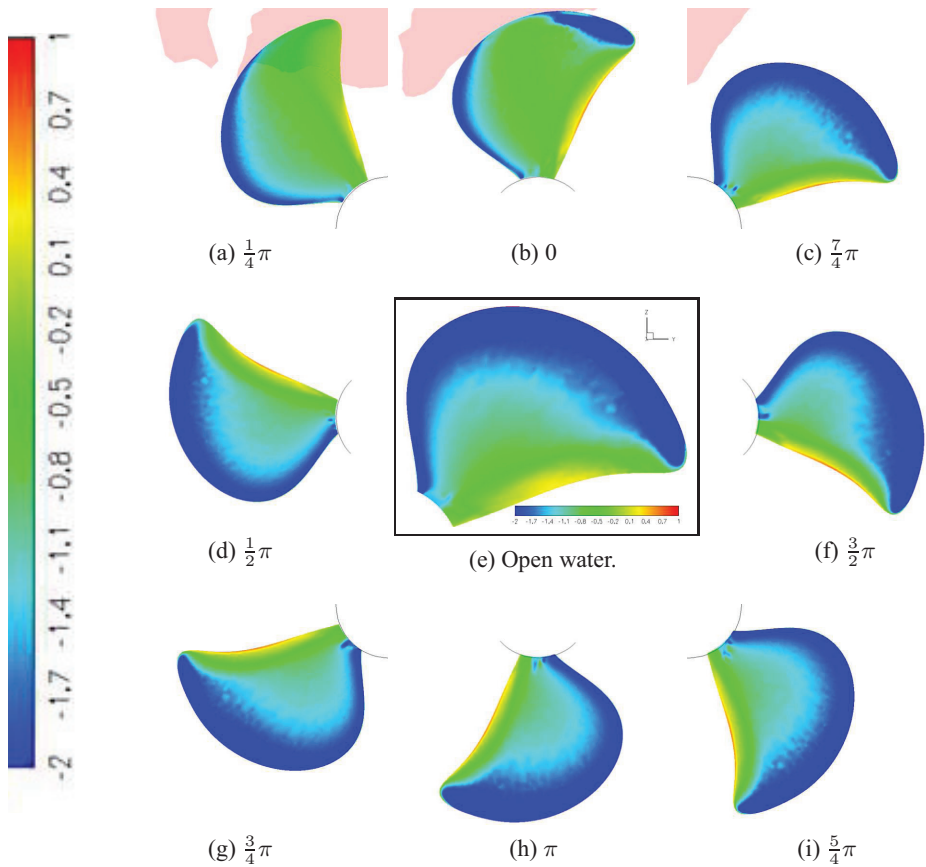


Figure 5.6: Pressure coefficient on the suction side at various angular positions, comparison with open water [ $h/R = 1.4$ ;  $\alpha_p = 0.1$ ,  $\alpha_{u\ell} = 0.2$ ,  $\alpha_\gamma = 0.2$ ].

Air above the free-surface on the propeller plane is visible in the three up-most pictures (Sub-figures (a), (b) and (c)).

The effect of the free-surface is visible only at 0 and  $\pi/4$  rad, where the tip region of the blade shows higher contours of pressure. The lowest levels are achieved at  $\pi/4$  rad, confirming the results obtained in Figure 5.5a.

The corresponding pressure coefficients on the pressure side are shown in Figure 5.7, where the blade tip at 0 and  $\pi/4$  rad show lower contours of pressure.

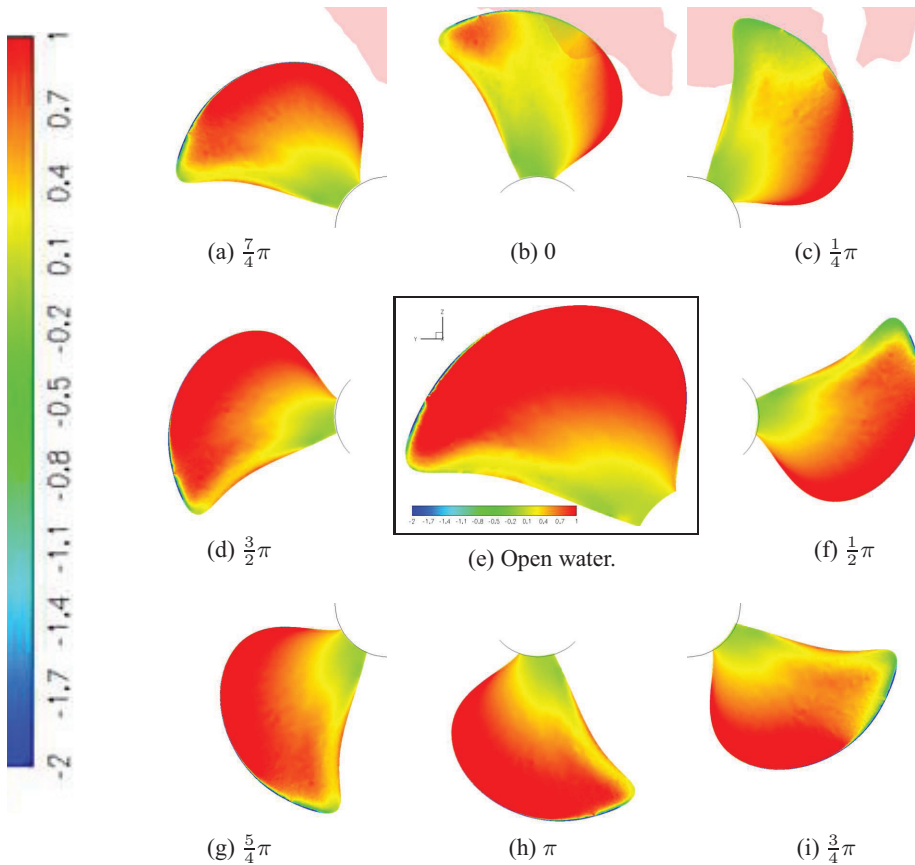
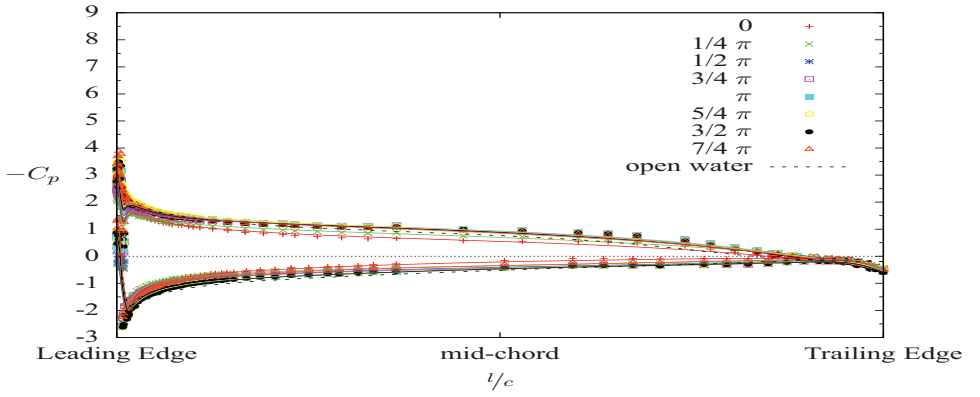
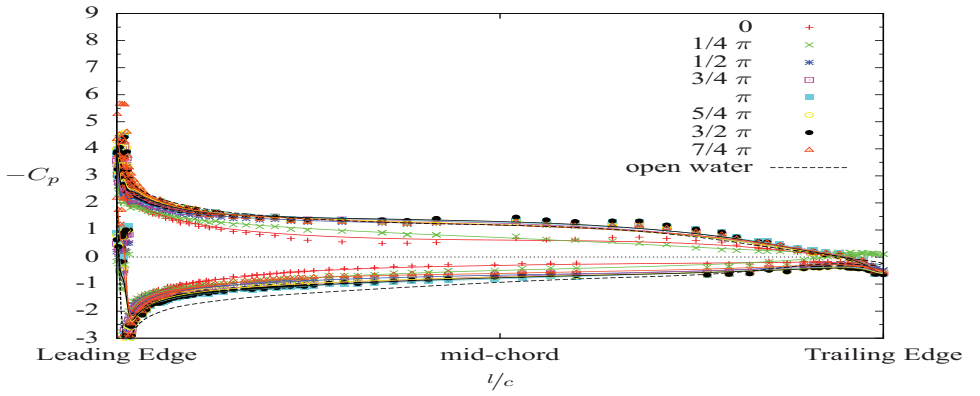


Figure 5.7: Pressure coefficient on the pressure side at various angular positions, comparison with open water [ $h/R = 1.4$ ;  $\alpha_p = 0.1$ ,  $\alpha_{u_\ell} = 0.2$ ,  $\alpha_\gamma = 0.2$ ].

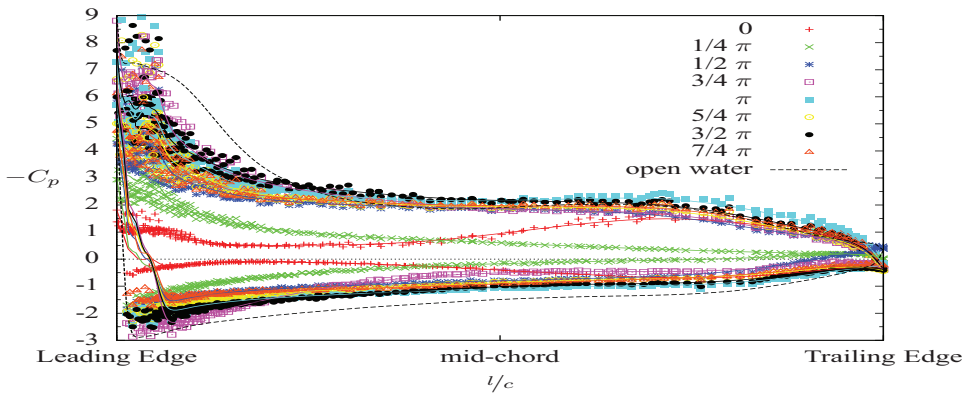
Figure 5.8 shows the pressure coefficient along the chord-line on three radial stations—0.5, 0.7 and 0.9 of the radius represented respectively in Sub-figures (a), (b), and (c)—and along the radius on the blade axis line (Figure 5.9).



(a)  $r/R = 0.5$



(b)  $r/R = 0.7$



(c)  $r/R = 0.9$

Figure 5.8: Pressure coefficients at various stations and angular positions [ $h/R = 1.4$ ;  $\alpha_p = 0.05$ ,  $\alpha_{u_\ell} = 0.1$ ,  $\alpha_\gamma = 0.1$ ].

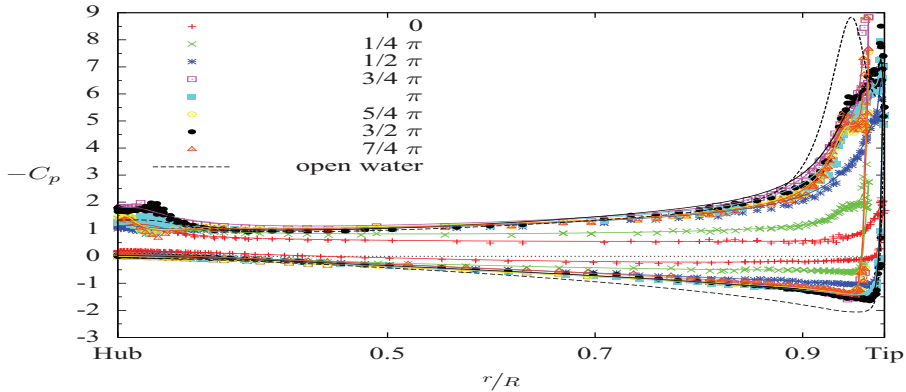


Figure 5.9: Pressure coefficients along the blade axis [ $h/R = 1.4$ ;  $\alpha_p = 0.05$ ,  $\alpha_{u_\ell} = 0.1$ ,  $\alpha_\gamma = 0.1$ ].

The plotted lines are spline interpolations between the given points. All the stations present a general reduction (in absolute value) of the pressure with respect to open water, but only for the blades at  $0$  and  $\pi/4$  (red and green lines in Figures 5.8 and 5.9) this behavior appears remarkable. This reduction is stronger on the suction side and most localized around the tip region, above 50% of the radius. At 90% of the radius (Figure 5.8c) the blade at  $0$  is subject to a pressure drop extending from the leading edge to the mid-chord line, whereas at  $\pi/4$  pressure has dropped along the entire chord-line.

Figure 5.10 presents the contours of air-volume-fraction for the present case.

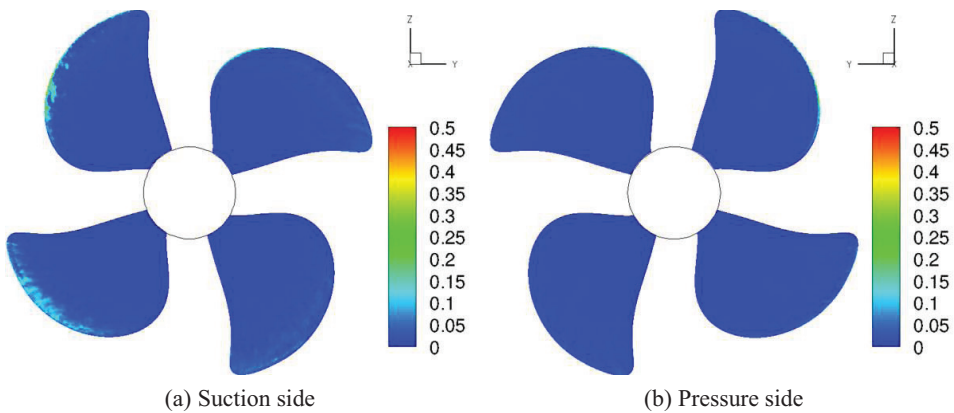
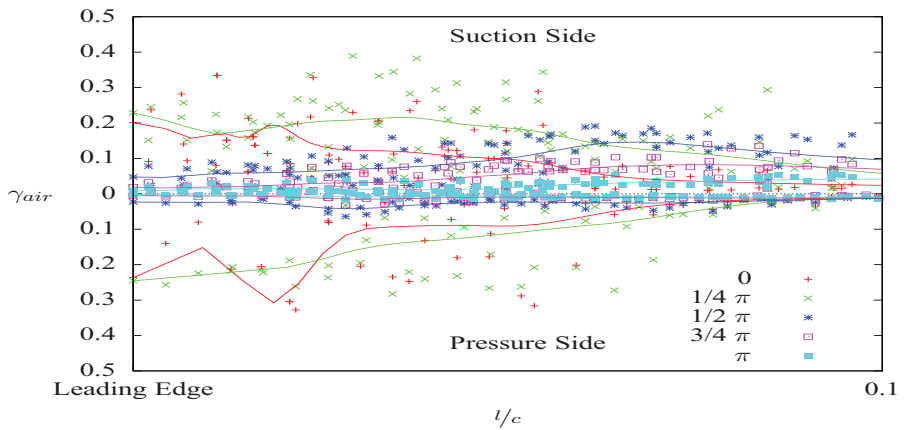


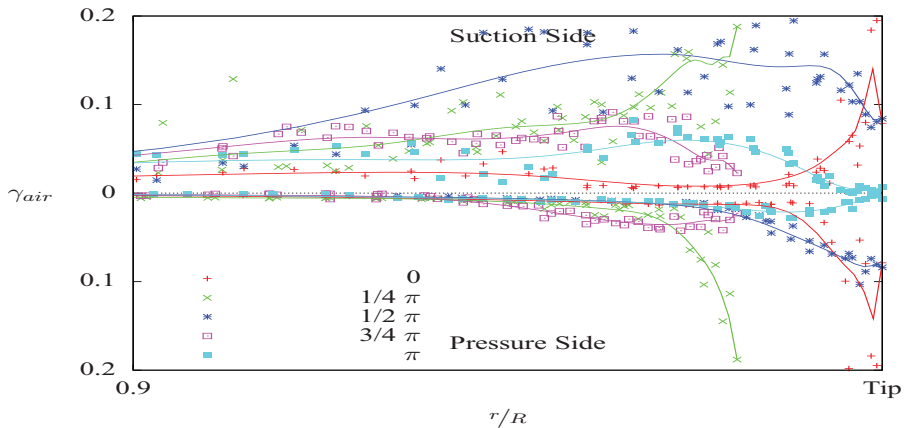
Figure 5.10: Air-volume-fractions contours during ventilation [ $h/R = 1.4$ ;  $\alpha_p = 0.1$ ,  $\alpha_{u_\ell} = 0.2$ ,  $\alpha_\gamma = 0.2$ ].

Recalling Figure 5.3 obtained with the MRF model, the SM model presents much lower air-contents on the propeller walls. This difference could be ascribed to the fact that the SM model studies the problem as unsteady and a longer simulation time could be necessary for the air to adhere to the propeller walls with respect to the computational time examined (about 15 revolutions). On the other hand, thrust losses obtained with SM are larger.

The details of the air-volume-fraction around the tip region and the leading edge are shown in Figure 5.11, only for the blade during the first half revolution. The plotted lines are spline interpolations between the given points.



(a)  $r/R = 0.9$



(b) axis

Figure 5.11: Air volume fraction at various stations and angular positions [ $h/R = 1.4$ ;  $\alpha_p = 0.05$ ,  $\alpha_{u_\ell} = 0.1$ ,  $\alpha_\gamma = 0.1$ ].

Figure 5.12 shows the contours of  $z$ -vorticity on the free-surface. The tip vortex of the blade piercing the free-surface at  $\pi/4$  is imposing starboard a vorticity along  $+z$  (red levels in Subfigure (a)), whereas the corresponding vorticity is directed along  $-z$  on the port side (blue levels in Subfigure (b)).

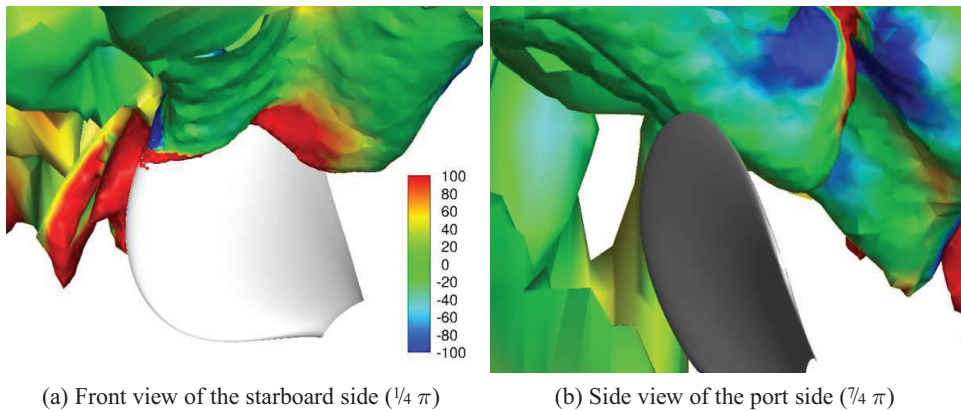


Figure 5.12: Vorticity contours along  $z$  on the free-surface [ $h/R = 1.4$ ;  $\alpha_p = 0.1$ ,  $\alpha_{u_\ell} = 0.2$ ,  $\alpha_\gamma = 0.2$ ].

### 5.2.3 Turbulence

The effect of turbulence was taken into account introducing a SST- $k-\omega$  turbulence model. Adding turbulence to the given set of equations had the effect to make the simulation unstable, leading often to the divergence of the numerical solution. The thrust coefficient is compared in Figure 5.13 with the corresponding results obtained neglecting the turbulence terms. The solution including turbulence shows a single revolution which was obtained further reducing the URFs in order to help improve convergence. The effect of changing the URFs will be extensively covered in a later section. With the obtained results, turbulence does not seem to affect the global loads the propeller is subject to. However, results including turbulence have not reached a stable oscillatory solution, thus a more consistent comparison should be made having available several revolutions including turbulence.

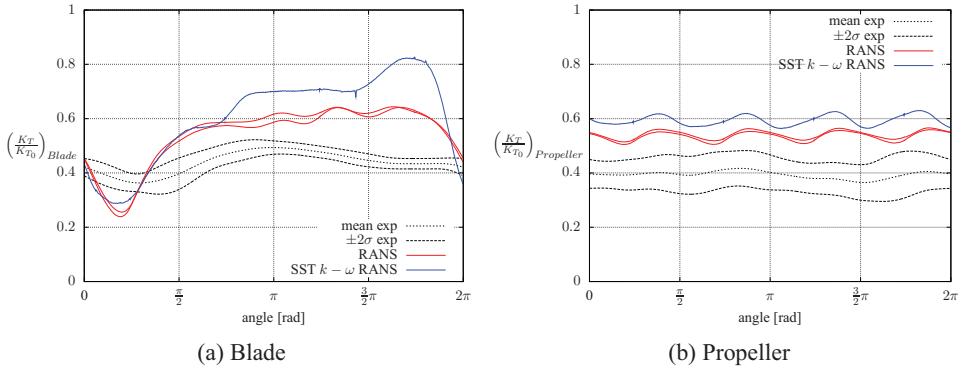


Figure 5.13: Thrust ratio averaged for each angular position [ $h/R = 1.4$ ;  $\alpha_p = 0.05$ ,  $\alpha_{u_\ell} = 0.1$ ,  $\alpha_\gamma = 0.1$ ].

### 5.2.4 Surface tension

The contribution to the pressure due to surface tension is proportional to the curvature of the free-surface location and thus implies the computation of a  $2^{nd}$  order derivative. This operation performed on a tetrahedral mesh can lead to inaccuracy, and eventually solution instability. Figure 5.14 shows a comparison of the thrust coefficient obtained with and without surface tension, where differences in terms of global loads between the two simulations are very small.

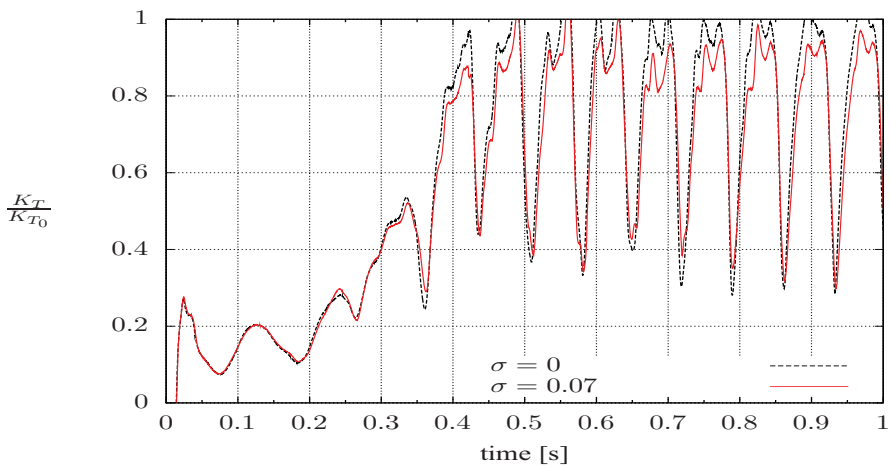


Figure 5.14: Effect of surface tension on the blade thrust ratio.

Its presence seems not to modify the obtained loads during ventilation, but it should be mentioned that simulations including surface tension are more unstable and tend promptly to diverge. Its effect can be important in the formation/destruction mechanism of bubbles from the air-sheet sucked from the propeller and in the formation of the free-surface vortex.

### 5.2.5 Grid refinement

A systematic verification of the grid used to perform the computations could not be performed, due to very long computational time. Each mesh refinement requires a subsequent reduction of the time-step for the stability of the solution, increasing the CPU time of a simulation to several weeks—between 4 and 12—, using a node with 16 processors. The grid size was then chosen according to the results obtained in open water, which obviously do not take into account the presence of the free-surface. In order to assess the effect of the grid size on the free-surface, the grid was refined once only in that part of the domain where the free-surface was expected to be located, as shown in Figure 5.15. With respect to a dynamic grid-refinement, this approach was deemed as more robust and less computationally expensive in this case, where the presence of the free-surface around the propeller is rather constant in space. The choice of a dynamic grid-refinement would have reduced the number of cells to refine, but certainly increased the operation of refinement and coarsening at each time step.

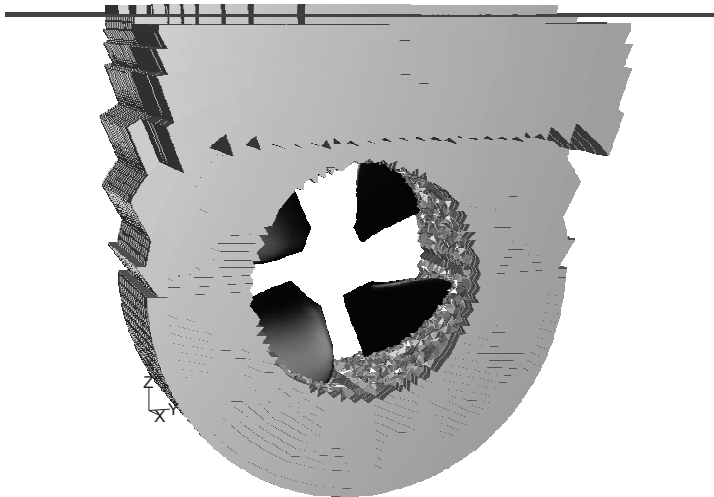


Figure 5.15: Refined region.

Figure 5.16 examines the influence of the described local grid-refinement, comparing the obtained thrust coefficient with the default mesh. The solution obtained with the refined grid presents a larger spreading, better approaching the experimental results. The improvements can be observed especially for the propeller thrust, indicating that the refined grid is able to better capture ventilation occurring on the deeper submerged blades. However, overall improvements are modest, and not such to fill the gap between the numerics and the experimental results. Due to the numerical difficulties connected to a simulation with a refined grid, in terms of computational resources and tuning of the numerical parameters, this mesh sensitivity study is not fully comprehensive, and the independence of the obtained solution can not be ensured.

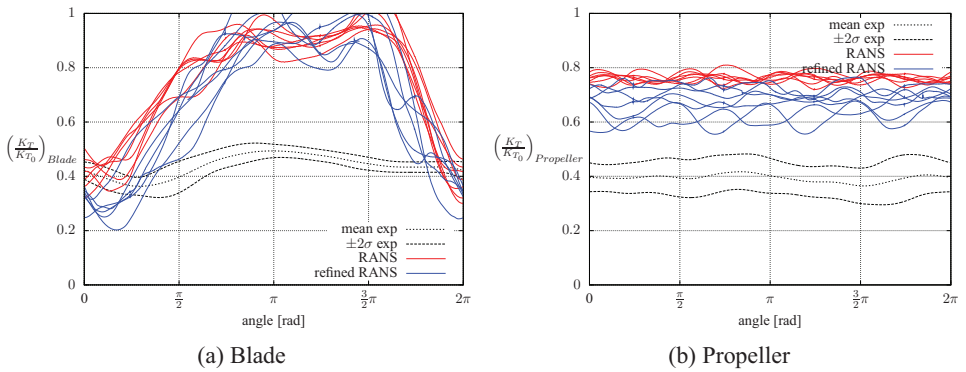


Figure 5.16: Thrust ratio averaged for each angular position, effect of local refinement [ $h/R = 1.4$ ;  $\alpha_p = 0.1$ ,  $\alpha_{u_\ell} = 0.2$ ,  $\alpha_\gamma = 0.2$ ].

### 5.2.6 Integration time-step

The choice of the integration time-step can change the computational time drastically, thus care was taken to use the highest value leading to a converged solution. The differences obtained changing the time step for the default, not-refined grid at a submergence ratio of 1.4 are plotted in Figure 5.17, and a time-step of  $1 \times 10^{-4}$  s was chosen, corresponding to about half degree of rotation for  $n = 14$  Hz. The differences between the curves with  $\Delta t = 1 \times 10^{-4}$  and  $5 \times 10^{-5}$  s are barely visible and the first time instants computed further reducing the time step seem also to follow the same trend. The results for those lower time steps— $\Delta t = 2 \times 10^{-5}$  and  $1 \times 10^{-6}$  s—are available for a shorter time interval due to the divergence of the numerical solution.

For the chosen time step, there are only 5 cells exceeding the cell Courant number of 40 required by the solver for a stable calculation (Fluent, 2006). The Courant

number is the ratio of the time step  $\Delta t$  to the characteristic convection time ( $\Delta x/u$  in 1D) which is required for a disturbance to be convected a distance  $\Delta x$ .

For a generic 3D domain, the local cell Courant number is defined by:

$$Co = \Delta t \frac{U_c}{L_c} \quad (5.8)$$

where  $U_c$  is the magnitude of the cell velocity and  $L_c$  the minimum cell edge length.

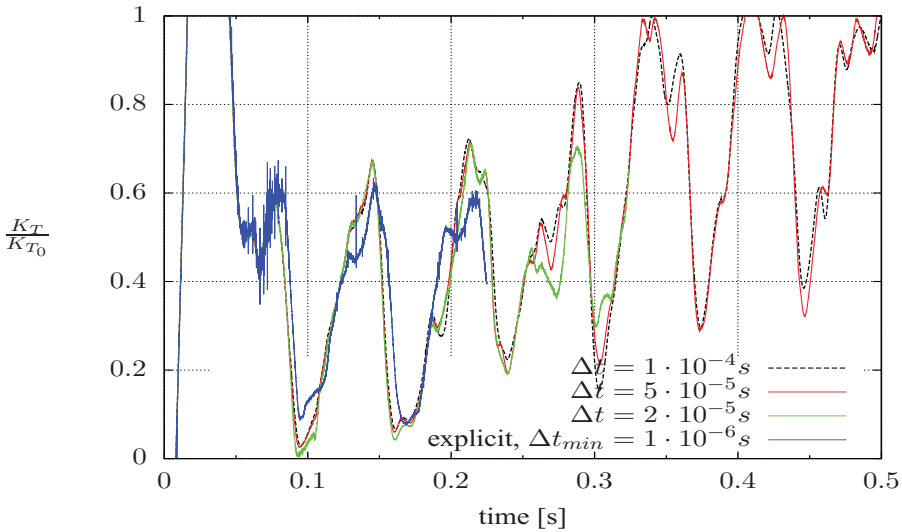


Figure 5.17: Effect of the chosen time-step on the blade thrust ratio [ $h/R = 1.4$ ].

Simulations have shown different converged solutions when varying the time-step size, requiring a further understanding of the obtained results.

The effect of the time-step size will be explained showing the results obtained while assessing its influence after refining the grid at  $h/R = 1.72$  (Figure 5.18). At this deeper submergence the blade at  $\pi$  rad, farther from the free surface, is completely wet, and should thus have a thrust very close to the open-water value  $K_{T_0}$ , except for the Wagner effect, which was described in Chapter 2, and consisting in a delay of the thrust build-up. Decreasing the time-step size by a factor of 10 has the effect of increasing the thrust by a factor of 2.

The values of maximum, i.e. non-ventilating, thrust coefficient  $N \cdot K_T$  on the pressure and suction side are reported in Table 5.2, with the relative error with respect to the open water results. Thrust is underestimated especially on the pressure side, which is still 20% below the open water value for the smallest time-step.

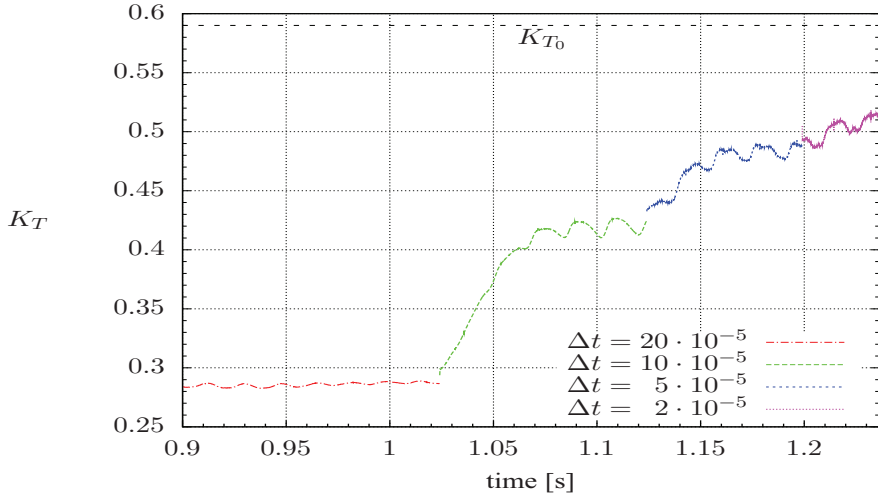


Figure 5.18: Comparison of the propeller thrust coefficient obtained using different integration time steps with the open water result  $K_{T_0}$  [ $h/R = 1.72$ , refined grid].

$\Delta t \cdot 10^5$ [s]	Pressure Side	$\Delta\%$	Suction Side	$\Delta\%$	Propeller	$\Delta\%$
20	-0.03	-117.2%	0.34	-11.9%	0.31	-47.4%
10	0.10	-50.2%	0.35	-9.5%	0.45	-23.2%
5	0.14	-27.0%	0.38	-2.6%	0.52	-10.9%
2	0.16	-19.5%	0.39	0.2%	0.55	-6.4%

Table 5.2: Thrust coefficient  $N \cdot K_T$  obtained varying the time step and relative error with respect to the open water results  $K_{T_0}$  [ $h/R = 1.72$ , refined grid].

For the solution obtained using this refined grid, a time-step of  $5 \times 10^{-5}$  s was chosen, mainly dictated by the computer's capacity. Values of the time step above  $5 \times 10^{-5}$  s seem inadequate to capture the characteristic convection time. About 200 cells located above the tip region of the blade exceed  $Co = 40$  for  $\Delta t = 20 \times 10^{-5}$ . Only 3 cells for  $\Delta t = 10 \times 10^{-5}$  exceed  $Co = 40$ , but the number of cells with  $20 < Co < 40$  is much larger with respect to the not-refined grid using the same time-step size.

Different levels of the pressure coefficient can be observed on the suction (Figure 5.19) and pressure side (Figure 5.20) varying the time step, and the pattern obtained for the fully submerged blade with the chosen time-step size is similar to the one obtained in open water (Figures 5.6e and 5.7e).

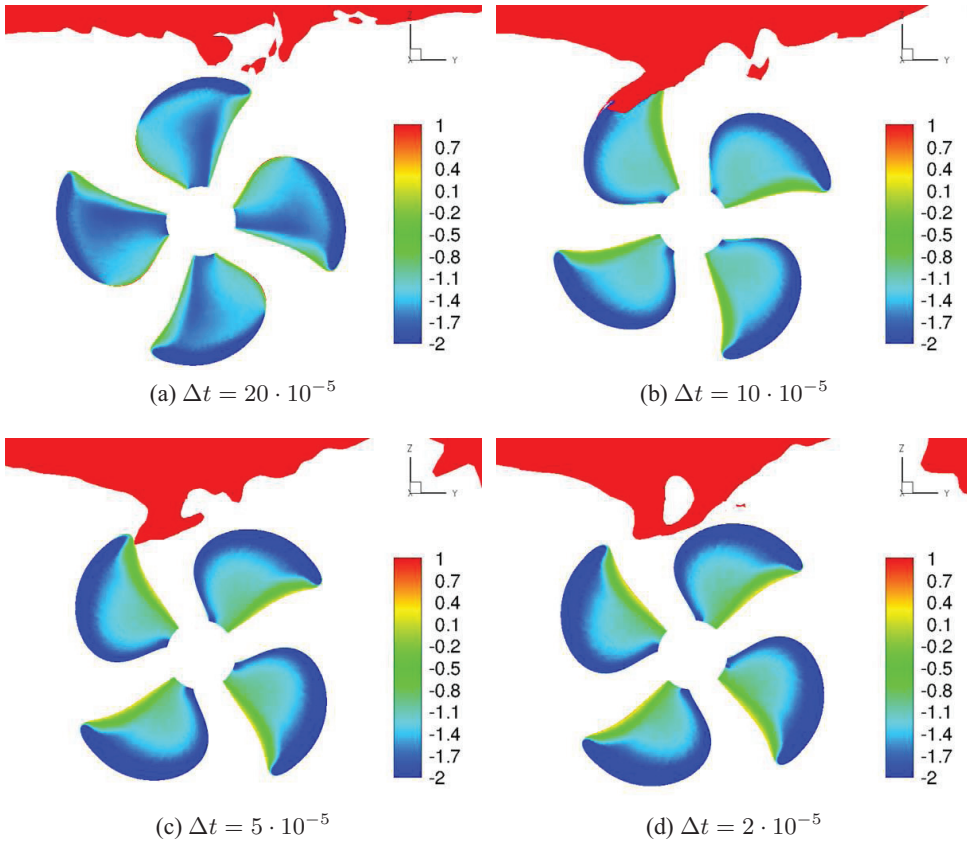
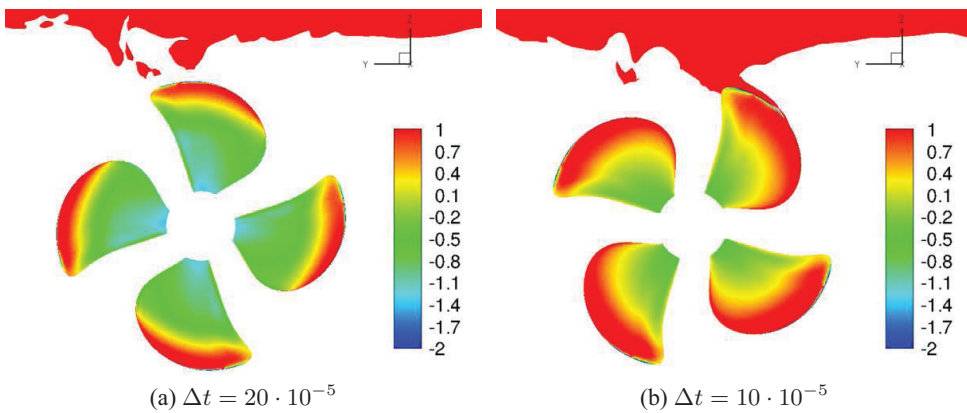


Figure 5.19: Comparison of the pressure coefficient on the suction side obtained using different integration time steps [ $h/R = 1.72$ , refined grid].



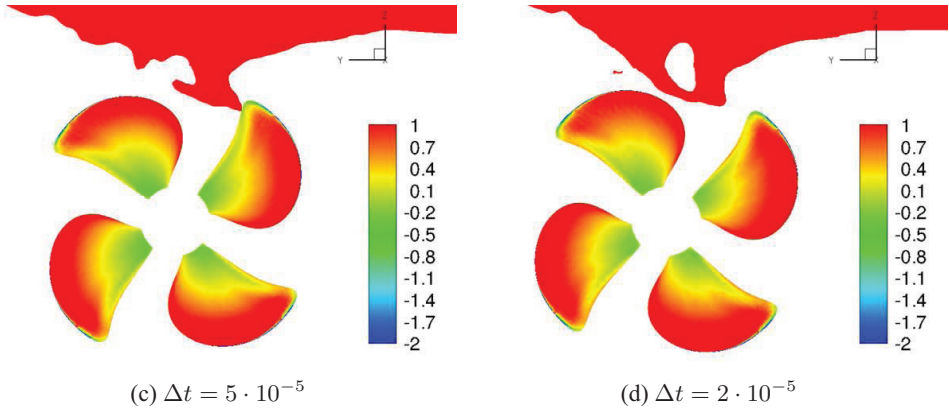


Figure 5.20: Comparison of the pressure coefficient on the pressure side obtained using different integration time steps  $K_{T0}$  [ $h/R = 1.72$ , refined grid].

### 5.2.7 Under-relaxation factors

The default Under-Relaxation Factors (URF)s suggested by the solver were reduced in order to stabilize the performed simulations (Figure 5.21).

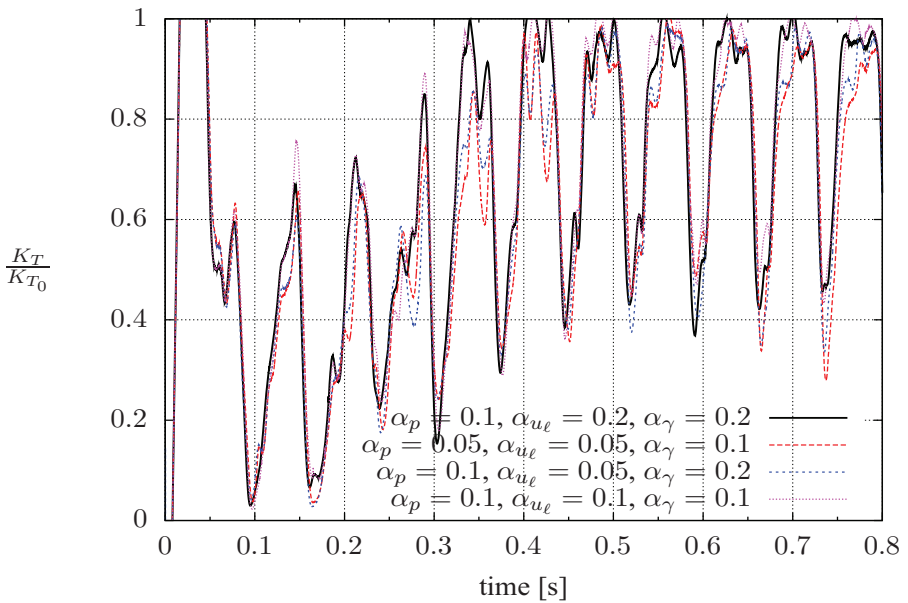


Figure 5.21: Effect of the URFs on the blade thrust ratio [ $h/R = 1.4$ ].

The results of the new simulations are obtained reducing:

- (i) all the URFs to  $\alpha_p = 0.05, \alpha_{u_\ell} = 0.1, \alpha_\gamma = 0.1$ ,
- (ii) only the momentum equation URFs to  $\alpha_{u_\ell} = 0.1$ ,
- (iii) only the volume-fraction equation URF to  $\alpha_\gamma = 0.1$ .

Differences in terms of thrust losses among different simulations are barely visible (Figure 5.21).

A further analysis has shown that under-relaxing the governing equations *after a quasi-steady oscillatory solution at the default values was obtained* leads to different solutions.

The thrust ratio obtained halving the URFs ( $\alpha_p = 0.05, \alpha_{u_\ell} = 0.1, \alpha_\gamma = 0.1$ ) is shown in Figure 5.22a and 5.22b. The blade thrust (Figure 5.22a) decreases over all angular positions while the blade is submerged, better capturing the experimental results. The corresponding propeller thrust coefficient (Figure 5.22b) is also reduced.

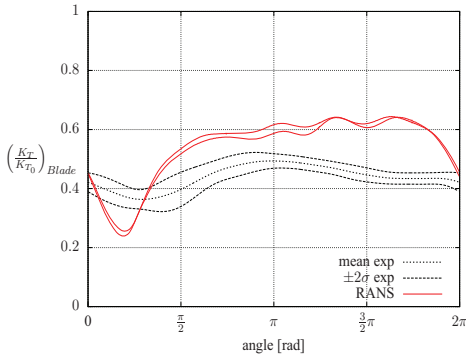
Another reduction of the URFs ( $\alpha_p = 0.02, \alpha_{u_\ell} = 0.05, \alpha_\gamma = 0.05$ ) has the effect to further reduce the thrust ratio. Both the blade (Figures 5.22c) and propeller (Figures 5.22d) thrust ratio are now lying below the experimental data.

A further reduction of the URFs ( $\alpha_p = 0.01, \alpha_{u_\ell} = 0.02, \alpha_\gamma = 0.02$ ) leads to an increase of the thrust ratio, which is over-estimated with respect to the experiments, for the blade (Figures 5.22e) and the whole propeller (Figures 5.22f).

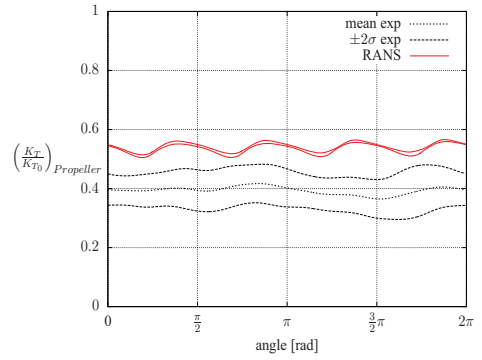
A summary of the values of maximum, i.e. non-ventilating, thrust coefficient  $N \cdot K_T$  on the pressure and suction side are reported in Table 5.3, with the relative error with respect to the open water results. A reduction of the URFs leads to an increased error for the non-ventilating blade, especially on the pressure side, exerting for  $\alpha_p = 0.02, \alpha_{u_\ell} = 0.05, \alpha_\gamma = 0.05$  a resistance—a negative thrust—of the same magnitude of the thrust normally encountered. This error does not seem to have a linear relation with the URFs.

$\alpha_p$	URF		Press. Side	$\Delta\%$	Suct. Side	$\Delta\%$	Propeller	$\Delta\%$
	$\alpha_{u_\ell}$	$\alpha_\gamma$						
0.1	0.2	0.2	0.15	-22.6%	0.39	0.2%	0.54	-7.5%
0.05	0.1	0.1	0.06	-69.3%	0.34	-11.7%	0.40	-31.1%
0.02	0.05	0.05	-0.14	-168.8%	0.37	-4.8%	0.23	-60.1%
0.01	0.02	0.02	0.12	-37.4%	0.39	0.6%	0.52	-12.2%

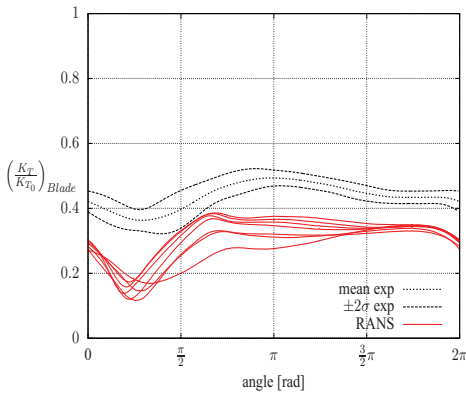
Table 5.3: Thrust coefficient  $N \cdot K_T$  obtained varying the URFs and relative error with respect to the open water results  $K_{T_0}$  [ $h/R = 1.4$ ].



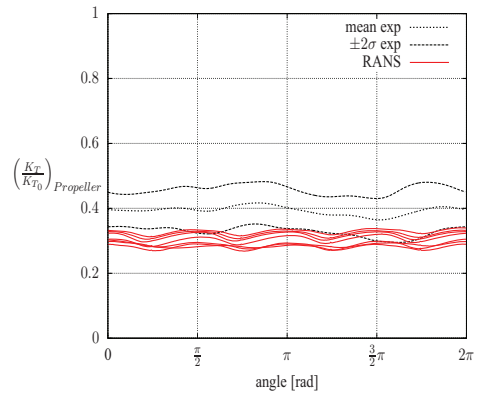
(a) Blade;  $\alpha_p = 0.05$ ,  $\alpha_{u_\ell} = 0.1$ ,  $\alpha_\gamma = 0.1$



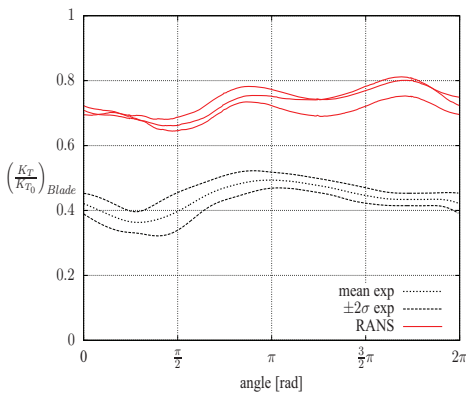
(b) Propeller;  $\alpha_p = 0.05$ ,  $\alpha_{u_\ell} = 0.1$ ,  $\alpha_\gamma = 0.1$



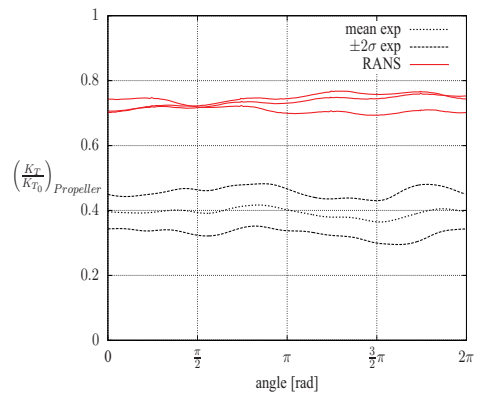
(c) Blade;  $\alpha_p = 0.02$ ,  $\alpha_{u_\ell} = 0.05$ ,  $\alpha_\gamma = 0.05$



(d) Propeller;  $\alpha_p = 0.02$ ,  $\alpha_{u_\ell} = 0.05$ ,  $\alpha_\gamma = 0.05$



(e) Blade;  $\alpha_p = 0.01$ ,  $\alpha_{u_\ell} = 0.02$ ,  $\alpha_\gamma = 0.02$



(f) Propeller;  $\alpha_p = 0.01$ ,  $\alpha_{u_\ell} = 0.02$ ,  $\alpha_\gamma = 0.02$

Figure 5.22: Thrust ratio averaged for each angular position for the blade (left) and the propeller (right) obtained varying the URFs [ $h/R = 1.4$ ].

The corresponding pressure contours are shown in Figure 5.23 and Figure 5.24, for the suction and pressure side, respectively. The non-ventilating blades of Figures 5.23a and 5.24a obtained for  $\alpha_p = 0.1$ ,  $\alpha_{u_\ell} = 0.2$ ,  $\alpha_\gamma = 0.2$  show a contour very similar to the open water tests, while the pattern radically changes for the other sets of URFs. The pressure drop obtained for  $\alpha_p = 0.02$ ,  $\alpha_{u_\ell} = 0.05$ ,  $\alpha_\gamma = 0.05$  on the leading edge of the pressure side (Figure 5.24c) is clearly visible. Although the blade loads are closer to the experimental values, the blade's pressures obtained reducing the URFs reach values deemed as not physical, far from both the open water and ventilated case.

The air-volume-fraction on the suction side obtained using different URFs is shown in Figure 5.25, where the free-surface location is also depicted. Decreasing the URFs, the air covering the blade is moving from the tip to the leading edge. At the same time, more air is visible all around the propeller disc. The higher air content at lower URFs can be better observed on the propeller mid-plane (Figure 5.26).

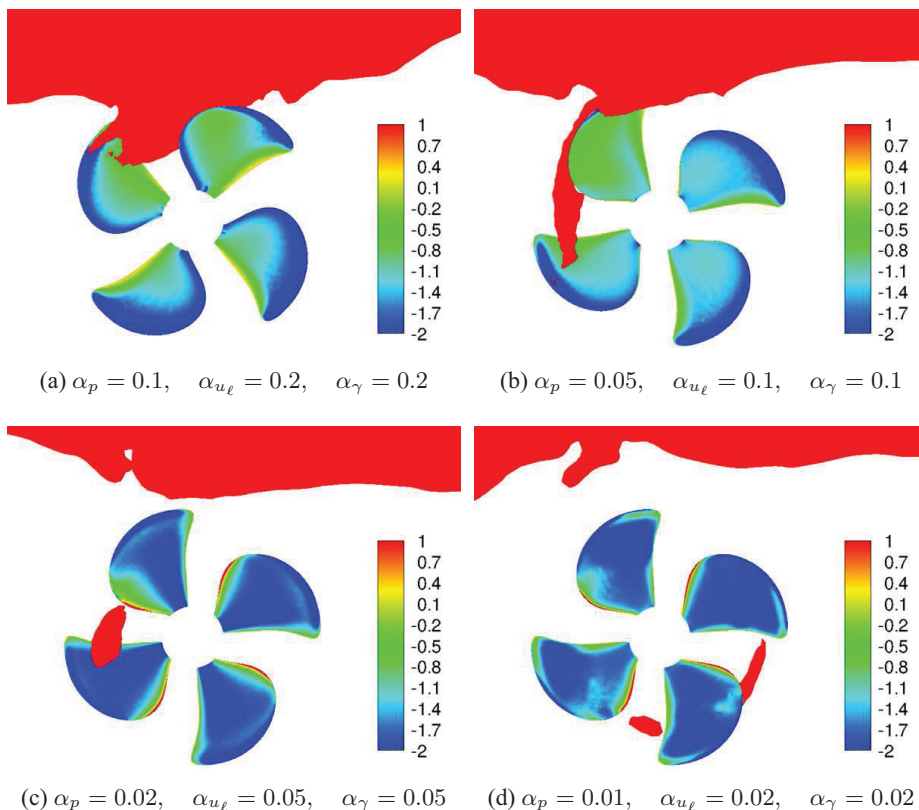


Figure 5.23: Pressure coefficient on the suction side using different URFs [ $h/R = 1.4$ ].

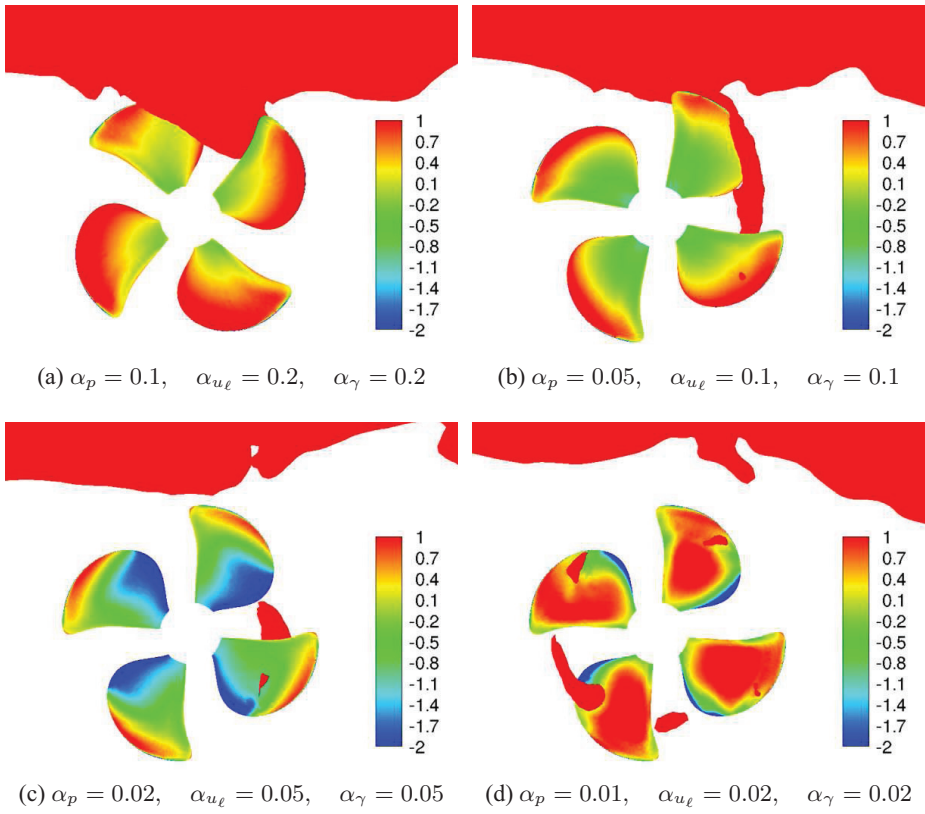
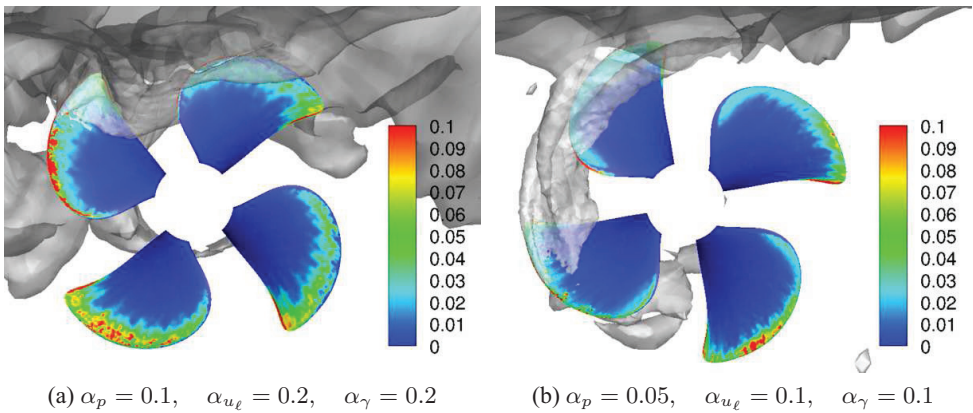


Figure 5.24: Pressure coefficient on the pressure side using different URFs [ $h/R = 1.4$ ].



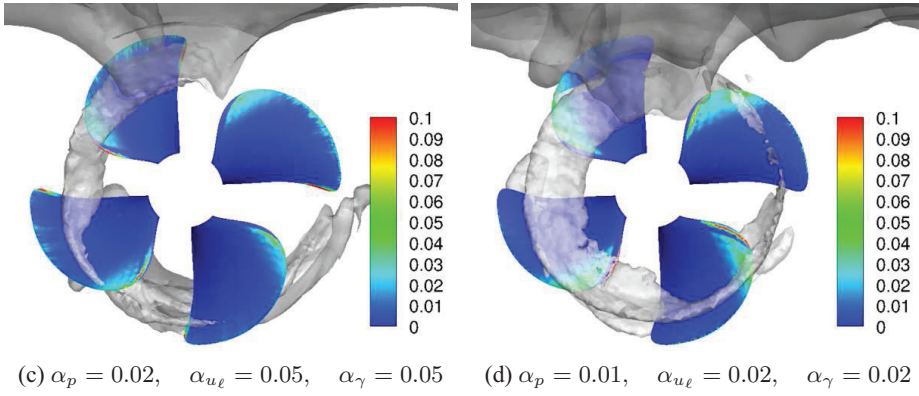


Figure 5.25: Air-volume-fraction on the suction side using different URFs [ $h/R = 1.4$ ].

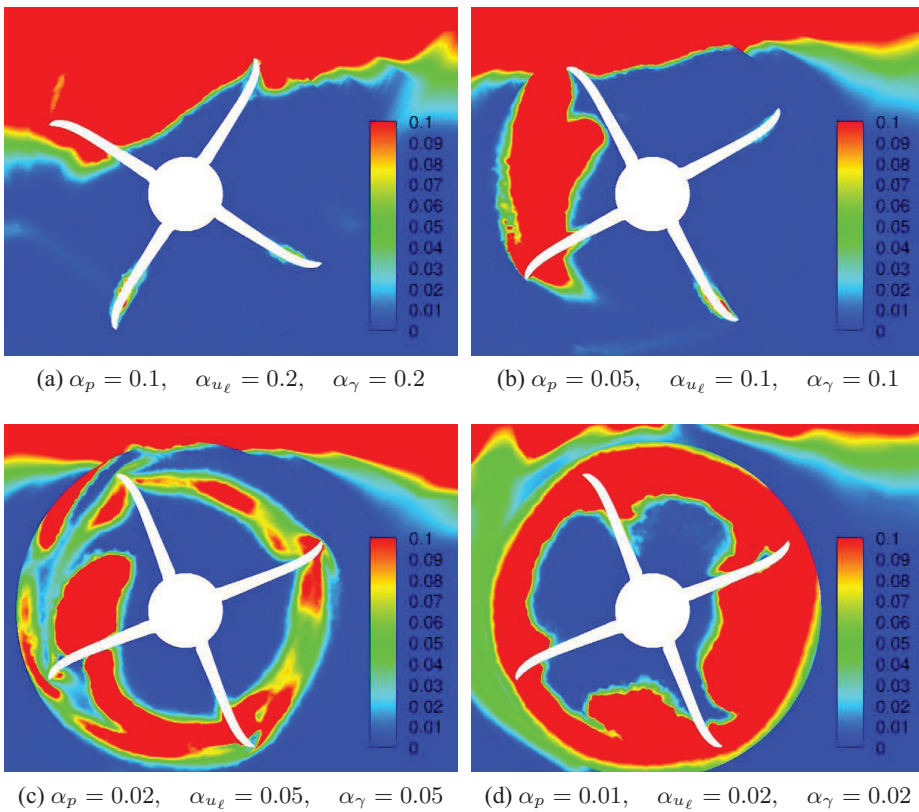


Figure 5.26: Air-volume-fraction on the mid  $x$ -plane using different URFs [ $h/R = 1.4$ ].

The reduction of the URFs, although improving the stability of the solution limiting the influence of the correction term, slows down the convergence of the solver. In view of this consideration, the results obtained decreasing the URFs after a quasi-steady oscillatory solution is obtained, can be thought of as a "stable" transient solution. This transient solution would eventually evolve towards the quasi-steady oscillatory solution which is obtained starting from time 0, but this is not achieved during the simulated time.

Both the URFs and the integration time-step have shown to affect strongly the obtained solution. Their effect can be analyzed within the discrete form of the variable updates of the SIMPLE scheme (Equation 5.5). The update for the  $u$ -momentum equation is rewritten below:

$$u_{i,j}^{k+1} = u_{i,j}^* + \alpha_u \frac{\Delta t}{A_{i,j}^u \Delta x} (p'_{i,j} - p'_{i+1,j})$$

where  $A_{i,j}^u$  will also depend on  $\Delta x$  and  $\Delta t$  (Equation 5.6).

The combination of the URFs, the time-step and the grid size will determine in a non-trivial manner how the term with the pressure correction will contribute to the new velocity field.

There is a strong similarity between the algebraic equations resulting from the use of under-relaxation when solving steady problems and those resulting from implicit Euler scheme applied to unsteady equations. The following relation between the under-relaxation factor  $\alpha$  and time step  $\Delta t$  can be derived by requiring that the contributions be same in both cases (Ferziger and Perić, 2002):

$$\Delta t \propto \frac{\alpha}{1 - \alpha} \frac{V}{\sum_c F_f} \quad (5.9)$$

where  $F_f$  is the volumetric flow rate through the face  $f$  and the sum is taken over all the faces of the cell  $c$  with volume  $V$ . The use of a constant under-relaxation factor is equivalent to applying a different time step to each control volume.

### 5.3 Surface-piercing propeller

The simulations performed on a submerged propeller have shown a general over-estimation of the thrust in the angular positions different from 0, and a strong dependency on the simulation parameters. The simulation of a surface-piercing propeller was attempted in order to test the capabilities of the solver on a different type of ventilation, where blades are surface-piercing already from rest.

Figure 5.27 shows the blade thrust ratio obtained for  $h/R = 0$  and  $h/R = 0.24$ . The corresponding contours of air-volume-fraction and pressure coefficient are visualized in Figure 5.28 and 5.29.

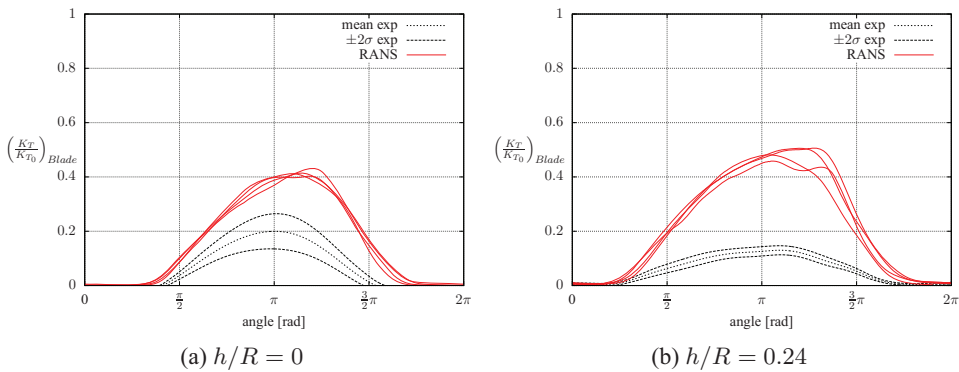


Figure 5.27: Thrust ratio [ $\alpha_p = 0.1$ ,  $\alpha_{u_\ell} = 0.2$ ,  $\alpha_\gamma = 0.2$ ].

The experimental results were obtained during two different test campaigns, *Kou05* ( $h/R = 0$ ) and *Koz10*. The differences among these two test campaigns were underlined in Chapter 4, and they could explain the differences between the two experimental results which were performed in the same ventilation regime, at similar submergences.

Although the numerical results better approach the experimental trend, thrust is still over-estimated for the angular positions where the blade is submerged. RANS simulations of a surface-piercing propeller with a supercavitating profile were performed by Caponnetto (2003), showing a good agreement with the experimental results. This type of propellers has a sharp leading edge—being able to separate the two phases after the impact with water—and are especially designed to work with an air cavity extending over the entire suction side, whereas the pressure side is giving the thrust while submerged. Starting from rest with the shaft axis lying on the free surface, the cavity is rapidly formed on the suction side and seems continuously connected to the external air (see illustrations from the experiments of Olofsson, 1996).

The propeller used in the present study is of “conventional” type, with a blunt leading edge and a sharp trailing edge. Contours of air-volume-fraction in Figure 5.28 do not show a clear separation between the two phases among the pressure and suction side of the submerged blades.

Differences in the working conditions should also be mentioned; the present propeller is working at high propeller loadings characterized by strongly non-linear flow leading to low induced axial velocities on the tip. Air drawn from the free-surface would then stick to the tip region after ventilation inception.

Contours of the pressure coefficient (Figure 5.29) show values different from zero only on the submerged part of the propeller.

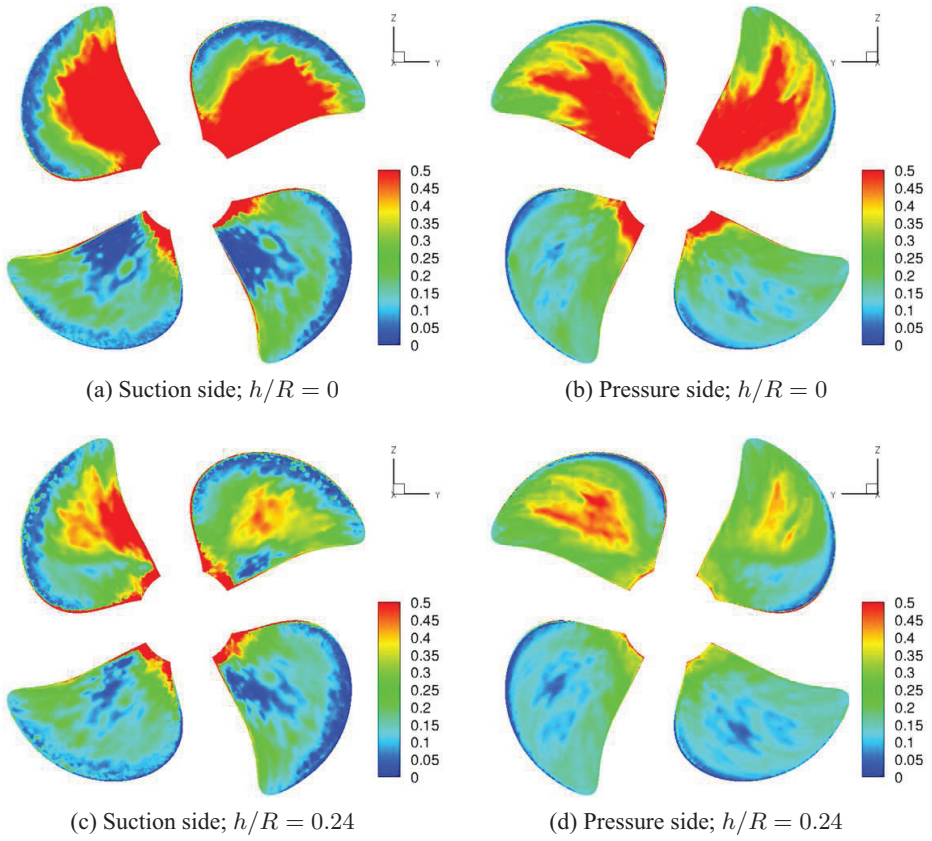
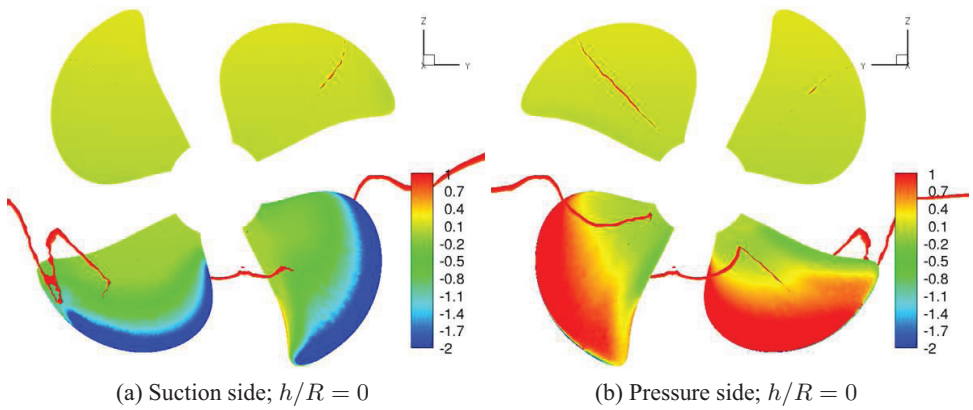


Figure 5.28: Air-volume-fraction contours [ $\alpha_p = 0.1$ ,  $\alpha_{u_\ell} = 0.2$ ,  $\alpha_\gamma = 0.2$ ].



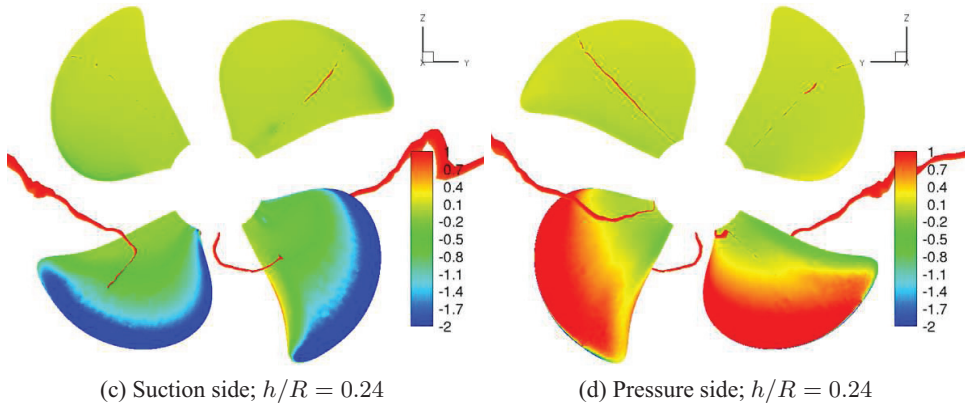


Figure 5.29: Pressure coefficient contours [ $\alpha_p = 0.1$ ,  $\alpha_{u_\ell} = 0.2$ ,  $\alpha_\gamma = 0.2$ ]; the plotted red line is the projection of the free surface on the mid  $x$ -plane.

## 5.4 Ventilation inception

This section will focus of the very first time instants where ventilation starts, before a quasi-steady oscillatory solution is obtained. Both inception due to surface-piercing propeller at moderate submergence ( $h/R = 1.4$ ) and by free-surface vortex formation at deeper submergence ( $h/R = 1.72$ ) will be described.

### 5.4.1 Surface-piercing

For moderate submergence ratios ( $h/R = 1.4$ ), the deformation of the free surface is such that the blades become surface-piercing. Figure 5.30 shows the time evolution of the thrust ratio for the whole propeller and for each blade for a shaft acceleration  $\dot{n} = 208.7 \text{ rad/s}^2$ . The initial thrust increase following the linear acceleration of the shaft can be observed, while the quasi-steady oscillatory value is lower than unity due to air-drawing. The volume of air contained in the cylinder embedding the propeller is monitored in order to follow the ventilation mechanism; its value is shown in the same figure in terms of percent ratio of the volume embedding the propeller. Air is rapidly drawn during the acceleration phase, and starts decreasing after is transported downstream by the axial free-stream and induced velocity. The air content would eventually reach a quasi-steady oscillatory value where the same amount of air drawn from the free-surface is transported downstream.

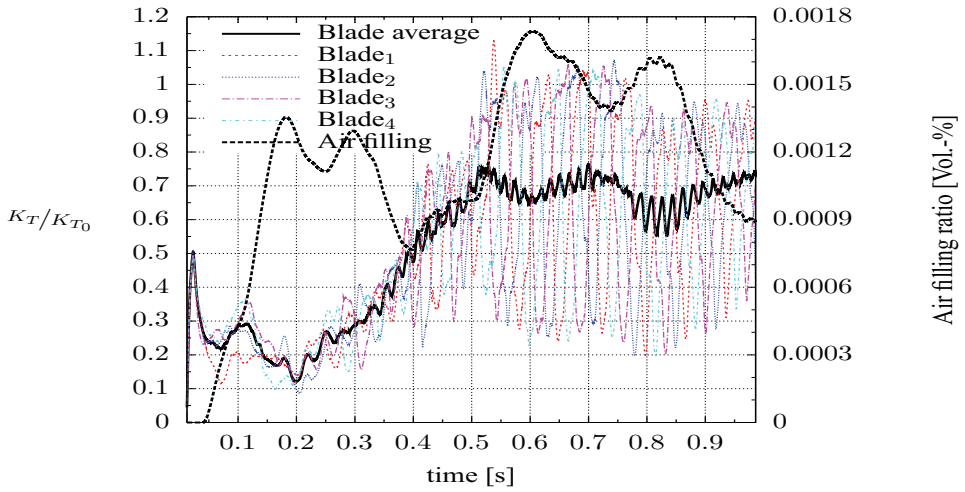


Figure 5.30: Time evolution of the thrust ratio for the whole propeller and for each blade [ $h/R = 1.4$ ,  $\dot{n} = 208.7 \text{ rad/s}^2$ ].

The time evolution of the thrust ratio for the whole propeller and for *Blade*<sub>1</sub> is plotted in Figure 5.31, where the shaft acceleration and the angular position of *Blade*<sub>1</sub> are also represented. The blade thrust interrupts its linear increase before the shaft frequency reaches its nominal value  $n_0$  around  $t = 0.42 \text{ s}$ . After this time instant, large thrust losses are visible around  $0 \text{ rad}$ .

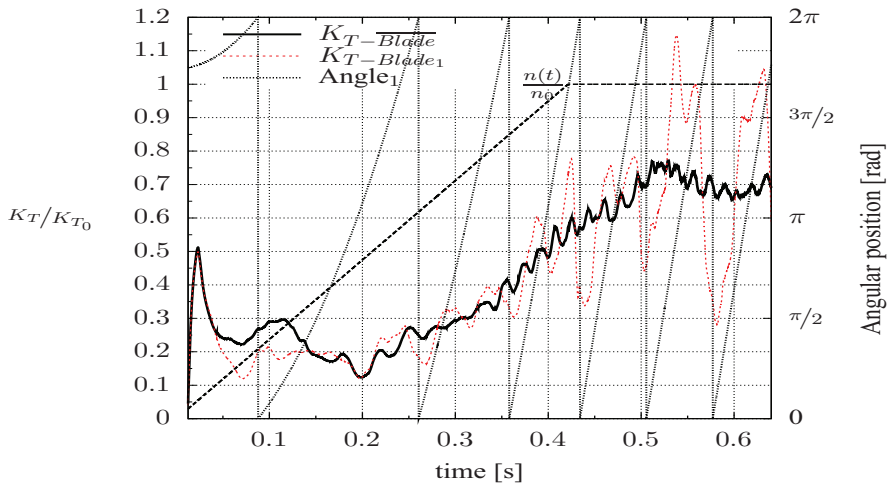


Figure 5.31: Thrust coefficient and azimuthal position of *Blade*<sub>1</sub> as a function of time; comparison with the whole propeller [ $h/R = 1.4$ ,  $\dot{n} = 208.7 \text{ rad/s}^2$ ].

After starting the rotation, the free-surface is rapidly pulled towards the propeller and ventilation starts after the first blade-crossing of the free-surface (around  $t = 0.06$  s, Figure 5.32). From this time on, air is continuously drawn from the free-surface down to the propeller disc.

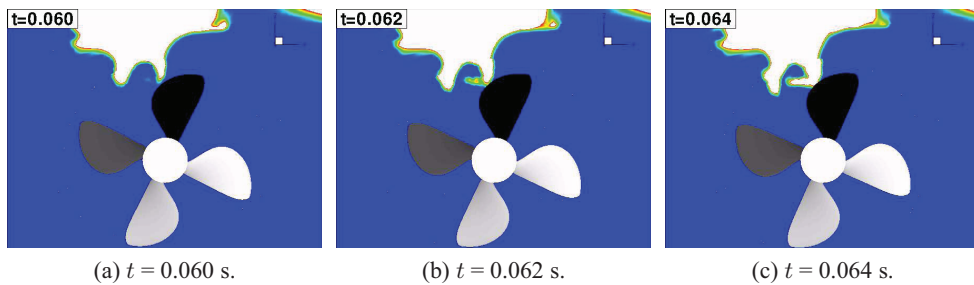


Figure 5.32: Ventilation inception [ $h/R = 1.4$ ,  $\dot{n} = 208.7$  rad/s<sup>2</sup>]. Air-volume-fraction on the propeller plane ( $x = 0$ ).

Besides this main pattern leading to ventilation, other events can be observed:

- The free-surface "breaks" for the first time (around  $t = 0.04$  s, Figure 5.33) in correspondence to a vortical structure forming downstream the propeller, allowing air to be entrapped in the surrounding water.
- The formation and subsequent collapse of a wave right-above the propeller (Figure 5.34).
- The formation of a vortical structure (around  $t = 0.05$  s) on the free-surface upstream the propeller: while approaching one blade, it rapidly vanishes (around  $t = 0.07$  s) after the violent ventilation occurring on the following blade (Figure 5.35).

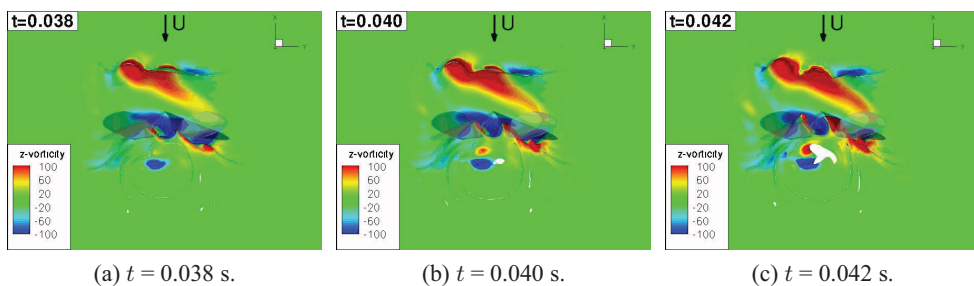


Figure 5.33: First opening on the free-surface [ $h/R = 1.4$ ,  $\dot{n} = 208.7$  rad/s<sup>2</sup>]. Contours of  $z$ -vorticity [m/s<sup>2</sup>] on the free surface (bottom view).

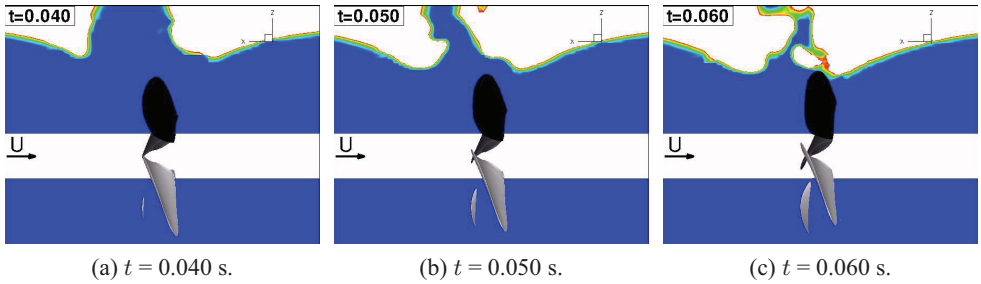


Figure 5.34: Formation and collapse of a wave above the propeller [ $h/R = 1.4$ ,  $\dot{n} = 208.7$  rad/s<sup>2</sup>]. Contours of air-volume-fraction on the longitudinal vertical mid-plane ( $y = 0$ ).

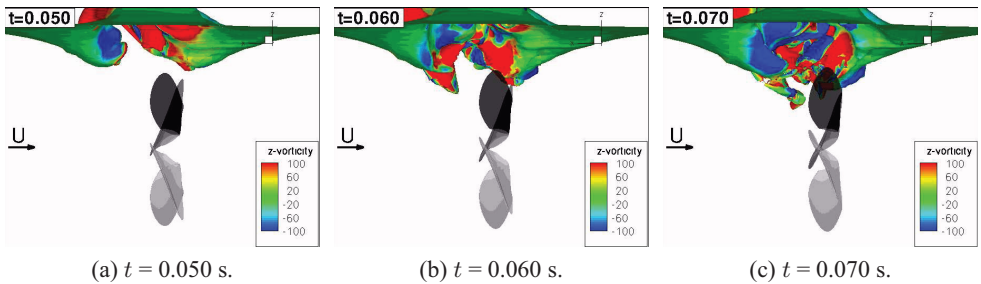


Figure 5.35: Evolution of a free-surface vortex approaching the propeller [ $h/R = 1.4$ ,  $\dot{n} = 208.7$  rad/s<sup>2</sup>]. Contours of  $z$ -vorticity [m/s<sup>2</sup>] on the free surface (side view).

### 5.4.2 Vortex formation

At deeper submergences the induced velocities exerted by the propeller are not strong enough to pull the free-surface down to the propeller disc. However, vortical structures will now form on the free-surface and possibly attach to the propeller tip leading to a different type of ventilation, where air is continuously drawn through the free-surface vortex. A typical example of the thrust losses obtained during such a ventilation event is depicted in Figure 5.36. The behavior is less repeatable, depending on the location of the impact of the free-surface vortex, and not only to the proximity to the undisturbed free-surface. Eventually, full ventilation by surface-piercing propeller can occur also at this deeper submergence.

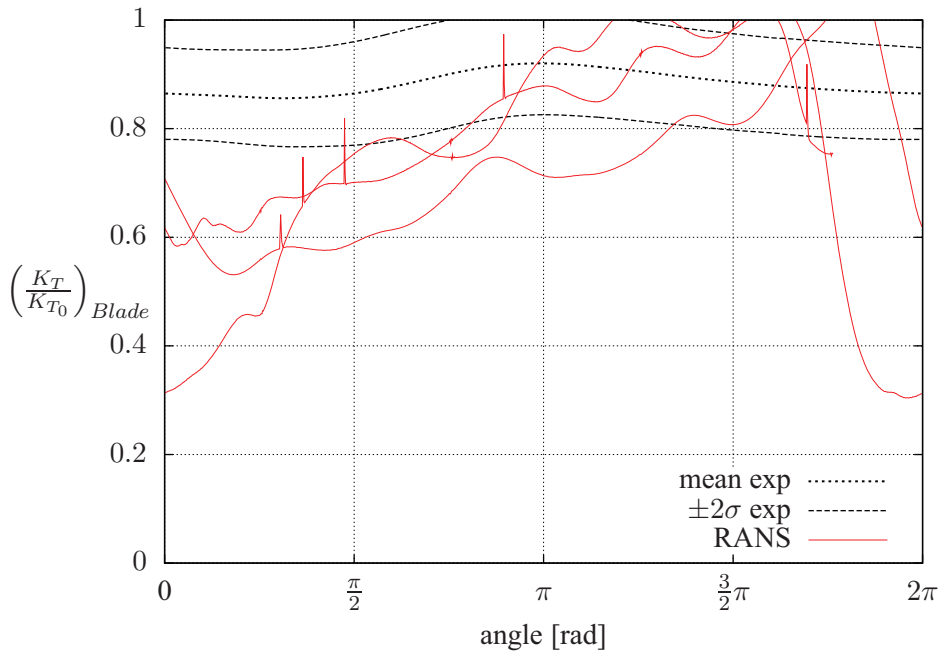


Figure 5.36: Thrust ratio averaged for each angular position [ $h/R = 1.72$ ;  $\alpha_p = 0.1$ ,  $\alpha_{u_e} = 0.2$ ,  $\alpha_\gamma = 0.2$ ].

Figure 5.37 shows the time evolution of the thrust ratio for the whole propeller and for each blade for a shaft acceleration  $\dot{n} = 208.7 \text{ rad/s}^2$ . Only the thrust ratio of  $Blade_1$  is plotted in Figure 5.38, where the shaft acceleration and the angular position of  $Blade_1$  are also represented.

Three main phases can be observed before full-ventilation by surface-piercing propeller starts:

- from start to  $t = 0.13 \text{ s}$ :  
Low variations with respect to average propeller thrust, only due to proximity to the free-surface.
- $t = 0.13 \text{ s}$ :  
Ventilation inception by vortex formation.
- from  $t = 0.13 \text{ s}$  to  $t = 0.49 \text{ s}$ :  
Ventilation through a free-surface vortex.

After  $t = 0.49$  a fully ventilating event by surface-piercing propeller occurs, leading to rapid sucking of air and sudden thrust loss. In these conditions the blade thrust presents large variations with respect to the average propeller thrust.

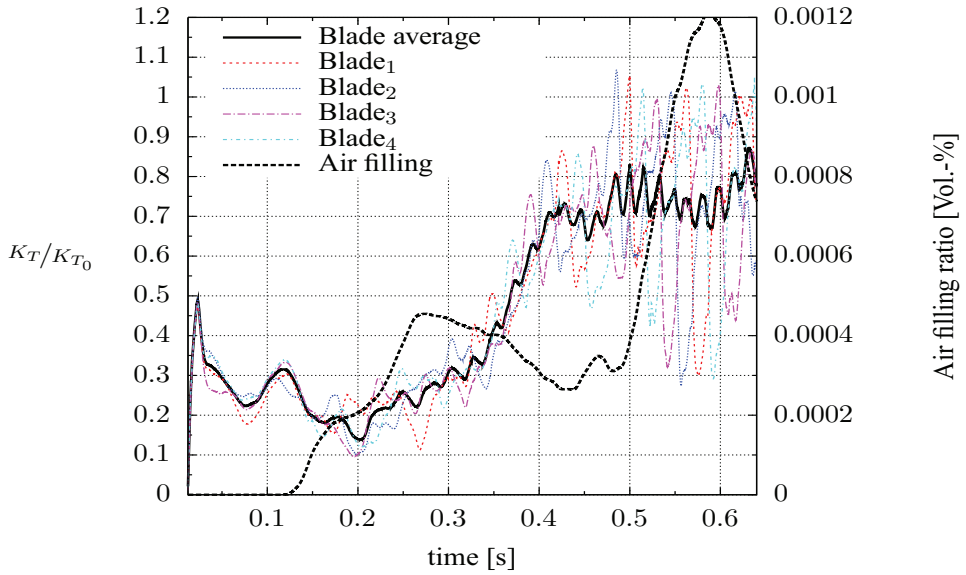


Figure 5.37: Time evolution of the thrust ratio for the whole propeller and for each blade [ $h/R = 1.72$ ,  $\dot{n} = 208.7 \text{ rad/s}^2$ ].

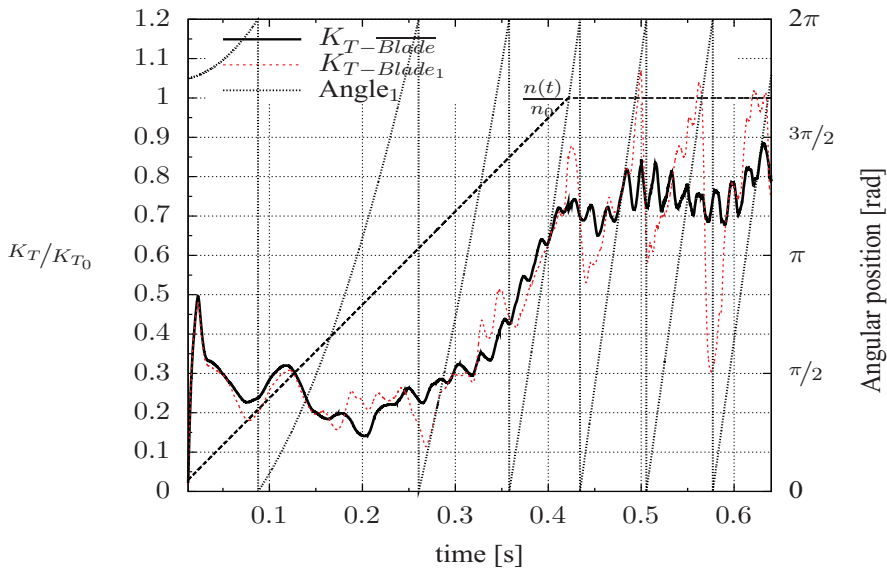


Figure 5.38: Thrust coefficient and angular position of *Blade*<sub>1</sub> as a function of time; comparison with the whole propeller [ $h/R = 1.72$ ,  $\dot{n} = 208.7 \text{ rad/s}^2$ ].

The vortex induced by the blade tip passing starboard attracts the free-surface, leading to the first "break" of the free-surface and forming a tube through which air can freely flow down to the propeller (Figure 5.39). Note the positive sign of the vorticity along  $z$ -direction and the simultaneous appearance of a counter-rotating vortex on the port side (respectively,  $z_+$  and  $z_-$  in Figure 5.39c).

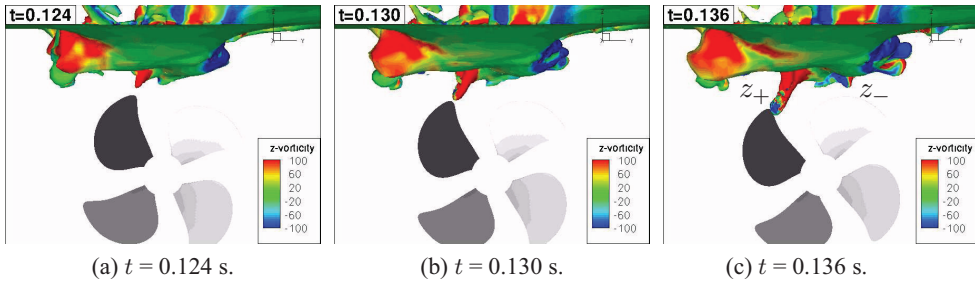


Figure 5.39: Ventilation inception by the free-surface vortex [ $h/R = 1.72$ ,  $\dot{n} = 208.7 \text{ rad/s}^2$ ]. Contours of  $z$ -vorticity [ $\text{m/s}^2$ ] on the free surface (front view).

Figure 5.40 shows the evolution of a second vortex on the port side, counter-rotating with respect to the first vortex, and impacting the following blade (respectively,  $z_+$  and  $z_-$  in Figure 5.40c).

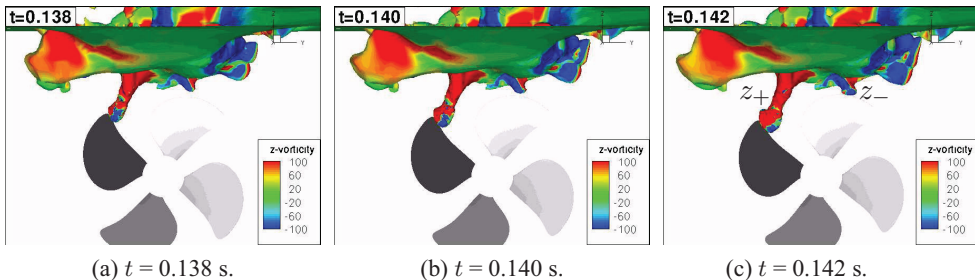


Figure 5.40: Formation of a second vortex on the port side [ $h/R = 1.72$ ,  $\dot{n} = 208.7 \text{ rad/s}^2$ ]. Contours of  $z$ -vorticity [ $\text{m/s}^2$ ] (front view).

The counter-rotating vortex located on the port side rapidly vanishes after each blade's crossing. On the other hand, the pressure overturn on the blade tip feeds with vorticity the starboard vortex, detaching from the previous blade and reattaching on the following one, as shown in Figure 5.41.

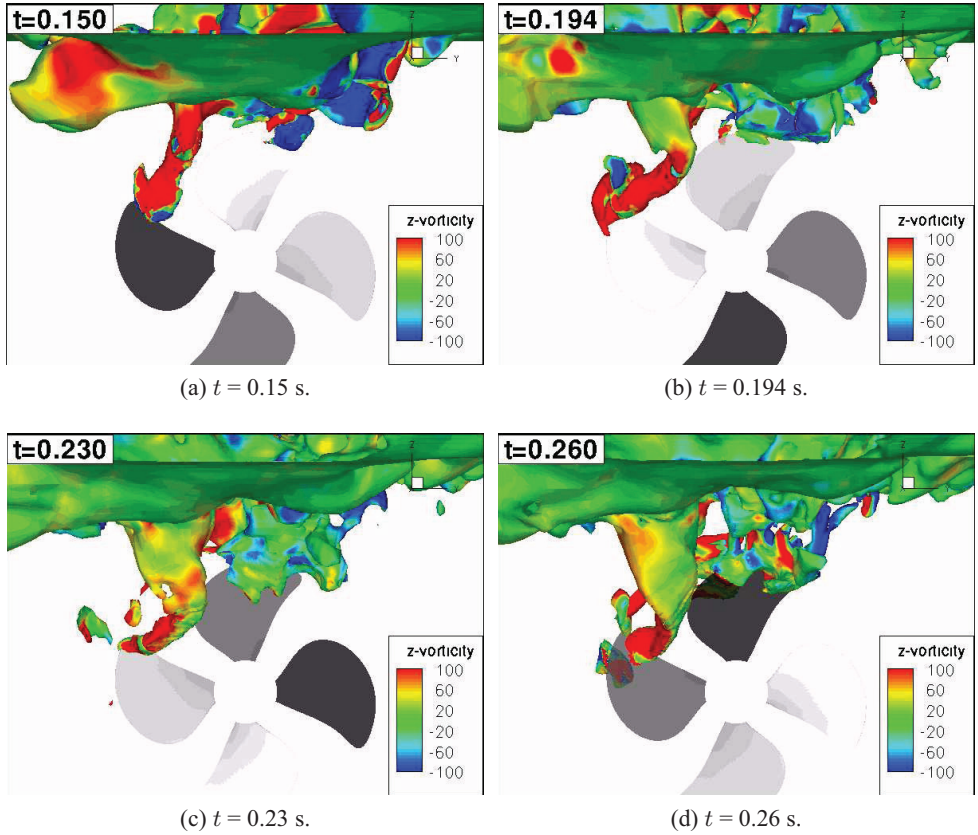


Figure 5.41: Impingement of the starboard vortex on the blades [ $h/R = 1.72$ ,  $\dot{n} = 208.7$  rad/s<sup>2</sup>]. Contours of  $z$ -vorticity [m/s<sup>2</sup>] (front view).

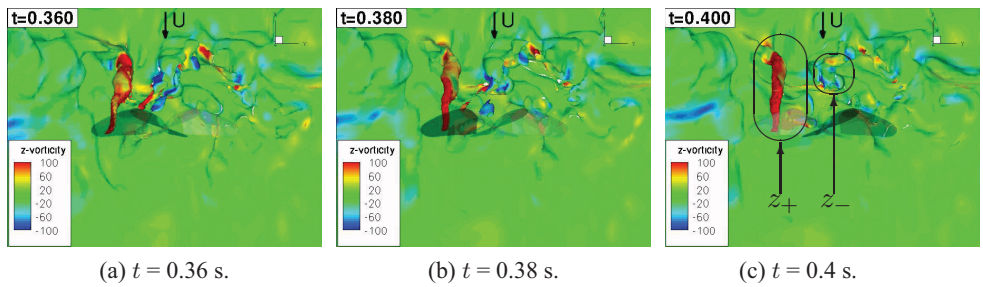
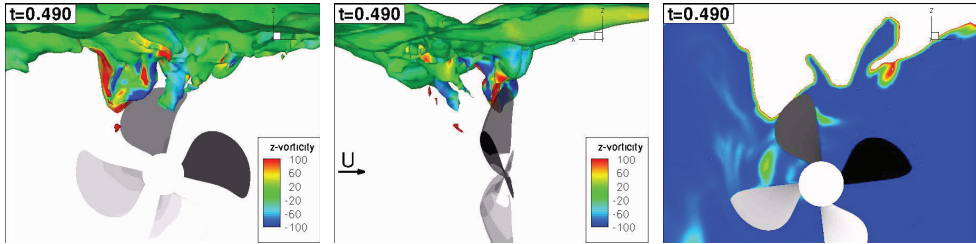


Figure 5.42: Ventilation through a free-surface vortex [ $h/R = 1.72$ ,  $\dot{n} = 208.7$  rad/s<sup>2</sup>]. Contours of  $z$ -vorticity [m/s<sup>2</sup>] on the free surface (bottom view).

The irregular vortex seen in Figure 5.41 can leave space temporarily to a more regular vortical structure, as shown in Figure 5.42, forming a vertical tube feeding air to the propeller. A weaker counter-rotating structure can simultaneously be observed on the port side.

The rupture of a larger vortical structure can lead to a temporary fully-ventilating event. Its inception is shown in Figure 5.43.

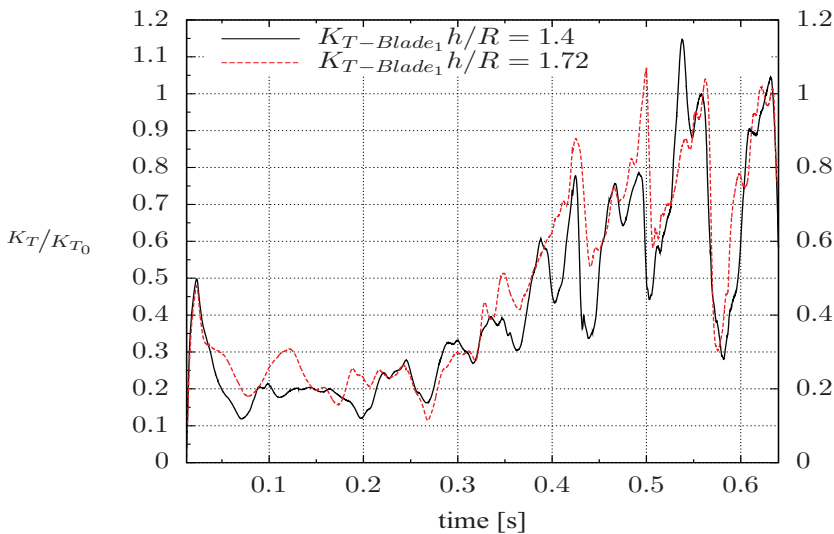


(a) Contours of vorticity [ $\text{m/s}^2$ ] along  $z$ -direction (front view). (b) Contours of vorticity [ $\text{m/s}^2$ ] along  $z$ -direction (side view). (c) Contours of air volume fraction on the propeller plane ( $x=0$ ).

Figure 5.43: Start of a fully ventilating event [ $h/R = 1.72$ ,  $\dot{n} = 208.7 \text{ rad/s}^2$ ,  $t = 0.49 \text{ s}$ ].

### 5.4.3 Comparison

A comparison between the two analyzed submergences is shown in Figure 5.44.



(a) Blade thrust

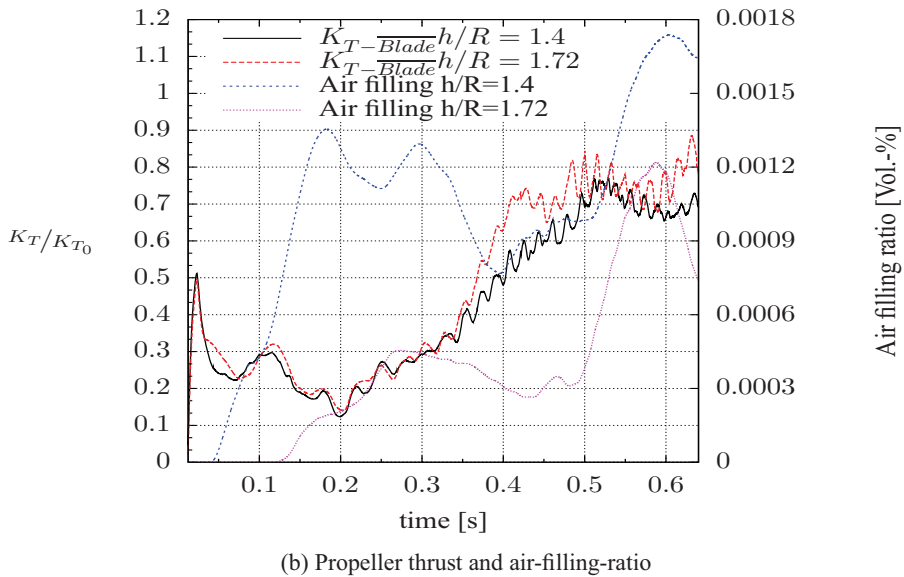


Figure 5.44: Comparison of the thrust ratio as a function of time between moderate ( $h/R = 1.4$ ) and deep ( $h/R = 1.72$ ) submergences [ $\dot{n} = 208.7 \text{ rad/s}^2$ ].

As expected, at moderate submergence ( $h/R = 1.4$ ) air-drawing occurs earlier and with stronger intensities. The only remarkable differences in terms of loads are visible after ventilation inception and before fully-ventilation occurs for the deeper case ( $h/R = 1.72$ ), between  $t = 0.35$  and  $t = 0.5$  s. In this time interval, the propeller thrust is lower at moderate submergence ( $h/R = 1.4$ ) and the blade thrust is subject to large oscillations. The blade thrust is the same in the two conditions after  $t = 0.5$  s, when fully ventilation occurs also for  $h/R = 1.72$ , while the propeller thrust for this deeper submergence case remains higher.

## 5.5 Summary

Numerical simulations were performed in order to investigate the characteristics of the inherently unsteady ventilation phenomenon. A moderate submergence ratio was chosen ( $h/R = 1.4$ ), leading to full-ventilation after the propeller becomes surface-piercing. The complexity of the phenomenon itself leads to unstable numerical simulations, very sensitive to the used numerical parameters, somehow reflecting the large deviation found in the experiment.

The Multiple Reference Frame (MRF) model allows to capture the main features observed during the experiments; air is sucked down from the free-surface and transported through the propeller rotation. However, global loads are generally

over-estimated.

The Sliding Mesh (SM) model was adopted in order to handle the unsteady nature of the phenomenon. A stable solution could be obtained only reducing the Under Relaxation Factors (URFs) for the solved equations. The obtained quasi-steady oscillatory thrust is generally over-estimated along the rotation. A modest improvement is obtained with respect to the MRF model in the upright position, where the blade is piercing the free surface. At this angular position the agreement of both numerical models with the experimental data is satisfactory, whereas thrust is overestimated at all the other angular positions.

The simulation of a surface-piercing propeller was performed in order to test the capabilities of the solver on a different type of ventilation, where blades are surface-piercing already from rest ( $h/R = 0$  and  $h/R = 0.24$ ). A previous work on a surface-piercing propeller with supercavitating-type profile (sharp leading edge and thick abrupt trailing edge) exists (Caponnetto, 2003), showing a good agreement with the experimental results. Although present results approach the experimental trend better than for the deeper submergence, thrust is still over-estimated for the angular positions where the blade is submerged. This difference between experimental and numerical results could be ascribed to the specific geometry and conditions object of this study:

- the blade sections are not of the supercavitating type, but designed with a conventional lifting foil (blunt leading edge and sharp trailing edge):  
⇒ the blunt leading edge will not work as a sharp interface, not being able to separate the two phases after the impact with water;
- the propeller is working at very high propeller loadings:  
⇒ characterized by strongly non-linear flow leading to low induced axial velocities on the tip.

The analysis of the first time instants, before a quasi-steady oscillatory solution is obtained, allows a deeper insight into two different types of ventilation inception:

- surface-piercing propeller at moderate submergence ( $h/R = 1.4$ ):  
the deformation of the free surface is such that the blades become surface-piercing;
- by free-surface vortex formation at deeper submergence ( $h/R = 1.72$ ):  
vortical structures forming on the free-surface reach the propeller tip.

The thrust loss due to ventilation by vortex formation is less repeatable, depending on the location of the impact of the free-surface vortex, and not only to the proximity to the undisturbed free-surface. Eventually, full ventilation by surface-piercing propeller can occur also at this deeper submergence.

# Chapter 6

## Discussion

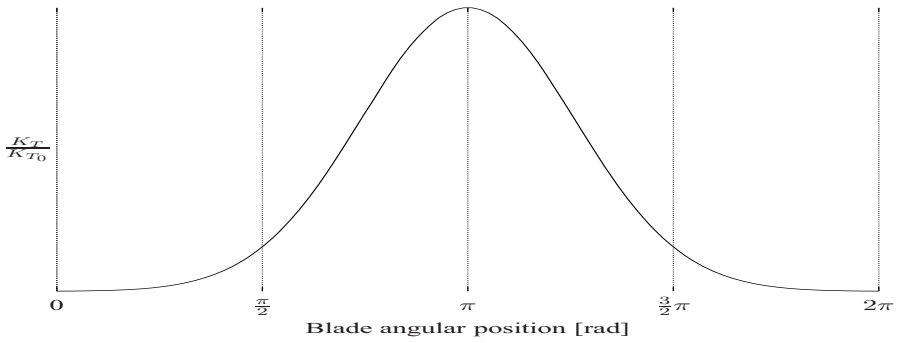
### 6.1 Dynamic loads

The amount and type of ventilation have been shown to depend on submergence, propeller loading and advance ratio. Despite the differences among different cases, some recurring characteristics could be observed. In proximity of the free surface, the oscillatory loads on a blade occurring during one revolution can be ascribed to three different reasons:

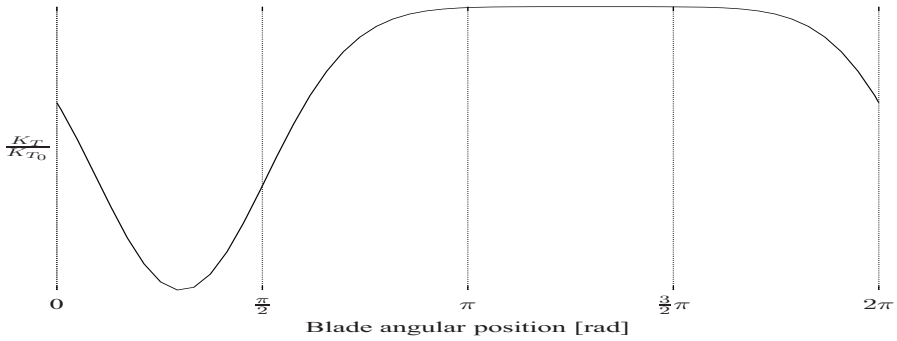
- The proximity of the free-surface leads to a thrust loss around 0 rad, sketched in Figure 6.1a.
- A thrust loss between 0 and  $\pi/2$  occurs due to air-sucking through a free-surface vortex (at deeper submergence) or a tip vortex (at moderate submergence, Figure 6.2a).
- For the surface-piercing ventilation type, around  $3/2 \pi$  a thrust loss occurs due to the impact with the air drawn through the tip vortex trailing from the blade preceding the blade where measurements are taken (Figure 6.2b).

The most severe thrust loss is not located at 0 rad, but slightly after, around  $\pi/4$ . At this angular position the skewed part of the blade is completely out of water, and the effect of the low-pressure region leading to the tip vortex (Figure 6.2a) is stronger than in the upright position—where the tip vortex would be located in air. The identified model of loads is visualized in qualitative sketches in Figure 6.1 for ventilation by free-surface vortex and in Figure 6.3 for surface-piercing propellers. These sketches can be thought of as the dynamic loads obtained averaging the results from several revolutions. They agree quite well with the trend observed both with numerical and experimental results. However, experiments show that for each revolution the trend could be different, where the peaks due to thrust

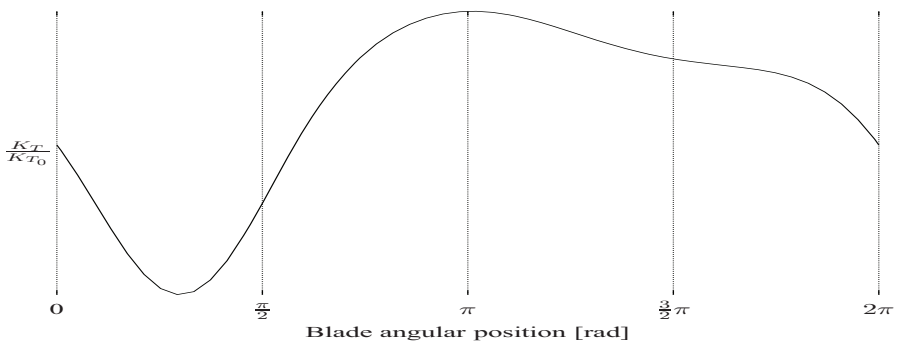
losses can be located on a slightly different angular position and can exist in a higher number, such that the blade is impacting the air mass several times during its rotation.



(a) Thrust loss around 0 rad due to proximity to the free-surface.



(b) Thrust loss around  $\pi/4$  rad due to air-sucking, corresponding to Figure 6.2a.



(c) Total thrust loss, Figure 6.1a + Figure 6.1b

Figure 6.1: Dynamic loads during ventilation through a free-surface vortex.

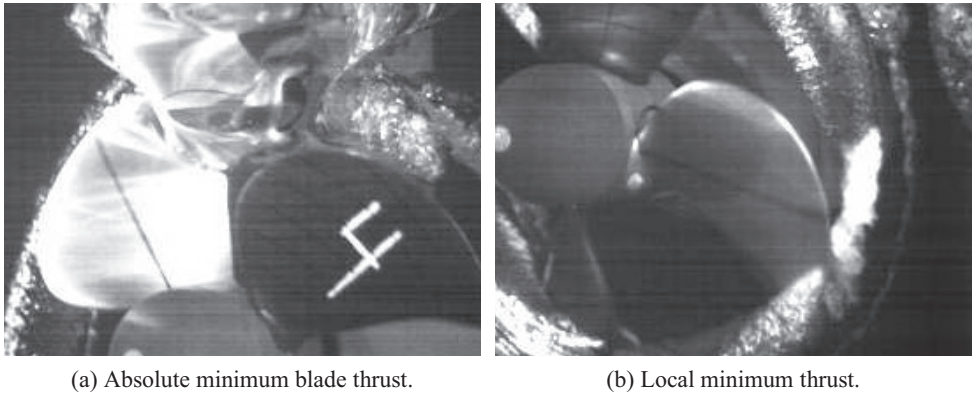


Figure 6.2: Tip vortex [ $h/R = 1.4, \dot{n} = 208.7 \text{ rad/s}^2$ ].

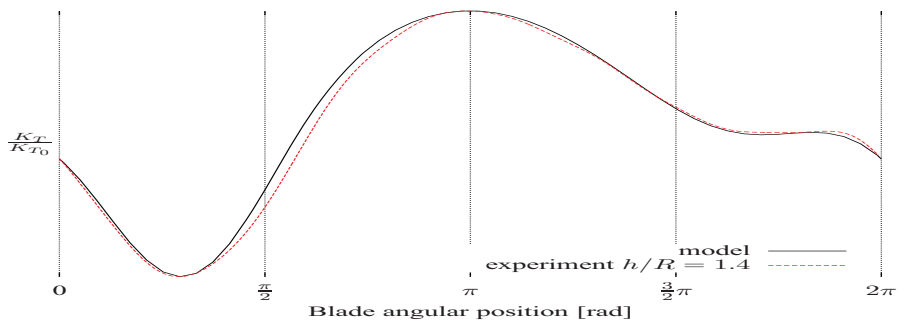
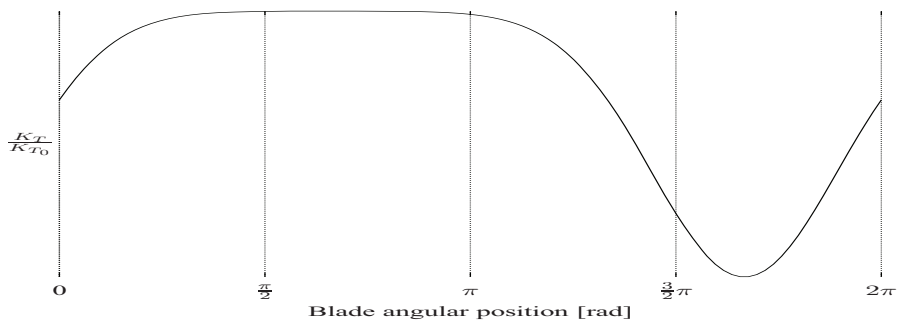


Figure 6.3: Dynamic loads during ventilation of a surface-piercing propeller.

## 6.2 Comparison

Although the agreement of the CFD results with the experiments is qualitatively good, being able to capture the occurrence of thrust losses during the propeller rotation, numerical results generally under-estimate the thrust loss relative to the experiments.

In order to understand the causes of this discrepancy, the instantaneous flow field of the fully-ventilated flow for the numerical simulation and the experiments will be compared, starting from a qualitative point of view. The presence of air is an excellent marker describing ventilation, and its content can be compared in Figure 6.4. The free-surface visualized in the CFD results (Figure 6.4a) is the location where  $\gamma_{air} = 0.5$ .

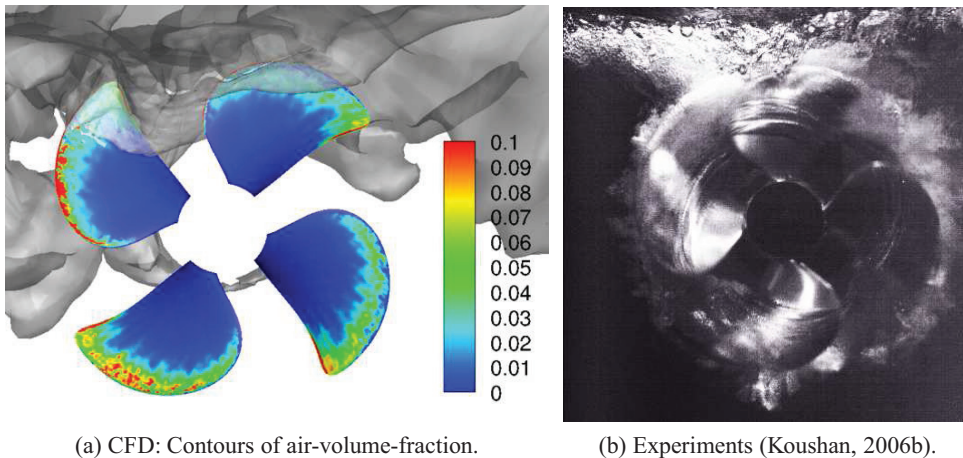


Figure 6.4: Instantaneous flow field.

The fully-ventilated flow observed during experiments (Figure 6.4b) is characterized by a thin sheet cavity covering the suction side of the blades, extending radially from the tip to roughly half of the blade radius. An additional air-flow characterized by small bubbles is superimposed, extending radially as much as the sheet cavities, and covering the entire propeller disc, including the blade-to-blade passage. This secondary bubbly flow is quasi-steady, while the sheet cavities follow the rotation of the propeller.

Comparing the results obtained with the numerical simulation (Figure 6.4a), although the air pattern is very similar, substantial differences can be observed:

- *Extension of the cavities*

- *Angular*

The air initially drawn from the free surface is convected from the blade rotation only for half a revolution. Only a small amount of air is able to follow partially the remaining half revolution (residuals of air are visible on the blade at  $3/2 \pi$  rad). Most of it is instead being transported downstream by the axial flow.

- *Radial*

The blade is covered by air only in proximity of the tip.

- *Bubbles*

The rapid formation of bubbles observed during the experiment is not visualized in the contours of volume fraction.

The ventilation phenomenon simulated numerically is a simplified model of the complex physical phenomenon, and is based on several assumptions, the most restrictive being incompressibility, absence of turbulence and cavitation. Furthermore, the spatial discretization of the domain might neglect important flow features, such as bubbles and discrete vortices.

The following list enumerates the approximations which might possibly invalidate the present numerical results. The listed parameters will then be analyzed in detail in the remaining of this section.

- *Simulation time.*

- *Turbulence.*

- *Cavitation.*

- *Air loss.*

- Through the *sliding interface*.

- Within the *rotating domain*.

- *Bubbly flow mechanics.*

- *Compressibility.*

- Flow around the *blade*.

### 6.2.1 Simulation time

The simulated time—only one second for most simulations, corresponding to about 15 revolutions—is much shorter than the duration of an experimental test, but long enough to reach oscillatory, quasi-steady forces. This assumption is corroborated by the fact that a steady-state flow pattern is achieved in less than 10 revolutions during experiments.

Recent experiments<sup>1</sup> have shown different ventilation modes occurring during the same test, where the blade loads are moving from one level of quasi-steady oscillatory forces to a completely different level, without changing any parameter. This change occurs after several seconds, at a time much longer than the one reached with a numerical simulation. Although simulating different ventilation modes is out of the scope of this study, it is possible that a simulation of much longer time could capture other flow modes.

### 6.2.2 Turbulence

All the results presented in Chapter 5 were obtained using a laminar flow, without introducing a turbulence modeling, unless otherwise stated.

This assumption was based on the fact that the free-surface deformation due to an attached flow over a lifting surface is due to the pressure forces exerted from the body, while viscosity plays a marginal damping role.

However, turbulence is important for flow separation, and it is not known *a priori* what role it is playing when ventilation occurs. A simulation including turbulence was thus attempted (Figure 5.13), showing very little changes with respect to the laminar solution.

### 6.2.3 Cavitation

While rotating in water, the pressure on the blade might fall below the vapor pressure leading to cavitation. The propeller is specifically designed not to cavitate when fully submerged. Nevertheless, Nishiyama (1986) has shown that the low pressure achieved at the core of vortical systems—tip-vortex or free-surface vortex—might induce cavitation on the blade surface.

For the present fully ventilated case, ventilation should always occur before cavitation, since the vapor pressure leading to cavitation is lower than atmospheric pressure. This is questionable for a partially ventilated case, where a link might exist between ventilation and cavitation (Kozłowska et al., 2009).

The possible cavitation inception can trigger bubble formation through a nucleation process and interact with the ongoing ventilation. If occurring, this phe-

---

<sup>1</sup>Preliminary results from A.M. Kozłowska during the ventilation test campaign *Koz10*.

nomenon is not captured with the present formulation, whereas a cavitation model should be introduced in order to account for:

- the formation and transport of vapor bubbles,
- the turbulent fluctuations of pressure and velocity,
- the magnitude of noncondensable gases, which are dissolved or ingested in the operating liquid.

Singhal et al. (2002) have derived the phase-change rate expressions from a reduced form of Rayleigh-Plesset equation for bubble dynamics. These rates depend upon local flow conditions (pressure, velocities, turbulence) as well as fluid properties (saturation pressure, densities, and surface tension). The phase-change rate expressions employ two empirical constants, which have been calibrated with experimental data covering a very wide range of flow conditions, and do not require adjustments for different problems.

#### 6.2.4 Air loss

In this section the possibility of air losses due to the adopted numerical implementation is investigated.

##### 6.2.4.1 Through the sliding interface

Air mass-flow might be lost through the sliding interface, i.e. the air flowing through the interface rotating with the propeller is smaller than the air flowing through the corresponding fixed surface.

The source of this error could be searched in:

- *interpolation*  
the projection of the nodes from the rotating to the fixed surface can lead to interpolation errors in the areas through which fluxes are computed;
- *grid size*
  - time step too high with respect to the grid size;
  - air bubbles of the size of a few grid cells could be numerically lost through the sliding interface.

The air mass-flow-rate is conserved through all the sliding interfaces, as shown in Figure 6.5, where the results obtained on the fixed and moving interfaces are perfectly overlapped—and thus can not be distinguished.

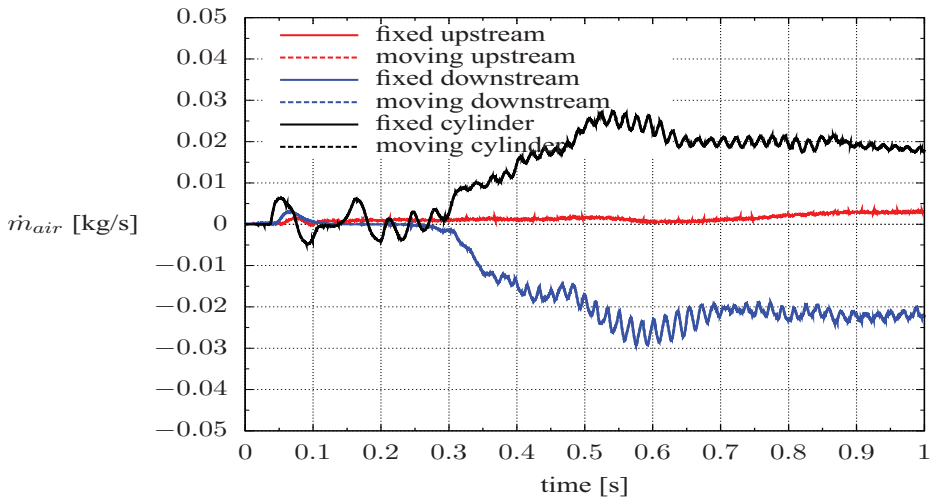
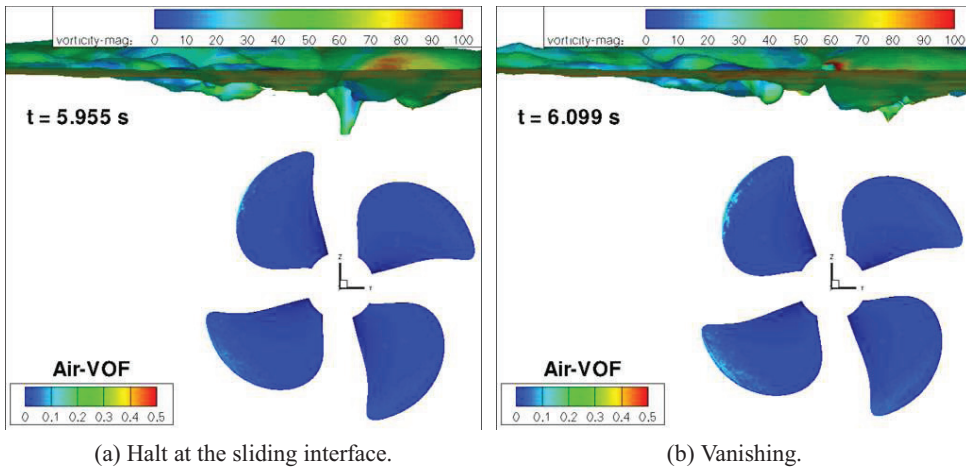


Figure 6.5: Air mass-flow-rate through the static and moving sliding interfaces.

However, air bubbles smaller than the cell size might still be filtered out at the sliding interface, as observed for the free-surface vortex halting (Figure 6.6a) and then vanishing (Figure 6.6b).



(a) Halt at the sliding interface.

(b) Vanishing.

Figure 6.6: Halt and vanishing of the free-surface vortex impinging the sliding interface.

### 6.2.4.2 Within the rotating domain

The air mass-flow-rate is conserved: the flow rate of air entering and leaving the sliding interface over a certain simulation time is equal to the rate of change of air contained in the rotating cylinder delimited by the sliding interfaces (Figure 6.7).

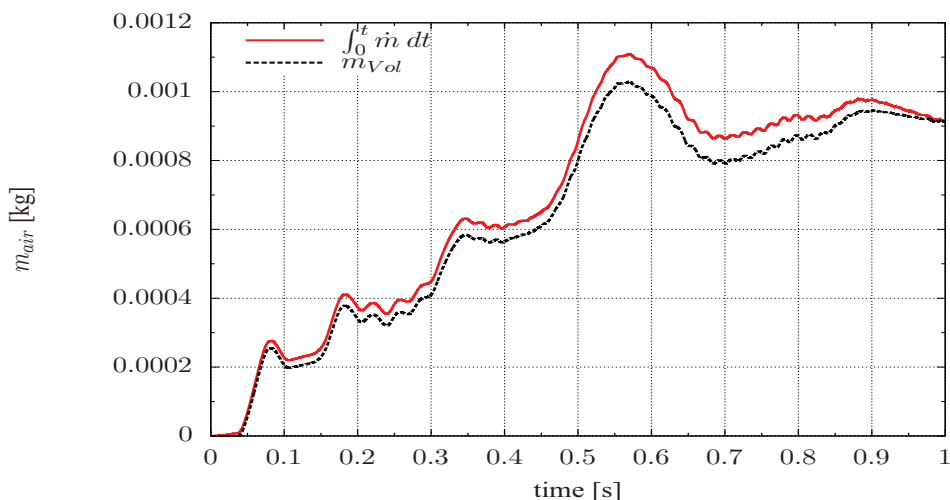


Figure 6.7: Air-mass content as a function of time.

### 6.2.5 Bubbly flow

Experiments show—from the very beginning, when ventilation occurs—a rather uniform mixture of air and water around the propeller disc, rather than two distinct phases with a sharp separation between air and water, as seen from the CFD calculations.

The tiny bubbles seen in the experiments, characterized by a diameter of  $\mathcal{O}(10^{-2})$  m, are not captured by the numerics with the used discretization. The buoyancy force acting on a bubble of diameter  $D$  is  $\mathcal{O}(D^3)$ , while the drag force is  $\mathcal{O}(D^2)$ . The larger bubbles simulated with CFD will thus be subject to higher buoyancy-to-drag force ratio—compared to the small bubbles filling the same enveloped volume. As a result, the simulated entrapped air will rise quicker and dissolve faster than in reality.

Looking at Figure 6.4a, the display of the interface with  $\gamma_{air} = 0.5$  does not give a complete picture of the presence of air in the numerical domain. The visualizations of air-volume-fractions between 0 and 0.5 (Figure 6.8) show a larger domain with smaller air content, giving a final picture compatible with the presence of bubbles observed during the experiments (Figure 6.4b).

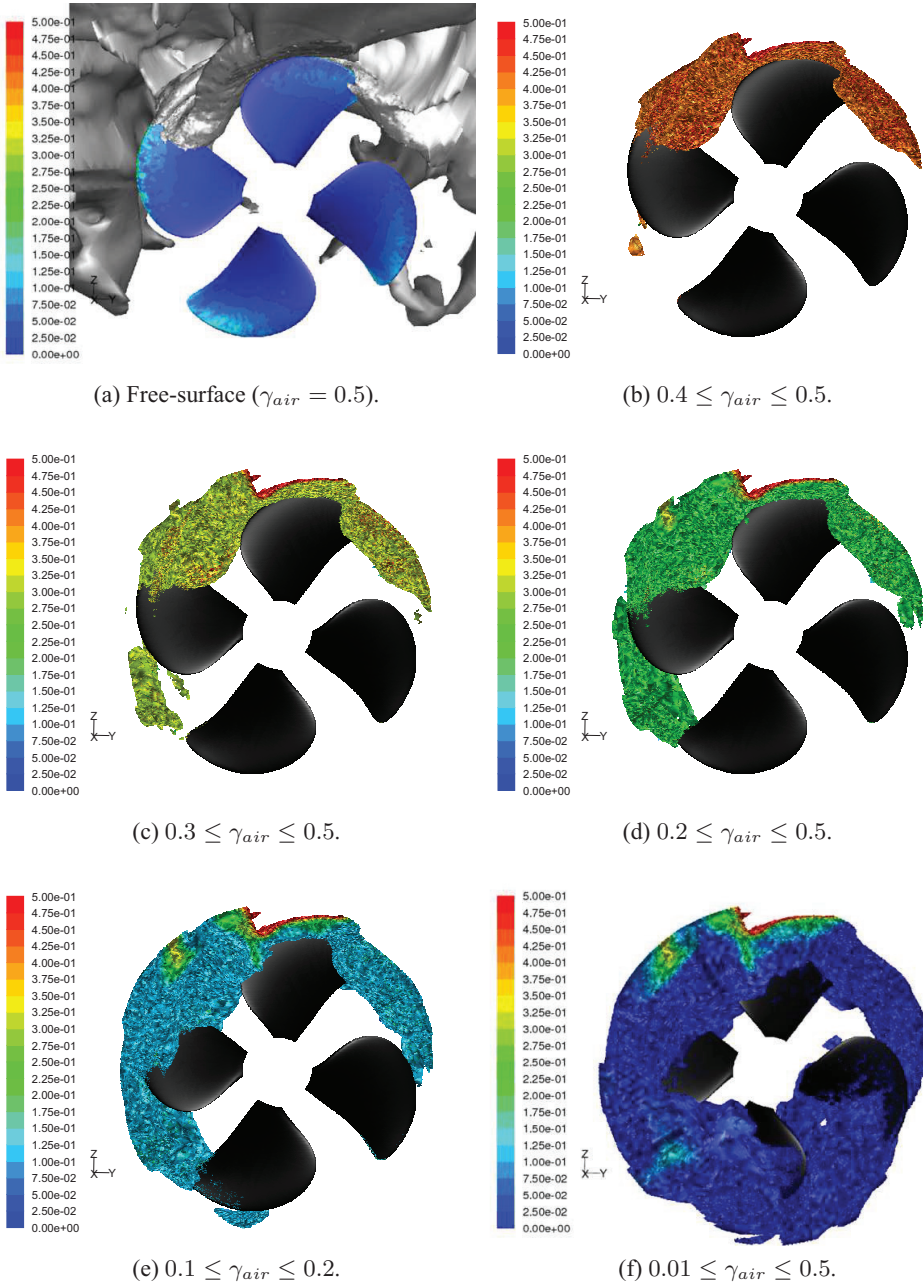


Figure 6.8: Instantaneous flow field

This qualitative similarity does not allow us to draw a final conclusion about the effect of these bubbles on the forces on the blade. The presence of air with  $\gamma_{air} < 0.5$  can be the result of the numerical diffusion introduced by the VOF method, which tends to spatially diffuse the originally sharp air-water interface while the time is marching.

On the other hand, the domain with  $\gamma_{air} < 0.5$  can be due to the physical nucleation of air bubbles and following coalescence at the high pressures achieved in proximity of the propeller. Bubble dynamics — breakup, coalescence and interactions — is strongly dependent (Clift et al., 1978; Brennen, 2005) on the mutual action of surface tension and turbulence.

Surface tension acts as the force restraining deformation and tends to stabilize the interface, while viscous forces slow the rate of growth of unstable surface waves. The total local shear stress,  $\tau$ , imposed by the continuous phase acts to deform a drop or bubble, and to break it if the counter-balancing surface tension forces and viscous stresses inside the fluid particle are overcome.

Where implemented, turbulence is treated with a two-equation model, or Eulerian model, that treats the discrete phase as a continuum and use conservation equations for mass and momentum and closure equations for the turbulence parameters of the flow, in order to solve for the turbulence field and the average behavior of the dispersed phase. Michaelides (2006) has described the intrinsic limitations of the Eulerian model in bubble dynamics. Being essentially a continuum model for interacting fluids, this approach does not allow to properly account for the effects of particle interactions and collisions.

A different approach to solve the turbulent flow field is given from the Lagrangian models, that treat the air bubbles as discrete elements separated from the continuous phase and use an equation of motion to determine the trajectories of a number of immersed objects. The Lagrangian models treat the immersed objects in turbulence individually. The main characteristics of the Lagrangian models are that they determine the trajectories of a number of elements of the dispersed phase by using an explicit equation of motion for the immersed objects, which stems from Newton's second law. This equation accounts fully and explicitly for the forces acting on the dispersed phase and is written in a Lagrangian frame of reference that coincides with the geometric center of the elements of the dispersed phase. The continuous phase is modeled in a Eulerian frame of reference.

### 6.2.6 Compressibility

Compressibility was neglected throughout the present work. This is an established assumption for water, but could be too stringent within the gaseous phase. The region containing air was cut with a  $x - y$  plane passing through the propeller axis

(Figure 6.9a) in order to show the contours of pressure (Figure 6.9b)—subtracted from the atmospheric pressure—which is everywhere negative.

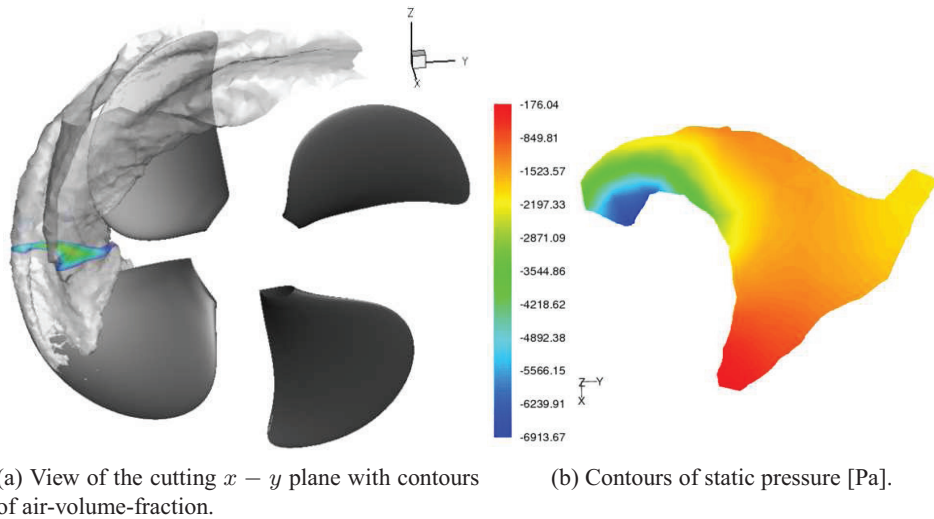


Figure 6.9: Contours of air-volume fraction and static pressure on the  $x - y$  mid-plane cutting the region with air.

Assuming an isentropic process, i.e. adiabatic and reversible, of an ideal gas, pressure and density can be expressed by the isentropic relationship:

$$\left(\frac{p}{\rho}\right)^\gamma = \text{constant} \quad (6.1)$$

where  $\gamma = c_p/c_V$  is the heat capacity ratio, which is equal to 1.4 for a diatomic ideal gas (air).  $c_P$  and  $c_V$  are the specific heat capacities of the gas, suffix  $P$  and  $V$  referring to constant pressure and constant volume conditions, respectively. According to Equation 6.1, a volume expansion would follow a pressure decrease of an air bubble drawn down from the free surface. The constant in the isentropic relation (Equation 6.1) can be referred to the initial state above the free surface in order to determine the expansion of the drawn bubble:

$$\left(\frac{p}{\rho}\right)^\gamma = \left(\frac{p_0}{\rho_{air}}\right)^\gamma \quad (6.2)$$

The maximum pressure-difference computed with CFD in the region of air (Figure 6.9b) is about 7000 Pa, which is small with respect to the atmospheric pressure (101325 Pa). According to Equation 6.2, the corresponding density inside this region will not differ significantly from the air density, and the expansion the air

volume would be subject to—including compressibility—would be negligible. It will later be stressed that the pressure difference computed by CFD can be underestimated within the core of the tip vortex. A larger pressure difference might invalidate the assumption of incompressibility, leading to a volume expansion which can not be neglected.

Full-scale pressure-differences will also be larger, as computed from the equality of the pressure coefficients in model ( $m$ ) and full ( $s$ ) scale:

$$\frac{p_s - p_0}{\frac{1}{2}\rho U_s^2} \equiv \frac{p_m - p_0}{\frac{1}{2}\rho U_m^2} \Rightarrow p_s - p_0 = \left(\frac{U_s}{U_m}\right)^2 (p_m - p_0) = \lambda(p_m - p_0) \quad (6.3)$$

Using a typical full-scale diameter of 4 m, the pressure difference in full scale would be  $\lambda = D_s/D_m = 16$  times the corresponding model-scale value, about  $16 \times (-7000) = -112000$  Pa, thus larger than the atmospheric pressure in absolute value. It is clear that for this obtained vacuum pressure compressibility will matter and the air drawn by the full-scale propeller will be subject to an expansion leading to a stronger ventilation.

This consideration was drawn assuming that the gaseous phase is only constituted of air. The contours of air-volume-fraction on the  $x - y$  mid-plane cutting the region with air (Figure 6.10) identifies a mixture of air and water, where the air content at the center of this region is about 80%. This mixture is rapidly formed after air is drawn and mixed with water due to propeller rotation.

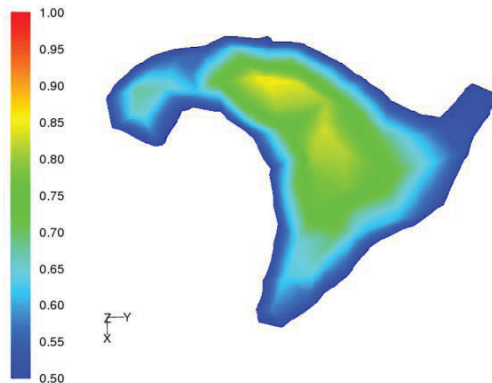


Figure 6.10: Contours of air-volume fraction on the  $x - y$  mid-plane cutting the region with air.

In order to assess the assumption of incompressibility, we start writing the

Bernoulli equation for an inviscid compressible flow:

$$\frac{U^2}{2} + \frac{\gamma}{\gamma - 1} \frac{p}{\rho} = \text{constant} \quad (6.4)$$

The sound speed  $a$  can be written for an isentropic process:

$$a^2 = \frac{dp}{d\rho} = \gamma \frac{p}{\rho} \quad (6.5)$$

We now assume that the entropy level is constant not only in time (isentropic), but also in space, i.e. the process is homentropic. Equation 6.4 can be re-written as:

$$\frac{U^2}{2} + \frac{\gamma}{\gamma - 1} \frac{p}{\rho} = \frac{\gamma}{\gamma - 1} \frac{p_a}{\rho_a} \quad (6.6)$$

with  $p_a$  and  $\rho_a$  computed at a stagnation point, i.e. where the velocity is zero. Using Equation 6.5, the previous formula becomes:

$$\frac{\gamma - 1}{2} U^2 + a^2 = a_a^2 \quad (6.7)$$

Dividing by  $a^2$  and introducing the Mach number  $M = U/a$  a different expression for the Bernoulli equation can be found:

$$\frac{a_a^2}{a^2} = 1 + \frac{\gamma - 1}{2} M^2 \quad (6.8)$$

Using the isentropic relation (Equation 6.1) and the ideal gas law  $p/\rho = \mathcal{R}T$  ( $\mathcal{R}$  and  $T$  are the ideal gas constant and the absolute temperature, respectively), an analogous expression for pressure and density can be found:

$$\frac{p_a^2}{p^2} = \left( 1 + \frac{\gamma - 1}{2} M^2 \right)^{\frac{\gamma}{\gamma - 1}} \quad (6.9a)$$

$$\frac{\rho_a^2}{\rho^2} = \left( 1 + \frac{\gamma - 1}{2} M^2 \right)^{\frac{\gamma}{\gamma - 1}} \quad (6.9b)$$

According to Equations 6.9, considering the flow as incompressible is a reasonable assumption for  $M \rightarrow 0$ . An acceptable upper limit is  $M = 0.3$ , where it can be shown that the error obtained from the incompressible Bernoulli equation is about 2.3% (it is about 1% for  $M = 0.2$ ).

The maximum velocity attained around the propeller in corresponding open water conditions is about 12 m/s. Using the value of 340 m/s for the sound speed in air, the corresponding Mach number is 0.04, thus well below the upper limit for incompressibility just found.

It was earlier found that the air drawn from the propeller is rapidly mixed with water along its rotation, such that a mixture is formed with a concentration of the two phases variable in space and time. For such a mixture, the speed of sound will be different from those of the single phases. An expression was derived by Wood (1930):

$$a_{mixture} = \sqrt{\frac{E_l E_g}{[(1 - \gamma)\rho_l + \gamma\rho_g][(1 - \gamma)E_g + \gamma E_l]}} \quad (6.10)$$

where  $E$  is the bulk modulus and subscripts  $l$  and  $g$  are referred to the liquid and gaseous phase, respectively. Equation 6.10 is plotted in Figure 6.11. For a wide range of the air-filling-ratio between 0.1 and 0.9 the mixture sound speed is below 40, reaching at 0.5 the minimum value, around 24 m/s. Using the maximum velocity found in open water, the Mach number can increase up to 0.5 for a 50% air-volume-fraction. The corresponding error obtained using the incompressible Bernoulli equation is still modest, about 6.4%, but might invalidate the assumption of incompressibility.

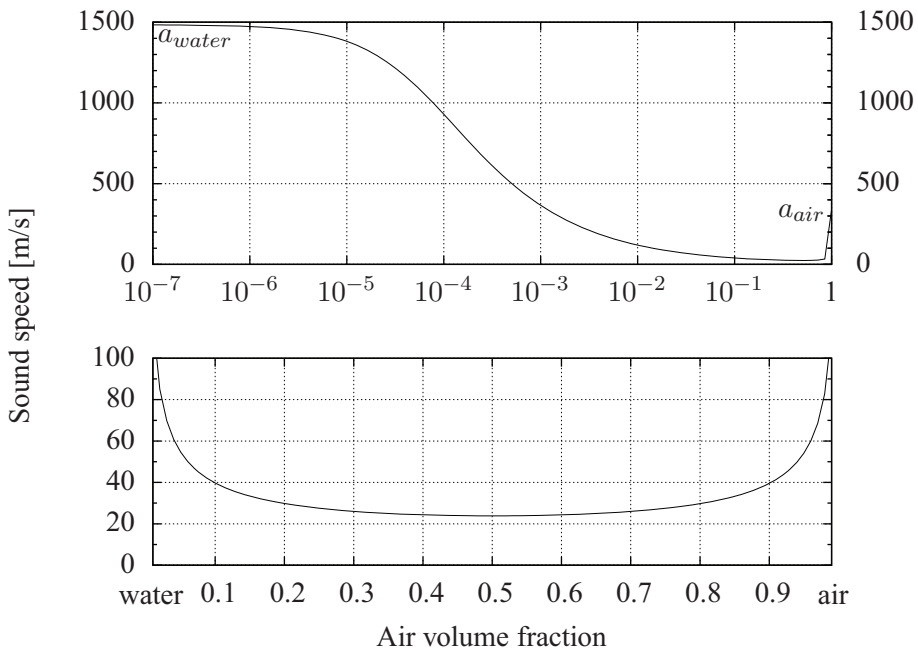


Figure 6.11: Sound speed for the mixture phase computed using Equation 6.10 (Wood, 1930).

### 6.2.7 Pressure drop

The thin cavity-sheet visible on the blade wall (Figure 6.4b) suggests that the suction side is completely covered with air. In these conditions, the minimum thrust measured in the experiments is about one third of that measured in deep water, and it corresponds to the thrust exerted only by the pressure side when fully submerged.

The corresponding picture from the numerical simulations (Figure 6.4a) shows a suction side covered with air only partially, and computes subsequently a thrust higher than in the experiments.

Two mechanisms are introduced in order to explain the under-estimation of air content on the surface of the blade:

- I. the amount of air reaching the blade is not sufficient;
- II. the amount of air reaching the blade, although being sufficient, remains confined around the tip, not being able to propagate to the remaining surface of the blade;

Both mechanisms assert that the pressure drop is not sufficient to suck enough air, respectively:

- (i) along the air channel connecting the blade with the free surface;
- (ii) locally, on those locations of the surface of the blade not reached by the air;

The capture of the pressure field inside the surface of the blade is normally achieved accurately with present RANS methods. However, an inappropriate modeling of turbulence could lead to local errors in the pressure field (ii). The flow on the blade is assumed completely laminar or turbulent, depending on whether turbulence modeling was implemented. In reality, a laminar-to-turbulent transition will occur somewhere on the suction side, in presence of adverse pressure gradients. The location of the transition would in turn modify the local pressure field on the walls.

The under-estimation of the pressure locally in the computational domain can be related to the mesh refinement and to the numerical accuracy achieved.

The unsteady nature of the phenomenon required an unsteady simulation over a truncated computational domain sufficiently large to avoid unphysical reflections from the boundaries. Although run in parallel, this type of simulations requires long-time simulations, ranging between 4 and 12 weeks on a 16 cores cluster.

In this framework, a consistent mesh refinement study could not be performed and the uncertainty of the obtained results (Roache, 1997) could not be assessed. Nevertheless, in order to establish the differences with respect to the base-line grid, all the cells encompassing the ventilated region were refined once halving the size

of the segments forming a cell. A comparison of the thrust coefficient obtained with the base-line and locally-refined grids was shown in Figure 5.16. The trend achieved with the refined grid is very similar, and the differences obtained can not explain the substantial discrepancy of the numerical simulations with respect to the experiments.

However, the mesh refinement was probably not adequate to resolve some local flow features where strong pressure gradients exist, such as at the leading edge of the blade and in the core of the tip vortex, connecting the blade to the free surface through an air channel (*i*). Once ventilation has started, the amount of drawn air will depend on the sectional area of the channel and on the achieved pressure drop.

### 6.2.7.1 Tip vortex

The under-pressure computed in the tip vortex connecting the blade with the atmospheric pressure might be insufficient to allow more air-mass-flow entering the blade surface.

In § 4.5.1 the inception of ventilation for a moderately submerged propeller was described by means of the visualization of the tip vortex "breaking" a hole in the free surface. This tip vortex could still play an important role after the blade has become surface-piercing, acting as a channel continuously supplying air to the blade's surface. The air mass-flow-rate through this channel will depend on its diameter and on the minimum pressure achieved in correspondence to the blade.

Accurate predictions of the vortex flow phenomena require a very fine mesh in the vortex core. The exact location of the vortex core and the level of its under-pressure depend strongly on the mesh refinement, due to the high velocity gradients present in the flow (Chen, 2000; Bulten and Oprea, 2006; Li et al., 2006).

Assuming a solid body rotation distribution within the core of the tip vortex, the radius  $R_{tip}$  can be expressed in terms of the pressure in its center  $p(0)$ :

$$R_{tip} = \frac{\gamma_{tip}}{2\pi} \sqrt{\frac{\rho}{p_0 - p(0)}} \quad (6.11)$$

where  $\gamma_{tip}$  is the circulation of the tip vortex.

Assuming along the blade a span-wise circulation  $\Gamma(r)$ , the circulation of the free vortices  $\gamma_F(r)$  shed at each radial position can be obtained as:

$$\gamma_F(r) = -\frac{\partial\Gamma(r)}{\partial r} dr \quad (6.12)$$

The total circulation of the tip vortex  $\gamma_{tip}$  can then be computed summing up all the free vortices rolling up to form a concentrated tip vortex. The observation of the path-lines along the blade in open water (Figure 6.12) can give a rough estimation

of the radial location above which free vortices merge to form the tip vortex, about  $r = 0.1$  m ( $r/R = 0.8$ ).

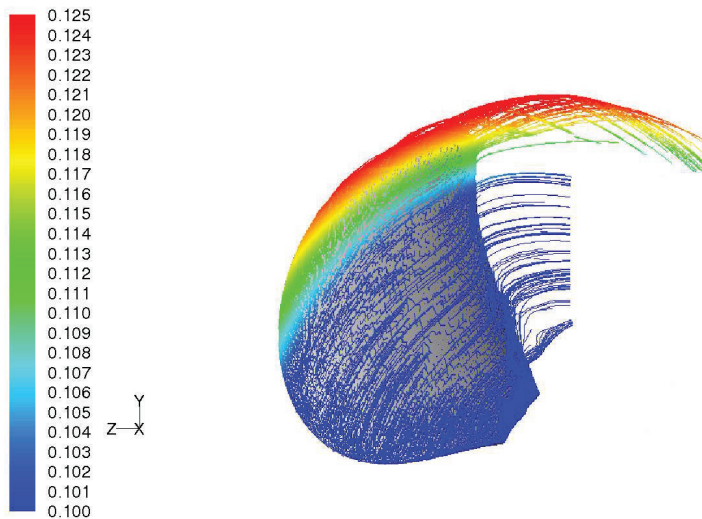


Figure 6.12: Path-lines in open water colored with the radial position [m].

Using the span-wise circulation obtained using the BEM solver AKPA,  $\gamma_{tip}$  was found to be equal to  $0.13$  m<sup>2</sup>/s.

Introducing the pressure computed from CFD calculations (Figure 6.13), Equation 6.11 gives  $R_{tip} \approx 5$  mm. With this value, one would expect that the vortex is properly described close to the blade, where the cell size is smaller than 1 mm.

Since the distance traveled by the vortex from the tip to the free-surface is very short, we will assume for simplicity that the radius would remain constant along this path, neglecting the effect of diffusion. In proximity of the undisturbed free-surface—where the cell size is about 5 mm—the diameter of the tip vortex is distributed over only two grid cells, which seem inadequate to capture the strong gradients occurring within the vortex core.

Another consideration should be made about RANS. Being based on the *time averaging* of the turbulent quantities, the flow field obtained with these methods can be smoothed out, obtaining poor performances while attempting to properly describe vortical structures. Solving directly the turbulent quantities could help resolving the unsteady nature of the vortices. Whereas a Direct Numerical Simulation (DNS) can not be attempted due to the large extent of the present numerical domain, the use of Large Eddy Simulations (LES) could be an option in order to better resolve the tip vortices, since the only limitation for this model is given by

the grid size (*space filtering*).

Among other applications, Karlsson and Fuchs (2000) and Secareanu et al. (2005) have satisfactorily applied LES methods to study the evolution of the ground vortex. Nagahara et al. (2006) concluded that RANS calculations have inherent limitations in resolving the unsteady flow of the vortex sucked in a pump intake sump, when compared with LES. On the other hand, LES models are very sensitive to the grid size, and care should be taken in the discretization of the domain, especially close to the blades.

There is a mutual interaction between the tip vortex and the drawn region with air. Figure 6.13 shows the pressure coefficient on the  $x - y$  mid-plane, together with the position of the mixture phase (starboard). The intersection of the blades with the  $x - y$  mid-plane is also visualized. It was earlier suggested that the tip vortex located starboard carrying along  $z_+$  vorticity is responsible for ventilation inception for this moderate submergence. The same vortex is in turn affected by the presence of the mixture phase, showing much smaller intensities with respect to the tip vortex "freely" traveling in water on the port side.

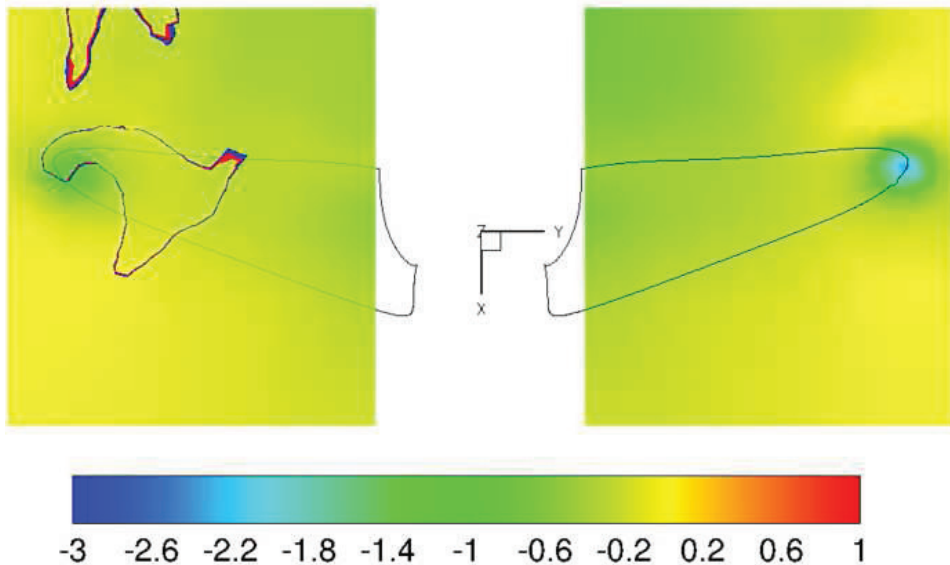


Figure 6.13: Pressure coefficient contours on the  $x - y$  mid-plane.

A visual estimation of  $R_{tip}$  can be obtained from the contours of vortex tangential velocity—axial (Figure 6.15a) and radial velocity (Figure 6.15b) in the fixed reference frame. Assuming for the diameter of the tip vortex the distance

between velocities with opposite signs, the value obtained for the radius  $R_{tip}$  is about 6 mm, which is in agreement with the one found using Equation 6.11 ( $R_{tip} \approx 5$  mm). Assuming that the width of the vortex core remains unchanged after air is drawn—which seems reasonable comparing the port and starboard side in Figures 6.13, 6.15a and 6.15b—and using the corresponding pressure computed from CFD (Figure 6.13), the resulting air-volume-fraction is 0.67, thus within the range shown from Figure 6.10.

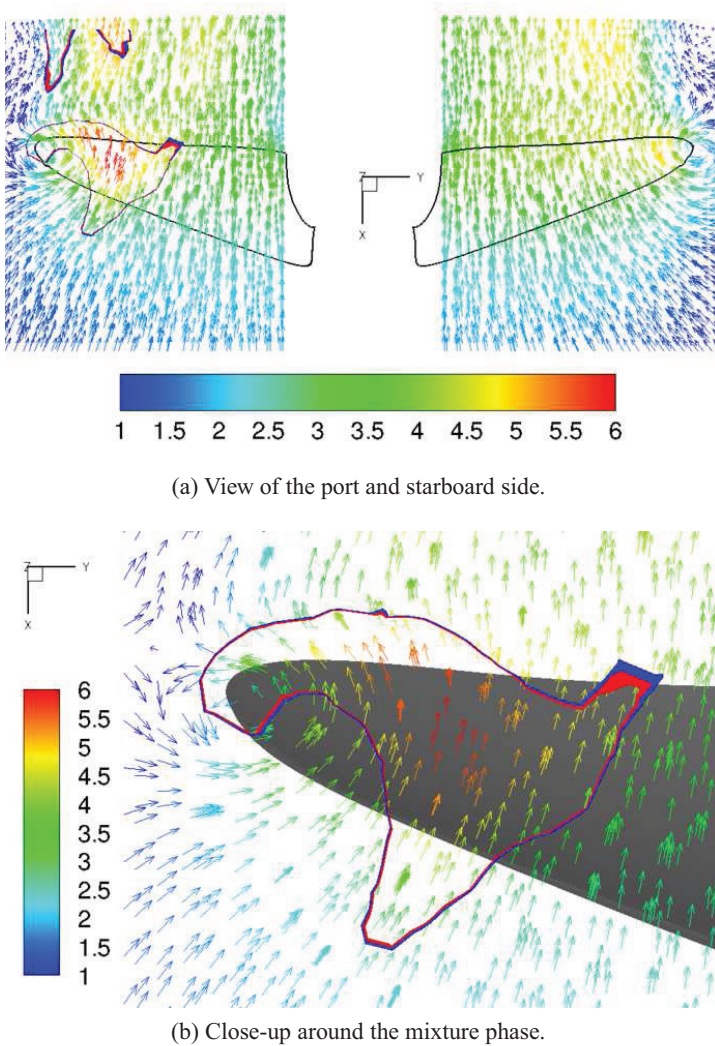
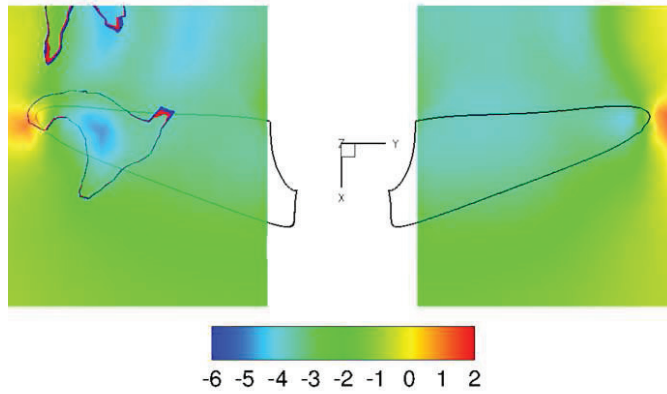
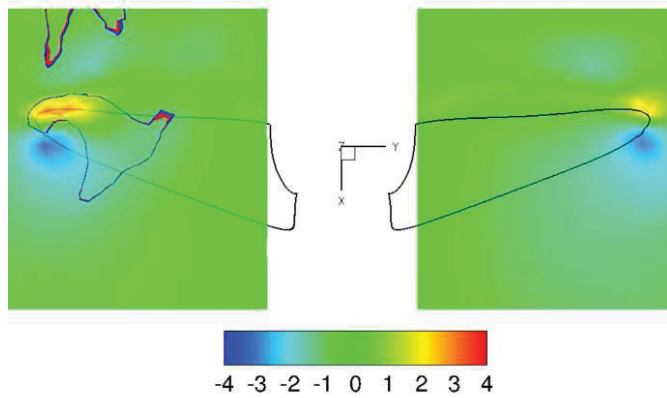


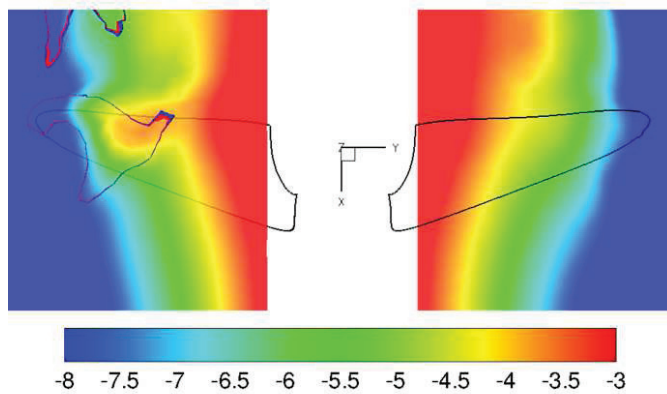
Figure 6.14: Velocity vectors colored with velocity magnitude on the  $x - y$  mid-plane.



(a) Axial velocity.



(b) Radial velocity.



(c) Relative tangential velocity.

Figure 6.15: Velocity contours [m/s] on the  $x - y$  mid-plane.

The presence of air has the effect to accelerate the flow, as shown in Figure 6.14 and 6.15. Since the circulation must remain constant (Kelvin's theorem), vorticity must increase after stretching of the tip vortex towards the free surface, leading to increased tangential velocities in the vortex plane (axial velocities in Figure 6.15a and radial velocities in Figure 6.15b). Vorticity amplification by vortex stretching is a well known phenomenon within a single phase, but it is not clear whether the presence of air itself has the effect of increasing the velocity field, reducing the density of the mixture phase.

Within the vortical channel entraining air a larger velocity parallel to the channel can also be observed (tangential velocity relative to the propeller rotation in Figure 6.15c).

# Chapter 7

## Conclusions

### 7.1 Summary

By means of model tests and numerical simulations the present work aimed at understanding the physical mechanisms underpinning propeller ventilation.

The combination of the propeller submergence, loading and advance ratio determines the nature of the ventilation mechanism, (i) at deeper submergences through a free-surface vortex and (ii) at moderate submergences through the blade itself piercing the free-surface.

Three different ventilation regimes could be identified, depending on the influence of the above mentioned mechanisms.

- *Free-surface vortex*  
characterized by severe and discontinuous thrust losses occurring when the vortex reaches the surface of the blade; the amplitude during a ventilation event can deviate significantly from the mean value, which is slightly lower than the nominal one.
- *Surface-piercing*  
characterized by uniform thrust losses during the complete revolution; the thrust encompasses a narrow amplitude range around the mean value, which is in turn significantly lower than the nominal one.
- *Intermediate*  
where both mechanisms (i) and (ii) act alternately during the same test case; the thrust encompasses a broad and uniform amplitude range and the mean value is somewhere in between those found in the previous two regimes.

The high-speed video recordings synchronized with the measurements allowed establishing a relation between dynamic forces and ventilation. This was achieved

both for the recurring loads during a cycle of full ventilation and for the ventilation through a free-surface vortex.

For the latter case, the literature study allowed identifying analogies with other phenomena seen in fields different from marine applications, such as the inlet vortex in pump sumps and the ground vortex at the inlet of aircraft engines—for which an extensive literature exists.

The analysis of the first time instants, before a quasi-steady oscillatory solution is obtained, allows a deeper insight into two distinctive types of ventilation inception:

(a) *Surface-piercing* at moderate submergence ( $h/R = 1.4$ ): Blades become surface-piercing after the deformation of the free surface.  
 (b) By *free-surface vortex formation* at deeper submergence ( $h/R = 1.72$ ): Vortical structures forming on the free surface reach the propeller tip.

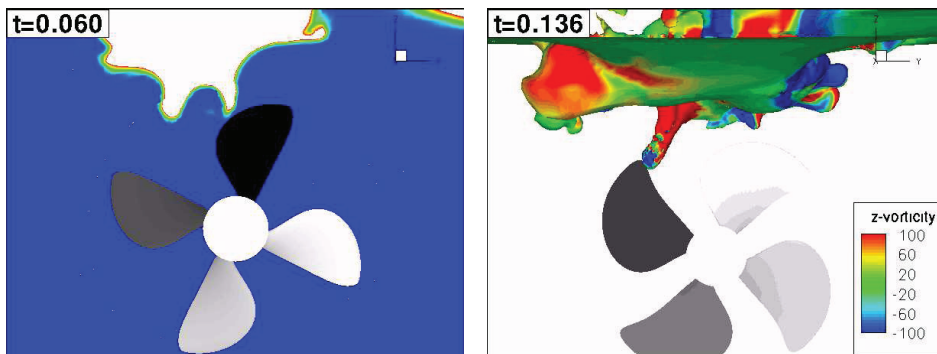
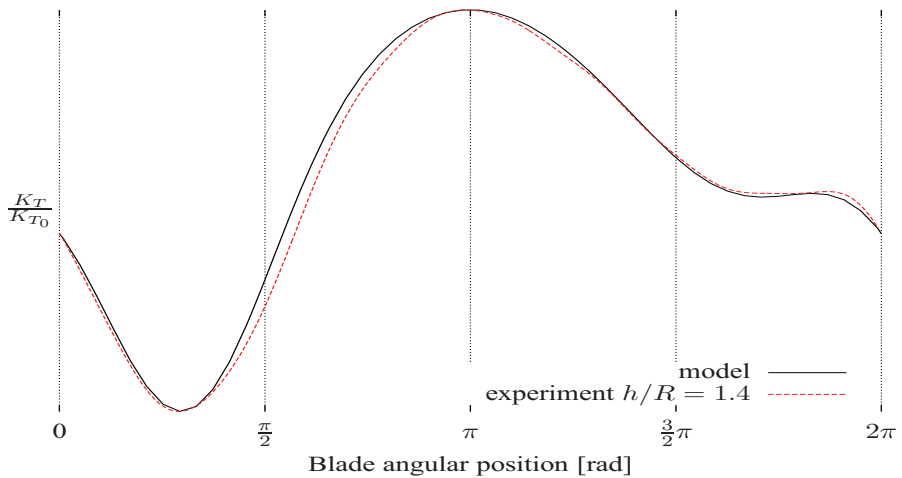


Figure 7.1: Two types of ventilation inception, from numerical simulations.

Unlike ventilation of surface-piercing propellers with supercavitating profile, it was found that the tip vortex has a dominant role in the ventilation of conventional propellers. A qualitative model was derived (Figure 7.2a) based on the tip-vortex system transporting air to the propeller and leading to two main thrust losses: (i) about  $\pi/4$  leading to an absolute minimum load and (ii) about  $3/2 \pi$  leading to a local minimum load.

The complexity of the ventilation phenomenon itself leads to unstable numerical simulations, very sensitive to the used numerical parameters, somehow reflecting the large deviation found in the experiments. The dynamic loads computed with the numerical model are in satisfactory agreement with the experimental data at the upright position where the blade is piercing the free surface, whereas thrust is over-estimated at all the other angular positions. A thorough analysis of the causes of this deviation was performed, identifying the under-estimation in the numerical simulations of the pressure difference—from the atmospheric pressure—in the tip vortex as the most likely responsible factor.

Among other causes, the assumption of incompressibility was found to be too stringent within the ventilated region, consisting of a mixture of air and water, characterized by a density lower than in water and a speed of sound lower than in air and in water alone.



(a) Total thrust loss

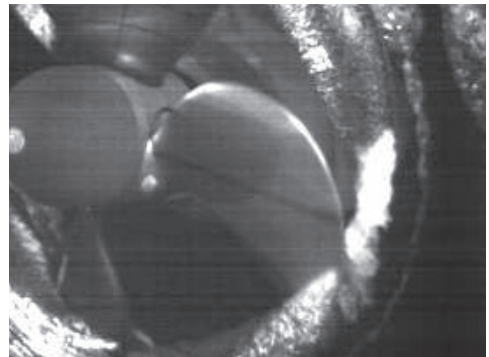
(b) Absolute minimum blade thrust about  $\pi/4$ .(c) Local minimum thrust about  $3\pi/2$ .

Figure 7.2: Dynamic loads during ventilation of a surface-piercing propeller.

## 7.2 Recommendations for future work

Research in ventilation of submerged bodies, with special emphasis to propellers, has been a subject of study already for many years, with renewed interest following the new technology achievements and the always growing computer capabilities. Within this framework, the present research activity can be seen as an intermediate

step towards a fully comprehensive understanding of the mechanisms underpinning the physical phenomenon, which can make its modeling possible. A more general form of the model derived for the dynamic loads occurring during ventilation is thus foreseen as the natural evolution of the present work. This model should contain not only qualitative information about dynamic loads, but also a prediction of their intensities.

RANS methods used in the present calculations have shown their limits in predicting accurately the dynamic loads during ventilation. These limits could be summarized in the difficulty to accurately capture the pressure in the core of the tip vortex that both model tests and numerical simulations have shown to be a key mechanism for ventilation. In this respect, every attempt to refine the grid in order to better capture the low pressures within the tip vortex would result in an increase of the already long computational times and worsen the stability of the simulation. The research of the solution through simpler, less computationally expensive methods is suggested. This could be achieved by modeling the tip vortex, instead of resolving the complex flow-field within its core.

Manzke and Rung (2010) have implemented a "vortex confinement" method in a RANS-based solver to model the tip vortices of a marine propeller, showing how such an approach is able to follow for a longer time the evolution of the tip vortex and better capture the low pressure within its core.

Vortex-confinement involves "regularizing" the numerical diffusion by adding a term depending on local variables—such as grid size and vorticity—to the momentum equation, obtaining confined vortical regions even on coarse grids with low-order discretization schemes (Steinhoff and Underhill, 1994).

Modeling of the tip vortex could also be achieved by an *a priori* knowledge, which might be built upon simpler methods, less sensitive to numerical diffusion, such as potential methods. The obtained fluid-dynamics quantities about the tip vortex could then be fed to the RANS solver to simulate the occurrence of ventilation.

An attempt to include compressibility should also be made in order to verify whether the ventilated region is able to expand and spread on a wider area of the propeller, causing higher thrust losses while the blade is fully submerged.

Concerning strictly the numerics, for this transient calculations the discretization of the pressure-velocity coupling with a typical projection method (Bell et al., 1989; Gresho, 1990) would remove the difficulties inherently related to the SIMPLE method. A more accurate time advancement scheme within two-phase flow is also envisaged.

Some recommendations about experiments will also be made, based on the present experience. Although giving a valuable contribution, especially when combined with synchronized video recordings, blade dynamic loads still remain a *global* measure of the ventilation phenomenon, which depends on *local* pressures

falling below the atmospheric pressure. Whenever possible, force and moments measurements should be accompanied by pressure transducers located on regions expected to have low pressure, such as on the suction side, close to the leading edge and around the tip. This is in practice hard to achieve, due to limited space inside the blade able to fit at the same time a dynamo-meter and one or several pressure transducers.

The investigation of simpler geometries is thus recommended, using for instance a submerged hydrofoil, where pressure sensitive films can be applied. These results can in turn be used to test the capabilities of RANS methods with vorticity confinement on the air drawing through the tip vortex of a submerged foil with finite span and at high angle of attack.

Velocity measurement techniques, such as Particle Image Velocimetry (PIV), are also envisaged in order to better follow vortical structures leading to ventilation. Although some experimental studies on multiphase flow using the PIV technique have been reported, the presence of the dispersed gas bubbles or columns usually introduces problems to the PIV measurements (Deen et al., 2002), thus advanced techniques have been developed. Among others, Defocusing PIV is used to determine a 3D-3C (three components in three dimensions) velocity field using a volume illumination. The separation of the two phases can also be achieved by the combined use of PIV with Laser Induced Fluorescence (LIF), where seeded particles—coated or embedded with a fluorescent dye—fluoresce at a wavelength different from the incident laser light. Nevertheless, PIV measurements technique used for bubbly flow is limited to relatively low volume fractions of the dispersed phase, typically 1-4%.

Image techniques such as PIV are instead particularly suitable to free-surface flow applications, being capable to determine the location of the free surface in an open-channel type flow (Li et al., 2005). The gas phase and liquid phase show different patterns on a PIV photograph—a relatively bright region for the gas phase and a dark region with dense bright points (tracing particles) for the liquid phase—which allow the free-surface level to be detected by an algorithm.

Pressure and velocity measurements will also create an important database for validation of numerical results.

As a last recommendation, all the present and future activities should have in mind the process of extrapolation to full scale. With respect to model scale, lower pressures obtained in the corresponding full-scale conditions would be responsible not only for an easier ventilation inception with more severe thrust losses, but will also lead more quickly to cavitation and make the assumption of incompressibility less valid. A scenario where both cavitation and ventilation coexist, and compressibility of air can not be neglected, would lead to a physical phenomenon more complex than the one described throughout this dissertation.



# Appendix A

## Experimental results

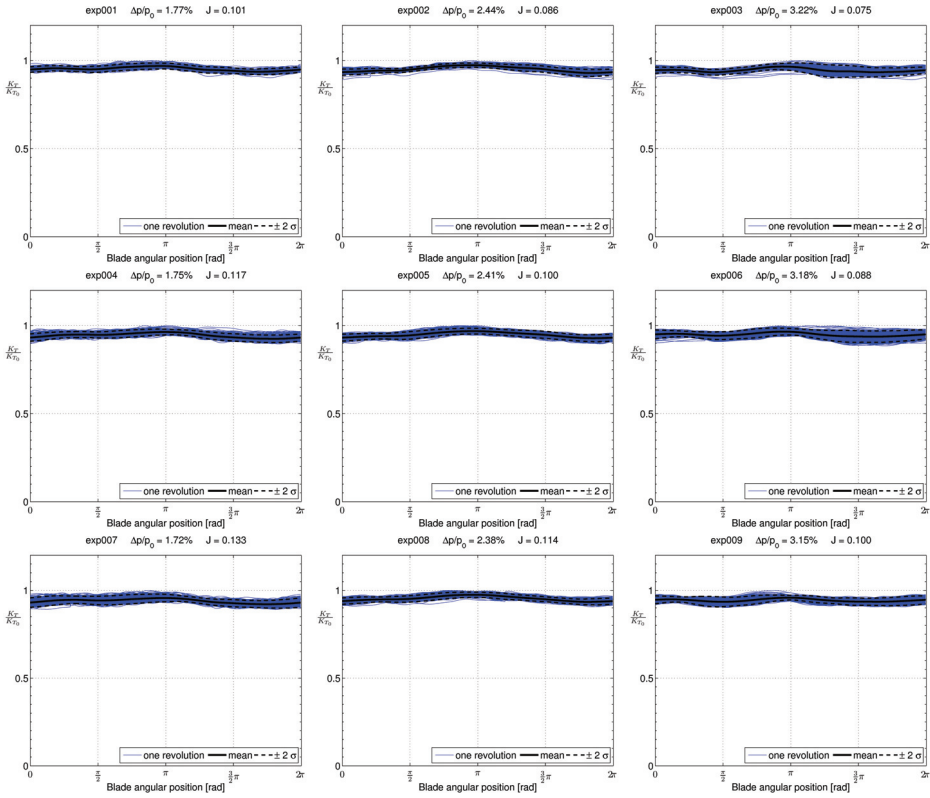
### A.1 Constant shaft frequency

	experiment #	name of the experiment;
	$h/R$	[/] water-depth ratio;
	$U$	[m/s] speed of advance;
Acronyms:	$n$	[1/s] shaft frequency;
	$J$	[/] advance ratio;
	$\Delta p/p_0$	[/] propeller loading;
	$\theta$	[deg] blade correction angle.

$$h/R = 2.97$$

experiment #	$h/R$ [/]	$U$ [m/s]	$n$ [1/s]	$J$ [/]	$\Delta p/p_0$ [%]	$\theta$ [deg]
exp001	2.97	0.30	12	0.100	1.77%	0
exp002	2.97	0.30	14	0.086	2.44%	4
exp003	2.97	0.30	16	0.075	3.22%	14
exp004	2.97	0.35	12	0.117	1.75%	1
exp005	2.97	0.35	14	0.100	2.41%	21
exp006	2.97	0.35	16	0.088	3.18%	35
exp007	2.97	0.40	12	0.133	1.72%	4
exp008	2.97	0.40	14	0.114	2.38%	25
exp009	2.97	0.40	16	0.100	3.15%	42

Table A.1: Test specifications [ $h/R=2.97$ ].

Figure A.1:  $[h/R = 2.97]$ 
 $h/R = 2.44$ 

experiment #	$h/R$ [ $\uparrow$ ]	$U$ [m/s]	$n$ [1/s]	$J$ [ $\uparrow$ ]	$\Delta p/p_0$ [ $\uparrow$ ]	$\theta$ [deg]
exp010	2.44	0.30	12	0.100	1.77%	10
exp011	2.44	0.30	14	0.086	2.44%	20
exp012	2.44	0.30	16	0.075	3.22%	41

Table A.2: Test specifications  $[h/R=2.44]$ .

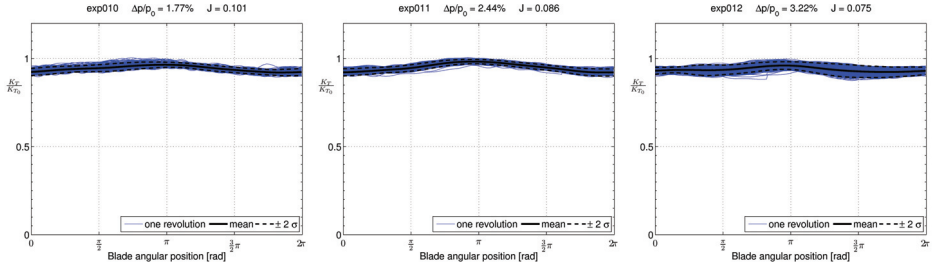


Figure A.2: [ $h/R = 2.44$ ]

$h/R = 2.24$

experiment #	$h/R$ [l]	$U$ [m/s]	$n$ [1/s]	$J$ [l]	$\Delta p/p_0$ [l]	$\theta$ [deg]
exp013	2.24	0.30	12	0.100	1.77%	13
exp014	2.24	0.30	14	0.086	2.44%	26
exp015	2.24	0.30	16	0.075	3.22%	50

Table A.3: Test specifications [ $h/R=2.24$ ].

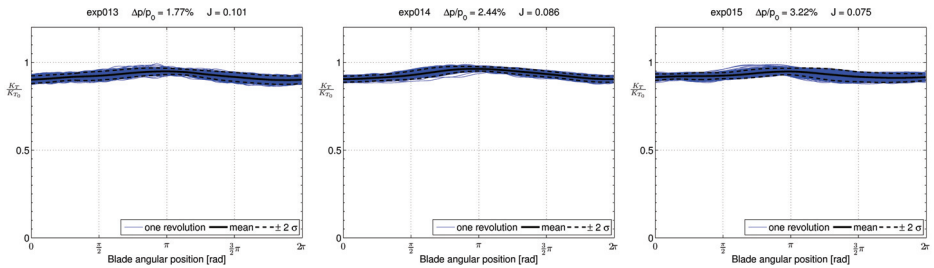


Figure A.3: [ $h/R = 2.24$ ]

$$h/R = 2.04$$

experiment #	$h/R$ [ ]	$U$ [m/s]	$n$ [1/s]	$J$ [ ]	$\Delta p/p_0$ [ ]	$\theta$ [deg]
exp016	2.04	0.30	12	0.100	1.77%	17
exp017	2.04	0.30	14	0.086	2.44%	31
exp020	2.04	0.30	16	0.075	3.22%	58
exp021	2.04	0.35	16	0.088	3.18%	76
exp023	2.04	0.40	16	0.100	3.15%	65

Table A.4: Test specifications [ $h/R=2.04$ ].

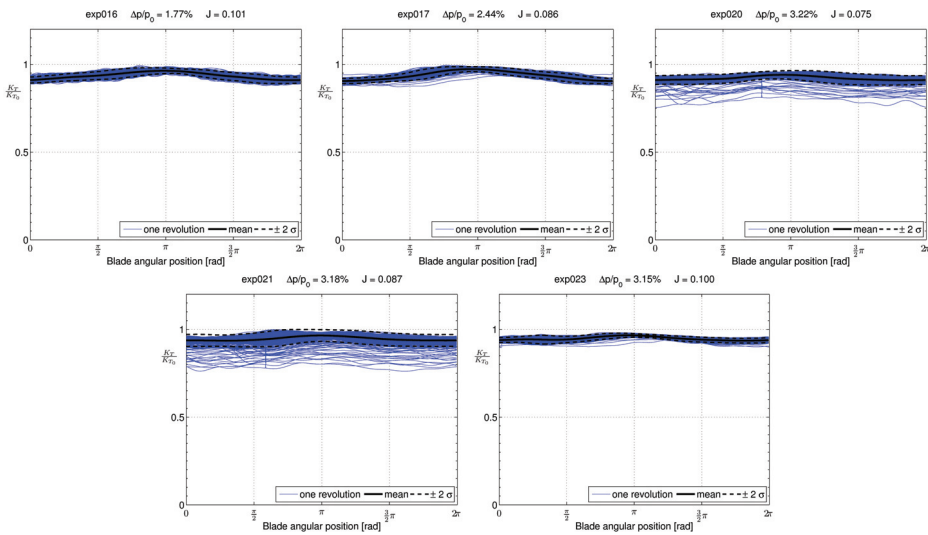


Figure A.4: [ $h/R = 2.04$ ]

$$h/R = 1.96$$

experiment #	$h/R$ [/]	$U$ [m/s]	$n$ [1/s]	$J$ [/]	$\Delta p/p_0$ [/]	$\theta$ [deg]																				
exp024	1.96	0.30	12	0.100	1.77%	36																				
exp025	1.96	0.30	14	0.086	2.44%	46																				
exp026	1.96	0.30	16	3.22%	74	exp027	1.96	0.35	16	0.088	3.18%	72	exp028	1.96	0.35	14	0.100	2.41%	56	exp030	1.96	0.40	16	0.100	3.15%	73
exp027	1.96	0.35	16	0.088	3.18%	72																				
exp028	1.96	0.35	14	0.100	2.41%	56																				
exp030	1.96	0.40	16	0.100	3.15%	73																				

Table A.5: Test specifications [ $h/R=1.96$ ].

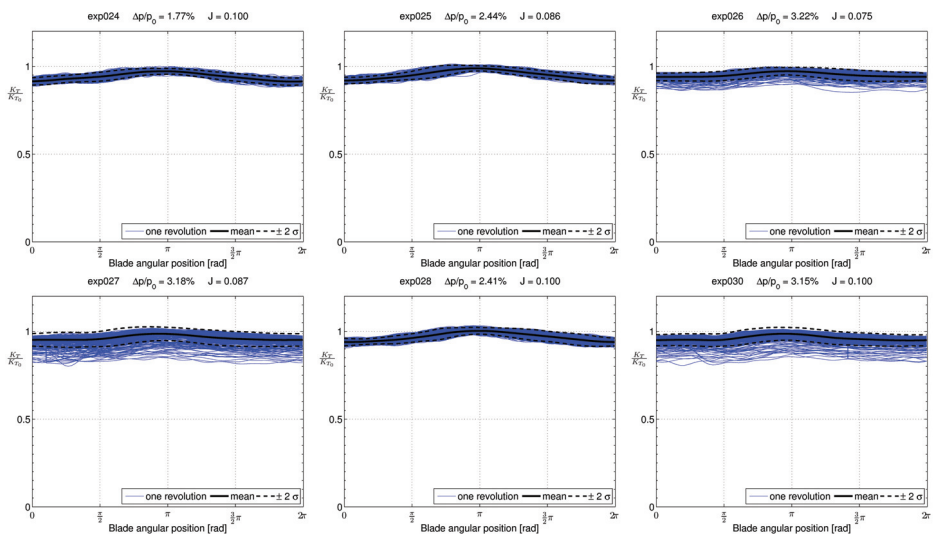


Figure A.5: [ $h/R = 1.96$ ]

$$h/R = 1.88$$

experiment #	$h/R$ [ ]	$U$ [m/s]	$n$ [1/s]	$J$ [ ]	$\Delta p/p_0$ [ ]	$\theta$ [deg]
exp031	1.88	0.30	12	0.100	1.77%	41
exp032	1.88	0.30	14	0.086	2.44%	60
exp033	1.88	0.30	16	3.22%	89	
exp034	1.88	0.35	14	0.100	2.41%	58
exp037	1.88	0.35	16	0.088	3.18%	87
exp039	1.88	0.40	14	0.114	2.38%	64
exp040	1.88	0.40	16	0.100	3.15%	88

Table A.6: Test specifications [ $h/R=1.88$ ].

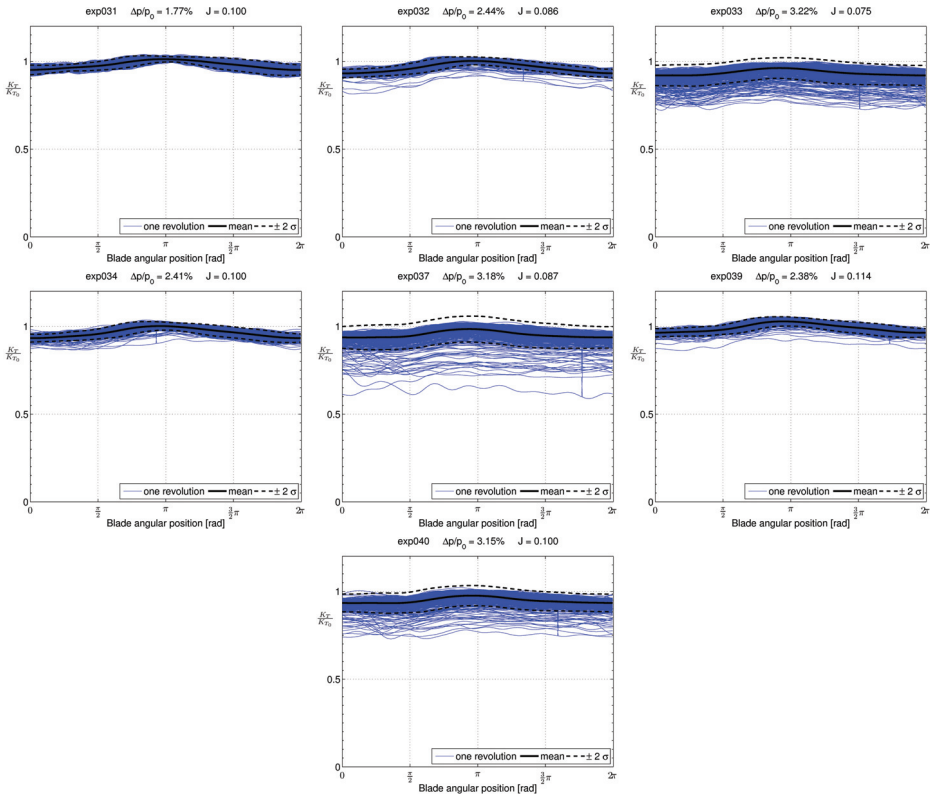


Figure A.6: [ $h/R = 1.88$ ]

$$h/R = 1.80$$

experiment #	$h/R$ [ ]	$U$ [m/s]	$n$ [1/s]	$J$ [ ]	$\Delta p/p_0$ [ ]	$\theta$ [deg]
exp041	1.80	0.30	12	0.100	1.77%	53
exp042	1.80	0.30	14	0.086	2.44%	77
exp043	1.80	0.30	16	0.075	3.22%	95
exp044	1.80	0.35	12	0.117	1.75%	46
exp045	1.80	0.35	14	0.100	2.41%	80
exp046	1.80	0.35	16	0.088	3.18%	95
exp047	1.80	0.40	12	0.133	1.72%	53
exp048	1.80	0.40	14	0.114	2.38%	71
exp049	1.80	0.40	16	0.100	3.15%	90

Table A.7: Test specifications [ $h/R=1.8$ ].

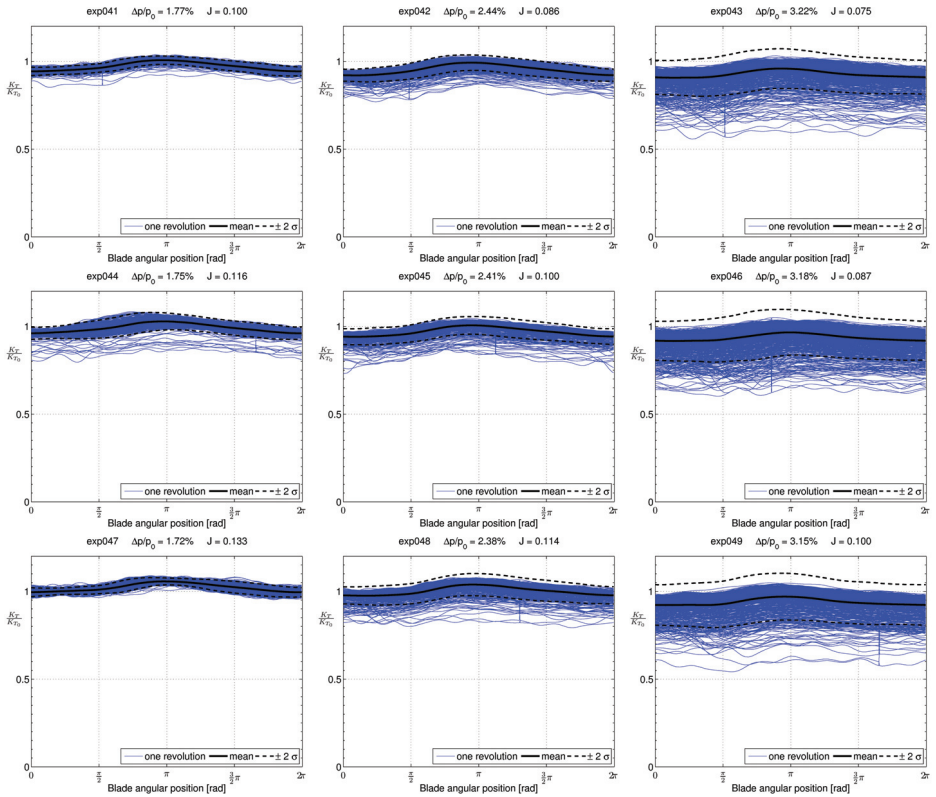


Figure A.7: [ $h/R = 1.80$ ]

$$h/R = 1.72$$

experiment #	$h/R$ [l]	$U$ [m/s]	$n$ [1/s]	$J$ [l]	$\Delta p/p_0$ [l]	$\theta$ [deg]
exp050	1.72	0.30	12	0.100	1.77%	63
exp051	1.72	0.30	14	0.086	2.44%	79
exp052	1.72	0.30	16	0.075	3.22%	100
exp053	1.72	0.35	12	0.117	1.75%	57
exp079	1.72	0.35	16	0.088	3.18%	103
exp080	1.72	0.35	14	0.100	2.41%	92
exp081	1.72	0.40	12	0.133	1.72%	64
exp082	1.72	0.40	14	0.114	2.38%	85
exp083	1.72	0.40	16	0.100	3.15%	104

Table A.8: Test specifications [ $h/R=1.72$ ].

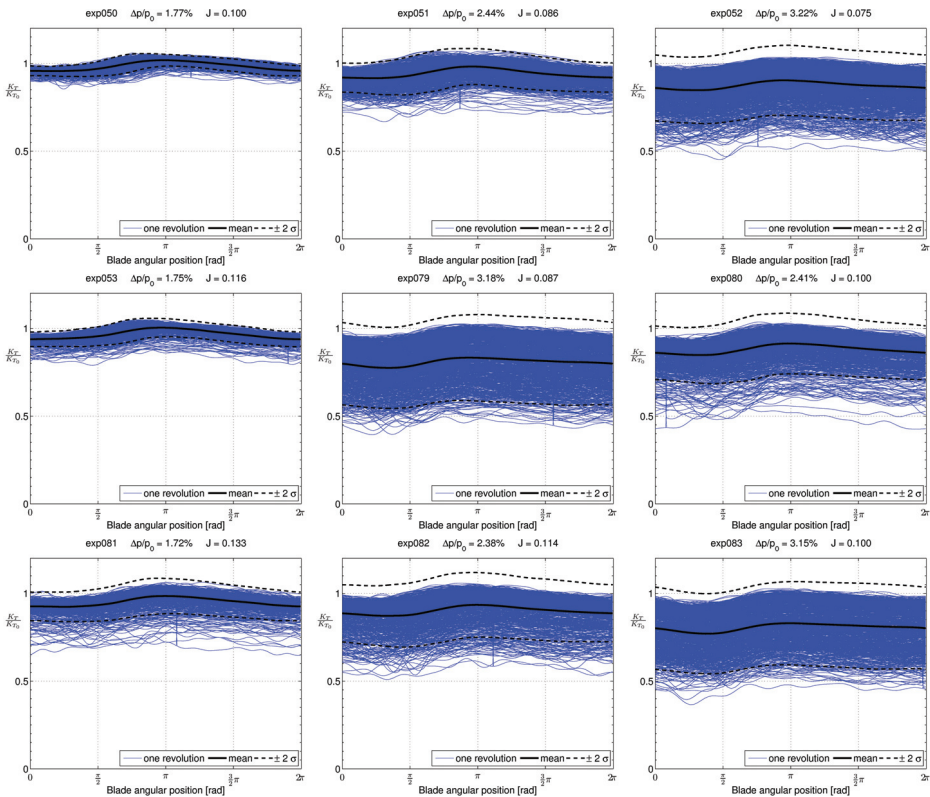


Figure A.8: [ $h/R = 1.72$ ]

$$h/R = 1.64$$

experiment #	$h/R$ [ ]	$U$ [m/s]	$n$ [1/s]	$J$ [ ]	$\Delta p/p_0$ [ ]	$\theta$ [deg]																																									
exp084	1.64	0.30	12	0.100	1.77%	79																																									
exp085	1.64	0.30	14	0.086	2.44%	97																																									
exp086	1.64	0.30	16	3.22%	111	exp087	1.64	0.35	12	0.117	1.75%	67	exp088	1.64	0.35	14	0.100	2.41%	92	exp089	1.64	0.35	16	0.088	3.18%	103	exp091	1.64	0.40	14	0.114	2.38%	85	exp092	1.64	0.40	16	0.100	3.15%	96	exp093	1.64	0.40	12	0.133	1.72%	81
exp087	1.64	0.35	12	0.117	1.75%	67																																									
exp088	1.64	0.35	14	0.100	2.41%	92																																									
exp089	1.64	0.35	16	0.088	3.18%	103																																									
exp091	1.64	0.40	14	0.114	2.38%	85																																									
exp092	1.64	0.40	16	0.100	3.15%	96																																									
exp093	1.64	0.40	12	0.133	1.72%	81																																									

Table A.9: Test specifications [ $h/R=1.64$ ].

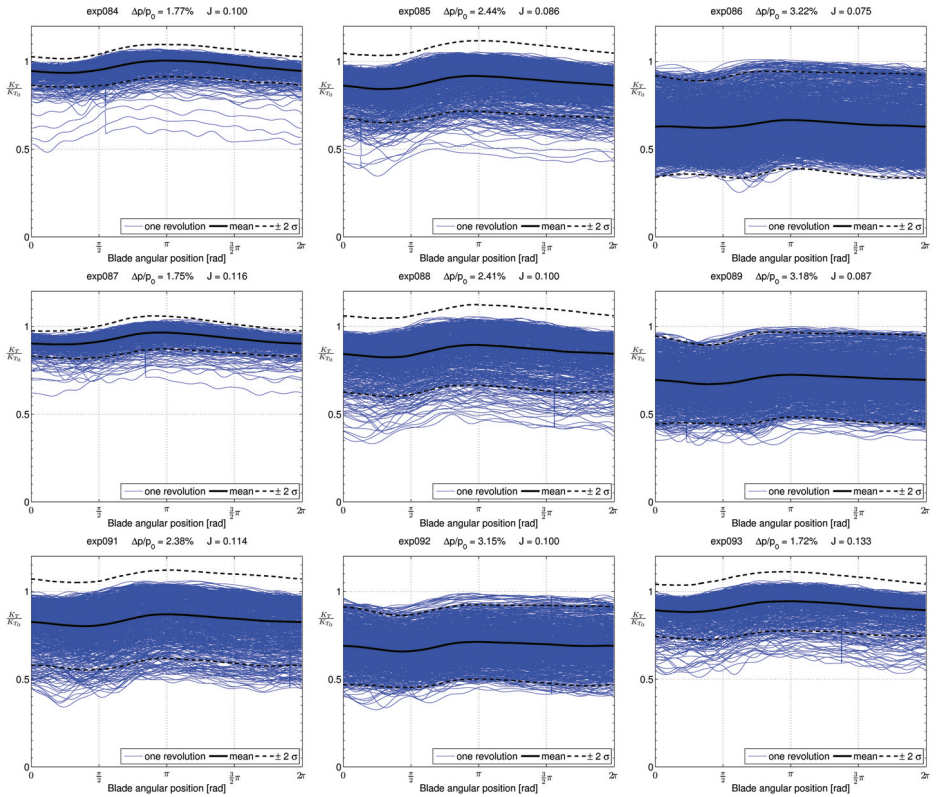


Figure A.9: [ $h/R = 1.64$ ]

$$h/R = 1.56$$

experiment #	$h/R$ [l]	$U$ [m/s]	$n$ [1/s]	$J$ [l]	$\Delta p/p_0$ [l]	$\theta$ [deg]
exp068	1.56	0.30	12	0.100	1.77%	83
exp069	1.56	0.30	14	0.086	2.44%	97
exp070	1.56	0.30	16	0.075	3.22%	114
exp071	1.56	0.35	12	0.117	1.75%	68
exp072	1.56	0.35	14	0.100	2.41%	84
exp073	1.56	0.35	16	0.088	3.18%	105
exp074	1.56	0.40	12	0.133	1.72%	61
exp075	1.56	0.40	14	0.114	2.38%	77
exp076	1.56	0.40	16	0.100	3.15%	99

Table A.10: Test specifications [ $h/R=1.56$ ].

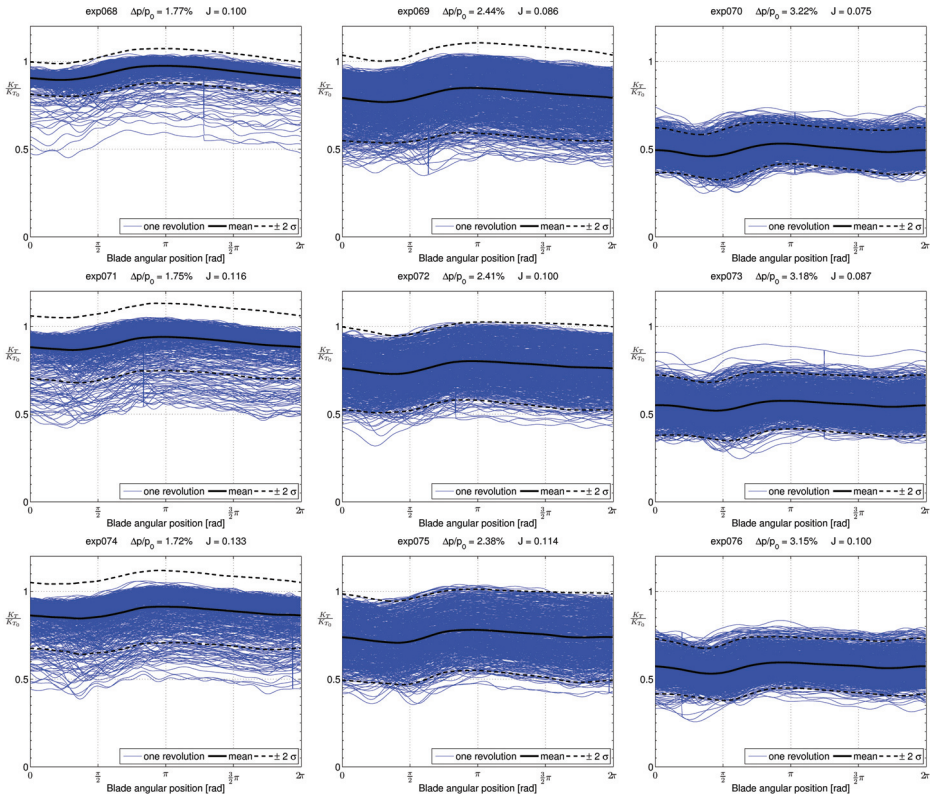


Figure A.10: [ $h/R = 1.56$ ]

$$h/R = 1.48$$

experiment #	$h/R$ [ ]	$U$ [m/s]	$n$ [1/s]	$J$ [ ]	$\Delta p/p_0$ [ ]	$\theta$ [deg]
exp094	1.48	0.30	12	0.100	1.77%	78
exp096	1.48	0.30	14	0.086	2.44%	117
exp097	1.48	0.30	16	0.075	3.22%	142
exp098	1.48	0.35	12	0.117	1.75%	75
exp099	1.48	0.35	14	0.100	2.41%	105
exp100	1.48	0.35	16	0.088	3.18%	128
exp101	1.48	0.40	12	0.133	1.72%	66
exp102	1.48	0.40	14	0.114	2.38%	100
exp103	1.48	0.40	16	0.100	3.15%	120

Table A.11: Test specifications [ $h/R=1.48$ ].

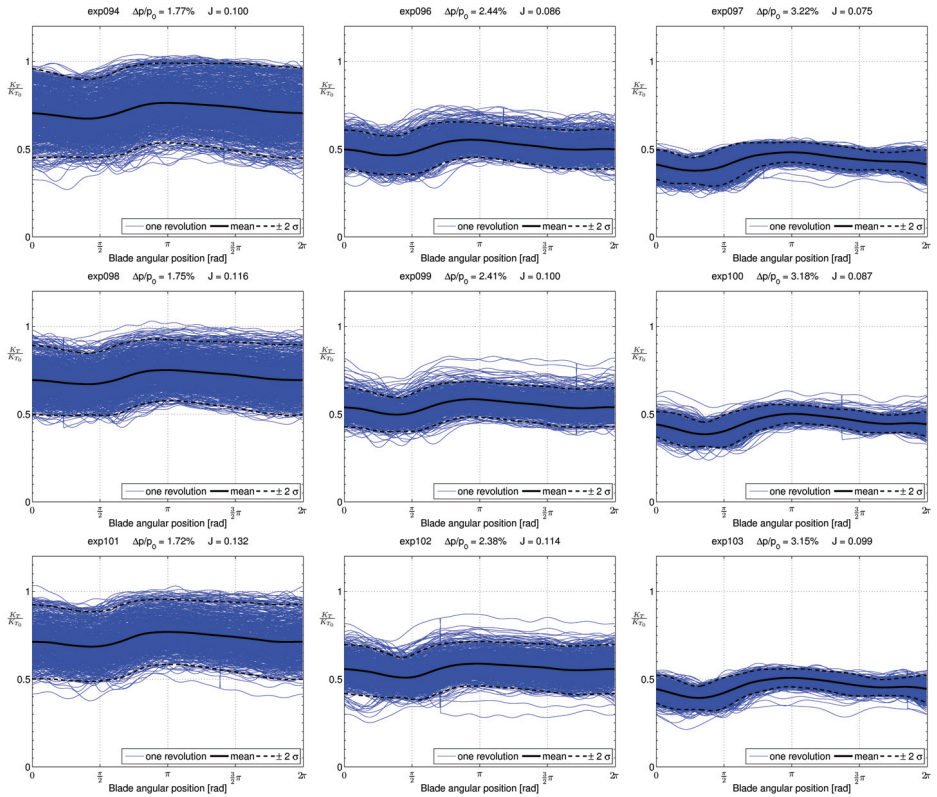


Figure A.11: [ $h/R = 1.48$ ]

$$h/R = 1.40$$

experiment #	$h/R$ [l]	$U$ [m/s]	$n$ [1/s]	$J$ [l]	$\Delta p/p_0$ [l]	$\theta$ [deg]
exp104	1.40	0.30	12	0.100	1.77%	95
exp105	1.40	0.30	14	0.086	2.44%	132
exp106	1.40	0.30	16	0.075	3.22%	140
exp107	1.40	0.35	12	0.117	1.75%	86
exp108	1.40	0.35	14	0.100	2.41%	114
exp109	1.40	0.35	16	0.088	3.18%	130
exp110	1.40	0.40	12	0.133	1.72%	72
exp111	1.40	0.40	14	0.114	2.38%	111
exp112	1.40	0.40	16	0.100	3.15%	130

Table A.12: Test specifications [ $h/R=1.4$ ].

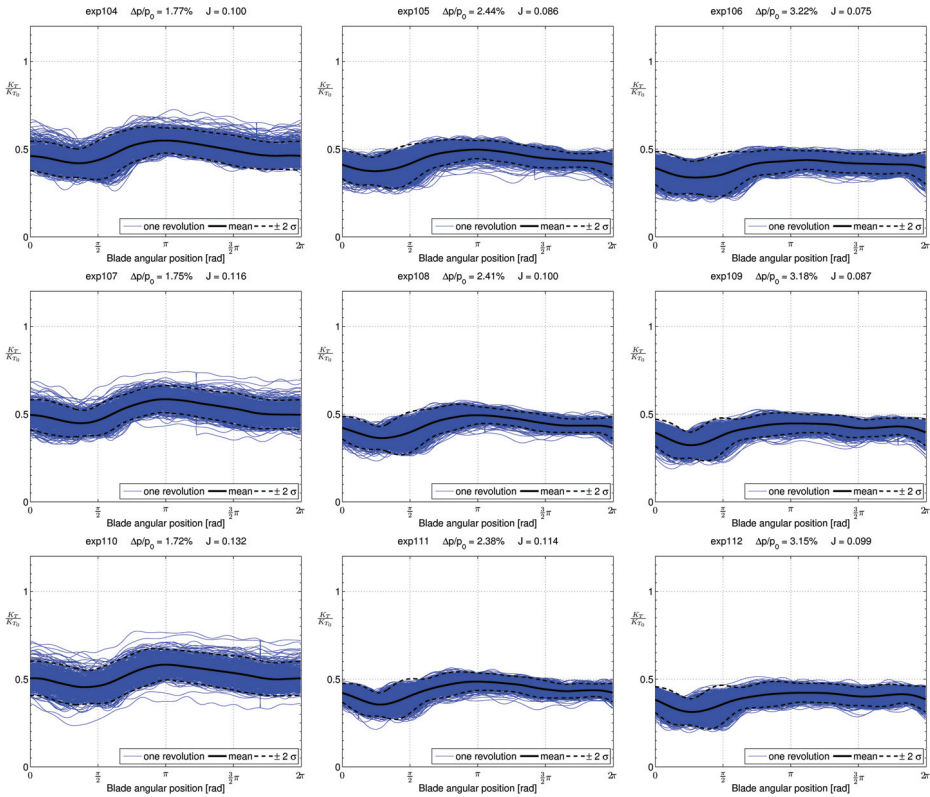


Figure A.12: [ $h/R = 1.4$ ]

$$h/R = 1.32$$

experiment #	$h/R$ [ ]	$U$ [m/s]	$n$ [1/s]	$J$ [ ]	$\Delta p/p_0$ [ ]	$\theta$ [deg]
exp113	1.32	0.30	12	0.100	1.77%	105
exp114	1.32	0.30	14	0.086	2.44%	150
exp115	1.32	0.30	16	0.075	3.22%	150
exp116	1.32	0.35	12	0.117	1.75%	88
exp117	1.32	0.35	14	0.100	2.41%	140
exp118	1.32	0.35	16	0.088	3.18%	150
exp119	1.32	0.40	12	0.133	1.72%	82
exp120	1.32	0.40	14	0.114	2.38%	130
exp121	1.32	0.40	16	0.100	3.15%	140

Table A.13: Test specifications [ $h/R=1.32$ ].

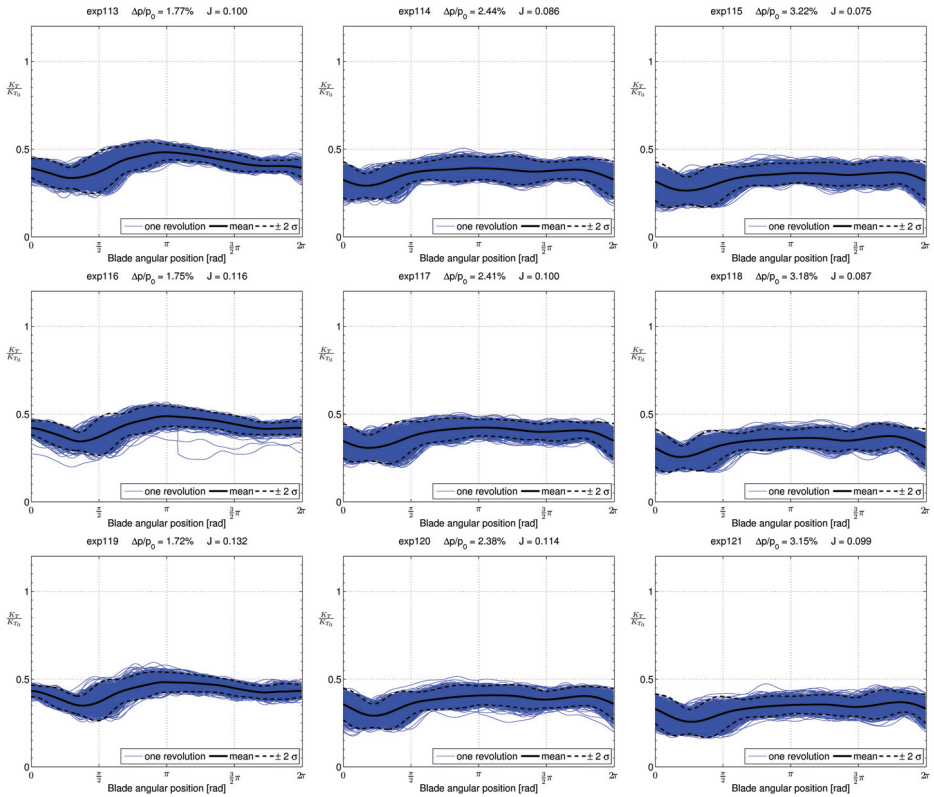


Figure A.13: [ $h/R = 1.32$ ]

$$h/R = 1.24$$

experiment #	$h/R$ [l]	$U$ [m/s]	$n$ [1/s]	$J$ [l]	$\Delta p/p_0$ [l]	$\theta$ [deg]
exp159	1.24	0.30	12	0.100	1.77%	120
exp160	1.24	0.30	16	0.075	3.22%	150
exp161	1.24	0.30	14	0.086	2.44%	147
exp162	1.24	0.35	12	0.117	1.75%	116
exp163	1.24	0.35	14	0.100	2.41%	141
exp164	1.24	0.35	16	0.088	3.18%	150
exp166	1.24	0.40	12	0.133	1.72%	115
exp167	1.24	0.40	14	0.114	2.38%	136
exp168	1.24	0.40	16	0.100	3.15%	150

Table A.14: Test specifications [ $h/R=1.24$ ].

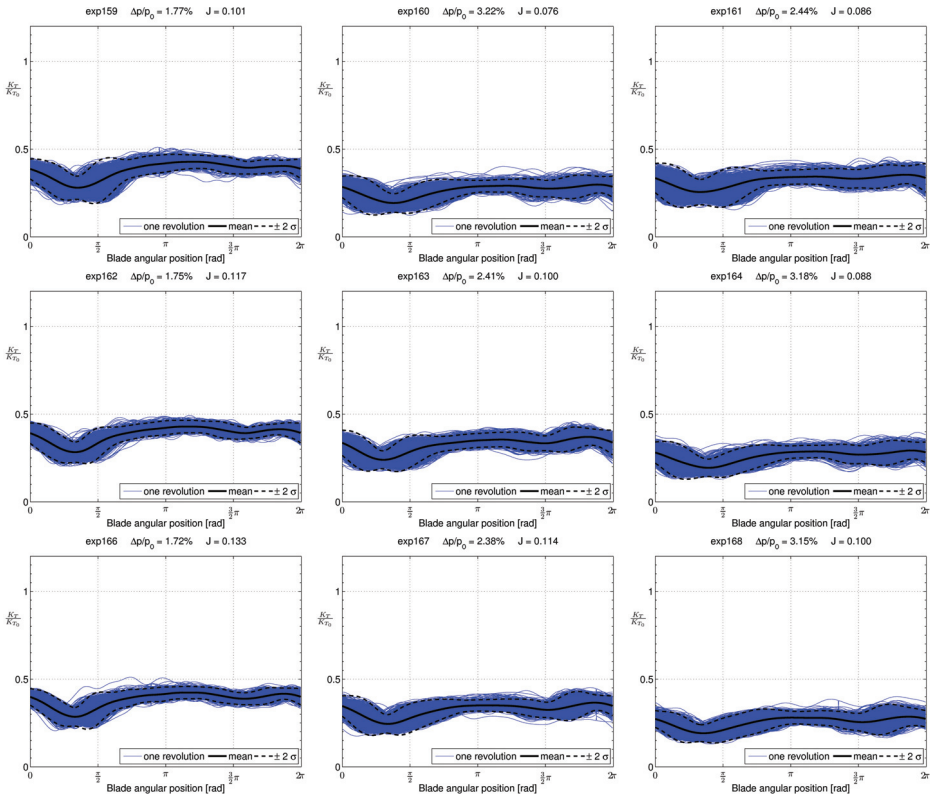


Figure A.14: [ $h/R = 1.24$ ]

$$h/R = 1.00$$

experiment #	$h/R$ []	$U$ [m/s]	$n$ [1/s]	$J$ []	$\Delta p/p_0$ [%]	$\theta$ [deg]
exp169	1.00	0.30	12	0.100	1.77%	127
exp170	1.00	0.30	14	0.086	2.44%	150
exp171	1.00	0.30	16	0.075	3.22%	150
exp172	1.00	0.35	12	0.117	1.75%	120
exp173	1.00	0.35	14	0.100	2.41%	130
exp174	1.00	0.35	16	0.088	3.18%	150
exp175	1.00	0.40	12	0.133	1.72%	110
exp176	1.00	0.40	14	0.114	2.38%	128
exp177	1.00	0.40	16	3.15%	143	

Table A.15: Test specifications [ $h/R=1$ ].

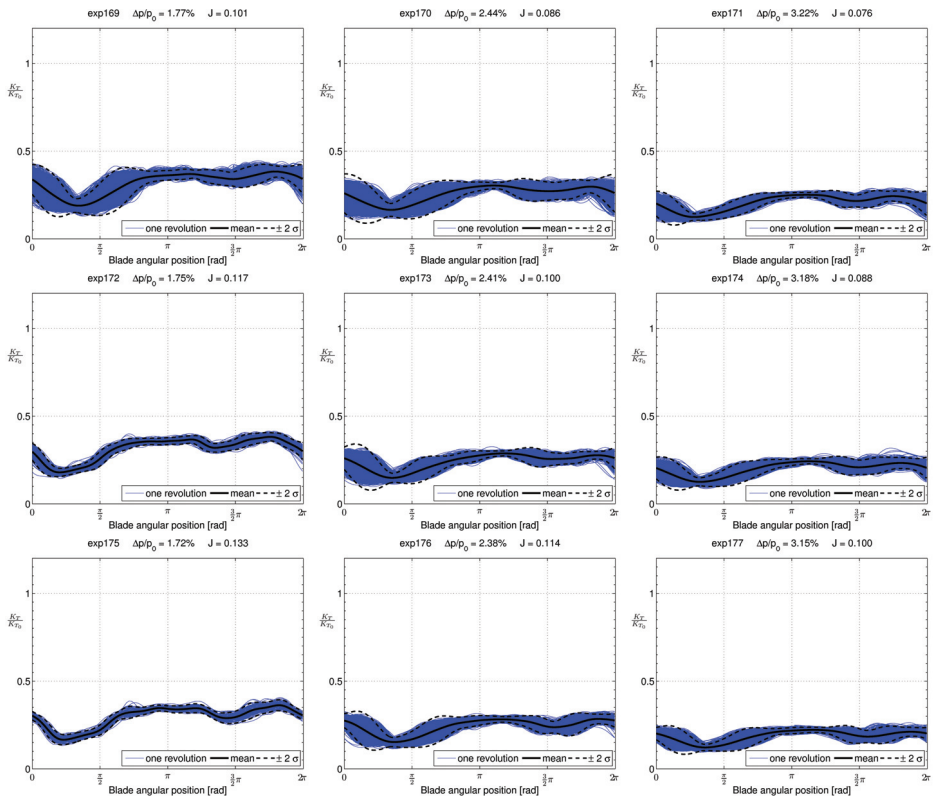


Figure A.15: [ $h/R = 1$ ]

## A.2 Linear accelerations

Acronyms:	experiment	#	name of the experiment;
	$h/R$	[/]	water-depth ratio;
	$U$	[m/s]	speed of advance;
	$n$	[1/s]	shaft frequency;
	$J$	[/]	advance ratio;
	$\Delta p/p_0$	[/]	propeller loading;
	$\theta$	[deg]	blade correction angle;
	$\dot{n}$	[rad/s <sup>2</sup> ]	linear acceleration.

experiment #	$h/R$ [/]	$U$ [m/s]	$n$ [1/s]	$J$ [/]	$\Delta p/p_0$ [/]	$\theta$ [deg]	$\dot{n}$ [rad/s <sup>2</sup> ]
exp180	1.40	0.30	12	0.100	1.77%	100	208.7
exp181	1.40	0.30	14	0.086	2.44%	100	208.7
exp182	1.40	0.30	16	0.075	3.22%	100	208.7
exp183	1.40	0.30	12	0.100	1.77%	100	104.3
exp184	1.40	0.30	14	0.086	2.44%	100	104.3
exp185	1.40	0.30	16	0.075	3.22%	100	104.3
exp186	1.40	0.30	12	0.100	1.77%	100	52.2
exp187	1.40	0.30	14	0.086	2.44%	100	52.2
exp188	1.40	0.30	16	0.075	3.22%	100	52.2
exp189	1.40	0.30	12	0.100	1.77%	100	26.1
exp190	1.40	0.30	14	0.086	2.44%	100	26.1
exp191	1.40	0.30	16	0.075	3.22%	100	26.1
exp192	1.40	0.30	16	0.075	3.22%	100	26.1

Table A.16: Test specifications [ $h/R=1.4$ ,  $U=0.3$  m/s].

experiment #	$h/R$ [ $\backslash$ ]	$U$ [m/s]	$n$ [1/s]	$J$ [ $\backslash$ ]	$\Delta p/p_0$ [ $\backslash$ ]	$\theta$ [deg]	$\dot{n}$ [rad/s <sup>2</sup> ]
exp193	1.40	0.35	12	0.117	1.75%	100	208.7
exp194	1.40	0.35	14	0.100	2.41%	100	208.7
exp195	1.40	0.35	16	0.088	3.18%	100	208.7
exp196	1.40	0.35	12	0.117	1.75%	100	104.3
exp197	1.40	0.35	14	0.100	2.38%	100	104.3
exp198	1.40	0.35	16	0.088	3.15%	100	104.3
exp199	1.40	0.35	12	0.117	1.75%	100	52.2
exp200	1.40	0.35	14	0.100	2.44%	100	52.2
exp201	1.40	0.35	16	0.088	3.22%	100	52.2
exp202	1.40	0.35	12	0.117	1.75%	100	26.1
exp203	1.40	0.35	14	0.100	2.44%	100	26.1
exp204	1.40	0.35	14	0.100	3.22%	100	26.1
exp205	1.40	0.35	14	0.100	1.77%	100	26.1
exp206	1.40	0.35	16	0.088	2.44%	100	26.1

Table A.17: Test specifications [ $h/R=1.4$ ,  $U=0.35$  m/s].

experiment #	$h/R$ [ $\backslash$ ]	$U$ [m/s]	$n$ [1/s]	$J$ [ $\backslash$ ]	$\Delta p/p_0$ [ $\backslash$ ]	$\theta$ [deg]	$\dot{n}$ [rad/s <sup>2</sup> ]
exp207	1.40	0.40	12	0.133	1.72%	100	26.1
exp208	1.40	0.40	14	0.114	2.38%	100	26.1
exp209	1.40	0.40	16	0.100	3.15%	100	26.1
exp210	1.40	0.40	16	0.100	3.15%	100	26.1
exp211	1.40	0.40	12	0.133	1.72%	100	52.2
exp212	1.40	0.40	14	0.114	2.38%	100	52.2
exp213	1.40	0.40	16	0.100	3.15%	100	52.2
exp214	1.40	0.40	12	0.133	1.72%	100	104.3
exp215	1.40	0.40	14	0.114	2.38%	100	104.3
exp216	1.40	0.40	16	0.100	3.15%	100	104.3
exp217	1.40	0.40	12	0.133	1.72%	100	208.7
exp218	1.40	0.40	14	0.114	2.38%	100	208.7
exp219	1.40	0.40	16	0.100	3.15%	100	208.7

Table A.18: Test specifications [ $h/R=1.4$ ,  $U=0.4$  m/s].

experiment #	$h/R$ [/]	$U$ [m/s]	$n$ [1/s]	$J$ [/]	$\Delta p/p_0$ [/]	$\theta$ [deg]	$\dot{n}$ [rad/s <sup>2</sup> ]
exp220	1.24	0.35	14	0.100	2.38%	100	26.1
exp221	1.24	0.35	14	0.100	2.38%	100	52.2
exp222	1.24	0.35	14	0.100	2.38%	100	104.3
exp223	1.24	0.35	14	0.100	2.38%	100	208.7

Table A.19: Test specifications [ $h/R=1.24$ ].

A.3 Effect of submergence [ $J=0.1, n=14$  Hz]

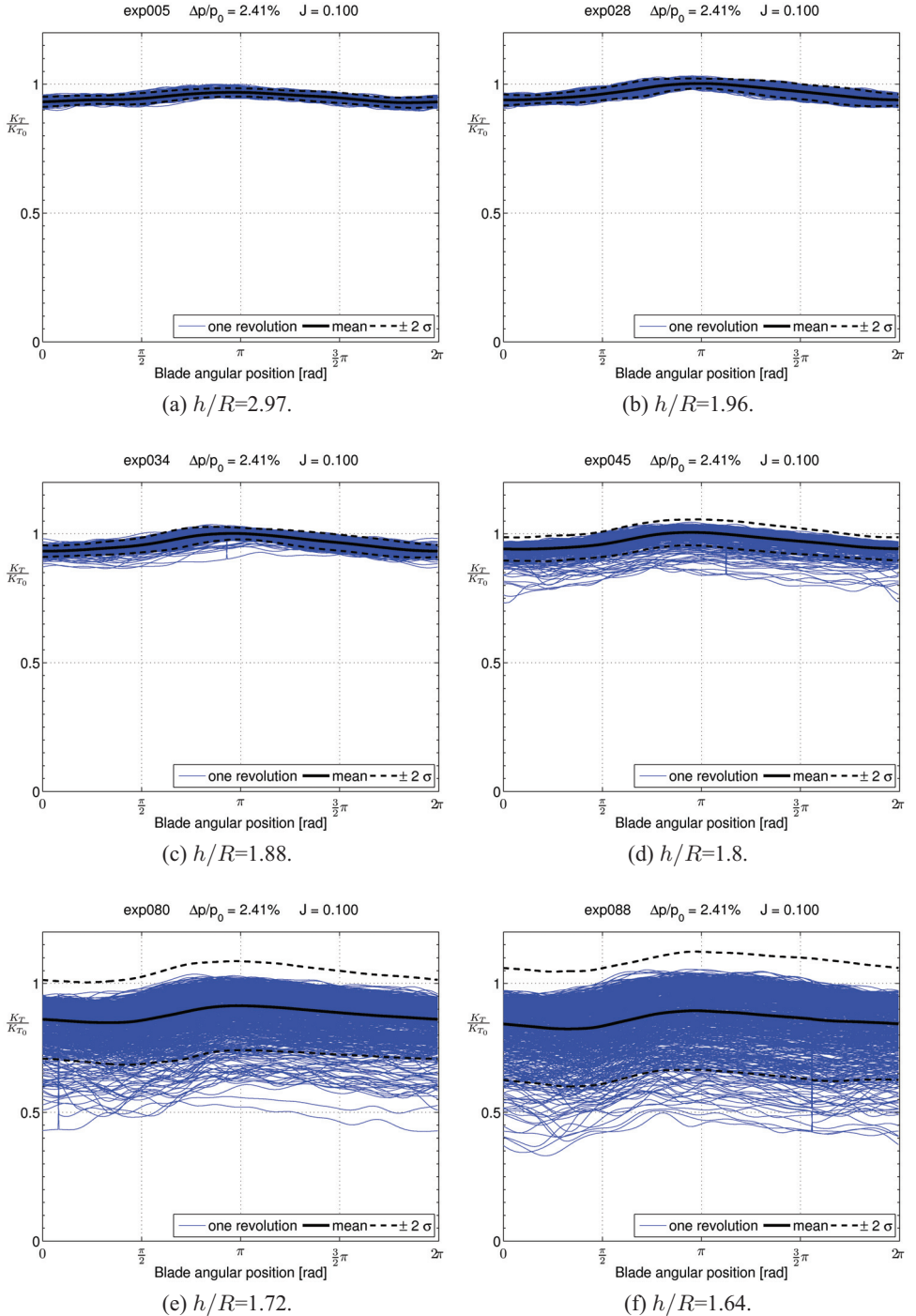


Figure A.16: [ $J=0.1, n=14$  Hz].

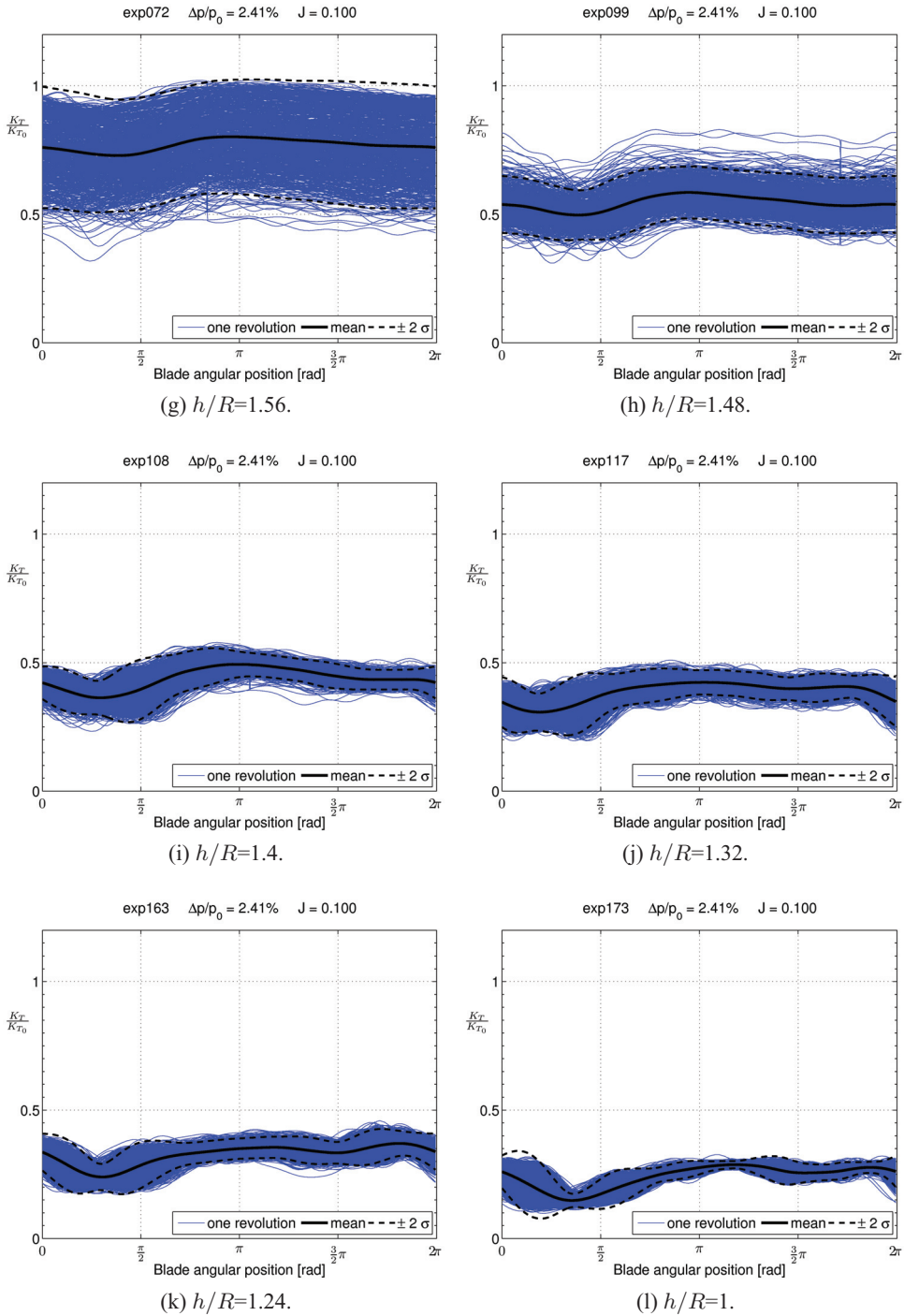


Figure A.16: [ $J=0.1$ ,  $n=14$  Hz].

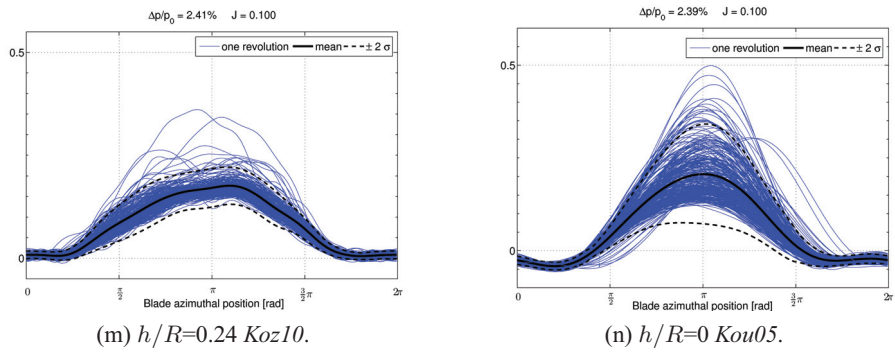


Figure A.16: [ $J=0.1$ ,  $n=14$  Hz].



# Bibliography

- Achkinadze, A. S. and Krasilnikov, V. I. (2001). A velocity based boundary element method with modified trailing edge for prediction of the partial cavities on the wings and propeller blades. In *CAV2001: Fourth International Symposium on Cavitation*, Pasadena, CA.
- Acosta, A. J. (1973). Hydrofoils and hydrofoil craft. *Annual Review of Fluid Mechanics*, 5(1):161–184.
- Barron, R. M. and Neyshabouri, A. A. S. (2003). Effects of under-relaxation factors on turbulent flow simulations. *International Journal for Numerical Methods in Fluids*, 42(8):923–928.
- Barton, I. E. (1998). Comparison of simple- and piso-type algorithms for transient flows. *International Journal for Numerical Methods in Fluids*, 26(4):459–483.
- Bell, J., Colella, P., and Glaz, H. (1989). A second-order projection method for the incompressible navier-stokes equations. *Journal of Computational Physics*, 85(2):257 – 83.
- Berchiche, N. and Janson, C.-E. (2008). Grid influence on the propeller open-water performance and flow field. *Ship Technology Research*, 55(1):87 – 96.
- Bissinger, N. C. and Braun, G. W. (1974). On the inlet vortex system. *NASA CR-132536*, pages 106p –.
- Brandt, H. (1973). Modellversuche mit schiffspropellern an der wasseroberfläche. *Schiff und Hafen*, 25(5):415–422. In German: "Model Tests with Ship Propellers at the Water Surface".
- Brennen, C. E. (2005). *Fundamentals of Multiphase Flows*. Cambridge University Press.
- Brix, S., Neuwerth, G., and Jacob, D. (2000). The inlet-vortex system of jet engines operating near the ground. In *AIAA-2000-3998, 18th Applied Aerodynamics Conference*, volume 1, Denver, CO.

- Bulten, N. and Oprea, I. (2005). Explanation of deviations in torque prediction for waterjets and propellers with rans codes. In *Marine CFD 2005*.
- Bulten, N. and Oprea, I. (2006). Evaluation of mccormick's rule for propeller tip vortex cavitation inception based on cfd results. In *Sixth International Symposium on Cavitation - CAV2006*, Wageningen (NL).
- Califano, A. (2008a). Cfd calculations of ventilating propeller. In *Presentation at UTC Workshop*, Ulsteinvik, Norway. Rolls-Royce Marine.
- Califano, A. (2008b). Influence of the near wall treatment on the flow features around a two-dimensional hydrofoil close to the free surface. In *11th Numerical Towing Tank Symposium - NuTTS'08*.
- Califano, A. (2009). Numerical study of a submerged two-dimensional hydrofoil using different solvers. In *12th Numerical Towing Tank Symposium - NuTTS'09*.
- Califano, A. and Steen, S. (2009). Analysis of different propeller ventilation mechanisms by means of rans simulations. In *First International Symposium on Marine Propulsor - smp'09*, Trondheim, Norway.
- Caponnetto, M. (2003). Rans simulations of surface piercing propellers. In *6th Numerical Towing Tank Symposium - NuTTS'03*.
- Chen, B. (2000). *RANS Simulations of Tip Vortex Flows for a Finite-Span Hydrofoil and a Marine Propulsor*. PhD thesis, University of Iowa.
- Clift, R., Grace, J. R., and Weber, M. E. (1978). *Bubbles, drops, and particles*. Academic Press, New York.
- Cointe, R. and Tulin, M. P. (1994). A theory of steady breakers. *Journal of Fluid Mechanics Digital Archive*, 276(-1):1–20.
- Constantinescu, G. and Patel, V. (2000). Role of turbulence model in prediction of pump-bay vortices. *Journal of Hydraulic Engineering*, 126(5):387 – 391.
- Cox, G. (1966). Supercavitating propeller theory. part i. the derivation of induced velocity equations and formulation of an initial design procedure. *United States Navy Department – David Taylor Model Basin – Report*, (2166):22 –.
- De Siervi, F., Viguier, H., Greitzer, E., and Tan, C. (1982). Mechanisms of inlet-vortex formation. *Journal of Fluid Mechanics*, 124:173 – 207.
- Deen, N. G., Westerweel, J., and Delnoij, E. (2002). Two-phase piv in bubbly flows: Status and trends. *Chemical Engineering and Technology*, 25(1):97 – 101.

- Denny, D. (1956). Experimental study of air-entraining vortices in pump sumps. *Institution of Mechanical Engineers – Proceedings*, 170(2):106 – 116.
- Duncan, J. H. (1981). Experimental investigation of breaking waves produced by a towed hydrofoil. *Proceedings of The Royal Society of London, Series A: Mathematical and Physical Sciences*, 377(1770):331 – 348.
- Duncan, J. H. (1983). Breaking and non-breaking wave resistance of a two-dimensional hydrofoil. *Journal of Fluid Mechanics*, 126:507 – 520.
- Duncan, J. H. (2001). Spilling breakers. *Annual Review of Fluid Mechanics*, 33:519 – 547.
- Faltinsen, O. M. (1990). *Sea loads on ships and offshore structures*. Cambridge University Press, Cambridge.
- Faltinsen, O. M. (2005). *Hydrodynamics of High-Speed Marine Vehicles*. Cambridge University Press.
- Faltinsen, O. M., Minsaas, K. J., Liapis, N., and Skjørdal, S. O. (1981). Prediction of resistance and propulsion of a ship in a seaway. In *Proceedings of 13th symposium on naval hydrodynamics*, pages 505 – 529.
- Faltinsen, O. M. and Semenov, Y. A. (2008). The effect of gravity and cavitation on a hydrofoil near the free surface. *Journal of Fluid Mechanics*, 597(-1):371–394.
- Ferziger, J. H. and Perić, M. (2002). *Computational methods for fluid dynamics*. Number 3rd, rev. ed. Springer, Berlin.
- Fleischer, K. P. (1973). Untersuchungen über das Zusammenwirken von Schiff und Propeller bei teilgetauchten Propellern (investigations of the interaction between ship and propeller for partly submerged propellers). *Bericht Nr. 35/73 Forschungszentrum des deutschen Schiffbaus*. Hamburg, Germany (in German).
- Fluent (2006). *Fluent 6.3 User's Guide*. Fluent Inc.
- Furuya, O. (1985). Performance-prediction theory for partially submerged ventilated propellers. *Journal of Fluid Mechanics*, 151:311 – 335.
- Green, S. I. (1995). *Fluid vortices*, volume 30, chapter I - Introduction to Vorticity, pages 1–34. Kluwer Academic Publishers, Dordrecht.
- Greenberg, M. (1972). Nonlinear actuator disk theory. *Zeitschrift für Flugwissenschaften*, 20(3):90 – 8.

- Gresho, P. (1990). On the theory of semi-implicit projection methods for viscous incompressible flow and its implementation via a finite element method that also introduces a nearly consistent mass matrix. i. theory. volume 11, pages 587 – 620, UK.
- Gutsche, F. (1967). Einfluss der tauchung auf schub und wirkungsgrad von schiffspopellern (influence of submergence on thrust and efficiency of propellers). *Shiffbauforschung* 6 5/6 67, page pp. 256 277. Berlin, Germany (in German).
- Hadler, J. B. and Hecker, R. (1968). Performance of partially submerged propellers. In *7th Symposium on Naval Hydrodynamics*, Rome, Italy. Office of Naval Research.
- Hino, T. (1997). An unstructured grid method for incompressible viscous flows with a free surface. In *35th Aerospace Sciences Meeting & Exhibit.*, number AIAA-97-0862.
- Hough, G. and Moran, J. (1969). Froude number effects on two-dimensional hydrofoils. *Journal of Ship Research*, 13(1):53 – 60.
- Hough, G. R. and Ordway, D. E. (1965). The generalized actuator disk. *Developments in Theoretical Applied Mechanics*, II:317–336.
- Huse, E. (1973). Performance of tilted ducts. In *Symposium on ducted propellers*, volume 16, London. Royal Institution of Naval Architects - RINA.
- Jeong, J. and Hussain, F. (1995). On the identification of a vortex. *Journal of Fluid Mechanics*, 285:69 – 94.
- Jermy, M. and Ho, W. (2008). Location of the vortex formation threshold at suction inlets near ground planes by computational fluid dynamics simulation. *Proceedings of the Institution of Mechanical Engineers, Part G: Journal of Aerospace Engineering*, 222(3):393 – 402.
- Karlsson, A. and Fuchs, L. (2000). Time evolution of the vortex between an air inlet and the ground. In *AIAA-2000-990, 38th AIAA Aerospace Sciences Meeting and Exhibit*, Reno, NV.
- Kempf, G. (1934). The influence of viscosity on thrust and torque of a propeller working near the surface. In *Transactions of the Institution of Naval Architects*, page pp. 321 326, London, UK.
- Koushan, K. (2004). Environmental and interaction effects on propulsion systems used in dynamic positioning, an overview. In *9th Int. Symp. Practical Design of*

- Ships and Other Floating Structures (PRADS04)*., pages 1013–1020., Lübeck-Travemünde, Germany.
- Koushan, K. (2006a). Dynamics of propeller blade and duct loadings on ventilated ducted thrusters operating at zero speed. In *Proceedings of T-POD06 - 2nd International Conference on Technological Advances in Podded Propulsion*, Brest, France.
- Koushan, K. (2006b). Dynamics of ventilated propeller blade loading on thrusters. In *World Maritime Technology Conference - WMTC'06*, London, UK.
- Koushan, K. (2006c). Dynamics of ventilated propeller blade loading on thrusters due to forced sinusoidal heave motion. In *26th Symp on Naval Hydrodynamics*, Rome, Italy.
- Koushan, K. (2007a). Dynamics of propeller blade and duct loadings on ventilated ducted thrusters due to forced periodic heave motion. In *International Conference on Violent Flows (VF-2007)*, Fukuoka, Japan. RIAM, Kyushu University.
- Koushan, K. (2007b). Dynamics of propeller blade and duct loadings on ventilated thrusters in dynamic positioning mode. In *Dynamic Positioning Conference*, Houston, TX.
- Kozłowska, A. M., Steen, S., and Koushan, K. (2009). Classification of different type of propeller ventilation and ventilation inception mechanism. In *First International Symposium on Marine Propulsor - smp'09, 2009*, Trondheim, Norway.
- Lamb, H. (1932). *Hydrodynamics*. Cambridge University Press.
- Landrini, M., Lugni, C., and Bertram, V. (1999). Numerical simulation of the unsteady flow past a hydrofoil. *Ship Technology Research*, 46(1):14 – 30.
- Li, D., Berchiche, N., and Janson, C. (2006). Influence of turbulence models on the prediction of full-scale propeller open water characteristics with rans methods. In *26th Symposium on Naval Hydrodynamics*.
- Li, F.-C., Kawaguchi, Y., Segawa, T., and Suga, K. (2005). Simultaneous measurement of turbulent velocity field and surface wave amplitude in the initial stage of an open-channel flow by piv. *Experiments in Fluids*, 39(6):945 – 953.
- MackAldener and Olsson (2000). Interior fatigue fracture of gear teeth. *Fatigue & Fracture of Engineering Materials & Structures*, 23(4):283–292.

- MackAldener, M. and Olsson, M. (2002). Analysis of crack propagation during tooth interior fatigue fracture. *Engineering Fracture Mechanics*, 69(18):2147 – 2162.
- Manzke, M. and Rung, T. (2010). Propeller-flow predictions using turbulent vorticity-confinement. In Pereira, J. C. F. and Sequeira, A., editors, *V European Conference on Computational Fluid Dynamics*, Lisbon, Portugal.
- Markland, E. and Pope, J. (1956). Experiments on small pump suction well, with particular reference to vortex formations. *Institution of Mechanical Engineers – Proceedings*, 170(2):95 – 105.
- McDonough, J. M. (2007). *Lectures in Computational Fluid Dynamics of Incompressible Flow: Mathematics, Algorithms and Implementations*.
- Menter, F. (1994). Two-equation eddy-viscosity turbulence models for engineering applications. *AIAA Journal*, 32(8):1598 – 1605.
- Michaelides, E. (2006). *Particles, bubbles & drops: their motion, heat and mass transfer*. World Scientific, Hackensack, N.J.
- Minsaas, K. J., Faltinsen, O. M., and Persson, B. (1983). On the importance of added resistance, propeller immersion and propeller ventilation for large ships in a seaway. In *Proceedings of International Symposium on Practical Design of Ships and other Floating Structures - PRADS'83*.
- Minsaas, K. J., Thon, H. J., Kauczynski, W., and Karlsen, S. I. (1987). Estimation of required capacity for operation of offshore vessels under severe weather conditions. In *Proceedings of International Symposium on Practical Design of Ships and other Floating Structures - PRADS'87*.
- Mori, K. H. and Shin, M. S. (1988). Sub-breaking wave: Its characteristics, appearing condition and numerical simulation. In *Proceedings 17th Symposium on Naval Hydrodynamics*, The Hague, The Netherlands.
- Moroianu, D., Karlsson, A., and Fuchs, L. (2004). Les of the flow and particle ingestion into an air intake of a jet engine running on the ground. In *Proceedings of the ASME Turbo Expo 2004*, volume 2, pages 209 – 217, Vienna, Austria.
- Motycka, D., Walter, W., and Muller, G. (1973). An analytical and experimental study of inlet ground vortices. In *AIAA/SAE 9th Propulsion Conference AIAA-1973-1313*, page 8 p, Las Vegas, Nev.
- Muscari, R. and Di Mascio, A. (2003). A model for the simulation of steady spilling breaking waves. *Journal of Ship Research*, 47(1):13–23.

- Nagahara, T., Sato, T., and Kato, C. (2006). Unsteady simulation of the flow field around a submerged vortex cavitation occurred in a pump intake sump. In *Sixth International Symposium on Cavitation - CAV2006*, Wageningen (NL).
- Nakayama, A. and Jones, J. R. (1996). Vortex formation in inlet flow near a wall. In *34th Aerospace Sciences Meeting and Exhibit, AIAA 96-0803*.
- Napier, D. D. (1912). *DAVID NAPIER - ENGINEER - 1790 - 1869. An Autobiographical Sketch, with Notes*. James Maclehose and Sons - Publishers to the University (Glasgow), Glasgow, UK.
- Nishikawa, E. and Uchida, M. (1989). An experimental study on the ventilation of marine propeller and its effects on the propeller performance and shaft force. In *Proceedings of the 4th International Symposium on Practical Design of Ships and Mobile Units - PRADS'89*, Varna, Bulgaria.
- Nishiyama, S. (1986). Experimental research on propeller-hull vortex cavitation. In *Transactions of the West-Japan Society of Naval Architects*.
- Nishiyama, T. (1961). Air-drawing and ventilating flow characteristics of shallowly submerged hydrofoil sections. *American Society of Naval Engineers - Journal*, 73(3):593 – 602.
- Oberembt, H. (1968). Zur bestimmung der instationären flügelkräfte bei einem propeller mit aus dem wasser herausschlagenden flügeln. Technical report, Inst. fr Schiffbau der Universitt Hamburg, Bericht Nr. 247.
- Olofsson, N. (1996). *Forces and Flow Characteristics of a Partially Submerged Propeller*. PhD thesis, Chalmers Tekniska Högskola.
- OpenFOAM (2009). *OpenFOAM User Guide*. OpenCFD Ltd.
- Paik, B.-G., Lee, J.-Y., and Lee, S.-J. (2008). Effect of propeller immersion depth on the flow around a marine propeller. *Journal of Ship Research*, 52(2):102 – 113.
- Raithby, G. D. (1979). Numerical solution of problems in incompressible fluid flow: treatment of the velocity-pressure coupling. *Numerical heat transfer*, 2(4):417–40.
- Rajendran, V., Constantinescu, S., and Patel, V. (1999). Experimental validation of numerical model of flow in pump-intake bays. *Journal of Hydraulic Engineering*, 125(11):1119 – 1125.

- Rajendran, V. P., Constantinescu, G., and Patel, V. (1998). Experiments on flow in a model water-pump intake sump to validate a numerical model. In *American Society of Mechanical Engineers, Fluids Engineering Division (Publication) FED*, Washington, DC, USA.
- Ramsen, J. A. (1957). An experimental hydrodynamic investigation of the inception of vortex ventilation. Technical Report NACA-TN-3903, NASA.
- Reynolds, O. (1874). On the effect of immersion on screw propellers. *Transactions of Institution of Naval Architects*.
- Rhee, S. H. and Joshi, S. (2006). Computational validation for flow around a marine propeller using unstructured mesh based navier-stokes solver. *JSME International Journal, Series B: Fluids and Thermal Engineering*, 48(3):562 – 570.
- Rhee, S. H. and Stern, F. (2002). Rans model for spilling breaking waves. *Journal of Fluids Engineering, Transactions of the ASME*, 124(2):424 – 432.
- Roache, P. (1997). *Quantification of uncertainty in computational fluid dynamics*, volume 29, pages 123 – 160.
- Rodert, L. A. and Garrett, F. B. (1955). Ingestion of foreign objects into turbine engines by vortices. *NACA TN 3330*.
- Rott, N. (1958). On the viscous core of a line vortex. *Zeitschrift fur Angewandte Mathematik und Physik*, 9b(5-6):543 – 553.
- Ruth, E. (2008). *Propulsion control and thrust allocation on marine vessels*. PhD thesis, Norwegian University of Science and Technology, Faculty of Engineering Science and Technology, Department of Marine Technology.
- Sadeh, W., Suter, S., and Maeder, P. (1970a). Analysis of vorticity amplification in the flow approaching a two-dimensional stagnation point. *Zeitschrift fur Angewandte Mathematik und Physik*, 21(5):699 – 716.
- Sadeh, W., Suter, S., and Maeder, P. (1970b). An investigation of vorticity amplification in stagnation flow. *Zeitschrift fur Angewandte Mathematik und Physik*, 21(5):717 – 42.
- Secareanu, A., Moroianu, D., Karlsson, A., and Fuchs, L. (2005). Experimental and numerical study of ground vortex interaction in an air-intake. In *43rd AIAA Aerospace Sciences Meeting and Exhibit - Meeting Papers*, pages 4645 – 4654, Reno, NV, United states.

- Shiba, H. (1953). Air-drawing of marine propellers. Technical Report 9, Transportation Technical Research Institute.
- Shih, T.-H., Liou, W. W., Shabbir, A., Yang, Z., and Zhu, J. (1995). New  $k-\epsilon$  eddy viscosity model for high reynolds number turbulent flows. *Computers and Fluids*, 24(3):227 – 238.
- Shin, H., Greitzer, E., Cheng, W., Tan, C., and Shippee, C. (1986a). Circulation measurements and vortical structure in an inlet-vortex flow field. *Journal of Fluid Mechanics*, 162:463 – 87.
- Shin, H. W., Cheng, W. K., Greitzer, E. M., and Tan, C. S. (1986b). Inlet vortex formation due to ambient vorticity intensification. *AIAA Journal*, 24(4):687 – 689.
- Singhal, A., Athavale, M., Li, H., and Jiang, Y. (2002). Mathematical basis and validation of the full cavitation model. *Transactions of the ASME. Journal of Fluids Engineering*, 124(3):617 – 24.
- Smogeli (2006). *Control of Marine Propellers: From Normal to Extreme Conditions*. PhD thesis, Norwegian University of Science and Technology, Faculty of Engineering Science and Technology, Department of Marine Technology.
- Steinhoff, J. and Underhill, D. (1994). Modification of the euler equations for vorticity confinement: application to the computation of interacting vortex rings. *Physics of Fluids*, 6(8):2738 – 44.
- Swainston, M. (1974). Vortex formation near the intakes to turbomachinery and duct systems. *Heat and Fluid Flow*, 4(2):92 – 100.
- Swainston, M. (1976). Experimental and theoretical identification of air ingestion regimes in pump sumps. *Proceedings of the Institution of Mechanical Engineers (London)*, 190(59):671 – 678.
- Tulin, M. (1964). Supercavitating flows – small perturbation theory. *Journal of Ship Research*, 7(3):16 – 37.
- Tulin, M. P. (1956). Supercavitating flow past foils and struts. In *National Physical Laboratory International Symposium on Cavitation in Hydrodynamics (1955)*, London, UK. H.M.S.O.
- Tulin, M. P. and Burkart, M. P. (1955). Linearized theory for flows about lifting foils at zero cavitation number. Technical Report C-638, DTMB Report C-638, Navy Department, Washington, D.C.

- Tzabiras, G. (1997). Numerical investigations of 2d, steady free surface flows. *International Journal for Numerical Methods in Fluids*, 25(5):567 – 598.
- Wadlin, K. L. (1958). Mechanics of ventilation inception. In *Proceedings 2nd Symposium on Naval Hydrodynamics*, volume 425.
- Wadlin, K. L., Ramsen, J. A., and Vaughan, V. L. (1955). Hydrodynamic characteristics of modified rectangular flat plates having aspect ratios of 1.00, 0.25, and 0.125 and operating near a free water surface. Technical Report NACA-TR-1246, NASA.
- Wagner, H. (1925). Über die entstehung des dynamischen auftriebes von tragflügeln (dynamic buoyancy of bearing wings). *Zeitschrift für angewandte Mathematik und Mechanik*, 5(1):17 – 35. (in German).
- Wang, D. P. (1977). Water entry and exit of a fully ventilated foil. *Journal of Ship Research*, 21:44 – 68.
- Wang, D. P. (1979). Oblique water entry and exit of a fully ventilated foil. *Journal of Ship Research*, 23(1):43 – 54.
- Wang, G. Q., Jia, D. S., and Sheng, Z. B. (1992). Study on propeller characteristics near water surface. In *Proceedings of the 2nd Symposium on Propeller and Cavitation*.
- Weissinger, J. (1947). Lift distribution of swept-back wings. pages 51p –.
- Wilcox, D. C. (1998). *Turbulence Modeling for CFD*. DCW Industries, Inc., 2nd edition.
- Wood, A. (1930). *A textbook of sound: being an account of the physics of vibrations with special reference to recent theoretical and technical developments*. G. Bell and Sons, London.
- Wu, T. Y.-T. (1962). Flow through a heavy loaded actuator disc. *Schiffstechnik*, 9(Heft 47):134–138. Symposium on Ship Theories, University of Hamburg, Institut für Schiffbau.
- Yegorov, I. T. and Sadovnikov, Y. M. (1961). Effect of instability on hydrodynamic characteristics of a propeller cutting the water surface. *Sudostroyeniye*, 1:15 – 17 (in Russian).
- Young, Y. L. and Kinnas, S. A. (2004). Performance prediction of surface-piercing propellers. *Journal of Ship Research*, 48(4):288 – 304.

**R A P P O R T E R**  
**UTGITT VED**  
**INSTITUTT FOR MARIN TEKNIKK**  
**(tidligere: FAKULTET FOR MARIN TEKNIKK)**  
**NORGES TEKNISK-NATURVITENSKAPELIGE UNIVERSITET**

<b>Report No.</b>	<b>Author</b>	<b>Title</b>
	Kavlie, Dag	Optimization of Plane Elastic Grillages, 1967
	Hansen, Hans R.	Man-Machine Communication and Data-Storage Methods in Ship Structural Design, 1971
	Gisvold, Kaare M.	A Method for non-linear mixed -integer programming and its Application to Design Problems, 1971
	Lund, Sverre	Tanker Frame Optimization by means of SUMT-Transformation and Behaviour Models, 1971
	Vinje, Tor	On Vibration of Spherical Shells Interacting with Fluid, 1972
	Lorentz, Jan D.	Tank Arrangement for Crude Oil Carriers in Accordance with the new Anti-Pollution Regulations, 1975
	Carlsen, Carl A.	Computer-Aided Design of Tanker Structures, 1975
	Larsen, Carl M.	Static and Dynamic Analysis of Offshore Pipelines during Installation, 1976
UR-79-01	Bright Hatlestad, MK	The finite element method used in a fatigue evaluation of fixed offshore platforms. (Dr.Ing. Thesis)
UR-79-02	Erik Pettersen, MK	Analysis and design of cellular structures. (Dr.Ing. Thesis)
UR-79-03	Sverre Valsgård, MK	Finite difference and finite element methods applied to nonlinear analysis of plated structures. (Dr.Ing. Thesis)
UR-79-04	Nils T. Nordsve, MK	Finite element collapse analysis of structural members considering imperfections and stresses due to fabrication. (Dr.Ing. Thesis)
UR-79-05	Ivar J. Fylling, MK	Analysis of towline forces in ocean towing systems. (Dr.Ing. Thesis)
UR-80-06	Nils Sandsmark, MM	Analysis of Stationary and Transient Heat Conduction by the Use of the Finite Element Method. (Dr.Ing. Thesis)
UR-80-09	Sverre Haver, MK	Analysis of uncertainties related to the stochastic modeling of ocean waves. (Dr.Ing. Thesis)
UR-81-15	Odland, Jonas	On the Strength of welded Ring stiffened cylindrical Shells primarily subjected to axial Compression

UR-82-17	Engesvik, Knut	Analysis of Uncertainties in the fatigue Capacity of Welded Joints
UR-82-18	Rye, Henrik	Ocean wave groups
UR-83-30	Eide, Oddvar Inge	On Cumulative Fatigue Damage in Steel Welded Joints
UR-83-33	Mo, Olav	Stochastic Time Domain Analysis of Slender Offshore Structures
UR-83-34	Amdahl, Jørgen	Energy absorption in Ship-platform impacts
UR-84-37	Mørch, Morten	Motions and mooring forces of semi submersibles as determined by full-scale measurements and theoretical analysis
UR-84-38	Soares, C. Guedes	Probabilistic models for load effects in ship structures
UR-84-39	Aarsnes, Jan V.	Current forces on ships
UR-84-40	Czujko, Jerzy	Collapse Analysis of Plates subjected to Biaxial Compression and Lateral Load
UR-85-46	Alf G. Engseth, MK	Finite element collapse analysis of tubular steel offshore structures. (Dr.Ing. Thesis)
UR-86-47	Dengody Sheshappa, MP	A Computer Design Model for Optimizing Fishing Vessel Designs Based on Techno-Economic Analysis. (Dr.Ing. Thesis)
UR-86-48	Vidar Aanesland, MH	A Theoretical and Numerical Study of Ship Wave Resistance. (Dr.Ing. Thesis)
UR-86-49	Heinz-Joachim Wessel, MK	Fracture Mechanics Analysis of Crack Growth in Plate Girders. (Dr.Ing. Thesis)
UR-86-50	Jon Taby, MK	Ultimate and Post-ultimate Strength of Dented Tubular Members. (Dr.Ing. Thesis)
UR-86-51	Walter Lian, MH	A Numerical Study of Two-Dimensional Separated Flow Past Bluff Bodies at Moderate KC-Numbers. (Dr.Ing. Thesis)
UR-86-52	Bjørn Sortland, MH	Force Measurements in Oscillating Flow on Ship Sections and Circular Cylinders in a U-Tube Water Tank. (Dr.Ing. Thesis)
UR-86-53	Kurt Strand, MM	A System Dynamic Approach to One-dimensional Fluid Flow. (Dr.Ing. Thesis)
UR-86-54	Arne Edvin Løken, MH	Three Dimensional Second Order Hydrodynamic Effects on Ocean Structures in Waves. (Dr.Ing. Thesis)
UR-86-55	Sigurd Falch, MH	A Numerical Study of Slamming of Two-Dimensional Bodies. (Dr.Ing. Thesis)
UR-87-56	Arne Braathen, MH	Application of a Vortex Tracking Method to the Prediction of Roll Damping of a Two-Dimension Floating Body. (Dr.Ing. Thesis)

UR-87-57	Bernt Leira, MK	Gaussian Vector Processes for Reliability Analysis involving Wave-Induced Load Effects. (Dr.Ing. Thesis)
UR-87-58	Magnus Småvik, MM	Thermal Load and Process Characteristics in a Two-Stroke Diesel Engine with Thermal Barriers (in Norwegian). (Dr.Ing. Thesis)
MTA-88-59	Bernt Arild Bremdal, MP	An Investigation of Marine Installation Processes – A Knowledge - Based Planning Approach. (Dr.Ing. Thesis)
MTA-88-60	Xu Jun, MK	Non-linear Dynamic Analysis of Space-framed Offshore Structures. (Dr.Ing. Thesis)
MTA-89-61	Gang Miao, MH	Hydrodynamic Forces and Dynamic Responses of Circular Cylinders in Wave Zones. (Dr.Ing. Thesis)
MTA-89-62	Martin Greenhow, MH	Linear and Non-Linear Studies of Waves and Floating Bodies. Part I and Part II. (Dr.Tech. Thesis)
MTA-89-63	Chang Li, MH	Force Coefficients of Spheres and Cubes in Oscillatory Flow with and without Current. (Dr.Ing. Thesis)
MTA-89-64	Hu Ying, MP	A Study of Marketing and Design in Development of Marine Transport Systems. (Dr.Ing. Thesis)
MTA-89-65	Arild Jæger, MH	Seakeeping, Dynamic Stability and Performance of a Wedge Shaped Planing Hull. (Dr.Ing. Thesis)
MTA-89-66	Chan Siu Hung, MM	The dynamic characteristics of tilting-pad bearings
MTA-89-67	Kim Wikstrøm, MP	Analysis av projekteringen for ett offshore projekt. (Licenciat-avhandling)
MTA-89-68	Jiao Guoyang, MK	Reliability Analysis of Crack Growth under Random Loading, considering Model Updating. (Dr.Ing. Thesis)
MTA-89-69	Arnt Olufsen, MK	Uncertainty and Reliability Analysis of Fixed Offshore Structures. (Dr.Ing. Thesis)
MTA-89-70	Wu Yu-Lin, MR	System Reliability Analyses of Offshore Structures using improved Truss and Beam Models. (Dr.Ing. Thesis)
MTA-90-71	Jan Roger Hoff, MH	Three-dimensional Green function of a vessel with forward speed in waves. (Dr.Ing. Thesis)
MTA-90-72	Rong Zhao, MH	Slow-Drift Motions of a Moored Two-Dimensional Body in Irregular Waves. (Dr.Ing. Thesis)
MTA-90-73	Atle Minsaas, MP	Economical Risk Analysis. (Dr.Ing. Thesis)
MTA-90-74	Knut-Arild Farnes, MK	Long-term Statistics of Response in Non-linear Marine Structures. (Dr.Ing. Thesis)
MTA-90-75	Torbjørn Sotberg, MK	Application of Reliability Methods for Safety Assessment of Submarine Pipelines. (Dr.Ing. Thesis)

MTA-90-76	Zeuthen, Steffen, MP	SEAMAID. A computational model of the design process in a constraint-based logic programming environment. An example from the offshore domain. (Dr.Ing. Thesis)
MTA-91-77	Haagensen, Sven, MM	Fuel Dependant Cyclic Variability in a Spark Ignition Engine - An Optical Approach. (Dr.Ing. Thesis)
MTA-91-78	Løland, Geir, MH	Current forces on and flow through fish farms. (Dr.Ing. Thesis)
MTA-91-79	Hoen, Christopher, MK	System Identification of Structures Excited by Stochastic Load Processes. (Dr.Ing. Thesis)
MTA-91-80	Haugen, Stein, MK	Probabilistic Evaluation of Frequency of Collision between Ships and Offshore Platforms. (Dr.Ing. Thesis)
MTA-91-81	Sødahl, Nils, MK	Methods for Design and Analysis of Flexible Risers. (Dr.Ing. Thesis)
MTA-91-82	Ormberg, Harald, MK	Non-linear Response Analysis of Floating Fish Farm Systems. (Dr.Ing. Thesis)
MTA-91-83	Marley, Mark J., MK	Time Variant Reliability under Fatigue Degradation. (Dr.Ing. Thesis)
MTA-91-84	Krokstad, Jørgen R., MH	Second-order Loads in Multidirectional Seas. (Dr.Ing. Thesis)
MTA-91-85	Molteberg, Gunnar A., MM	The Application of System Identification Techniques to Performance Monitoring of Four Stroke Turbocharged Diesel Engines. (Dr.Ing. Thesis)
MTA-92-86	Mørch, Hans Jørgen Bjelke, MH	Aspects of Hydrofoil Design: with Emphasis on Hydrofoil Interaction in Calm Water. (Dr.Ing. Thesis)
MTA-92-87	Chan Siu Hung, MM	Nonlinear Analysis of Rotordynamic Instabilities in Highspeed Turbomachinery. (Dr.Ing. Thesis)
MTA-92-88	Bessason, Bjarni, MK	Assessment of Earthquake Loading and Response of Seismically Isolated Bridges. (Dr.Ing. Thesis)
MTA-92-89	Langli, Geir, MP	Improving Operational Safety through exploitation of Design Knowledge - an investigation of offshore platform safety. (Dr.Ing. Thesis)
MTA-92-90	Sævik, Svein, MK	On Stresses and Fatigue in Flexible Pipes. (Dr.Ing. Thesis)
MTA-92-91	Ask, Tor Ø., MM	Ignition and Flame Growth in Lean Gas-Air Mixtures. An Experimental Study with a Schlieren System. (Dr.Ing. Thesis)
MTA-86-92	Hessen, Gunnar, MK	Fracture Mechanics Analysis of Stiffened Tubular Members. (Dr.Ing. Thesis)
MTA-93-93	Steinebach, Christian, MM	Knowledge Based Systems for Diagnosis of Rotating Machinery. (Dr.Ing. Thesis)

MTA-93-94	Dalane, Jan Inge, MK	System Reliability in Design and Maintenance of Fixed Offshore Structures. (Dr.Ing. Thesis)
MTA-93-95	Steen, Sverre, MH	Cobblestone Effect on SES. (Dr.Ing. Thesis)
MTA-93-96	Karunakaran, Daniel, MK	Nonlinear Dynamic Response and Reliability Analysis of Drag-dominated Offshore Platforms. (Dr.Ing. Thesis)
MTA-93-97	Hagen, Arnulf, MP	The Framework of a Design Process Language. (Dr.Ing. Thesis)
MTA-93-98	Nordrik, Rune, MM	Investigation of Spark Ignition and Autoignition in Methane and Air Using Computational Fluid Dynamics and Chemical Reaction Kinetics. A Numerical Study of Ignition Processes in Internal Combustion Engines. (Dr.Ing. Thesis)
MTA-94-99	Passano, Elizabeth, MK	Efficient Analysis of Nonlinear Slender Marine Structures. (Dr.Ing. Thesis)
MTA-94-100	Kvålsvold, Jan, MH	Hydroelastic Modelling of Wetdeck Slamming on Multihull Vessels. (Dr.Ing. Thesis)
MTA-94-102	Bech, Sidsel M., MK	Experimental and Numerical Determination of Stiffness and Strength of GRP/PVC Sandwich Structures. (Dr.Ing. Thesis)
MTA-95-103	Paulsen, Hallvard, MM	A Study of Transient Jet and Spray using a Schlieren Method and Digital Image Processing. (Dr.Ing. Thesis)
MTA-95-104	Hovde, Geir Olav, MK	Fatigue and Overload Reliability of Offshore Structural Systems, Considering the Effect of Inspection and Repair. (Dr.Ing. Thesis)
MTA-95-105	Wang, Xiaozhi, MK	Reliability Analysis of Production Ships with Emphasis on Load Combination and Ultimate Strength. (Dr.Ing. Thesis)
MTA-95-106	Ulstein, Tore, MH	Nonlinear Effects of a Flexible Stern Seal Bag on Cobblestone Oscillations of an SES. (Dr.Ing. Thesis)
MTA-95-107	Solaas, Frøydis, MH	Analytical and Numerical Studies of Sloshing in Tanks. (Dr.Ing. Thesis)
MTA-95-108	Hellan, Øyvind, MK	Nonlinear Pushover and Cyclic Analyses in Ultimate Limit State Design and Reassessment of Tubular Steel Offshore Structures. (Dr.Ing. Thesis)
MTA-95-109	Hermundstad, Ole A., MK	Theoretical and Experimental Hydroelastic Analysis of High Speed Vessels. (Dr.Ing. Thesis)
MTA-96-110	Bratland, Anne K., MH	Wave-Current Interaction Effects on Large-Volume Bodies in Water of Finite Depth. (Dr.Ing. Thesis)
MTA-96-111	Herfjord, Kjell, MH	A Study of Two-dimensional Separated Flow by a Combination of the Finite Element Method and Navier-Stokes Equations. (Dr.Ing. Thesis)
MTA-96-112	Æsøy, Vilmar, MM	Hot Surface Assisted Compression Ignition in a Direct Injection Natural Gas Engine. (Dr.Ing. Thesis)

MTA-96-113	Eknes, Monika L., MK	Escalation Scenarios Initiated by Gas Explosions on Offshore Installations. (Dr.Ing. Thesis)
MTA-96-114	Erikstad, Stein O., MP	A Decision Support Model for Preliminary Ship Design. (Dr.Ing. Thesis)
MTA-96-115	Pedersen, Egil, MH	A Nautical Study of Towed Marine Seismic Streamer Cable Configurations. (Dr.Ing. Thesis)
MTA-97-116	Moksnes, Paul O., MM	Modelling Two-Phase Thermo-Fluid Systems Using Bond Graphs. (Dr.Ing. Thesis)
MTA-97-117	Halse, Karl H., MK	On Vortex Shedding and Prediction of Vortex-Induced Vibrations of Circular Cylinders. (Dr.Ing. Thesis)
MTA-97-118	Igland, Ragnar T., MK	Reliability Analysis of Pipelines during Laying, considering Ultimate Strength under Combined Loads. (Dr.Ing. Thesis)
MTA-97-119	Pedersen, Hans-P., MP	Levendefiskteknologi for fiskefartøy. (Dr.Ing. Thesis)
MTA-98-120	Vikestad, Kyrre, MK	Multi-Frequency Response of a Cylinder Subjected to Vortex Shedding and Support Motions. (Dr.Ing. Thesis)
MTA-98-121	Azadi, Mohammad R. E., MK	Analysis of Static and Dynamic Pile-Soil-Jacket Behaviour. (Dr.Ing. Thesis)
MTA-98-122	Ulltang, Terje, MP	A Communication Model for Product Information. (Dr.Ing. Thesis)
MTA-98-123	Torbergsen, Erik, MM	Impeller/Diffuser Interaction Forces in Centrifugal Pumps. (Dr.Ing. Thesis)
MTA-98-124	Hansen, Edmond, MH	A Discrete Element Model to Study Marginal Ice Zone Dynamics and the Behaviour of Vessels Moored in Broken Ice. (Dr.Ing. Thesis)
MTA-98-125	Videiro, Paulo M., MK	Reliability Based Design of Marine Structures. (Dr.Ing. Thesis)
MTA-99-126	Mainçon, Philippe, MK	Fatigue Reliability of Long Welds Application to Titanium Risers. (Dr.Ing. Thesis)
MTA-99-127	Haugen, Elin M., MH	Hydroelastic Analysis of Slamming on Stiffened Plates with Application to Catamaran Wetdecks. (Dr.Ing. Thesis)
MTA-99-128	Langhelle, Nina K., MK	Experimental Validation and Calibration of Nonlinear Finite Element Models for Use in Design of Aluminium Structures Exposed to Fire. (Dr.Ing. Thesis)
MTA-99-129	Berstad, Are J., MK	Calculation of Fatigue Damage in Ship Structures. (Dr.Ing. Thesis)
MTA-99-130	Andersen, Trond M., MM	Short Term Maintenance Planning. (Dr.Ing. Thesis)
MTA-99-131	Tveiten, Bård Wathne, MK	Fatigue Assessment of Welded Aluminium Ship Details. (Dr.Ing. Thesis)

MTA-99-132	Søreide, Fredrik, MP	Applications of underwater technology in deep water archaeology. Principles and practice. (Dr.Ing. Thesis)
MTA-99-133	Tønnessen, Rune, MH	A Finite Element Method Applied to Unsteady Viscous Flow Around 2D Blunt Bodies With Sharp Corners. (Dr.Ing. Thesis)
MTA-99-134	Elvekrok, Dag R., MP	Engineering Integration in Field Development Projects in the Norwegian Oil and Gas Industry. The Supplier Management of Norne. (Dr.Ing. Thesis)
MTA-99-135	Fagerholt, Kjetil, MP	Optimeringsbaserte Metoder for Ruteplanlegging innen skipsfart. (Dr.Ing. Thesis)
MTA-99-136	Bysveen, Marie, MM	Visualization in Two Directions on a Dynamic Combustion Rig for Studies of Fuel Quality. (Dr.Ing. Thesis)
MTA-2000-137	Storteig, Eskild, MM	Dynamic characteristics and leakage performance of liquid annular seals in centrifugal pumps. (Dr.Ing. Thesis)
MTA-2000-138	Sagli, Gro, MK	Model uncertainty and simplified estimates of long term extremes of hull girder loads in ships. (Dr.Ing. Thesis)
MTA-2000-139	Tronstad, Harald, MK	Nonlinear analysis and design of cable net structures like fishing gear based on the finite element method. (Dr.Ing. Thesis)
MTA-2000-140	Kroneberg, André, MP	Innovation in shipping by using scenarios. (Dr.Ing. Thesis)
MTA-2000-141	Haslum, Herbjørn Alf, MH	Simplified methods applied to nonlinear motion of spar platforms. (Dr.Ing. Thesis)
MTA-2001-142	Samdal, Ole Johan, MM	Modelling of Degradation Mechanisms and Stressor Interaction on Static Mechanical Equipment Residual Lifetime. (Dr.Ing. Thesis)
MTA-2001-143	Baarholm, Rolf Jarle, MH	Theoretical and experimental studies of wave impact underneath decks of offshore platforms. (Dr.Ing. Thesis)
MTA-2001-144	Wang, Lihua, MK	Probabilistic Analysis of Nonlinear Wave-induced Loads on Ships. (Dr.Ing. Thesis)
MTA-2001-145	Kristensen, Odd H. Holt, MK	Ultimate Capacity of Aluminium Plates under Multiple Loads, Considering HAZ Properties. (Dr.Ing. Thesis)
MTA-2001-146	Greco, Marilena, MH	A Two-Dimensional Study of Green-Water Loading. (Dr.Ing. Thesis)
MTA-2001-147	Heggelund, Svein E., MK	Calculation of Global Design Loads and Load Effects in Large High Speed Catamarans. (Dr.Ing. Thesis)
MTA-2001-148	Babalola, Olusegun T., MK	Fatigue Strength of Titanium Risers – Defect Sensitivity. (Dr.Ing. Thesis)

MTA-2001-149	Mohammed, Abuu K., MK	Nonlinear Shell Finite Elements for Ultimate Strength and Collapse Analysis of Ship Structures. (Dr.Ing. Thesis)
MTA-2002-150	Holmedal, Lars E., MH	Wave-current interactions in the vicinity of the sea bed. (Dr.Ing. Thesis)
MTA-2002-151	Rognebakke, Olav F., MH	Sloshing in rectangular tanks and interaction with ship motions. (Dr.Ing. Thesis)
MTA-2002-152	Lader, Pål Furset, MH	Geometry and Kinematics of Breaking Waves. (Dr.Ing. Thesis)
MTA-2002-153	Yang, Qinzhen, MH	Wash and wave resistance of ships in finite water depth. (Dr.Ing. Thesis)
MTA-2002-154	Melhus, Øyvinn, MM	Utilization of VOC in Diesel Engines. Ignition and combustion of VOC released by crude oil tankers. (Dr.Ing. Thesis)
MTA-2002-155	Ronæss, Marit, MH	Wave Induced Motions of Two Ships Advancing on Parallel Course. (Dr.Ing. Thesis)
MTA-2002-156	Økland, Ole D., MK	Numerical and experimental investigation of whipping in twin hull vessels exposed to severe wet deck slamming. (Dr.Ing. Thesis)
MTA-2002-157	Ge, Chunhua, MK	Global Hydroelastic Response of Catamarans due to Wet Deck Slamming. (Dr.Ing. Thesis)
MTA-2002-158	Byklum, Eirik, MK	Nonlinear Shell Finite Elements for Ultimate Strength and Collapse Analysis of Ship Structures. (Dr.Ing. Thesis)
IMT-2003-1	Chen, Haibo, MK	Probabilistic Evaluation of FPSO-Tanker Collision in Tandem Offloading Operation. (Dr.Ing. Thesis)
IMT-2003-2	Skaugset, Kjetil Bjørn, MK	On the Suppression of Vortex Induced Vibrations of Circular Cylinders by Radial Water Jets. (Dr.Ing. Thesis)
IMT-2003-3	Chezian, Muthu	Three-Dimensional Analysis of Slamming. (Dr.Ing. Thesis)
IMT-2003-4	Buhaug, Øyvind	Deposit Formation on Cylinder Liner Surfaces in Medium Speed Engines. (Dr.Ing. Thesis)
IMT-2003-5	Tregde, Vidar	Aspects of Ship Design: Optimization of Aft Hull with Inverse Geometry Design. (Dr.Ing. Thesis)
IMT-2003-6	Wist, Hanne Therese	Statistical Properties of Successive Ocean Wave Parameters. (Dr.Ing. Thesis)
IMT-2004-7	Ransau, Samuel	Numerical Methods for Flows with Evolving Interfaces. (Dr.Ing. Thesis)
IMT-2004-8	Soma, Torkel	Blue-Chip or Sub-Standard. A data interrogation approach of identity safety characteristics of shipping organization. (Dr.Ing. Thesis)

IMT-2004-9	Ersdal, Svein	An experimental study of hydrodynamic forces on cylinders and cables in near axial flow. (Dr.Ing. Thesis)
IMT-2005-10	Brodtkorb, Per Andreas	The Probability of Occurrence of Dangerous Wave Situations at Sea. (Dr.Ing. Thesis)
IMT-2005-11	Yttervik, Rune	Ocean current variability in relation to offshore engineering. (Dr.Ing. Thesis)
IMT-2005-12	Fredheim, Arne	Current Forces on Net-Structures. (Dr.Ing. Thesis)
IMT-2005-13	Heggernes, Kjetil	Flow around marine structures. (Dr.Ing. Thesis)
IMT-2005-14	Fouques, Sebastien	Lagrangian Modelling of Ocean Surface Waves and Synthetic Aperture Radar Wave Measurements. (Dr.Ing. Thesis)
IMT-2006-15	Holm, Håvard	Numerical calculation of viscous free surface flow around marine structures. (Dr.Ing. Thesis)
IMT-2006-16	Bjørheim, Lars G.	Failure Assessment of Long Through Thickness Fatigue Cracks in Ship Hulls. (Dr.Ing. Thesis)
IMT-2006-17	Hansson, Lisbeth	Safety Management for Prevention of Occupational Accidents. (Dr.Ing. Thesis)
IMT-2006-18	Zhu, Xinying	Application of the CIP Method to Strongly Nonlinear Wave-Body Interaction Problems. (Dr.Ing. Thesis)
IMT-2006-19	Reite, Karl Johan	Modelling and Control of Trawl Systems. (Dr.Ing. Thesis)
IMT-2006-20	Smogeli, Øyvind Notland	Control of Marine Propellers. From Normal to Extreme Conditions. (Dr.Ing. Thesis)
IMT-2007-21	Storhaug, Gaute	Experimental Investigation of Wave Induced Vibrations and Their Effect on the Fatigue Loading of Ships. (Dr.Ing. Thesis)
IMT-2007-22	Sun, Hui	A Boundary Element Method Applied to Strongly Nonlinear Wave-Body Interaction Problems. (PhD Thesis, CeSOS)
IMT-2007-23	Rustad, Anne Marthine	Modelling and Control of Top Tensioned Risers. (PhD Thesis, CeSOS)
IMT-2007-24	Johansen, Vegar	Modelling flexible slender system for real-time simulations and control applications
IMT-2007-25	Wroldsen, Anders Sunde	Modelling and control of tensegrity structures. (PhD Thesis, CeSOS)
IMT-2007-26	Aronsen, Kristoffer Høye	An experimental investigation of in-line and combined inline and cross flow vortex induced vibrations. (Dr. avhandling, IMT)
IMT-2007-27	Gao, Zhen	Stochastic Response Analysis of Mooring Systems with Emphasis on Frequency-domain Analysis of Fatigue due to Wide-band Response Processes (PhD Thesis, CeSOS)

IMT-2007-28	Thorstensen, Tom Anders	Lifetime Profit Modelling of Ageing Systems Utilizing Information about Technical Condition. (Dr.ing. thesis, IMT)
IMT-2008-29	Berntsen, Per Ivar B.	Structural Reliability Based Position Mooring. (PhD-Thesis, IMT)
IMT-2008-30	Ye, Naiquan	Fatigue Assessment of Aluminium Welded Box-stiffener Joints in Ships (Dr.ing. thesis, IMT)
IMT-2008-31	Radan, Damir	Integrated Control of Marine Electrical Power Systems. (PhD-Thesis, IMT)
IMT-2008-32	Thomassen, Paul	Methods for Dynamic Response Analysis and Fatigue Life Estimation of Floating Fish Cages. (Dr.ing. thesis, IMT)
IMT-2008-33	Pákozdi, Csaba	A Smoothed Particle Hydrodynamics Study of Two-dimensional Nonlinear Sloshing in Rectangular Tanks. (Dr.ing.thesis, IMT)
IMT-2007-34	Grytøyr, Guttorm	A Higher-Order Boundary Element Method and Applications to Marine Hydrodynamics. (Dr.ing.thesis, IMT)
IMT-2008-35	Drummen, Ingo	Experimental and Numerical Investigation of Nonlinear Wave-Induced Load Effects in Containerships considering Hydroelasticity. (PhD thesis, CeSOS)
IMT-2008-36	Skejic, Renato	Maneuvering and Seakeeping of a Singel Ship and of Two Ships in Interaction. (PhD-Thesis, CeSOS)
IMT-2008-37	Harlem, Alf	An Age-Based Replacement Model for Repairable Systems with Attention to High-Speed Marine Diesel Engines. (PhD-Thesis, IMT)
IMT-2008-38	Alsos, Hagbart S.	Ship Grounding. Analysis of Ductile Fracture, Bottom Damage and Hull Girder Response. (PhD-thesis, IMT)
IMT-2008-39	Graczyk, Mateusz	Experimental Investigation of Sloshing Loading and Load Effects in Membrane LNG Tanks Subjected to Random Excitation. (PhD-thesis, CeSOS)
IMT-2008-40	Taghipour, Reza	Efficient Prediction of Dynamic Response for Flexible and Multi-body Marine Structures. (PhD-thesis, CeSOS)
IMT-2008-41	Ruth, Eivind	Propulsion control and thrust allocation on marine vessels. (PhD thesis, CeSOS)
IMT-2008-42	Nystad, Bent Helge	Technical Condition Indexes and Remaining Useful Life of Aggregated Systems. PhD thesis, IMT
IMT-2008-43	Soni, Prashant Kumar	Hydrodynamic Coefficients for Vortex Induced Vibrations of Flexible Beams, PhD thesis, CeSOS
IMT-2009-43	Amlashi, Hadi K.K.	Ultimate Strength and Reliability-based Design of Ship Hulls with Emphasis on Combined Global and Local Loads. PhD Thesis, IMT

IMT-2009-44	Pedersen, Tom Arne	Bond Graph Modelling of Marine Power Systems. PhD Thesis, IMT
IMT-2009-45	Kristiansen, Trygve	Two-Dimensional Numerical and Experimental Studies of Piston-Mode Resonance. PhD-Thesis, CeSOS
IMT-2009-46	Ong, Muk Chen	Applications of a Standard High Reynolds Number Model and a Stochastic Scour Prediction Model for Marine Structures. PhD-thesis, IMT
IMT-2009-47	Hong, Lin	Simplified Analysis and Design of Ships subjected to Collision and Grounding. PhD-thesis, IMT
IMT-2009-48	Koushan, Kamran	Vortex Induced Vibrations of Free Span Pipelines, PhD thesis, IMT
IMT-2009-49	Korsvik, Jarl Eirik	Heuristic Methods for Ship Routing and Scheduling. PhD-thesis, IMT
IMT-2009-50	Lee, Jihoon	Experimental Investigation and Numerical in Analyzing the Ocean Current Displacement of Longlines. Ph.d.-Thesis, IMT.
IMT-2009-51	Vestbøstad, Tone Gran	A Numerical Study of Wave-in-Deck Impact using a Two-Dimensional Constrained Interpolation Profile Method, Ph.d.thesis, CeSOS.
IMT-2009-52	Bruun, Kristine	Bond Graph Modelling of Fuel Cells for Marine Power Plants. Ph.d.-thesis, IMT
IMT 2009-53	Holstad, Anders	Numerical Investigation of Turbulence in a Skewed Three-Dimensional Channel Flow, Ph.d.-thesis, IMT.
IMT 2009-54	Ayala-Uraga, Efrén	Reliability-Based Assessment of Deteriorating Ship-shaped Offshore Structures, Ph.d.-thesis, IMT
IMT 2009-55	Kong, Xiangjun	A Numerical Study of a Damaged Ship in Beam Sea Waves. Ph.d.-thesis, IMT/CeSOS.
IMT 2010-56	Kristiansen, David	Wave Induced Effects on Floaters of Aquaculture Plants, Ph.d.-thesis, IMT/CeSOS.
IMT 2010-57	Ludvigsen, Martin	An ROV-Toolbox for Optical and Acoustic Scientific Seabed Investigation. Ph.d.-thesis IMT.
IMT 2010-58	Hals, Jørgen	Modelling and Phase Control of Wave-Energy Converters, Ph.d.thesis, CeSOS.
IMT 2010-59	Shu, Zhi	Uncertainty Assessment of Wave Loads and Ultimate Strength of Tankers and Bulk Carriers in a Reliability Framework, Ph.d.-thesis, IMT.
IMT 2010-60	Jakobsen, Ken-Robert G.	Turbulence Modeling of Transverse Flow on Ship Hulls in Shallow Water, Ph.d.thesis, IMT.
IMT 2010-61	Shao, Yanlin	Numerical Potential-Flow Studies on Weakly-Nonlinear Wave-Body Interactions with/without Small Forward Speed, Ph.d.thesis, IMT.